

ABSTRACT

Title of dissertation: ENHANCED TRANSPORT OF SPIN-ORBIT
COUPLED BOSE GASES IN DISORDERED
POTENTIALS

Yuchen Yue
Doctor of Philosophy, 2020

Dissertation directed by: Dr. Ian B. Spielman
Joint Quantum Institute,
National Institute of Standards and Technology
and the University of Maryland

Anderson localization is a single particle localization phenomena in disordered media that is accompanied by an absence of diffusion. Spin-orbit coupling (SOC) describes an interaction between a particle's spin and its momentum that directly affects its energy dispersion, for example creating dispersion relations with gaps and multiple local minima. We show theoretically that combining one-dimensional spin-orbit coupling with a transverse Zeeman field suppresses the effects of disorder, thereby increasing the localization length and conductivity. This increase results from a suppression of back scattering between states in the gap of the SOC dispersion relation. Here, we focus specifically on the interplay of disorder from an optical speckle potential and SOC generated by two-photon Raman processes in quasi-1D Bose-Einstein condensates. We first describe back-scattering using a Fermi's golden rule approach, and then numerically confirm this picture by solving the time-dependent 1D Gross Pitaevskii equation for a weakly interacting Bose-Einstein

condensate with SOC and disorder. We find that on the 10's of millisecond time scale of typical cold atom experiments moving in harmonic traps, initial states with momentum in the zero-momentum SOC gap evolve with negligible back-scattering, while without SOC these same states rapidly localize.

ENHANCED TRANSPORT OF SPIN-ORBIT COUPLED BOSE
GASES IN DISORDERED POTENTIALS

by

Yuchen Yue

Dissertation submitted to the Faculty of the Graduate School of the
University of Maryland, College Park in partial fulfillment
of the requirements for the degree of
Doctor of Philosophy
2020

Advisory Committee:
Professor Ian B. Spielman, Advisor
Professor Steven Rolston, Chair
Professor Edo Waks
Professor Jay Sau
Professor Trey Porto

© Copyright by
Yuchen Yue
2020

To my parents and grandparents

Acknowledgments

First of all, I would like to thank my parents and grandparents for everything they have done for me, and their love and support. I began to realize how important they are and how much I miss them after I studied in a foreign country for years.

Next, I would like to thank my Ph.D. advisor, Dr. Ian Spielman. Ian has been a great advisor. He is always patient in our discussions and always tries to explain physics most intuitively. He would draw nice sketches on the whiteboard which helps him explaining his idea. He would also come to the lab and dig into the hardware together with us and find out why something is not working. When I first joined the group, I had a hard time understanding him because he speaks extremely fast. Over the years, I got much better in communication and I learned a lot from him, not just physics, but also being optimistic when facing uncertainties and difficulties.

During the years, I worked with other members of the RbChip lab. Seiji Sugawa, Francisco Salces-Cárcoba, Andika Putra, Christopher Billington, and Emine Altuntas, thank you for making RbChip lab an enjoyable place to work. I miss the old times when we can have lunch together, especially after being quarantined at home for half a year in the Covid-19 pandemic.

Lastly, I would like to thank my girlfriend, Dr. Yuchen Yang, who also got her Ph.D. in 2020. We are together nearly the entire time of our Ph.D., we share not only our first name in English but our values of life. I'm very lucky to meet you.

Table of Contents

Dedication	ii
Acknowledgements	iii
Table of Contents	iv
List of Tables	vii
List of Figures	viii
List of Abbreviations	xiii
1 Theoretical description of Bose-Einstein condensates	1
1.1 Bose-Einstein statistics	2
1.1.1 Classical description of particles	2
1.1.2 Quantum description of particles	3
1.1.3 Distinguishability	4
1.1.4 Exchange symmetry of identical particles	4
1.1.5 Bosons, Fermions and spin statistics	5
1.1.6 Bose-Einstein statistics and non-interacting BEC	6
1.2 Manybody BEC system	8
1.2.1 Second quantization	8
1.2.2 GPE of scalar BEC	10
1.2.3 GPE of spinor BEC	12
2 Laser cooling and trapping of neutral atoms	15
2.1 Hyperfine Structures	16
2.1.1 Energy Level Splitting	16
2.1.2 Zeeman splitting of ^{87}Rb hyperfine ground states	18
2.2 Laser cooling techniques	23
2.2.1 A two level system interacting with the reservoir	23
2.2.2 Optical force	29
2.2.3 Doppler Cooling	33
2.2.4 Doppler Cooling Limit	35
2.2.5 Sub-Doppler Cooling	36
2.2.6 MOT	40
2.2.7 Dipole Trap and evaporative cooling	43

3	Spin-Orbit coupling and Anderson localization in a cold-atoms system	47
3.1	Spin-orbit coupling	48
3.1.1	The Origin of SOC in a solid-state system	48
3.1.2	SOC in cold atoms	49
3.1.3	Raman coupling Hamiltonian	50
3.2	Anderson Localization	55
3.2.1	Introduction to Anderson Localization	55
3.2.2	AL in cold atoms	58
4	Optical speckle, a Gaussian beam model	61
4.1	Gaussian beam equations with speckle	62
4.2	Correlation length	67
4.3	Impact of apertures	69
4.4	Field and intensity probability distribution	70
4.5	Simulated speckle and the comparison to experiment	71
5	Enhanced transport of spin-orbit-coupled Bose gases in disordered potentials	75
5.1	Scattering of an SOBEC from a speckle potential	76
5.1.1	Spinless atoms	78
5.1.2	Spin-orbit coupled atoms	80
5.1.3	Computed scattering rates	82
5.2	Numerical simulation of GPE	84
5.2.1	Gross-Pitaevskii equations	84
5.2.2	Single component systems	87
5.2.3	SOBECs	90
5.3	Conclusion	94
6	The evolution of BECs in disordered potentials	96
6.1	Optical design	98
6.1.1	Speckle beam design	98
6.1.2	Raman beams design	99
6.2	Evolution of spinless BEC under speckle pulsing	100
6.2.1	Short term speckle pulsing	104
6.2.2	Long term speckle pulsing	111
6.3	Transport of spinless BECs in speckle potentials	115
A	Calculation results of field-field correlation function	124
B	Derivation of the moments of random phase factors	126
C	Squared coupling strength between momentum states	129
D	Speckle beam width in the focal plane from a ray optics model	131
E	Second Chern number of a quantum-simulated non-Abelian Yang monopole	133

F	Equations of state from individual one-dimensional Bose gases	141
G	Spatial Coherence of Spin-Orbit-Coupled Bose Gases	155
	Bibliography	162

List of Tables

5.1 Simulation parameters	88
-------------------------------------	----

List of Figures

2.1	Energy splitting of the ^{87}Rb ground state and the first excited state.	18
2.2	Zeeman splitting of ^{87}Rb ground states $ F, m_F\rangle$.	22
2.3	A two level system with energy difference ω in a light field with frequency ν . $\delta = \nu - \omega$ is the detuning.	23
2.4	1D Doppler Cooling.	33
2.5	Energy levels of Na atoms ground state and the first excited state. The Clebsch-Gordon coefficients are labelled for each transition.	37
2.6	The polarization as a function of z in lin \perp lin scheme.	39
2.7	MOT. (a) A sketch of MOT, three pairs of counter propagating laser beams are combined with a pair of anti-Helmholtz coil. (b) Energy levels of $ J = 0\rangle$ and $ J = 1\rangle$, coupled by σ_+ and σ_- polarized beams.	42
2.8	Dipole evaporation. (a) A sketch of crossed dipole trap formed by two red detuned laser beams. (b) Dipole evaporative cooling process.	45
3.1	Raman coupling. (a). Two laser beams perpendicular to each other are detuned by $\Delta\omega_L$, they intersect at the atoms. (b). Hyperfine states coupled by Raman lasers.	51
3.2	The band structure of a two-level system with SOC, detuning $\delta = 0$. (a). The band structures with Ω_R ranging from 0 to $6E_R$. (b). The locations of the minima of the lower branch for different Ω_R .	54
4.1	Optical speckle schematic. (a) A collimated beam is transmitted through a rough medium and its intensity is measured in plane z . (b) The diverged beam after the rough medium is imaged by a lens at plane $z = z_L$ and f is the focal point of the lens. (c) Field-field correlation length for a Gaussian speckle beam initially with $\sigma = 100 \mu\text{m}$ and $w = 25 \text{ mm}$ as a function of propagation distance. The red curves plot $c_E(z)$ computed with (solid) and without (dashed) a lens with focal length $f = 100 \text{ mm}$ at $z_L = 25 \text{ mm}$.	63

4.2	Simulated and measured optical speckle. The columns in the figure correspond to: simulated speckle with uniform laser beam, simulated speckle from a Gaussian laser beam and measured speckle. In each column, the first row shows the intensity of the optical speckle field. The second row shows the PSD of the intensity shown in the first row (symbols). The red curve shows a fit of Eq. (4.20) to the data, along with the resulting k_c . The third row histograms the intensity from the first row.	72
5.1	Fermi's Golden Rule. Momentum are expressed in units of the single-photon recoil momentum k_R used to create SOC in (c). (a) Representative PSD for optical speckle with $k_c = 6k_R$. (b) Free particle dispersion relation. The dashed arrow marks the boundary above which the FGR rate vanishes, while the solid arrow provide an example with non-zero rate. (c) SOC dispersion relations computed for $\delta = 0$ add $\Omega_R = 1E_R$ colored according to the expectation value $\langle \sigma_z(q) \rangle$, with arrows marked as in (b). Note the transition through the gap in the dispersion relation at $E \approx E_R$ where the FGR rate is nearly zero.	77
5.2	Fermis golden rule scattering rate for $\Omega_R/E_R = 0, 0.5, 2.5$ and 4.0 . Left column shows SOC dispersion relations computed for each Ω_R , colored as in Fig. (5.1). Right column shows normalized scattering rate as a function of initial energy for the initial state $ q_0, -\rangle$ with $q_0 \geq q_{\min}$, i.e., in the bottom dispersion and to the right of the higher momentum local energy minimum. The backscattering rate is plotted in black and the forward scattering plotted in red.	83
5.3	Single-component GPE simulation with $k_c/k_R = 6$. (a). Representative disorder potential used in our simulations. The inset shows an expanded view with visible structure. (b) Density distributions. The filled red curve depicts the initial density distribution, while the black and red curves show the final-state density distributions for initial momenta $ k_0 = 0.2k_R\rangle$ and $ k_0 = 3.1k_R\rangle$, above and below $k_c/2$, respectively. (c) Mean momentum. $\langle k(t) \rangle$ averaged over 20 speckle realizations is plotted for a range of initial momentum in the range of 0 to $3.3k_R$, the $t = 0$ point of each curve marks the initial k_0 . (d) Deceleration. The colored symbols plot $k_f = \langle k(t = 16 \text{ ms}) \rangle$ as a function of k_0 along with their standard deviations, and the black line marks $k_f = k_0$ corresponding to ballistic motion.	89
5.4	Make SOC eigenstates $ q_0, -\rangle$. (a). The SOC dispersion relation with $\delta = 2\hbar^2(q_0 - q_{\min})k_R/m$, $\Omega_R = E_R$. The dashed line indicates the detuning $\Delta(q_{\min})$ between $ q_{\min}, -\rangle$ and $ q_{\min}, +\rangle$. (b). The SOC dispersion relation with $\delta = 0$, $\Omega_R = E_R$. The dashed line indicates the detuning $\Delta(q_0)$ between $ q_0, -\rangle$ and $ q_0, +\rangle$, with $q_0 = 2.0k_R$ as an example. δ in (a) is tuned such that $\Delta(q_{\min})$ is equal to $\Delta(q_0 = 2.0k_R)$ in (b).	91

5.5	Motion in the presence of speckle and SOC. The left column was computed without interactions and the right column added interactions. (a) and (b) Density distributions colored by their magnetization according to the color bar in Fig. 5.1. The shaded curve depicts the initial density distribution, while the remaining red and black curves were computed for $q_0 = 2.0k_R$ (in the SOC gap) and $q_0 = 1.2k_R$ (below the SOC gap), respectively. (c) and (d) Ensemble averaged final group velocity plotted as a function of initial group velocity for coupling strengths from $0.5E_R$ to $7.5E_R$, spaced by $1.0E_R$. The results in (c) and (d) were averaged over 20 random speckle realizations.	93
6.1	Optical design. (a). The design of optics viewed in two directions. OF denotes optical fiber. Lenses C_1 and C_2 are cylindrical lenses: C_1 focuses the beam in the vertical direction; and C_2 focuses the beam in the horizontal direction. L_1 is a spherical lens that collimates the beam. D is the optical diffuser that imprints random phase on the beam. L_2 is an aspherical lens that focuses the beam to the atoms labelled with A. (b) Experimental image of optical speckle with anisotropic correlation length.	97
6.2	Raman beams design. The optical diagram of Raman beams. We use a triangular prism to align two Raman beams, the distance between two Raman beams at the prism is mapped to the distance at the lens L_1 by two relay imaging systems. The prism is put on a transnational stage which can move in the perpendicular direction of the two incident Raman beams. By moving the prism, the distance between the two Raman beams can be changed which determines the angle θ_R .	101
6.3	Absorption images of atoms after the evolution under speckle potentials and TOF. The BECs are released from the dipole trap, the pulses of the speckle potentials are turned on immediately for a various amount of time, followed by TOF. The absorption images are stacked up horizontally according to the speckle pulse duration.	102
6.4	Simulation of short-term speckle pulsing. The left panel is for speckle potential with $k_c = 1.48k_r$, and the right panel for $k_c = 0.8k_r$. (a) and (b) verify the k_c of both speckle potentials by plotting their PSD. (c) and (d) are the momentum distribution of atoms after released from the dipole trap and evolve under speckle pulses for $50 \mu s$. The red curves are proportional to the corresponding PSD of the speckle potential. The momentum distribution is an average of 20 speckle realizations. (e) and (f) are the momentum distribution of atoms after released from the dipole trap and evolve under speckle pulses for $50 \mu s$ followed by a 20 ms free expansion. The results are averaged over 20 speckle realizations.	107

6.5	A sample of absorption images of atoms and analysis. The red square is a selected region of interest and the red arrow indicates the direction we take average. The masked and averaged spatial distribution of atoms (black curve) and a fitted Gaussian curve (blue dashed) are plotted below.	108
6.6	Momentum distribution after short-term speckle pulses and 18 mm TOF. (a). A few samples of momentum distribution of atoms without mask, along with fitted Gaussian curves to the masked momentum distribution. (b). The tails of the momentum distribution after short-term pulses of speckle potential with different PSD. The PSD of the speckle potentials are controlled by the iris sizes and the results are averaged for speckle pulsing time ranging from 80 μ s to 150 μ s.	109
6.7	The simulation and the experiments of the speckle beam pulsing. (a). The width of the momentum distribution of atoms evolving under the speckle potentials of different potential depth ranging from 0 to 1600 Hz. (b). The Gaussian width of atoms in the absorption images after TOF for different speckle pulsing duration.	114
6.8	Calibration of the average speckle potential depth. (a). In the numerical simulation, the average total energy inferred from the momentum distribution after 20 ms free evolution is plotted against the known average speckle potential depth. The red curve and the blue curve are for the speckle potentials with $k_c = 0.80k_r$ and $k_c = 1.48k_r$, respectively. The dashed line is diagonal. (b). In the experiment, the average total energy computed from long-term speckle pulsing data is plotted against the PD reading.	116
6.9	<i>insitu</i> absorption images of BECs with different dipole parameters. (a) A BEC with x trapping frequency of 21 Hz. (b) A BEC with x trapping frequency of 5.8 Hz	119
6.10	Center-of-mass motion in x direction of atoms during dipole oscillation. The blue dots show a full cycle of dipole oscillation without pulses of the speckle potentials. The orange dots show the dipole oscillation of atoms with the same initial velocity as the blue dots show, but with a 1 ms speckle pulse at 21 ms. The average speckle potential depth is ≈ 640 Hz.	120
6.11	Deceleration of atoms after a 1 ms pulse of the speckle potentials. The red circles are the results of measurements in the experiments. The average speckle potential depth inferred from the photo diode reading is ≈ 500 Hz. The blue curve and the yellow curve are the results of numerical simulations. The blue curve is the final velocities vs the initial velocities after evolving under speckle potentials with average potential depth of 800 Hz, and the yellow curve is for speckle potential with average potential depth of 500 Hz. Both the blue curve and the yellow curve are averaged over 20 speckle realizations and the error bars show the standard deviations. The purple line is diagonal.	123

D.1 A ray optics model to calculate the speckle beam width in the focal plane of a lens. 131

List of Abbreviations

SOC	Spin-orbit coupling
BEC	Bose-Einstein condensates
GPE	Gross-Pitaevskii equation
RWA	Rotating wave approximation
MOT	Magneto optical trap
AL	Anderson Localization
PSD	Power spectral density
CCF	Cross correlation function
SOBECs	Spin-orbit coupled BECs
FGR	Fermi's golden rule
TOF	Time-of-flight
PD	Photo diode

Chapter 1: Theoretical description of Bose-Einstein condensates

In this chapter, we discuss the fundamental theoretical description of non-interacting Bose-Einstein condensates (BEC) and interacting Bose-Einstein condensates.

The non-interacting BEC section (Sec. 1.1) starts from the difference in the description of particles between classical mechanics and quantum mechanics. Indistinguishability and the exclusion principle of identical quantum particles lead to dramatically different statistical properties from classical particles. Next, I briefly discuss the exchange symmetry along with the reason why it is related to particles' spin. After the discussion of exchange symmetry, I derive Bose-Einstein statistics and discuss how it leads to non-interacting BECs.

In the many-body BEC section (Sec. 1.2), I first introduce the second quantization description of many-body systems. Next, by making the mean-field approximation, I derive the Gross-Pitaevskii equation (GPE) for scalar and spinor bosonic systems.

1.1 Bose-Einstein statistics

1.1.1 Classical description of particles

Classical mechanics originate from Newtonian mechanics and have different but equivalent formulations. It assumes the position and velocity of an object can be measured and kept track of at any time. The dynamics of an object or a system of objects can be sufficiently described by their positions and velocities. For example, in one of the equivalent formulations, Hamiltonian mechanics [1], a classical system is described by a set of canonical coordinates $\vec{r} = (\vec{p}, \vec{q})$. Here $\vec{p} = (p_1, p_2, \dots, p_N)$ and $\vec{q} = (q_1, q_2, \dots, q_N)$, they are indexed by the N-dimensional frame of reference of the system. Hamiltonian $\mathcal{H} = \mathcal{H}(\vec{p}, \vec{q}, t)$ is a function of canonical coordinates and corresponds to total energy of a system. The dynamics of the system is governed by equations

$$\begin{aligned}\frac{d\vec{p}}{dt} &= -\frac{\partial \mathcal{H}}{\partial \vec{q}} \\ \frac{d\vec{q}}{dt} &= \frac{\partial \mathcal{H}}{\partial \vec{p}}\end{aligned}\tag{1.1}$$

Both \vec{p} and \vec{q} evolve with equation 1.1 deterministically and for a system of classical particles, each particle's trajectory can be traced during evolution, making them distinguishable from each other.

In classical statistical mechanics, the Maxwell-Boltzmann statistics describes the distribution of non-interacting particles in thermal equilibrium over energy states. The ensemble averaged number of particles in energy state ϵ_i is

$$n_i = \frac{g_i}{\exp\{(\epsilon_i - \mu)/k_B T\}}.\tag{1.2}$$

Here, g_i is the degeneracy of energy state ϵ_i , μ is the chemical potential which can be obtained from the conservation of particle number. k_B is the Boltzmann's constant and T is temperature.

1.1.2 Quantum description of particles

Quantum mechanics, formed by six postulates, is very powerful in explaining modern experiments in atomic, molecular, optical, and condensed matter physics and so on. It also introduces counter-intuitive concepts such as photons, matter-wave, and Pauli's exclusion principle. These concepts can not be well explained without a good understanding of the postulates.

As the first postulate states, a particle is described by its quantum state $|\Psi(t)\rangle$. $|\Psi(t)\rangle$ contains all the information about the particle and can be represented by projecting it in any complete basis. For example, $\Psi(\mathbf{r}, t) = \langle \mathbf{r} | \Psi(t) \rangle$ is defined as the spatial wave function of the particle. Since spatial states $\{|\mathbf{r}\rangle\}$ form a complete basis, wave function $\Psi(\mathbf{r}, t)$ is sufficient to represent state $|\Psi(t)\rangle$. Similarly, projecting $\Psi(t)$ in the basis of $\{|\mathbf{p}\rangle\}$, we can define wave functions in momentum space $\Psi(\mathbf{p}, t) = \langle \mathbf{p} | \Psi(t) \rangle$. As postulate four states, for a particle in state $|\Psi(t)\rangle$, without measurements, the information associated with the classical variables \mathbf{r} and \mathbf{p} are the probability of the particle being in position \mathbf{r} and momentum \mathbf{p} . It is not possible to know the position and momentum of the particle without measurements. Moreover, as postulate five states, immediately after the measurement of an observable, the state collapse to an eigenstate of the observable, meaning after a measurement, the

particle's state may be changed.

1.1.3 Distinguishability

For a group of identical quantum particles, their spatial states can overlap at any time. And when they do, the lack of information about their positions and the inability to do measurements without changing their states make it in principle impossible to track the particles. And thus, in quantum mechanics, identical particles are indistinguishable. This indistinguishability has a fundamental effect on the statistics of quantum particles.

1.1.4 Exchange symmetry of identical particles

For a group of identical particles, the many-body state describing the system should not have any measurable difference exchanging any two particles of them. In quantum mechanics, a state is determined up to a phase factor. For a state $|\Psi(t)\rangle$, $e^{i\theta} |\Psi(t)\rangle$ does not have any measurable difference for any $\theta \in \mathbb{R}$. So for a two-particle state $|\psi_1\psi_2\rangle$, exchange the two particles, in the most general case, the two-particle state should become $e^{i\theta} |\psi_2\psi_1\rangle$. People may argue that exchanging particles twice the state should return, $e^{i2\theta} = 1$, but it is not rigorous. It was introduced as symmetry postulate that $e^{i\theta}$ can only take the value of $+1$ or -1 , meaning the two-particle state can only be symmetric or anti-symmetric. It has deep consequences in particle statistics and is in good agreement with experimental facts. However, its theoretical justification remains unclear. In 1977, J.M.Leinass

and J. Myrheim introduced in their paper [2] a quantization formalism, in which the restriction on wave function to be either symmetric or antisymmetric appears in a natural way, without having to add any additional constraints. However, this is true only when space is at least three-dimensional. In one or two dimensions, $e^{i\theta}$ can take other values. Frank Wilczek invented the term "anyon" to describe this kind of particle and they are important in understanding the fractional quantum Hall effect.

1.1.5 Bosons, Fermions and spin statistics

In three dimensional space, particles' wave function can only be symmetric or anti-symmetric. The symmetry of the wave function is determined by the particles' spin. A particle is called Boson if it has an integer spin and Fermion if it has a half-integer spin. In consequence, the wave functions of Bosons and Fermions are symmetric and anti-symmetric, respectively. The spin statistics theorem is first formulated in 1939 by Markus Fierz [3] and rederived in a more systematic way in 1940 by Wolfgang Pauli [4]. A more conceptual argument was provided in 1950 by Julian Schwinger. It is fascinating and very non-intuitive how particles' spin determines their exchange symmetry. As Feynman commented in his book *Feynman Lectures on Physics* [5]: *An explanation has been worked out by Pauli from complicated arguments of QFT and relativity. But we have not found a way of reproducing his arguments on an elementary level. This probably means that we do not have a complete understanding of the fundamental principle involved.*

1.1.6 Bose-Einstein statistics and non-interacting BEC

Quantum statistics differ from classical statistics in two aspects, indistinguishability and exchange symmetry.

For a two-particle wave function $\psi(\mathbf{r}_1, \mathbf{r}_2)$, if the two particles are Fermions, they can not occupy the same state. $\psi(\mathbf{r}_1, \mathbf{r}_2) = -\psi(\mathbf{r}_2, \mathbf{r}_1)$, if $\psi(\mathbf{r}_1, \mathbf{r}_2) = \psi(\mathbf{r}_2, \mathbf{r}_1)$, $\psi(\mathbf{r}_1, \mathbf{r}_2) = 0$. For Bosons, this is not the case. Any number of Bosons can occupy the same state and the system has the lowest energy when all the Bosons are in the ground state.

The Bose-Einstein distribution can be derived from the principle of maximum entropy. A Boson system with N particles are distributed to states $\{|\epsilon_i\rangle\}$, each state $|\epsilon_i\rangle$ has degeneracy g_i and it is occupied by n_i particles. The number of micro-state is

$$\Omega(\{n_i\}) = \prod_i \frac{(n_i + g_i - 1)!}{n_i!(g_i - 1)!}. \quad (1.3)$$

Maximizing $\Omega(\{n_i\})$ under the constraints $\sum_i n_i = N$ and $\sum_i n_i \epsilon_i = U$, we can derive Bose-Einstein distribution

$$n_i = \frac{1}{\exp\{-\alpha - \beta \epsilon_i\} - 1}, \quad (1.4)$$

α and β are the Lagrange multipliers. From constraints $\sum_i n_i = N$ and $\sum_i n_i \epsilon_i = U$, it can be determined α is chemical potential μ over $k_B T$ and β is $-1/k_B T$ where k_B is Boltzmann constant and T is temperature.

To find out how does this distribution lead to Bose-Einstein condensates, we need to revisit the constraints. For a system of particles in a box of volume V . The

energy density of states is

$$g(\epsilon) = \frac{V}{4\pi^2} \left(\frac{2m}{\hbar}\right)^{3/2} \sqrt{\epsilon} \quad (1.5)$$

Replacing the sum in $\sum_i n_i = N$ with integral, we get

$$\frac{V}{4\pi^2} \left(\frac{2m}{\hbar}\right)^{3/2} \int_0^\infty \frac{\sqrt{\epsilon}}{\exp\{(\epsilon - \mu)/k_B T\} - 1} d\epsilon = N \quad (1.6)$$

Denote the integral as $I(\mu)$

$$I(\mu) = \int_0^\infty \frac{\sqrt{\epsilon}}{\exp\{(\epsilon - \mu)/k_B T\} - 1} d\epsilon \quad (1.7)$$

For Eq. (1.6) to hold, $I(\mu)$ should be a constant, and μ should be a function of T . As T decreases, μ should increase to keep $I(\mu)$ constant. But μ can not go positive because in that case, for states $\epsilon_i - \mu < 0$, n_i will be negative. So as T decreases to some critical temperature T_c , μ increases to 0 to keep $I(\mu)$ constant. As T continue decreasing, μ can not increase anymore and we have

$$\frac{V}{4\pi^2} \left(\frac{2m}{\hbar}\right)^{3/2} \int_0^\infty \frac{\sqrt{\epsilon}}{\exp\{(\epsilon - \mu)/k_B T\} - 1} d\epsilon < N \quad (1.8)$$

Where are the missing particles? The answer is they are condensed in the ground state with zero energy. If we look at the density of state $g(\epsilon)$, it is zero for the ground state. When T is high, the number of particles that are in the ground state is negligible, so the integral counts all the particles and equals N . When $T < T_c$, μ is zero, a significant amount of particles start to occupy the ground state, and the missed particles will cause the loss of atoms counts.

The critical temperature can be calculated from Eq. (1.6) with $\mu = 0$.

$$T_c = \frac{2\pi\hbar^2}{mk_B} \left(\frac{N}{\eta(3/2)V}\right)^{2/3} \quad (1.9)$$

where $\eta(x)$ is Riemann zeta function. And it can be shown the fraction of particles in the ground state is a function of T and T_c

$$\frac{N_0}{N} = 1 - \left(\frac{T}{T_c}\right)^{3/2}. \quad (1.10)$$

1.2 Manybody BEC system

1.2.1 Second quantization

An interacting system can be described by the second quantization Hamiltonian. In the second quantization framework, particles in a system are described by creation and annihilation operators on the basis of many-body Fock states. Creation operators \hat{a}_k^\dagger creates a particle in the Fock state $|n_1, \dots, n_k, \dots\rangle$ while annihilation operators \hat{a}_k annihilates a particle in the Fock state $|n_1, \dots, n_k, \dots\rangle$.

$$\begin{aligned} \hat{a}_k^\dagger |n_1, \dots, n_k, \dots\rangle &= \sqrt{n_k + 1} |n_1, \dots, n_k + 1, \dots\rangle \\ \hat{a}_k |n_1, \dots, n_k, \dots\rangle &= \sqrt{n_k} |n_1, \dots, n_k - 1, \dots\rangle \end{aligned} \quad (1.11)$$

With a change of basis, the spatial creation and annihilation operators can be defined as

$$\begin{aligned} \hat{\psi}(\vec{r}) &= \sum_k \hat{a}_k \langle \vec{r} | \vec{k} \rangle = \sum_k \hat{a}_k \frac{\exp\{i\vec{k} \cdot \vec{r}\}}{\sqrt{V}} \\ \hat{\psi}^\dagger(\vec{r}) &= \sum_k \hat{a}_k^\dagger \langle \vec{r} | \vec{k} \rangle = \sum_k \hat{a}_k^\dagger \frac{\exp\{-i\vec{k} \cdot \vec{r}\}}{\sqrt{V}}. \end{aligned} \quad (1.12)$$

$\hat{\psi}^\dagger(\vec{r})$ and $\hat{\psi}(\vec{r})$ creates and annihilates a particle at spatial coordinate \vec{r} . Operator $\hat{N}_k = \hat{a}_k^\dagger \hat{a}_k$ counts the number of particles in the momentum state $|k\rangle$. The two-

particle operator is defined as

$$\begin{aligned}\hat{V}_{int} &= \frac{1}{2} \sum_{i \neq j} \hat{N}_i \hat{N}_j V_{ij} + \frac{1}{2} \sum_i \hat{N}_i (\hat{N}_i - 1) V_{ii} \\ &= \frac{1}{2} \sum_{i,j} (\hat{N}_i \hat{N}_j - \hat{N}_i \delta_{ij}) V_{ij}\end{aligned}\tag{1.13}$$

where V_{ij} is the interaction between particles in states $|i\rangle$ and $|j\rangle$. From the orthogonality of Fock states and Pauli's exclusion principle, we can derive the commutators of creation and annihilation operators for both Bosons and Fermions. For Bosons,

$$\begin{aligned}[\hat{a}_i, \hat{a}_j^\dagger] &= \delta_{ij} \\ [\hat{a}_i, \hat{a}_j] &= [\hat{a}_i^\dagger, \hat{a}_j^\dagger] = 0\end{aligned}\tag{1.14}$$

where $[A, B] = AB - BA$ is the commutator of operators A and B . For Fermions,

$$\begin{aligned}\{\hat{a}_i, \hat{a}_j^\dagger\} &= \delta_{ij} \\ \{\hat{a}_i, \hat{a}_j\} &= \{\hat{a}_i^\dagger, \hat{a}_j^\dagger\} = 0\end{aligned}\tag{1.15}$$

where $\{A, B\} = AB + BA$ is the anti-commutator of operators A and B . With the change of basis, we can also obtain the commutation and anti-commutation relations of field operators $\hat{\psi}(\vec{r})$ and $\hat{\psi}^\dagger(\vec{r})$. For Bosons,

$$\begin{aligned}[\hat{\psi}(\vec{r}'), \hat{\psi}^\dagger(\vec{r}'')] &= \delta^3(\vec{r}' - \vec{r}'') \\ [\hat{\psi}(\vec{r}'), \hat{\psi}(\vec{r}'')] &= [\hat{\psi}^\dagger(\vec{r}'), \hat{\psi}^\dagger(\vec{r}'')] = 0.\end{aligned}\tag{1.16}$$

For Fermions,

$$\begin{aligned}\{\hat{\psi}(\vec{r}'), \hat{\psi}^\dagger(\vec{r}'')\} &= \delta^3(\vec{r}' - \vec{r}'') \\ \{\hat{\psi}(\vec{r}'), \hat{\psi}(\vec{r}'')\} &= \{\hat{\psi}^\dagger(\vec{r}'), \hat{\psi}^\dagger(\vec{r}'')\} = 0.\end{aligned}\tag{1.17}$$

With the commutators, we can rewrite the interaction operator \hat{V} ,

$$\hat{V}_{int} = \frac{1}{2} \sum_{i,j} \hat{a}_i^\dagger \hat{a}_j^\dagger V_{ij} \hat{a}_j \hat{a}_i,\tag{1.18}$$

which is valid for both Bosons and Fermions.

In general, the Hamiltonian of a system is

$$\hat{H} = \sum_i \frac{\hat{\mathbf{p}}_i^2}{2m} + \hat{V}(\hat{\mathbf{r}}_i) + \hat{V}_{int} \quad (1.19)$$

in the representation of field operators, it takes the form

$$\hat{H} = \int d\mathbf{r} \hat{\Psi}^\dagger(\mathbf{r}) \left[-\frac{\hbar^2}{2m} \nabla^2 + \hat{V}(\mathbf{r}) \right] \hat{\Psi}(\mathbf{r}) \quad (1.20)$$

$$+ \frac{1}{2} \int d\mathbf{r}' d\mathbf{r}'' d\mathbf{r}''' d\mathbf{r}'''' \hat{\Psi}^\dagger(\mathbf{r}') \hat{\Psi}^\dagger(\mathbf{r}'') \langle \mathbf{r}' \mathbf{r}'' | \hat{V}_{int} | \mathbf{r}''' \mathbf{r}'''' \rangle \hat{\Psi}(\mathbf{r}''') \hat{\Psi}(\mathbf{r}'''') \quad (1.21)$$

1.2.2 GPE of scalar BEC

For dilute and cold gases, it is proper to approximate the interactions between atoms with two-body collisions. At low energy, the two-body collision interactions can be represented by the s-wave pseudopotential which is characterized by s-wave scattering length.

$$\hat{V}_{int} = g\delta(\mathbf{r}' - \mathbf{r}''), \quad (1.22)$$

the constant g is a function of scattering length a ,

$$g = \frac{4\pi\hbar^2 a}{m}. \quad (1.23)$$

The Hamiltonian of the cold gases system takes the form

$$\begin{aligned} \hat{H} = & \int d\mathbf{r} \hat{\Psi}^\dagger(\mathbf{r}) \left[-\frac{\hbar^2}{2m} \nabla^2 + \hat{V}(\mathbf{r}) \right] \hat{\Psi}(\mathbf{r}) \\ & + \frac{g}{2} \int d\mathbf{r} \hat{\Psi}^\dagger(\mathbf{r}) \hat{\Psi}^\dagger(\mathbf{r}) \hat{\Psi}(\mathbf{r}) \hat{\Psi}(\mathbf{r}), \end{aligned} \quad (1.24)$$

and the dynamics of the field operators obey Heisenberg equation

$$\begin{aligned} i\hbar \frac{\partial}{\partial t} \hat{\Psi}(\mathbf{r}, t) &= [\hat{\Psi}, \hat{H}] \\ &= \left[-\frac{\hbar^2}{2m} \nabla^2 + \hat{V}(\mathbf{r}) + g \hat{\Psi}^\dagger(\mathbf{r}, t) \hat{\Psi}(\mathbf{r}, t) \right] \hat{\Psi}(\mathbf{r}, t) \end{aligned} \quad (1.25)$$

Bogoliubov formulated the mean-field approach [6] to solving the cold dilute gases system by expanding the field operators to the first order,

$$\hat{\Psi}(\mathbf{r}, t) = \Psi(\mathbf{r}, t) + \delta\hat{\Psi}(\mathbf{r}, t) \quad (1.26)$$

$\Psi(\mathbf{r}, t)$ is the mean-field, the expectation value of field operator $\hat{\Psi}(\mathbf{r}, t)$, $\Psi(\mathbf{r}, t) = \langle \hat{\Psi}(\mathbf{r}, t) \rangle$. And $\delta\hat{\Psi}(\mathbf{r}, t)$ is the excitation term which describes the variation of the field operator around its expectation value. $\Psi(\mathbf{r}, t)$ is a classical field and is often called the wave function of the condensate. When excitation is small and can be neglected, we arrive at the dynamics of the classical field

$$i\hbar \frac{\partial}{\partial t} \Psi(\mathbf{r}, t) = \left[-\frac{\hbar^2}{2m} \nabla^2 + V(\mathbf{r}) + g|\Psi(\mathbf{r}, t)|^2 \right] \Psi(\mathbf{r}, t) \quad (1.27)$$

This equation is known as the Gross-Pitaevskii equation (GPE) which is derived by Gross [7] and Pitaevskii [8] independently.

To obtain the ground state of the condensate, we can write the function $\Psi(\mathbf{r}, t)$ as $\Psi(\mathbf{r}, t) = \psi(\mathbf{r})e^{-i\mu t/\hbar}$. Then the GPE becomes

$$\mu\psi(\mathbf{r}) = \left[-\frac{\hbar^2}{2m} \nabla^2 + V(\mathbf{r}) + g|\psi(\mathbf{r})|^2 \right] \psi(\mathbf{r}) \quad (1.28)$$

μ is chemical potential and is subject to the conservation of particle numbers

$$\int d\mathbf{r} |\psi(\mathbf{r})|^2 = N \quad (1.29)$$

At low temperature, $T \ll T_c$, the chemical potential of the system is dominated by the interaction energy which is much larger than the kinetic energy, since the majority of atoms are in their ground states $|k = 0\rangle$. By making the Thomas-Fermi approximation, we can neglect the kinetic energy term and the ground state takes a simple form

$$\psi(\mathbf{r}) = \sqrt{\frac{\mu - V(\mathbf{r})}{g}} \quad (1.30)$$

This is the Thomas-Fermi wave function and given external potential $V(\mathbf{r})$, chemical potential μ can be calculated under the constraint of atom-number conservation.

1.2.3 GPE of spinor BEC

When we add the spin degree of freedom, we need to consider the spin-dependent potentials and the spin-spin interactions in the two-particle scattering processes. The two-body interaction takes the form

$$\hat{V}_{int}(\mathbf{r}_1, \mathbf{r}_2) = (c_0 + c_2 \vec{F}_1 \cdot \vec{F}_2) \delta(\mathbf{r}_1 - \mathbf{r}_2) \quad (1.31)$$

The total angular momentum is conserved in the processes of two spinor collisions. And for two spin-1 particles, their total angular momentum F can be 0 or 2, corresponding to scattering channel 0 and channel 2. The sign of the coefficient c_2 determines whether the system is ferromagnetic (FM) or anti-ferromagnetic (AFM). The s-wave pseudo-potential for both channels is

$$V_{int}^F(\mathbf{r}, \mathbf{r}') = g_F \delta(\mathbf{r}, \mathbf{r}') \quad (1.32)$$

where

$$g_F = \frac{4\pi\hbar^2}{M} a_F \quad (1.33)$$

and $F \in \{0, 2\}$, a_F is the scattering length. To calculate the coefficients c_0 and c_2 , we need to project the two spin states to the total spin states.

In second quantization representation, the interaction of a spin-1 system [9] is

$$\hat{V}_{int} = \frac{1}{2} \sum_{m_1, m_2, m'_1, m'_2} \int d\mathbf{r} C_{m_1, m_2}^{m'_1, m'_2} \hat{\Psi}_{m_1}^\dagger(\mathbf{r}) \hat{\Psi}_{m_2}^\dagger(\mathbf{r}) \hat{\Psi}_{m'_1}(\mathbf{r}) \hat{\Psi}_{m'_2}(\mathbf{r}) \quad (1.34)$$

where

$$C_{m_1, m_2}^{m'_1, m'_2} = \frac{4\pi\hbar^2}{M} \sum_{F=0,2} a_F \langle m_1; m_2 | \hat{P}_F | m'_1; m'_2 \rangle. \quad (1.35)$$

Here the operator

$$\hat{P}_F = \sum_{m_F=-F}^F |F, m_F\rangle \langle F, m_F| \quad (1.36)$$

projects the two-body angular momentum states onto the total angular momentum basis.

Back to the two-body angular momentum basis, the interaction can be written in the form

$$\hat{V}_{int} = \frac{1}{2} \sum_{m_1, m_2} \int d\mathbf{r} \hat{\Psi}_{m_1}^\dagger(\mathbf{r}) \hat{\Psi}_{m_2}^\dagger(\mathbf{r}) \hat{\Psi}_{m_1}(\mathbf{r}) \hat{\Psi}_{m_2}(\mathbf{r}) (c_0 + c_2 \vec{F}_{m_1} \cdot \vec{F}_{m_2}). \quad (1.37)$$

Here,

$$c_0 = \frac{4\pi\hbar^2}{M} \frac{g_0 + 2g_2}{3}, \quad \text{and} \quad c_2 = \frac{4\pi\hbar^2}{M} \frac{g_2 - g_0}{3}. \quad (1.38)$$

The Hamiltonian of the system is

$$\hat{H} = \sum_{m_1, m_2} \int d\mathbf{r} \hat{\Psi}_{m_1}^\dagger(\mathbf{r}) \left[-\frac{\hbar^2}{2m} \nabla^2 \delta_{m_1, m_2} + \hat{U}_{m_1, m_2}(\mathbf{r}) \right] \hat{\Psi}_{m_2}(\mathbf{r}) + \hat{V}_{int}. \quad (1.39)$$

$\hat{U}_{m_1, m_2}(\mathbf{r})$ can be any spin dependent potential. For example, Raman coupling is widely used in a BEC system as one way to realize the spin-orbit coupling. Intuitively, in a two-photon process, a particle in the spin state $|m_F\rangle$ absorbs a photon

with momentum k_R and emits a photon with momentum $-k_R$. The spin state jumps to $|m_F + 1\rangle$ and acquires momentum $2k_R$. In the reverse process, it jumps from $|m_F + 1\rangle$ to $|m_F\rangle$ and acquires momentum $-2k_R$. States $|k + 2k_R, m_F + 1\rangle$ and $|k - 2k_R, m_F\rangle$ are coupled.

From Heisenberg equation and the mean field approximation, we can derive the spin-1 GPE

$$\begin{aligned}
i\hbar\partial_t\psi_1 &= -\frac{\hbar^2}{2m}\nabla^2\psi_1 + \sum_{m_F}\hat{U}_{m_F,1}\psi_{m_F} + c_0n\psi_1 + c_2(n_1 + n_0 - n_{-1})\psi_1 + c_2\psi_{-1}^*\psi_0\psi_0 \\
i\hbar\partial_t\psi_0 &= -\frac{\hbar^2}{2m}\nabla^2\psi_0 + \sum_{m_F}\hat{U}_{m_F,0}\psi_{m_F} + c_0n\psi_0 + c_2(n_1 + n_{-1})\psi_0 + 2c_2\psi_0^*\psi_1\psi_{-1} \\
i\hbar\partial_t\psi_{-1} &= -\frac{\hbar^2}{2m}\nabla^2\psi_{-1} + \sum_{m_F}\hat{U}_{m_F,-1}\psi_{m_F} + c_0n\psi_{-1} + c_2(n_{-1} + n_0 - n_1)\psi_{-1} + c_2\psi_1^*\psi_0\psi_0
\end{aligned}$$

Chapter 2: Laser cooling and trapping of neutral atoms

Laser cooling techniques eventually lead to the observation of BECs in 1995. The first BEC was created by Eric Cornell, Carl Wieman, and co-workers at JILA on 5 June 1995 [10]. They cooled a dilute vapor of approximately two thousand ^{87}Rb atoms to below 170 nK using laser cooling and magnetic evaporative cooling. About four months later, an independent effort led by Wolfgang Ketterle at MIT condensed ^{23}Na [11]. The achievements of laser cooling and trapping won laser cooling pioneers Steven Chu, Claude Cohen-Tannoudji, and William D. Phillips the 1997 Nobel Prize in Physics. And Cornell, Wieman, and Ketterle won the 2001 Nobel Prize in Physics for their observations of BECs.

After more than twenty years, the research field of cold atoms is prosperous. The development of laser cooling techniques has made it possible to make stable and reliable BECs. The highly controllable optical and magnetic potentials, the tunable interaction between particles, and precision measurement techniques have made the BEC system a great platform for quantum simulation and quantum computation.

The Nobel Lecture of W. D. Phillips, *Laser cooling and trapping of neutral atoms* [12] tells a great story of the development of laser cooling techniques since the late 1970s. It is recommended for readers who not only want to learn the

laser cooling techniques but also take a close view of how researchers approach new physics and technology. It is aspiring to learn the mature technology that cold atom researcher uses on a daily basis nowadays results from the intelligence, efforts, and persistent pursuit of the early generations of physicists.

In this chapter, we use ^{87}Rb as an example. Start from its energy levels, its interaction with the light and the magnetic field, and then discuss the laser cooling techniques that are essential to make BECs.

2.1 Hyperfine Structures

2.1.1 Energy Level Splitting

The energy splitting of ^{87}Rb ground state and the first excited state can be found in Fig. (2.1) from [13], it is a great source of ^{87}Rb D lines data.

For the ground state of ^{87}Rb , the quantum number of orbital angular momentum \mathbf{L} is 0 and the first excited state $L = 1$. When we consider the spin of the single electron in the outer shell of the atom, $S = 1/2$, and the interaction between spin and orbital angular momentum $\mathbf{L} \cdot \mathbf{S}$, the excited state splits into a fine-structure doublet. The eigenvalue of total electron angular momentum

$$\mathbf{J} = \mathbf{L} + \mathbf{S} \tag{2.1}$$

becomes a good quantum number. For the ground state, $L = 0$, $S = 1/2$, and $J = 1/2$. The ground state is labeled as $5^2S_{1/2}$ where the atomic states are described

by term symbols of the form

$${}^{2S+1}L_J. \quad (2.2)$$

The interaction between the spin and the orbital angular momentum splits the excited state into doublet $5^2P_{1/2}$ and $5^2P_{3/2}$. The transition between the ground state and the excited state is split into two lines, D1 line ($5^2S_{1/2} \rightarrow 5^2P_{1/2}$) and D2 line ($5^2S_{1/2} \rightarrow 5^2P_{3/2}$).

Accounting for nuclear angular momentum \mathbf{I} , the states further split into hyperfine states and are represented on the basis of the total angular momentum

$$\mathbf{F} = \mathbf{J} + \mathbf{I}. \quad (2.3)$$

The quantum number of the nuclear spin of ${}^{87}\text{Rb}$ is $3/2$, as shown in Fig. (2.1), the ${}^{87}\text{Rb}$ ground state $5^2S_{1/2}$ splits into hyperfine states $|F = 1\rangle$ and $|F = 2\rangle$. The excited state $5^2P_{1/2}$ splits into hyperfine states $|F = 1\rangle$ and $|F = 2\rangle$. And the excited state $5^2P_{3/2}$ splits into hyperfine states $|F = 0\rangle$, $|F = 1\rangle$, $|F = 2\rangle$ and $|F = 3\rangle$. The Hamiltonian that leads to the hyperfine split consists of magnetic dipole interaction and electric quadrupole interaction,

$$\hat{H}_{hfs} = A_{hfs}\mathbf{I} \cdot \mathbf{J} + B_{hfs} \frac{3(\mathbf{I} \cdot \mathbf{J})^2 + 3/2\mathbf{I} \cdot \mathbf{J} - I(I+1)J(J+1)}{2I(2I-1)2J(2J-1)}. \quad (2.4)$$

Here A_{hfs} is the magnetic dipole constant and B_{hfs} is the electric quadrupole constant. The hyperfine energy splits for the states are

$$\Delta E_{hfs} = \frac{1}{2}A_{hfs}K + B_{hfs} \frac{3/2K(K+1) - 2I(I+1)J(J+1)}{2I(2I-1)2J(2J-1)} \quad (2.5)$$

where

$$K = F(F+1) - I(I+1) - J(J+1). \quad (2.6)$$

The numerical results of hyperfine states energy can be found in Fig. (2.1), they are calculated given the experimental measurement of A_{hfs} and B_{hfs} [14–16].

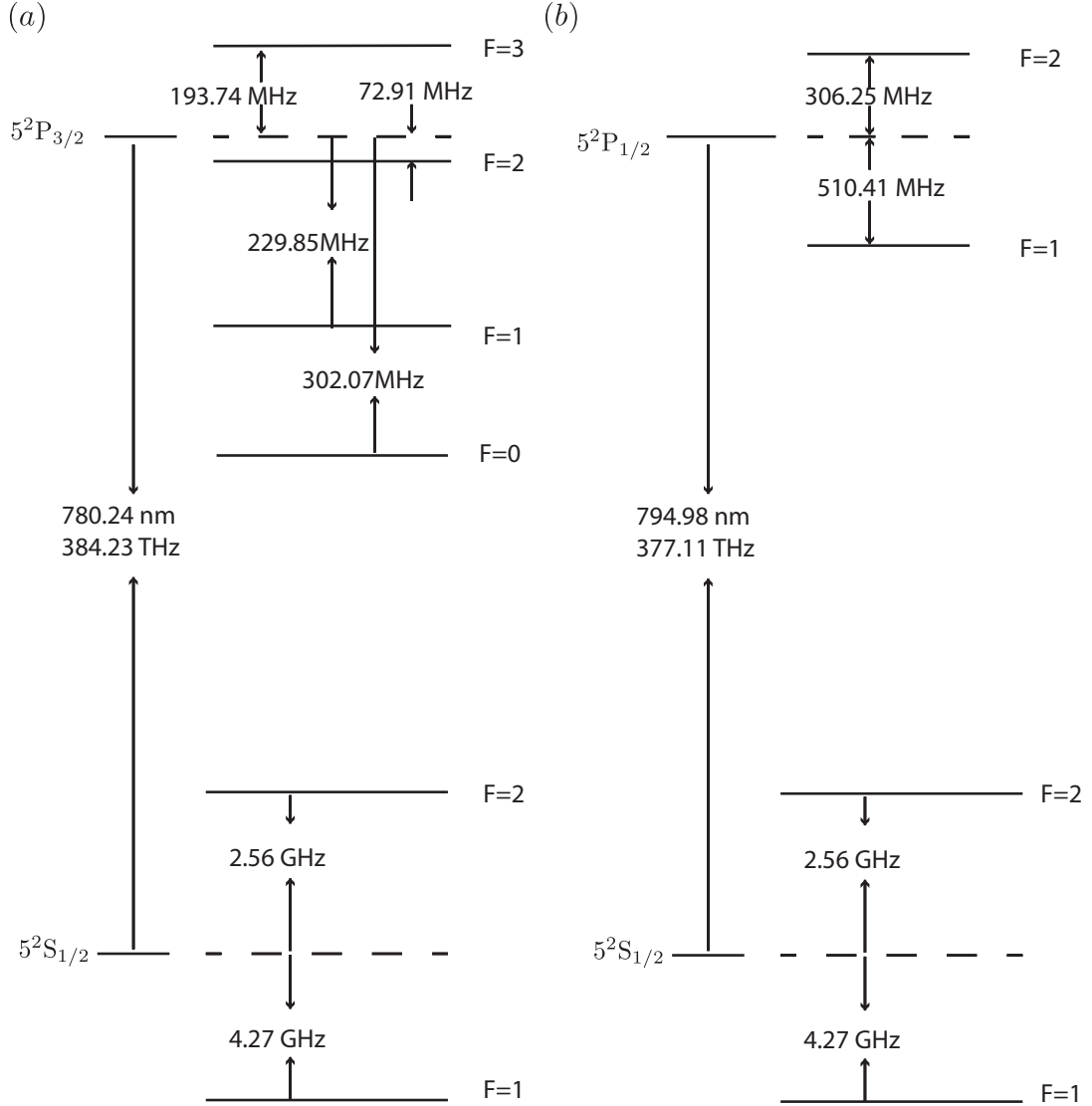


Figure 2.1: Energy splitting of the ^{87}Rb ground state and the first excited state.

2.1.2 Zeeman splitting of ^{87}Rb hyperfine ground states

The angular momentum of ^{87}Rb interacts with the external magnetic field and the hyperfine states split into sub-states. Here we use perturbation theory to

calculate the energy of each sub-states of ^{87}Rb ground state.

For the ^{87}Rb ground state, $J = 1/2$ and $I = 3/2$. It has hyperfine states $|F = 1\rangle$ and $|F = 2\rangle$. The Hamiltonian with external magnetic field is

$$\hat{H} = \hat{H}_{hfs} + (\mu_B g_J \vec{J} + \mu_N g_I \vec{I}) \cdot \vec{B}. \quad (2.7)$$

Here $\mu_B = 9.27 \times 10^{-24} \text{ J} \cdot \text{T}^{-1}$ is Bohr magneton, the natural unit for expressing the magnetic moment of an electron caused by either its orbital or spin angular momentum. $\mu_N = 5.05 \times 10^{-27} \text{ J} \cdot \text{T}^{-1}$ is the nuclear magneton. g_J and g_I are landé g-factors. For ^{87}Rb ground state, $g_J \approx 2.00233$ and $g_I \approx -0.00099$.

Define the direction of magnetic field z, the Zeeman Hamiltonian can be represented by the z-component of angular momentum

$$\hat{H} = \hat{H}_{hfs} + \mu_B (g_J \hat{J}_z + g_I \hat{I}_z) B_z, \quad (2.8)$$

\hat{J}_z and \hat{I}_z are the z-component of the angular momentum \mathbf{J} and \mathbf{I} , respectively. And the eigenvalues of \hat{J}_z and \hat{I}_z are m_J and m_I , the magnetic quantum numbers. \hat{H}_{hfs} is diagonal in the basis of $\{|F, m_F\rangle\}$, and we can proceed by representing states $|J = 1/2, m_J, I = 3/2, m_I\rangle$ with $\{|F, m_F\rangle\}$ and calculate the energy of states $|F, m_F\rangle$ to second order.

$$\begin{aligned}
\left|\frac{1}{2}, \frac{3}{2}\right\rangle &= |2, 2\rangle, & \left|\frac{1}{2}, \frac{1}{2}\right\rangle &= \frac{\sqrt{3}}{2} |2, 1\rangle - \frac{1}{2} |1, 1\rangle \\
\left|\frac{-1}{2}, \frac{3}{2}\right\rangle &= \frac{1}{2} |2, 1\rangle + \frac{\sqrt{3}}{2} |1, 1\rangle, & \left|\frac{-1}{2}, \frac{1}{2}\right\rangle &= \frac{1}{\sqrt{2}} |2, 0\rangle + \frac{1}{\sqrt{2}} |1, 0\rangle \\
\left|\frac{1}{2}, \frac{-1}{2}\right\rangle &= \frac{1}{\sqrt{2}} |2, 0\rangle - \frac{1}{\sqrt{2}} |1, 0\rangle, & \left|\frac{1}{2}, \frac{-3}{2}\right\rangle &= \frac{1}{2} |2, -1\rangle - \frac{\sqrt{3}}{2} |1, -1\rangle \\
\left|\frac{-1}{2}, \frac{-1}{2}\right\rangle &= \frac{\sqrt{3}}{2} |2, -1\rangle - \frac{1}{2} |1, -1\rangle, & \left|\frac{-1}{2}, \frac{-3}{2}\right\rangle &= |2, -2\rangle
\end{aligned} \tag{2.9}$$

In the $\{|F, m_F\rangle\}$ basis,

$$\hat{H}_{hfs} |F, m_F\rangle = E_F |F, m_F\rangle. \tag{2.10}$$

Treat the interaction with the external magnetic field as a perturbation, the first-order perturbed energy for state $|F, m_F\rangle$ is

$$\Delta E_1 = \langle F, m_F | (g_J \vec{J}_z + g_I \vec{I}_z) | F, m_F \rangle \mu_B B, \tag{2.11}$$

and the second order perturbed energy is

$$\Delta E_2 = \sum_{F', m'_F} \frac{|\langle F, m_F | (g_J \vec{J}_z + g_I \vec{I}_z) | F', m'_F \rangle|^2}{E_F - E_{F'}} (\mu_B B)^2. \tag{2.12}$$

The energy of $|F, m_F\rangle$ states are listed here, in the units of MHz, MHz/G and MHz/G². The numbers are useful for quick estimation of the magnetic field in the

lab.

$$|2, 2\rangle = 2.75 \times 10^3 h \text{ MHz} + 1.405h \text{ MHz/G} \times B + 0h \text{ MHz/G}^2 \times B^2 \quad (2.13)$$

$$|2, 1\rangle = 2.75 \times 10^3 h \text{ MHz} + 0.7026h \text{ MHz/G} \times B + 2.879 \times 10^{-4} h \text{ MHz/G}^2 \times B^2$$

$$|2, 0\rangle = 2.75 \times 10^3 h \text{ MHz} + 0h \text{ MHz/G} \times B + 3.839 \times 10^{-4} h \text{ MHz/G}^2 \times B^2$$

$$|2, -1\rangle = 2.75 \times 10^3 h \text{ MHz} - 0.7026h \text{ MHz/G} \times B + 2.879 \times 10^{-4} h \text{ MHz/G}^2 \times B^2$$

$$|2, -2\rangle = 2.75 \times 10^3 h \text{ MHz} - 1.405h \text{ MHz/G} \times B + 0h \text{ MHz/G}^2 \times B^2$$

$$|1, 1\rangle = -4.2896 \times 10^3 h \text{ MHz} - 0.7052h \text{ MHz/G} \times B - 2.879 \times 10^{-4} h \text{ MHz/G}^2 \times B^2$$

$$|1, 0\rangle = -4.2896 \times 10^3 h \text{ MHz} + 0h \text{ MHz/G} \times B - 2.879 \times 10^{-4} h \text{ MHz/G}^2 \times B^2$$

$$|1, -1\rangle = -4.2896 \times 10^3 h \text{ MHz} + 0.7052h \text{ MHz/G} \times B - 2.879 \times 10^{-4} h \text{ MHz/G}^2 \times B^2$$

The second-order perturbation leads to the quadratic Zeeman shift which has a sizable effect when the magnetic field on the order of 10G. In some our experiments, the quadratic Zeeman shift makes the energy difference between $|1, 0\rangle$ and $|1, -1\rangle$ large enough than the difference between $|1, 0\rangle$ and $|1, 1\rangle$. So we can effectively treat the $F = 1$ manifold as a two-level system by decoupling $|1, -1\rangle$.

For larger magnetic field, larger than 10^3G , the perturbation theory breaks

down and **Breit-Rabi formula** [17] is useful in the case $J = 1/2$.

$$E_{F=I\pm 1/2} = -\frac{A_{hfs}}{4} + m_F g_I \mu_N B \pm A_{hfs} \sqrt{1 + m_F x x^2}, m_F \neq 2, -2 \quad (2.14)$$

$$E_{F=2, m_F=\pm 2} = -\frac{A_{hfs}}{4} + m_F g_I \mu_N B + A_{hfs}(1 \pm x)$$

$$x = \frac{(g_J \mu_B - g_I \mu_N) B}{2A_{hfs}}$$

The energy of states $|F, m_F\rangle$ is shown in Fig. (2.2) for the magnetic field up to 15000

G.

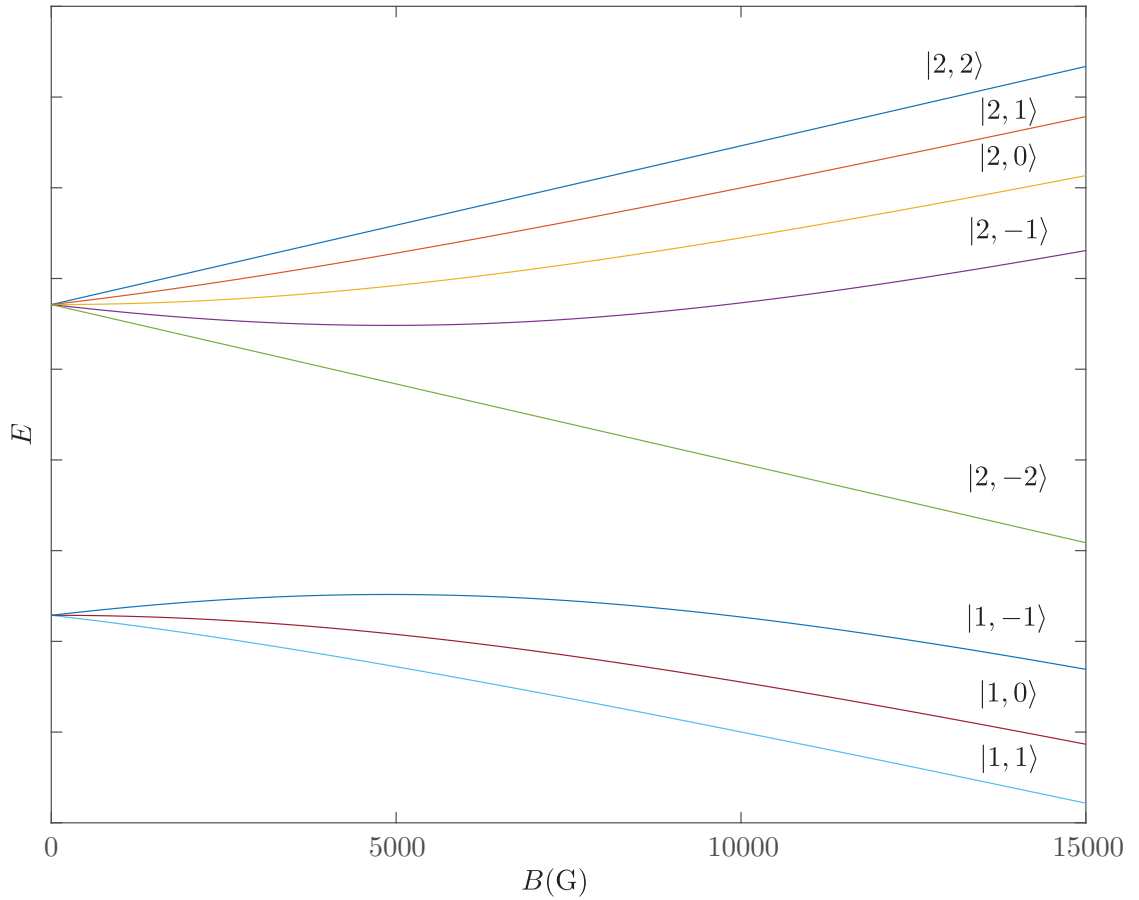


Figure 2.2: Zeeman splitting of ^{87}Rb ground states $|F, m_F\rangle$.

2.2 Laser cooling techniques

2.2.1 A two level system interacting with the reservoir

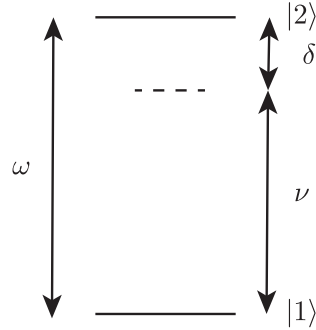


Figure 2.3: A two level system with energy difference ω in a light field with frequency ν . $\delta = \nu - \omega$ is the detuning.

A two-level system shown in Fig. (2.3) interacts with the light field via electric dipole interaction.

$$\hat{H} = -\vec{d} \cdot \vec{E} \quad (2.15)$$

is the electric dipole interaction Hamiltonian where $\vec{d} = e\vec{r}$ is the dipole operator. The matrix element of dipole operator $\langle L', m'_L | \vec{d} | L, m_L \rangle$ is nonzero only when $\Delta L = \pm 1$ and $\Delta m_L = 0$. The dipole operator doesn't interact with spin and nuclear angular momentum, so in the total angular momentum basis, the selection rule is

$$\Delta F = \pm 1. \quad (2.16)$$

The Electric field

$$\mathbf{E} = E_x \mathbf{e}_x + E_y \mathbf{e}_y + E_z \mathbf{e}_z \quad (2.17)$$

can be expressed in the basis of $\{\mathbf{e}_\pm, \mathbf{e}_z\}$,

$$\mathbf{E} = E_+ \mathbf{e}_+ + E_- \mathbf{e}_- + E_z \mathbf{e}_z. \quad (2.18)$$

Here,

$$\mathbf{e}_\pm = \frac{\mathbf{e}_x \pm i\mathbf{e}_y}{\sqrt{2}}. \quad (2.19)$$

The dipole interaction Hamiltonian is separated into the radial part and the angular part in the new basis,

$$\mathbf{e}_q \cdot \mathbf{r} = \sqrt{\frac{4\pi}{3}} \rho Y_{1,q}(\theta, \phi), \quad (2.20)$$

here $q = 1$ for \mathbf{e}_+ , $q = -1$ for \mathbf{e}_- and $q = 0$ for \mathbf{e}_z . $Y_{1,q}(\theta, \phi)$ is the spherical harmonic function.

A two level system with energy difference ω interacts with electromagnetic field

$$\vec{E}(\vec{r}, t) = \vec{E}_0 e^{-i(\omega_0 t - \vec{k} \cdot \vec{r})} + \vec{E}_0^* e^{i(\omega_0 t - \vec{k} \cdot \vec{r})}, \quad (2.21)$$

the Hamiltonian is

$$\hat{H} = \hbar\omega |2\rangle\langle 2| - (\vec{\mu} |1\rangle\langle 2| + \vec{\mu}^* |2\rangle\langle 1|) \cdot \vec{E}(\vec{r}, t). \quad (2.22)$$

By transforming into a rotating frame,

$$|\tilde{2}\rangle = e^{i\omega_0 t} |2\rangle, \quad (2.23)$$

and neglecting the fast oscillating term $e^{\pm 2i\omega_0 t}$, the Hamiltonian is transformed to

$$\hat{H} = \hbar\delta |\tilde{2}\rangle\langle \tilde{2}| + \hbar(\Omega |1\rangle\langle \tilde{2}| + \Omega^* |\tilde{2}\rangle\langle 1|), \quad (2.24)$$

Here,

$$\Omega = \frac{\vec{E}_0 \cdot \vec{\mu}}{\hbar}. \quad (2.25)$$

The frame transformation and the removal of the oscillating term are named after rotating wave approximation (RWA). It is widely used in atomic physics when atoms interact with a near resonance optical field, and satisfying the condition $\delta \ll \omega_0, \omega$.

The Hamiltonian above describes a closed system, where the two-level atom only interacts with the one single optical mode, and the evolution of atomic states and photon states is coherent. In reality, the atom interacts not only with the optical field but also with the vacuum modes in the environment. The vacuum modes are contiguous in free space and discrete in a cavity, the coupling between the atomic states to the vacuum modes leads to spontaneous emission of the excited state and causes decoherence. The Wigner-Weisskopf theory [18] represents the vacuum modes with quantized field operators and calculates spontaneous emission with Fermi's golden rule. The Hamiltonian of the atomic system and vacuum modes is

$$\hat{H} = \hbar\omega |2\rangle\langle 2| + \sum_j \hbar\omega_j (\hat{a}_j^\dagger \hat{a}_j + \frac{1}{2}) - \sum_j (\hbar g_j |2\rangle\langle 1| \hat{a}_j + \hbar g_j^* |1\rangle\langle 2| \hat{a}_j^\dagger), \quad (2.26)$$

and g_j is the coupling strength between the states $|2, 0\rangle$ and $|1, 1_k\rangle$. $|1, 1_k\rangle$ is the state with one photon occupying mode k .

$$\gamma = 2\pi \sum_j |g_j|^2 \delta(\omega_j - \omega) \quad (2.27)$$

is the result of spontaneous emission rate γ and in free space

$$\gamma = \frac{\omega^3 |\mu|^2}{3\pi\epsilon_0 \hbar c^3}, \quad (2.28)$$

which is also known as the Einstein A coefficient.

One way to describe both coherent and incoherent evolution is by using the density operator. The density operator is defined as

$$\hat{\rho} = \sum_{\alpha} p_{\alpha} |\phi_{\alpha}\rangle\langle\phi_{\alpha}|. \quad (2.29)$$

Here, $|\phi_{\alpha}\rangle$ a quantum state and p_{α} is the probability that the state is in $|\phi_{\alpha}\rangle$. The states $|\phi_{\alpha}\rangle$ are not necessarily orthogonal to each other, but to make the density operator representation valid, it has to satisfy the following condition,

$$\text{Tr}[\hat{\rho}] = 1. \quad (2.30)$$

For any orthonormal basis $\{|n\rangle\}$,

$$\sum_n \langle n|\hat{\rho}|n\rangle = 1, \text{Tr}[\hat{\rho}] = \sum_n \langle n|\hat{\rho}|n\rangle, \quad (2.31)$$

for the conservation of probability.

In the density operator representation, the expectation value of a dynamic variable \hat{A} can be calculated using

$$\langle \hat{A} \rangle = \text{Tr}[\hat{\rho}\hat{A}]. \quad (2.32)$$

In the orthonormal basis $\{|n\rangle\}$, the matrix element of the density operator is

$$\rho_{n,n'} = \langle n|\hat{\rho}|n'\rangle. \quad (2.33)$$

The diagonal elements $\rho_{n,n}$ represents the the probability that the state is in $|n\rangle$ and the off-diagonal elements $\rho_{n,n'}$ represents the expectation value of coherence between states $|n\rangle$ and $|n'\rangle$. If there exists a state $|\phi\rangle$ such that

$$\hat{\rho} = |\phi\rangle\langle\phi|, \quad (2.34)$$

the state represented by $\hat{\rho}$ is a pure state, otherwise, it is a mixed state. In quantum mechanics, the probability amplitude of the states bears the full information, probability, and coherence. The density operator representation loses the information of the coherence of some states.

For an open system, the physical system we are interested in interacts with the environment or sometimes called a reservoir. The reservoir can contain a large number of degrees of freedom, for example, vacuum modes and other electromagnetic fields modes. The large number of degrees of freedom of the reservoir makes it hard to study its dynamics, however, in many cases, we are not actually interested in learning about the evolution of the reservoir. In these cases, it is useful to ignore the dynamics of the reservoir and only keep the effect the reservoir has on the system. By making this assumption, the coherent evolution of the system and the reservoir is lost and there exists decoherence in the dynamics of the system, so the density operator is widely used to describe the open system.

The full Hamiltonian is

$$\hat{H} = \hat{H}_S + \hat{H}_R + \hat{H}_{SR} \quad (2.35)$$

and under Heisenberg's equation, the evolution of the density operator is

$$\frac{d}{dt}\hat{\rho} = \frac{1}{i\hbar} [\hat{H}, \hat{\rho}] \quad (2.36)$$

Assume the interaction operator takes the form

$$\hat{H}_{SR} = \hat{S}\hat{R}^\dagger + \hat{S}^\dagger\hat{R}. \quad (2.37)$$

To ignore the dynamics of the reservoir and only keep the effects it has on the

system, we need to make two assumptions. First, factorize the reservoir operator

$$\hat{R} \approx f(t)\hat{\hat{R}}. \quad (2.38)$$

The function $f(t)$ characterizes the time evolution of the reservoir, and it is often assumed that the reservoir is stationary in the stochastic process language. The auto-correlation function of $f(t)$ is defined as

$$ACF_f(t - t') = \langle (f(t) - \langle f(t) \rangle)(f(t') - \langle f(t') \rangle) \rangle. \quad (2.39)$$

The correlation time t_c of the function $f(t)$ is defined as the width of the peak of $ACF_f(t - t')$. The first assumption of the reservoir is that $t_c \ll 1$, which means the reservoir has Markovian property, it quickly forgets about its previous state and does not keep the memory of interacting with the system.

The second assumption is that the reservoir is large enough that the system can hardly affect its state. Again, this means that the reservoir is stationary. Under these assumptions, the dynamics of the system is derived and expressed in terms of the reduced density operator

$$\hat{\rho}_S = \text{Tr}_R[\hat{\rho}], \quad (2.40)$$

which takes the average of the reservoir state by tracing out the reservoir degrees of freedom.

For a two level system

$$\hat{H}_S = \hbar\delta |2\rangle\langle 2| + \hbar(\Omega |1\rangle\langle 2| + \Omega^* |2\rangle\langle 1|), \quad (2.41)$$

the density operator evolves under equation

$$\begin{aligned}
\dot{\rho}_{22} &= -\gamma(\bar{n} + 1)\rho_{22} + \gamma\bar{n}\rho_{11} + i\Omega^*\rho_{21} - i\Omega\rho_{12} & (2.42) \\
\dot{\rho}_{11} &= \gamma(\bar{n} + 1)\rho_{22} - \gamma\bar{n}\rho_{11} - i\Omega^*\rho_{21} + i\Omega\rho_{12} \\
\dot{\rho}_{12} &= -\frac{\gamma}{2}(2\bar{n} + 1)\rho_{12} - i\delta\rho_{12} - i\Omega^*(\rho_{22} - \rho_{11}) \\
\dot{\rho}_{21} &= -\frac{\gamma}{2}(2\bar{n} + 1)\rho_{21} + i\delta\rho_{21} + i\Omega(\rho_{22} - \rho_{11})
\end{aligned}$$

This is known as the **Optical Bloch equations**, and also called **Master equation** [19]. The first two equations describe the evolution of the probability of occupying the states $|2\rangle$ and $|1\rangle$. The third and fourth equations describe the evolution of expected coherence between states $|1\rangle$ and $|2\rangle$. The term $\gamma(\bar{n} + 1)\rho_{22}$ combines spontaneous emission ($\gamma\rho_{22}$) and stimulated emission ($\gamma\bar{n}\rho_{22}$).

2.2.2 Optical force

An atomic system interacts with optical fields, which leads to stimulated emission and Rabi oscillation when the frequency of the field is near resonance. When the field is far-detuned, the atoms see a spin-independent spatial potential, the force of which drives the atoms' center-of-mass motion. Also, the atoms interact with the vacuum modes that lead to spontaneous emission. The emitted photons have nonzero momentum, so the atoms acquire the recoil momentum when the spontaneous emission happens. From the classical physics point of view, the atoms should experience a "force" in the optical fields and the definition of the "force" can be

borrowed from classical physics.

$$\hat{F} = \frac{d}{dt}\hat{p} = \frac{1}{i\hbar}[\hat{p}, \hat{H}] \quad (2.43)$$

The same as classical physics, the force operator is defined as the rate of momentum change and it can be calculated for a two-level atomic system with Hamiltonian

$$\hat{H} = \hbar\delta |2\rangle\langle 2| + \hbar(\Omega(\vec{r}) |1\rangle\langle 2| + \Omega^*(\vec{r}) |2\rangle\langle 1|). \quad (2.44)$$

$\Omega(\vec{r})$ is a function of \vec{r} for the inhomogeneous field amplitude.

$$\vec{F} = -[\nabla, \vec{H}(\vec{r})] = \hbar\nabla\Omega(\vec{r}) |2\rangle\langle 1| + \hbar\nabla\Omega^*(\vec{r}) |1\rangle\langle 2| \quad (2.45)$$

The state of the system is represented by density operator $\hat{\rho}$ and the expectation value of operator \hat{F} is

$$\begin{aligned} \langle \hat{F} \rangle &= \text{Tr}[\hat{\rho}\hat{F}] \\ &= \hbar\nabla\Omega\rho_{12} + \hbar\nabla\Omega^*\rho_{21} \\ &= 2\hbar|\Omega|^2\nabla\phi\text{Im}\left(\frac{\rho_{21}}{\Omega}\right) + \hbar\nabla|\Omega|^2\text{Re}\left(\frac{\rho_{21}}{\Omega}\right) \end{aligned} \quad (2.46)$$

Here, ϕ is the phase of the field,

$$\Omega = |\Omega|e^{i\phi}. \quad (2.47)$$

The first term is interpreted as the dissipative force and the second term the reactive force. This can be more intuitively understood when we look at the form of the force in two extreme cases.

For the steady solution of the optical Bloch equation,

$$\begin{aligned}\rho_{21} &= \frac{i\Omega(\rho_{22} - \rho_{11})}{\gamma_{21} - i\delta} \\ \rho_{22} &= \frac{R}{\gamma(\bar{n} + 1) + 2R} \\ R &= \frac{2\gamma_{21}|\Omega|^2}{\gamma_{21}^2 + \delta^2}\end{aligned}\tag{2.48}$$

here, γ_{21} is the decay rate of coherence and R is the optical pumping rate, the rate the atoms are pumped from the ground state to the excited state. When the field is weak,

$$|\Omega| \ll \gamma\tag{2.49}$$

the time atoms spend in the excited state is close to zero, $\rho_{22} \approx 0$. The coherence ρ_{21} can be approximated with

$$\rho_{21} = \Omega \frac{\delta - i\gamma_{21}}{\gamma_{21}^2 + \delta^2}\tag{2.50}$$

The dissipative force takes the form

$$F_{dis} = 2\hbar|\Omega|^2\vec{k}\frac{\gamma_{21}}{\gamma_{21}^2 + \delta^2}\tag{2.51}$$

$$= \hbar\vec{k}R\tag{2.52}$$

Intuitively, it means every time the atom is pumped from the ground state to the excited state, it acquires momentum $\hbar\vec{k}$. When spontaneous emission happens, the photon is emitted in any direction with equal probability, on the average, the atom does not acquire momentum in spontaneous emission.

In the other case, when δ is large,

$$\delta \gg |\Omega|, \delta \gg \gamma_{21} \quad (2.53)$$

Optical pumping rate $R \approx 0$ and the population in the excited state $\rho_{22} \approx 0$.

$$\text{Im} \left[\frac{\rho_{21}}{\Omega} \right] \approx \frac{1}{\delta} \quad (2.54)$$

and the reactive force takes the form

$$F_{react} = \frac{\hbar \nabla |\Omega|^2}{\delta}. \quad (2.55)$$

Effectively, the atoms see a potential

$$V(\vec{r}) = -\frac{\hbar |\Omega(\vec{r})|^2}{\delta} \quad (2.56)$$

The potential is spin-independent, its strength is proportional to the intensity of the field $|\Omega(\vec{r})|^2$ and the sign of δ determines if the potential is repulsive or attractive. When $\delta > 0$, the field is red detuned, and the potential is lower for stronger intensity, so the potential is attractive. When the field is blue detuned, it is repulsive.

This potential is known as the dipole potential, it originates from the AC stark shift. Due to the large detuning, it does not drive the transition of internal states but changes the energy of the ground state so it is effectively a spin-independent potential. Dipole potential is widely used in atomic physics experiments. It can be used as an attractive trap, called a dipole trap, to trap atoms, to do evaporative cooling, and to make an optical lattice. The repulsive potential is also very useful, it can be used to make a 1D trap when the laser is in Laguerre-Gaussian mode [20] and make random repulsive potential (optical speckle) which is discussed in detail in Ch. (4).

2.2.3 Doppler Cooling

From the form of the dissipative force

$$F_{dis} = 2\hbar|\Omega|^2\vec{k}\frac{\gamma_{21}}{\gamma_{21}^2 + \delta^2}, \quad (2.57)$$

we can see the dissipative force not necessarily cools the atoms, it only injects momentum $\hbar\vec{k}$ at the optical pumping rate. To cool atoms down in one direction, there needs to be a pair of counter-propagating optical fields, and the total dissipative force needs to slow down high-speed atoms at a higher rate than to speedup low-speed atoms.



Figure 2.4: 1D Doppler Cooling.

When we account for the motion of atoms, the Doppler effect shifts the resonance and detuning. With adjusted detuning, the dissipative force takes the form

$$F_{dis} = 2\hbar|\Omega|^2\vec{k}\frac{\gamma_{21}}{\gamma_{21}^2 + (\delta - \vec{k} \cdot \vec{v})^2}. \quad (2.58)$$

When the speed of atoms is small, $\vec{k} \cdot \vec{v} \ll \delta, \gamma$, we expand the force to the first order of $\vec{k} \cdot \vec{v}$,

$$F_{dis} \approx 2\hbar|\Omega|^2\vec{k}\frac{\gamma_{21}}{\gamma_{21}^2 + \delta^2} \left(1 + \frac{2\delta\vec{k} \cdot \vec{v}}{\gamma_{21}^2 + \delta^2} \right). \quad (2.59)$$

The total force of A pair of counter-propagating beams cancels the first term and retains the velocity-dependent cooling force

$$F_{tot} = \frac{8\hbar|\Omega|^2\gamma_{21}\delta k^2 v}{(\gamma_{21}^2 + \delta^2)^2}. \quad (2.60)$$

The direction of the force depends on the sign of δ , when $\delta < 0$, the force is in the opposite direction of v and acts as a cooling force. When $\delta > 0$, the force heats the atoms up in a positive feedback mechanism. Intuitively, the cooling mechanism can be understood from the dependence of the optical pumping rate on the Doppler shift. When the light is red detuned, the atoms are closer to resonance with the light beam propagating in the opposite direction from the atoms' velocity. The optical pumping rate of this beam is thus higher than the other, so on average, the atoms absorb more photons from this beam and acquires a negative momentum.

The dissipative force applies to one-dimensional cooling, and to the first order of $\vec{k} \cdot \vec{v}$, the force is decoupled in different spatial directions. To cool down atoms in all three spatial directions, three pairs of counter-propagating red-detuned light are needed. This is the simplified version of optical molasses [21–23]. Fig. (13) in [21] is the sketch of one of the first experiments of Optical Molasses conducted in NIST, Gaithersburg. The result of the experiment demonstrated the cooling limit of Optical Molasses is well below the limit of Doppler cooling. The explanation requires a multi-level system and circular polarized cooling light which is discussed in the Doppler cooling limit and sub-Doppler cooling section.

2.2.4 Doppler Cooling Limit

The viscous force from a pair of counter-propagating light beams has a negative feedback effect on the velocity of atoms

$$F_{tot} = \frac{8\hbar|\Omega|^2\gamma_{21}\delta k^2 v}{(\gamma_{21}^2 + \delta^2)^2}. \quad (2.61)$$

It cools down the temperature of the atoms low enough that the spontaneous emission effect becomes significant. When spontaneous emission happens, the photon is emitted in any direction equally likely and the recoil effect heats the atoms. When cooling and spontaneous emission are balanced, the system reaches equilibrium and the temperature of the system is the lower bound of Doppler cooling.

The spontaneous emission can be treated as random kicks the atoms which are in a viscous force, this system resembles the classical Brownian motion which is studied in the early 1900s. William Sutherland in 1904 [24], Albert Einstein in 1905 [25], and Marian Smoluchowski in 1906 [26] studied the Brownian motion and the relation between equilibrium temperature, friction coefficient, and diffusion constant. The relation is named the Einstein relation (also known as Wright-Sullivan relation)

$$D = m\eta k_B T \quad (2.62)$$

Here η is the friction coefficient in the Langevin equation

$$\frac{d}{dt}p = -\eta p + f(t) \quad (2.63)$$

and D is the diffusion constant that characterizes the random force $f(t)$,

$$\langle (f(t) - \langle f(t) \rangle) (f(t') - \langle f(t') \rangle) \rangle = 2D\delta(t - t'). \quad (2.64)$$

The delta function is an approximation of the autocorrelation function of $f(t)$ when the random collision is fast and memoryless.

The Quantum version of the Langevin equation is the Heisenberg-Langevin equation, for the two-level system, it can be derived that

$$D = 4(\hbar k)^2 \frac{|\Omega|^2 \gamma/2}{(\gamma/2)^2 + \delta^2}, \quad (2.65)$$

and it can be calculated from the viscous force Eq. (2.61),

$$\eta = \frac{8\hbar|\Omega|^2 \gamma_{21} \delta k^2}{m(\gamma_{21}^2 + \delta^2)^2}. \quad (2.66)$$

When the coherence decay at the rate of spontaneous emission, $\gamma_{21} = \gamma/2$, the equilibrium temperature is

$$k_B T = \frac{\hbar(\delta^2 + (\gamma/2)^2)}{2\delta}. \quad (2.67)$$

The lower bound is

$$k_B T = \hbar \frac{\gamma}{2} \quad (2.68)$$

when $\delta = \gamma/2$. This was believed to be the limit of Doppler cooling, it is equal to 125 K for Cs, 140 K for Rb and 240 K for Na.

2.2.5 Sub-Doppler Cooling

The limit of Doppler cooling is intuitive, it was believed to be the limit of laser cooling until in 1989, the scientists in NIST Gaithersburg reported the measured temperature of Na atoms in an optical molasses to be ten times cooler [27]. The observation of temperature drastically lower than the theoretical prediction of the

Doppler cooling limit surprised scientists and was theoretically explained by Cohen-Tannoudji and collaborators in 1989 [28]. The temperature in optical molasses is sensitive to laser detuning and polarization, different polarization of light fields drives transition between different $|F, m_F\rangle$ states. To theoretically explain, a two-level system is insufficient and $|F, m_F\rangle$ hyperfine states in atoms' ground state, and the first excited state must be considered.

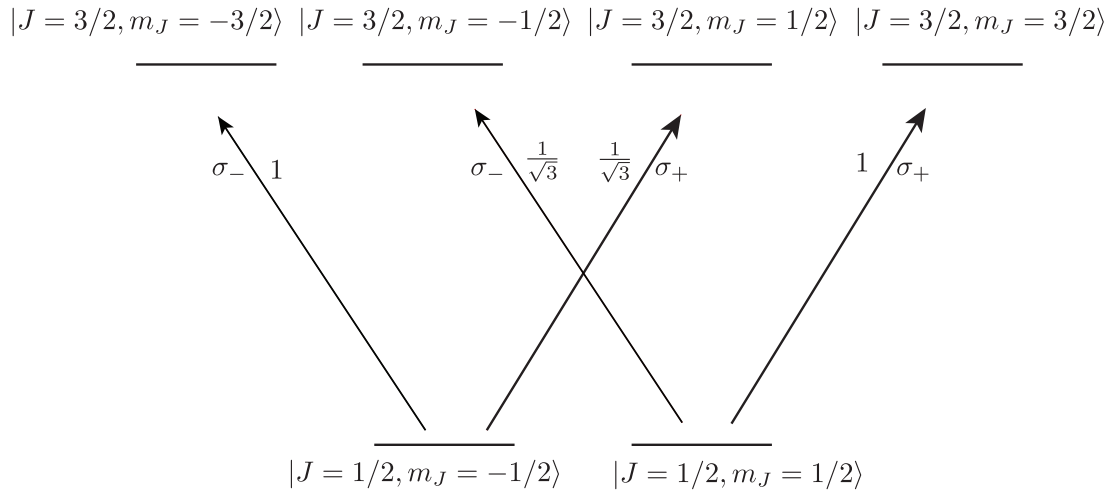


Figure 2.5: Energy levels of Na atoms ground state and the first excited state. The Clebsch-Gordon coefficients are labelled for each transition.

Fig. (2.5) shows the energy levels of Na atoms ground state and the first excited state. σ_+ polarized fields couple $|m_J\rangle$ states and $|m_J + 1\rangle$ states, σ_- polarized fields couples $|m_J\rangle$ states and $|m_J - 1\rangle$ states. The Clebsch-Gordon coefficients are labeled for each transition. In the optical molasses experiment that observed sub-Doppler limit temperature, the temperature in optical molasses was found to be sensitive to the polarization of light. And in the experiment, three pairs of counter-propagating, crossed linearly polarized laser beams are used.

The optical field in the lin \perp lin scheme is [19]

$$\vec{E} = \vec{E}_0 \hat{x} \cos \omega t - kz + \vec{E}_0 \hat{y} \cos \omega t + kz \quad (2.69)$$

$$= \vec{E}_0(\hat{x} + \hat{y}) \cos \omega t \cos kz + \vec{E}_0(\hat{x} - \hat{y}) \sin \omega t \sin kz \quad (2.70)$$

$$(2.71)$$

At $z = 0$ and $z = \lambda/4$, the atoms are in the linearly polarized field

$$\vec{E} = \vec{E}_0(\hat{x} \pm \hat{y}) \cos \omega t \quad (2.72)$$

and at $z = \lambda/8$, the atoms are in σ_- polarized field

$$\vec{E} = \vec{E}_0 \left[\hat{x} \sin \left(\omega t + \frac{\pi}{4} \right) - \hat{y} \cos \left(\omega t + \frac{\pi}{4} \right) \right]. \quad (2.73)$$

At $z = 3\lambda/8$, the atoms are in σ_+ polarized field. The polarization as a function of z is shown in Fig. (2.6).

The polarization is periodic in space in the lin \perp lin scheme, as atoms move, the coupling of $|m_J\rangle$ states changes. When the polarization is σ_+ , $|m_J = -\frac{1}{2}\rangle$ is optically pumped and spontaneously emitted to state $|m_J = \frac{1}{2}\rangle$. And when detuning is large, $|\Omega| \ll \gamma$, the state is in the dressed state of $|m_J = \frac{1}{2}\rangle$. As atoms move, the polarization changes from σ_+ to σ_- , and the states transfers from the dressed state of $|m_J = \frac{1}{2}\rangle$ to the dressed state of $|m_J = -\frac{1}{2}\rangle$.

When the detuning is large, the energy of the dressed states is mainly AC Stark shift,

$$\begin{aligned} E_{1/2}^{\sigma_+} &= -\frac{|\Omega|^2}{\delta}, E_{-1/2}^{\sigma_+} = -\frac{|\Omega|^2}{3\delta} \\ E_{1/2}^{\sigma_-} &= -\frac{|\Omega|^2}{3\delta}, E_{-1/2}^{\sigma_-} = -\frac{|\Omega|^2}{\delta} \end{aligned} \quad (2.74)$$

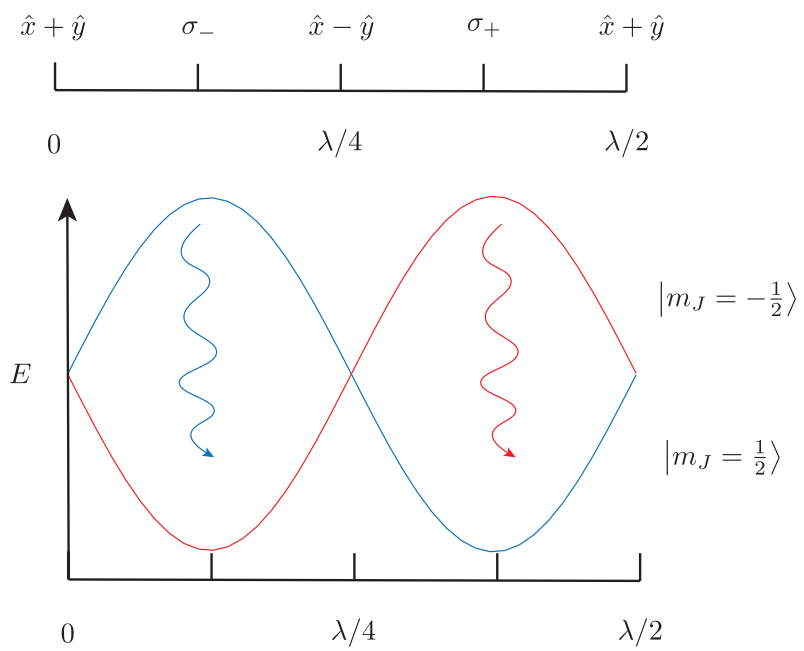


Figure 2.6: The polarization as a function of z in $\text{lin} \perp \text{lin}$ scheme.

The energy is sketched in Fig. (2.6) and the difference of denominator originates from the difference in Clebsch-Gordon coefficients between states $|m_J\rangle$, $|m_J + 1\rangle$ and $|m_J\rangle$, $|m_J - 1\rangle$.

When the atoms move from σ_- polarization to σ_+ , it starts from state $|m_J = -1/2\rangle$ and climbs uphill in potential energy. Along the way, polarization changes gradually, and as it reaches σ_+ polarization, the state transfers to $|m_J = 1/2\rangle$ which has lower potential energy. Then, the climbing process goes on in the periodically polarized field. When the atoms climb uphill it converts kinetic energy to potential energy and slows down. As polarization flips, the energy loss in the state transfer goes to the optical field because the state absorbs lower energy photons and emits higher energy photons in the spontaneous emission process. The technique is also named "Sisyphus cooling", in the Greek mythology, Sisyphus was doomed to roll a stone up a mountain only to have it roll down again.

The limit of Sisyphus cooling was found to be associated with the photon recoil momentum $\hbar k$ and in the early experiments, the temperature of atoms in Optical molasses was measured to be an order of magnitude smaller than the limit of Doppler cooling.

2.2.6 MOT

While the dissipative force slows atoms down, it does not provide spatial confinement. In cold atom experiments, to achieve quantum degeneracy, the phase space density needs to be high enough which requires a high spatial density. In [29],

scientists proposed to combine optical molasses with a magnetic field gradient, it cools and traps atoms at the same time.

Fig. (2.7)(a) shows the sketch of a MOT. It combines 3D optical molasses with a pair of the anti-Helmholtz coil. The magnetic field generated by the anti-Helmholtz coil is in the form

$$\vec{B}(\vec{r}) = b(x\mathbf{e}_x + y\mathbf{e}_y - 2z\mathbf{e}_z) \quad (2.75)$$

The energy levels of $|J = 0\rangle$ and $|J = 1\rangle$ states are drawn in Fig. (2.7)(b) as a function of position due to the Zeeman shift. The detuning of σ_+ and σ_- are thus a function of position [19].

$$\delta_{\pm}(\vec{v}, \vec{r}) = \delta_0 \mp \vec{k} \cdot \vec{v} \pm \mu' \cdot \vec{B}(\vec{r})/\hbar \quad (2.76)$$

Here $\mu' = (g_{J'}m_{J'} - g_Jm_J)\mu_B$.

Intuitively, as atoms move to the left of the trap center, the σ_+ beam is closer to resonance with the transition between $|m_J = 0\rangle$ and $|m_J = 1\rangle$. The optical pumping effect from the σ_+ beam is stronger and the overall force points to the right. As atoms move to the right, it is the other way around, the σ_- beam is closer to resonance and has a stronger optical pumping effect. Thus, MOT provides a spatial restoring force. Together with the dissipative force, the total force is

$$\vec{F} = -\beta\vec{v} - \kappa\vec{r}. \quad (2.77)$$

$$\kappa = \mu'\beta b/\hbar k.$$

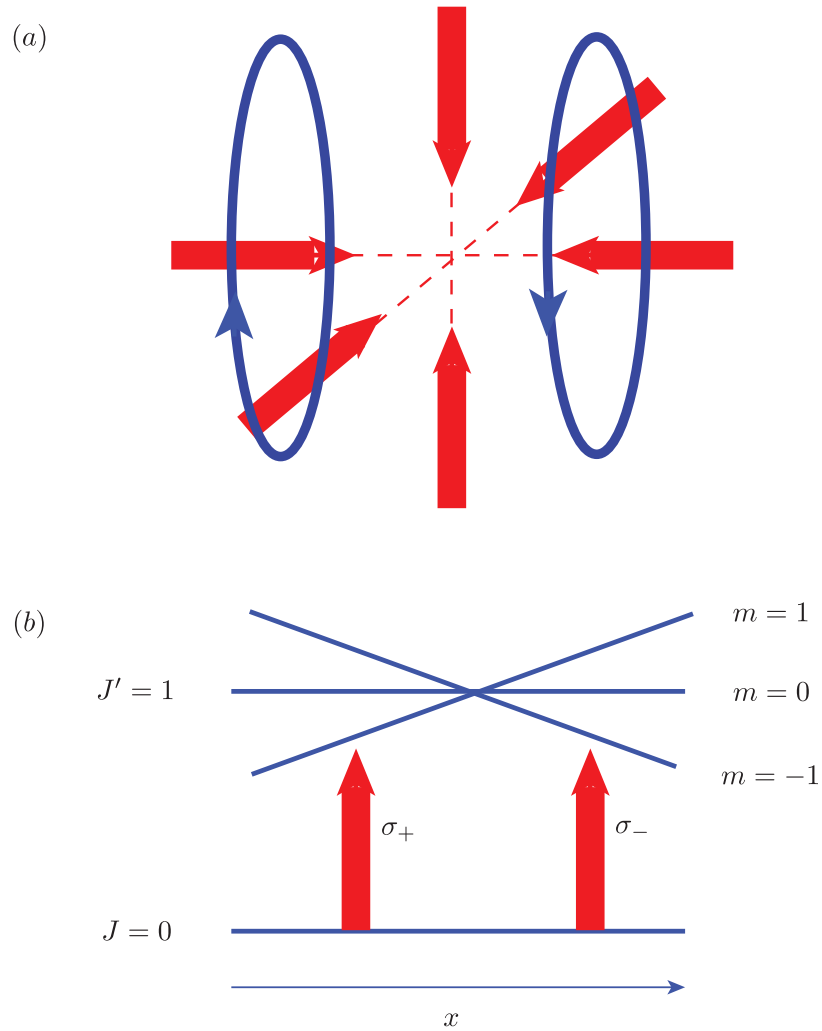


Figure 2.7: MOT. (a) A sketch of MOT, three pairs of counter propagating laser beams are combined with a pair of anti-Helmholtz coil. (b) Energy levels of $|J = 0\rangle$ and $|J = 1\rangle$, coupled by σ_+ and σ_- polarized beams.

2.2.7 Dipole Trap and evaporative cooling

The limit of Sisyphus Laser Cooling was not sufficient to cool atoms below the critical temperature. It was later achieved using evaporative cooling [30, 31], and has since been widely used as the last step to make BECs. Evaporative cooling can be done in an optical dipole trap in which the trap depth can be easily controlled.

The optical dipole potential for two-level atoms in the limit of large detuning is the AC Stark shift,

$$V(\vec{r}) = -\frac{\hbar|\Omega(\vec{r})|^2}{\delta}. \quad (2.78)$$

It is proportional to the intensity of the red detuned lasers [32],

$$V(\vec{r}) = \frac{3\pi c^2}{2\omega_0^3} \frac{\gamma}{\delta} I(\vec{r}). \quad (2.79)$$

Here γ is the spontaneous emission rate

$$\gamma = \frac{\omega^3 |\mu|^2}{3\pi\epsilon_0 \hbar c^3}, \quad (2.80)$$

and μ is the dipole matrix element between the two states.

$$\mu = \langle e | e\vec{r} | g \rangle \quad (2.81)$$

In the application of the dipole trap to Alkali atoms, for example, Rb as shown in Fig. (2.1), the fine structure and hyperfine structure of the ground and excited states need to be considered. Define γ with the dipole matrix element μ between the ground state and the excited state

$$\mu = \langle L = 0 | e\vec{r} | L = 1 \rangle. \quad (2.82)$$

For ground state $|F, m_F\rangle$, the dipole potential is

$$V(\vec{r}) = \frac{3\pi c^2 \gamma}{2\omega_0^3} I(\vec{r}) \times \sum_j \frac{c_j^2}{\delta_j}. \quad (2.83)$$

j denotes the states $|F, m_F\rangle$ is coupled to, depending on the polarization of the dipole laser. c_j is the dipole matrix element

$$|\mu_j| = |\langle F, m_F | e\vec{r} | j \rangle| = c_j |\mu| \quad (2.84)$$

in the unit of μ . Considering the fine structure of the excited state, the dipole potential is

$$V(\vec{r}) = \frac{\pi c^2 \gamma}{2\omega_0^3} \left(\frac{2 + P g_F m_F}{\delta_{2,F}} + \frac{1 - P g_F m_F}{\delta_{1,F}} \right) I(\vec{r}) \quad (2.85)$$

P denotes the polarization and P is 0 for π polarized beams, ± 1 for σ_{\pm} polarized beams. $\delta_{1,2}$ is the detuning from D_1 and D_2 transitions. It is valid for large detuning $|\delta_{2,F}|, |\delta_{1,F}| \gg \Delta_{FS}$.

Fig. (2.8)(a) shows a sketch of a crossed dipole trap which is widely used in cold atoms labs. A single Gaussian beam has a Gaussian intensity profile in its cross-sectional plane. Longitudinally, the width of the trapping potential is the Rayleigh length which is typically much larger than the beam width. So the confinement in the longitudinal direction is much weaker than it is in the cross-sectional directions. The crossed dipole trap solves this problem by adding the second dipole beam which provides confinement in the longitudinal direction of the first dipole beam.

Fig. (2.8)(b) shows the process of dipole evaporative cooling by continuously lowering the dipole trapping potential and allowing the high energy atoms to escape the trap and the rest of the atoms to thermalize to a lower temperature [33, 34].

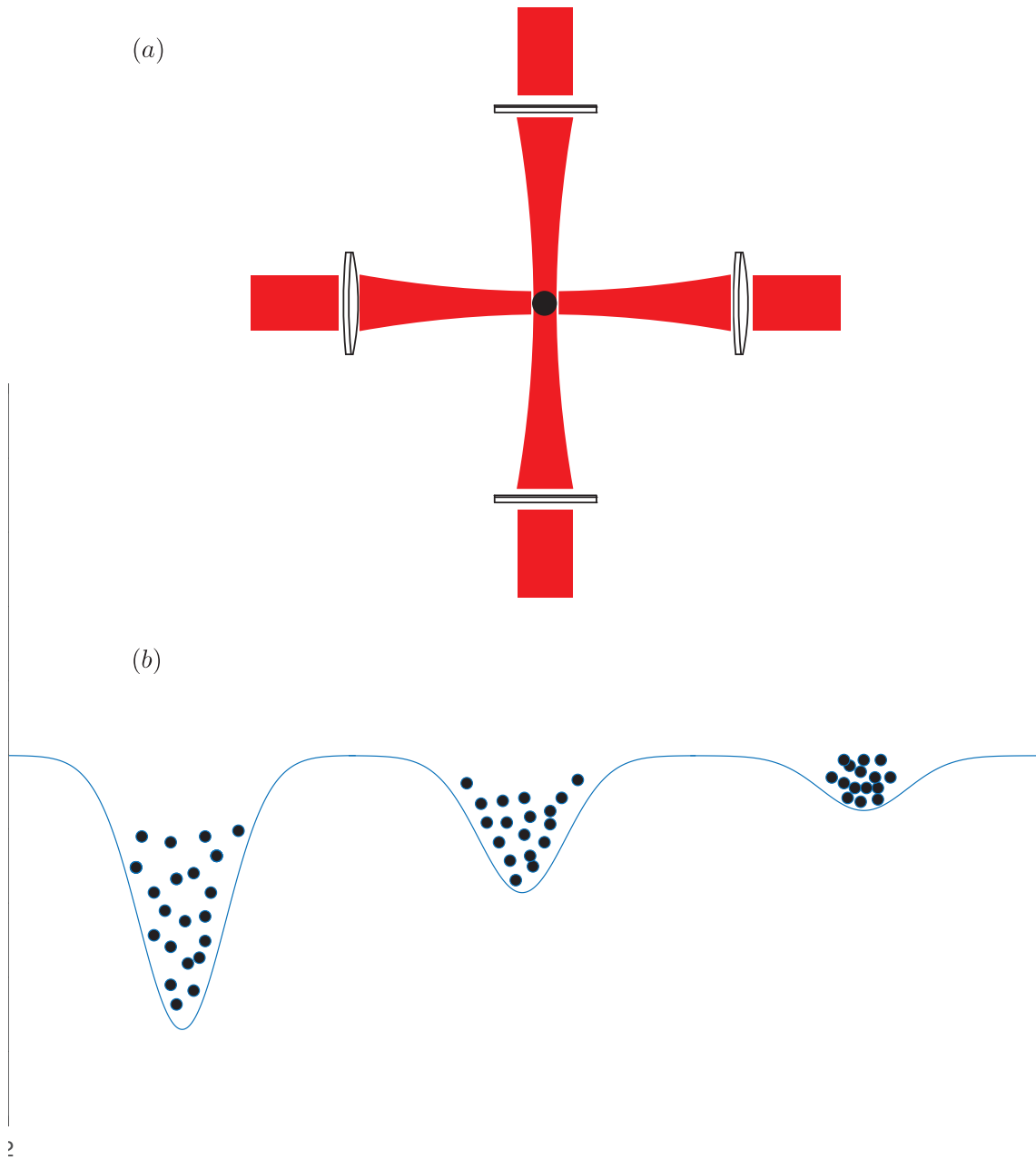


Figure 2.8: Dipole evaporation. (a) A sketch of crossed dipole trap formed by two red detuned laser beams. (b) Dipole evaporative cooling process.

In the escaping and rethermalizing process, the remaining atoms have much lower average energy and they tend to occupy a smaller volume at the center of the trap, thus increase the phase space density (1.5).

Chapter 3: Spin-Orbit coupling and Anderson localization in a cold-atoms system

In contrast to a condensed-matter system where we have little control over the material structure and the internal environment of particles, in a cold-atoms system, the external potential, the internal atomic states, and the interaction between particles can all be artificially engineered in the lab. Using the interaction between atoms and the electromagnetic fields, the Hamiltonian of the atoms can be engineered to simulate the essential properties present in condensed-matter systems. The parameters in the Hamiltonian can be tuned by changing the intensity of the light, frequency of the light, the strength of the electromagnetic fields, and etc. The high level of control over a cold-atoms system and the methods to simulate the Hamiltonian of a condensed-matter system make it an ideal platform to study fundamental condensed-matter physics that is otherwise hard to study in experiments.

Spin-orbit coupling and Anderson localization have been realized and studied in cold atoms over the last decade. In this chapter, we briefly review the progress of spin-orbit coupling and Anderson localization in cold atoms on which our research of spin-orbit coupling enhanced transport in a random field is based.

3.1 Spin-orbit coupling

3.1.1 The Origin of SOC in a solid-state system

Spin-orbit coupling (SOC) [35, 36] is ubiquitous in physical systems. It alters the electronic band structure in a solid-state system and it is crucial for the spin-Hall effect [37, 38], topological insulators [39–41] and some proposals for realizing the Majorana Fermions [42, 43].

SOC originates from a relativistic effect. Spin is a fundamental component of electrons described by the Dirac equation. In the non-relativistic limit, the Dirac equation reduces to Schrödinger equation with an additional term that couples the particle's spin to its momentum when external fields are present. A particle with spin moves with momentum $\hbar\vec{k} = \hbar(k_x, k_y, k_z)$ in an electric field $\vec{E} = E_0\hat{z}$, in its stationary frame of reference, the particle experiences a magnetic field in the frame co-moving with the electron. The Hamiltonian of the Zeeman interaction is

$$\hat{H} = -\vec{\mu} \cdot \vec{B}_{SO} \propto \sigma_x k_y - \sigma_y k_x, \quad (3.1)$$

where $\vec{\mu}$ is the magnetic moment parallel to the spin $\vec{\sigma}$ and

$$\vec{B}_{SO} = E_0(\hbar/mc^2)(-k_y, k_x, 0). \quad (3.2)$$

But this effect is extremely small and does not explain the prefactor of Rashba spin-orbit coupling which is determined quantitatively in [44].

In a condensed-matter system, there are two well-known forms of linear SOC in

2D depending on the symmetry of the fields in the materials. The Rashba SOC [44],

$$-\vec{\mu} \cdot \vec{B} \propto \sigma_x k_y - \sigma_y k_x. \quad (3.3)$$

And the Dresselhaus SOC [45],

$$-\vec{\mu} \cdot \vec{B} \propto -\sigma_x k_y - \sigma_y k_x. \quad (3.4)$$

The Rashba SOC originates from a lack of mirror symmetry in two-dimensional systems and the Dresselhaus SOC from a lack of inversion symmetry in bulk crystals [36, 44, 45]. In systems like GaAs, SOC can be engineered slightly, for example, the Rashba SOC can be tuned by changing the geometry of a heterostructure.

3.1.2 SOC in cold atoms

The methods of generating SOC in cold atoms are initially proposed in [46, 47]. It was first demonstrated in the observation of 1D SOC in a Bose-Einstein condensate [35]. Later, SOC was also realized in an atomic Fermi gas [48, 49]. Since then, a wide range of researches has been conducted or proposed in the field [50–65]

In the first experimental realization of SOC in cold atoms [35], the SOC Hamiltonian of neutral atoms was engineered to be equivalent to an electronic system with equal contributions of the Rashba and the Dresselhaus couplings.

$$\hat{H}_{SOC} \propto k_x \sigma_y. \quad (3.5)$$

In this neutral-atoms system, two internal hyperfine states $|F, m_F\rangle$ were selected to represent the pseudo-spin $|\uparrow\rangle$ and $|\downarrow\rangle$. And for a neutral atom, the internal electrons' spin is intrinsically coupled to the electrons' motion but the atomic spin

is not coupled to the center-of-mass motion of the neutral atom. Here using lasers and magnetic fields, the researchers created coupling between the internal hyperfine states $|\uparrow\rangle$ and $|\downarrow\rangle$, and the momentum states of the neutral atoms.

Fig. 3.1 and Fig. 3.2 show the scheme for creating SOC by using Raman coupling. In Fig. 3.1(b), the ^{87}Rb ground states $|F = 1, m_F = 0, \pm 1\rangle$ are coupled by a pair of Raman lasers with two-photon detuning δ relative to the Zeeman shift of states $|F = 1, m_F = 0, \pm 1\rangle$. Fig. 3.2(a) is the dispersion relation of spin-orbit coupled atoms, energy vs quasi-momentum q which is a good quantum number in the SOC system. Detailed discussions of the SOC Hamiltonian and quasi-momentum states are in Sec. (3.1.3). Also, SOC alters the mean-field interaction between quasi-momentum states in both energy bands, leading to two additional phases of a two-component BEC, the phase-mixed and the phase-separated. The phase transition was predicted and observed in [35, 66]. Later the stripe phase was studied in more detail using the Bragg scattering signal [65].

3.1.3 Raman coupling Hamiltonian

Here we derive Raman coupling Hamiltonian and discuss how Raman coupling leads to SOC. Intuitively, SOC generated by Raman coupling can be understood from the momentum transfer in the two-photon process. For example, state transfer from $|F = 1, m_F = -1\rangle$ to $|F = 1, m_F = 0\rangle$ is accompanied by stimulated absorption of a photon from light field \vec{E}_1 and stimulated emission of a photon to light field \vec{E}_2 . In this process, the state $|F = 1, m_F = -1\rangle$ acquires momentum $2k_L$ from the recoil

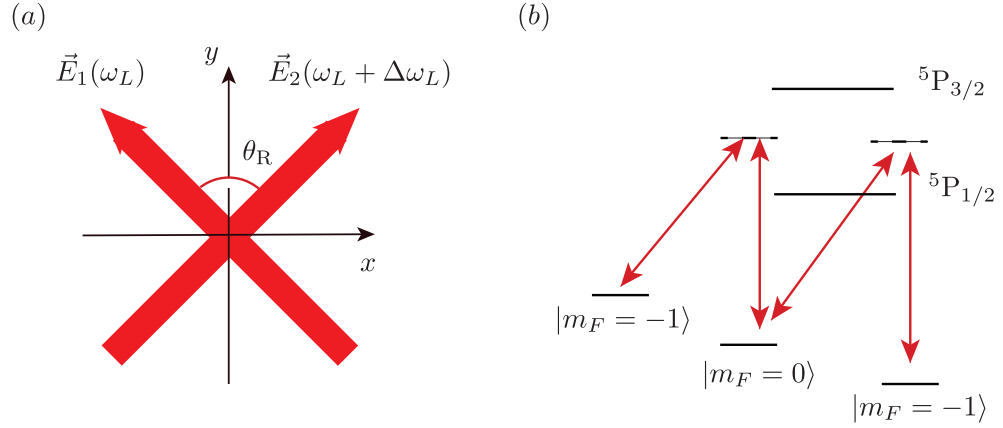


Figure 3.1: Raman coupling. (a). Two laser beams perpendicular to each other are detuned by $\Delta\omega_L$, they intersect at the atoms. (b). Hyperfine states coupled by Raman lasers.

momentum of the two photons. Here k_L is half the difference of k vectors between the two beams.

$$k_L = \frac{2\pi}{\omega_L} \sin \frac{\theta_R}{2}. \quad (3.6)$$

Similarly, state $|F = 1, m_F = 0\rangle$ transfer to $|F = 1, m_F = -1\rangle$ and acquires momentum $-2k_L$. The state transfer is always accompanied by a momentum transfer of $\pm 2k_L$, so the internal states of the atoms are coupled to the momentum states of the atoms.

Formally, we derive the Raman Hamiltonian in the $|F = 1\rangle$ manifold. The electric field of the two Raman lasers is

$$\vec{E} = \vec{E}_1 e^{i(kx \sin \theta_R/2 + ky \cos \theta_R/2 - \omega t)} + \vec{E}_2 e^{i[-kx \sin \theta_R/2 + ky \cos \theta_R/2 - (\omega + \Delta\omega_L)t]} + c.c \quad (3.7)$$

Electric dipole interaction Hamiltonian is

$$\hat{H}_{Dip} = E_e |e\rangle\langle e| + E_g |-1\rangle\langle -1| - E_g |1\rangle\langle 1| + \vec{E} \cdot \vec{\mu} (|e\rangle\langle -1| + |e\rangle\langle 0| + |e\rangle\langle 1|) + c.c \quad (3.8)$$

Expand the wave function in the four-state basis,

$$\psi(t) = a_e(t) |e\rangle + a_{-1}(t) |-1\rangle + a_0(t) |0\rangle + a_1(t) |1\rangle, \quad (3.9)$$

First, transform the frame of reference into a rotating frame,

$$\tilde{a}_e = a_e e^{i\omega_L t}, \tilde{a}_{-1} = a_{-1} e^{i\Delta\omega_L t}, \tilde{a}_1 = a_1 e^{-i\Delta\omega_L t} \quad (3.10)$$

and make rotating wave approximation. Next, due to the large single-photon detuning $\Delta = E_e - \hbar\omega_L$, the excited state $|\tilde{e}\rangle$ can be adiabatically eliminated ($\frac{d\tilde{a}_e}{dt} \approx 0$).

The effective Hamiltonian of dipole interaction in the $|F = 1\rangle$ manifold is

$$\hat{H}_{eff,Dip} = \begin{pmatrix} \hbar\delta & -\hbar\frac{\Omega_1^*\Omega_2}{\Delta}e^{-i2k_Lx} & 0 \\ -\hbar\frac{\Omega_1\Omega_2^*}{\Delta}e^{i2k_Lx} & 0 & -\hbar\frac{\Omega_1^*\Omega_2}{\Delta}e^{-i2k_Lx} \\ 0 & -\hbar\frac{\Omega_1\Omega_2^*}{\Delta}e^{i2k_Lx} & -\hbar\delta \end{pmatrix} - \hbar\frac{(|\Omega_1|^2 + |\Omega_2|^2)}{\Delta}. \quad (3.11)$$

The last term is the AC Stark shift for all the substates. $\delta = E_g - \Delta\omega_L$ is the two-photon detuning. When the quadratic Zeeman shift discussed in Sec. (2.1.2) is considered, state $|m_F = 1\rangle$ is far-detuned from the other two states and can be eliminated. The effective two-level Hamiltonian takes the form

$$\hat{H}_{eff} = \frac{\hbar^2 k^2}{2m} \hat{\mathbf{1}} + \frac{\delta}{2} \hat{\sigma}_z + \frac{\Omega_R}{2} \hat{\sigma}_x \cos 2k_L x - \frac{\Omega_R^*}{2} \hat{\sigma}_y \sin 2k_L x \quad (3.12)$$

here,

$$\frac{\Omega_R}{2} = -\hbar\frac{\Omega_1^*\Omega_2}{\Delta} \quad (3.13)$$

is the effective Raman coupling strength. Finally, by applying a position dependent rotational transformation

$$\exp\left\{\frac{i\hat{\sigma}_z 2k_L x}{\hbar}\right\}, \quad (3.14)$$

and a global rotation

$$\hat{\sigma}_x \rightarrow \hat{\sigma}_z, \hat{\sigma}_z \rightarrow \hat{\sigma}_y, \hat{\sigma}_y \rightarrow \hat{\sigma}_x. \quad (3.15)$$

we arrive at the SOC form of the Hamiltonian

$$\hat{H}_{SOC} = \frac{\hbar^2 \hat{k}^2}{2m} \hat{1} + \frac{\Omega_R}{2} \hat{\sigma}_z + \frac{\delta}{2} \hat{\sigma}_y + \frac{\hbar^2 k_L}{m} \hat{k}_x \hat{\sigma}_y \quad (3.16)$$

which has equal contribution of the Rashba and the Dresselhaus SOC.

\hat{k} does not commute with \hat{H}_{eff} , the Hamiltonian can be diagonalized in the basis of quasimomentum q which is a good quantum number. The eigenstates of the Hamiltonian are

$$|q, \pm\rangle \propto a_{\pm}(q) |q - k_R, m_F = 0\rangle + b_{\pm}(q) |q + k_R, m_F = -1\rangle.$$

Here, the \pm sign indicates the upper branch and lower branch of the SOC band structure. The coefficients are

$$a_{\pm}(q) = \mp \frac{\Omega_R}{2} \quad \text{and} \quad b_{\pm}(q) = \pm \frac{\Delta(q)}{2} + \frac{\sqrt{\Delta^2(q) + \Omega_R^2}}{2}.$$

with the quasi momentum dependent detuning defined as

$$\Delta(q) = \frac{2\hbar^2 q k_R}{m} + \delta \quad (3.17)$$

Fig. 3.2 shows the band structures of a two-level system with different SOC strengths and zero detuning. Fig. 3.2(a) is the band structure with Ω_R ranging from 0 to $6E_R$. SOC opens up a gap at the two-spin degeneracy $q = 0$ and the width of the gap is Ω_R . When $\Omega_R < 4E_R$, there are two minimas q_m in the lower branch

$$q_m = \pm \sqrt{1 - \frac{\Omega_R}{4E_R}} \quad (3.18)$$

as shown in Fig. 3.2(b). When $\Omega_R \geq 4E_R$, the two minimas start to merge and there is only one minima in the lower branch when $\Omega_R > 4E_R$.

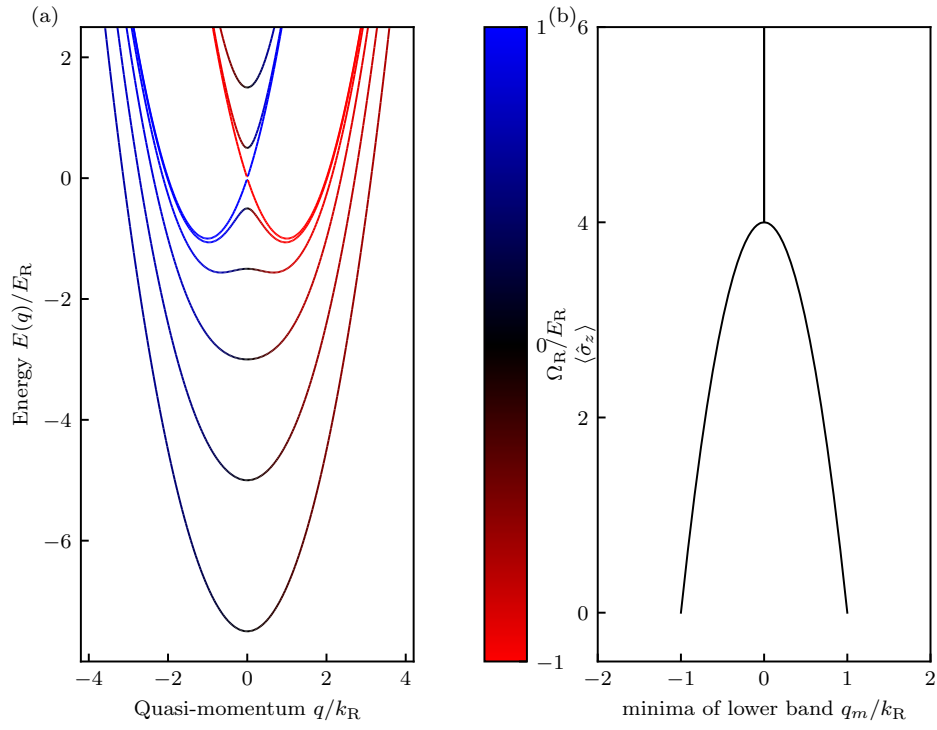


Figure 3.2: The band structure of a two-level system with SOC, detuning $\delta = 0$.

(a). The band structures with Ω_R ranging from 0 to $6E_R$. (b). The locations of the minima of the lower branch for different Ω_R .

3.2 Anderson Localization

Anderson Localization (AL), introduced in 1958 [67], describes the localization of quantum waves in disordered media. Anderson studied the evolution of a wave packet undergoing multiple scattering processes from a random potential and proved that the scattered waves can constructively interfere under certain conditions, leading to localization. This general starting point makes AL applicable to many quantum systems including: optical waves in disordered media [68–70], electrons in imperfect crystals [67], and matter waves in disordered optical potentials [71–75].

After AL was observed in multiple systems, in recent years, the analog to the AL phase transition in many-body systems (many-body localization) has attracted more attentions [76–80]. When the disorder strength is above a critical value, the many-body system undergoes a phase transition from thermalizing ergodic phase to a nonergodic phase. And in the nonergodic phase, the initial ordering of the many-body system persists, which leads to potential application in quantum information [78, 79].

In this section, we first introduce a simple model from [67] that catches the basic idea of single-particle AL. Next, we review the progress of AL in cold atoms.

3.2.1 Introduction to Anderson Localization

In the paper that introduced AL [67], the author studied the motion of some mobile entities in certain random lattices. It can be spins in a random field or electrons in a disordered crystal. The entities move by jumping from site to site.

Starting from the most general case, the wave function of an entity can be expanded in the basis of the Wannier functions on each lattice site,

$$\hat{\psi}(\vec{r}) = \sum_j W(\vec{r} - \vec{r}_j) \hat{a}_j. \quad (3.19)$$

The Hamiltonian is

$$\hat{H} = \sum_j E_j \hat{a}_j^\dagger \hat{a}_j + \sum_{j < k} (V_{jk} \hat{a}_j^\dagger \hat{a}_k + c.c) \quad (3.20)$$

Here E_j is the potential energy at site j , it is a random variable and has probability density distribution $E_j \sim \mathbb{P}(E)dE$ which is characterized by a width W . V_{jk} is the coupling of states on site j and site k , it can be random or non-random.

Under the following two conditions, it was proved in [67] the wave function will be localized in a small region without diffusion. Here localization means at $t = 0$, starting at site j , $a_j(0) = 1$, and $a_j(\infty)$ remains finite.

- Low density of sites. The average coupling strength between states at different lattice sites $\langle V_{jk} \rangle < V_c$, V_c is of the magnitude of W .
- $V(r)$ falls off faster than $\frac{1}{r^3}$ as $r \rightarrow \infty$.

Intuitively, the probability of diffusion from the initial site j depends on the number of energy matching sites k and the coupling strength between site j and sites k . Starting from the original state at site j , consider the sites k within the sphere of radius r originated from the site j . As r increases, the probability of finding more energy matching sites k within the sphere of radius r increases as r^3 in a 3-dimensional space. But if the coupling strength $V(r)$ decreases even faster,

as $r \rightarrow \infty$, the probability the initial state diffuses to other sites remains small. So under the two conditions above, no diffusion happens and the initial state is localized.

The following discussion in [67] shows in theory how diffusion happens. Laplace transform $a_j(t)$, the probability amplitude at site j ,

$$f_j(s) = \int_0^\infty e^{-st} a_j(t) dt \quad (3.21)$$

Schrödinger's equation is

$$i[sf_j(s) - a_j(0)] = E_j f_j + \sum_{k \neq j} V_{jk} f_k \quad (3.22)$$

By evaluating

$$\lim_{s \rightarrow 0^+} sf_j(s) = a_j(0) \quad (3.23)$$

the condition of localization can be studied. The following two infinite series describe how $f_j(s)$ evolves.

$$f_0(s) - \frac{i}{is - E_0} + \sum_k \frac{1}{is - E_0} V_{0k} \left(\frac{V_{0k}}{is - E_k} + \sum_l \frac{1}{is - E_l} V_{kl} \frac{1}{is - E_k} V_{l0} + \dots \right) f_0(s) \quad (3.24)$$

$$f_j(s) = \frac{1}{is - E_j} V_{j0} f_0(s) + \sum_k \frac{i}{is - E_j} V_{jk} \frac{i}{is - E_k} f_0(s) + \dots$$

The infinite series describe the high-order scattering processes, diffusion happens if the initial state goes through different scattering paths that constructively interfere at other sites. The term

$$V_c(s) = \sum_k \frac{V_{0k}^2}{is - E_k} + \sum_{k,l} \frac{V_{0k} V_{kl} V_{l0}}{(is - E_k)(is - E_l)} + \dots \quad (3.25)$$

describes the strength of diffusion through infinite orders of scattering. By considering only the direct connections between the initial site and the neighbors, the second-order approximation is made.

$$f_0(s) = \frac{i}{is(1+K) + (i/\tau) - (E_0 - \Delta E^{(2)})} \quad (3.26)$$

Here,

$$1/\tau = \sum_k V_{0k}^2 \delta(E_k) \quad (3.27)$$

$$K = \sum_{E_k \neq 0} \frac{V_{0k}^2}{E_k^{(2)}}$$

and $E^{(2)}$ is the second-order energy perturbation. When τ is finite, meaning there are some energy matching sites coupled to the initial site, the amplitude $a_0(t)$ decays at $e^{-t/\tau}$, and the diffusion happens. Otherwise, when no energy matching states are coupled to the initial site, the amplitude does not decay, instead, it spreads by the ratio $1/(1+K)$. No real transport happens in this case, the initial state is localized.

3.2.2 AL in cold atoms

AL was originally introduced in a condensed-matter system, for example, electrons in a disordered crystal and spins in a disordered field. But there are a number of difficulties for observing AL in a condensed-matter system. The interaction between electrons is hard to change, there are no good methods to directly measure the spatial probability density of electrons in a solid. In contrast, cold atoms is an ideal platform to study AL. The interaction between neutral atoms can be tuned negligible, the density profile of the atoms can be directly measured by absorption

imaging and the optical dipole potential has been used to generate optical lattices.

1D AL was first observed in cold atoms in 2008 [72]. In the same year, the metal-insulator transition described by the Anbry-André model [81,82] was studied in experiment [73]. In both the experiments, the disordered potential was realized using optical dipole potentials. In [72], optical speckle potential from far-blue-detuned light was used. The statistical properties of the optical speckle were well studied in the 1970s [83]. In [73], one-dimensional optical lattice perturbed by a second, weak incommensurate lattice yields localization effect. And the dependence of localization on the strength of the disorder was studied. Later in 2011, 3D AL was realized [74]. The researchers observed three-dimensional AL of noninteracting ultracold atoms by allowing a spin-polarized atomic Fermi gas to expand into a disordered potential. In this experiment, the mobility edge was extracted. In lower dimensions, the actual mobility edge does not exist but the quasi-mobility edge as a function of the correlation length of the disordered potential has significant effects on the spread of the wave function [71,72].

In the experiments of [72], a BEC is made in a hybrid trap consisting of a dipole trap and a magnetic trap providing longitudinal confinement. 1d optical speckle potential along the dipole trap was added. At $t=0$, the magnetic trap was turned off and the BEC started expanding due to the repulsive interaction of atoms. Without the optical speckle, the width of the atoms grows linearly in time, and as they expand, the density drops and the interaction becomes negligible. In this process, the interaction is converted into kinetic energy and the mean-field energy determines k_{max} in the momentum distribution after expansion. It is predicted

in theory [71], for a speckle potential with intensity correlation length σ_R , when $k_{max}\sigma_R < 1$, the localized wave function has a tail that exponentially decays. This is a feature of AL. When $k_{max}\sigma_R > 1$, the density profiles should have algebraic wings. σ_R determines the quasi-mobility edge in 1D.

In [73], 1D metal-insulator transition was observed in a one-dimensional quasi-periodic lattice. The system is described by an Anbry-André model [81, 82]

$$\hat{H} = J \sum_m (|w_m\rangle\langle w_{m+1}| + |w_{m+1}\rangle\langle w_m|) + \Delta \sum_m \cos 2\pi\beta m + \phi |w_m\rangle\langle w_m|. \quad (3.28)$$

$|w_m\rangle$ is the Wannier function at lattice site m , J is the tunneling energy and Δ is the strength of the disorder potential. The researcher makes the noninteracting BEC expand along the 1D lattice, and measure the spatial density of the atoms as a function of time and the disorder strength. As the ratio of the disorder strength and the tunneling strength, Δ/J goes above a critical value, they observed a crossover between the ballistic expansion of the BEC and no expansion. They demonstrated that the system has the feature as that in the case of purely-random disorder in higher dimensions.

These research works paved the way for more sophisticated AL studies in cold atoms and enables the interplay between AL and other well-studied topics in cold atoms, for example, the spin-orbit coupling.

Chapter 4: Optical speckle, a Gaussian beam model

An optical speckle is a powerful tool for creating disordered potentials for atomic systems [72, 74]. It was studied in the 1970s [83], the strength of the resultant potential is under direct experimental control: the spatial correlation length is tunable and the correlation function is well known.

Optical speckle can be understood as the self-interfering wave field of a laser after acquiring a random phase by reflection off rough surfaces or transmission through disordered media, called a diffuser [83]. We will focus on the transmission case and assume that the spatial scale of the disorder σ is small in comparison to the laser beam size and that the diffuser transmits light uniformly. The transmitted field can be intuitively thought of as of many waves scattered from microscopic elements comprising the diffuser. So randomness arises. As a disordered field, optical speckle is characterized by its intensity distribution, spatial intensity correlation function, and power spectral density (PSD).

As shown in Fig. 4.1 shows, ray optics in the paraxial limit provides a simple and useful approach to estimating the on-axis beam properties of a speckle beam a distance z beyond a diffuser. As a collimated laser beam of wavelength λ travels through a diffuser of diameter D_d , it acquires a local divergence angle $\theta_d \simeq \lambda/(2\sigma)$.

Fig. 4.1(a) depicts the simplest case consisting of an isolated diffuser, for which there are two qualitatively different regimes: A near-field regime with $z < D_d/(2\theta_d)$, where the typical length scale of optical speckle is σ , and a far-field regime where the numerical aperture (NA) of the diffuser increases the speckle scale to $(\lambda/2) \times (2z/D_d)$. This simple approach is insufficient because we are interested in micrometer scale speckle, which is far smaller than the 10 to 100 micrometer scale of σ for commercial diffusers.

In Fig. 4.1(b) we add a lens with diameter D_L and focal length f just after the diffuser. In the focal plane of the lens, the speckle scale is set by the lens NA, giving a speckle length scale $\lambda f/D_L$, independent of σ . In contrast, the beam width at the focal plane $w(f) \simeq 2f\theta_d$ is set by the speckle scale σ and not the lens diameter.

In this chapter, we will derive the origin of these design guidelines from the paraxial wave equation.

4.1 Gaussian beam equations with speckle

We focus on monochromatic optical electric fields $E(\mathbf{x}, t)$ with angular frequency ω traveling predominantly along \mathbf{e}_z . Such waves can be decomposed as $E(\mathbf{x}, t) = E_\perp(\mathbf{r}; z) \exp[i(k_0 z - \omega t)]$, where $E_\perp(\mathbf{r}; z)$ describes the transverse structure of the electric field with the high spatial frequencies associated with the nominal propagation along \mathbf{e}_z factored out. For spatial scales in excess of the optical wavelength the transverse field obeys the paraxial wave equation

$$-2ik_0\partial_z E_\perp(\mathbf{r}; z) = [-\nabla_\perp^2 + k_0^2\chi(\mathbf{r}; z)] E_\perp(\mathbf{r}; z) \quad (4.1)$$

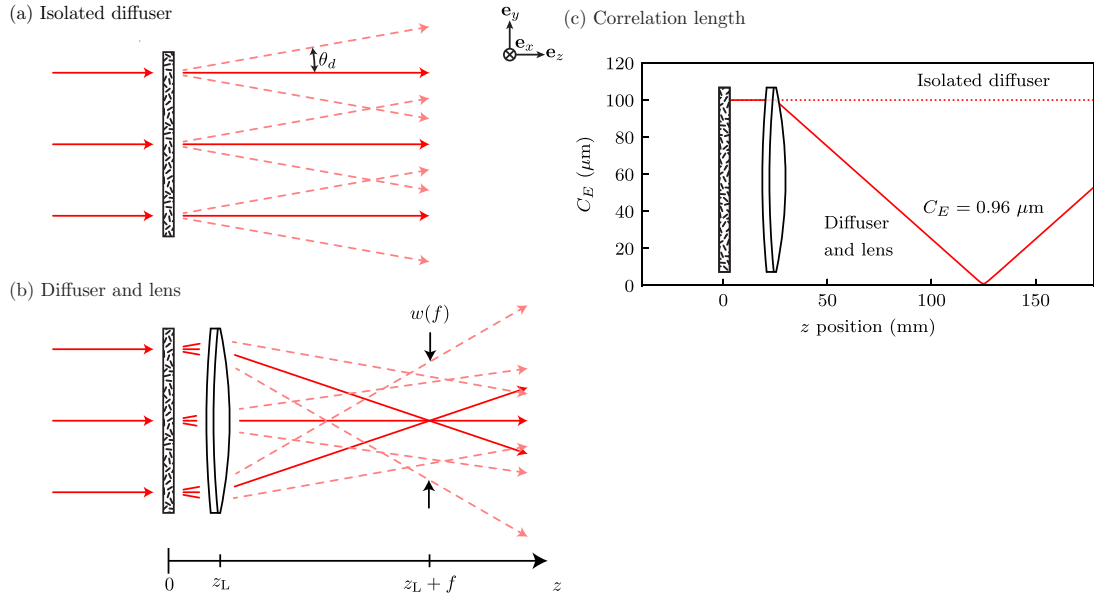


Figure 4.1: Optical speckle schematic. (a) A collimated beam is transmitted through a rough medium and its intensity is measured in plane z . (b) The diverged beam after the rough medium is imaged by a lens at plane $z = z_L$ and f is the focal point of the lens. (c) Field-field correlation length for a Gaussian speckle beam initially with $\sigma = 100 \mu\text{m}$ and $w = 25 \text{ mm}$ as a function of propagation distance. The red curves plot $c_E(z)$ computed with (solid) and without (dashed) a lens with focal length $f = 100 \text{ mm}$ at $z_L = 25 \text{ mm}$.

traveling in a material with relative susceptibility $\chi(\mathbf{r}; z)$. We will suppress the \perp subscript in the remainder of our discussion.

Upon traversing through a thin but disordered material with susceptibility $\chi(\mathbf{r})$ and thickness δz , an initially Gaussian wave field $E^-(\mathbf{r}, 0) = E_0 \exp\{-\mathbf{r}^2/w^2\}$ acquires a position dependent complex phase $\phi(\mathbf{r}) = \chi(\mathbf{r})k_0\delta z/2$. The resultant field

$$E^+(\mathbf{r}, 0) = E^-(\mathbf{r}, 0) \exp[-i\phi(\mathbf{r})] \quad (4.2)$$

carries the imprint of the disordered medium. The field a distance z beyond the speckle plate follows from

$$E(\mathbf{r}; z) = \frac{-ik_0}{2\pi z} \int d^2\mathbf{r}' E^+(\mathbf{r}'; 0) e^{-ik_0|\mathbf{r}-\mathbf{r}'|^2/2z}, \quad (4.3)$$

the formal solution to the paraxial wave equation Eq. (4.1). We model typical diffusion plates, for which: (1) the correlation function of the susceptibility $\langle\chi(\mathbf{r}_1)\chi(\mathbf{r}_2)\rangle$ depends only on relative distance $|\mathbf{r}_1 - \mathbf{r}_2|$, where $\langle\dots\rangle$ denotes the ensemble average over disorder realizations. (2) the variation of the imprinted phase $\phi(\mathbf{r})$ is much larger than 2π with

$$\langle\exp[-i\phi(\mathbf{r}_1)]\rangle = 0, \quad (4.4)$$

i.e., $\phi(\mathbf{r})$ is uniformly distributed over the interval $[-\pi, \pi]$.

We turn to the field-field correlation function

$$C_E(\mathbf{r}_1, \mathbf{r}_2; z) = \langle E(\mathbf{r}_1; z)E^*(\mathbf{r}_2; z) \rangle - \langle E(\mathbf{r}_1; z) \rangle \langle E^*(\mathbf{r}_2; z) \rangle \quad (4.5)$$

to characterize the statistical properties of the disordered electric field. Eq. (4.4) implies that the second term is zero. At $z = 0$, the uniform phase distribution

implies $\langle E^+(\mathbf{r}; 0) \rangle = 0$, giving

$$\frac{C_E(\mathbf{r}_1, \mathbf{r}_2; 0)}{E_0^2} = \exp\left(-\frac{\mathbf{r}_1^2 + \mathbf{r}_2^2}{w^2}\right) \langle \exp\{-i[\phi(\mathbf{r}_1) - \phi(\mathbf{r}_2)]\} \rangle.$$

Under the assumptions of the typical diffusion plates, we model the phase-phase correlation function

$$\langle \exp\{-i[\phi(\mathbf{r}_1) - \phi(\mathbf{r}_2)]\} \rangle = \exp\left(-\frac{|\mathbf{r}_1 - \mathbf{r}_2|^2}{\sigma^2}\right), \quad (4.6)$$

with a Gaussian decay of width σ that is amenable to the following analytic treatments. The relation

$$\langle \exp\{-i[\phi(\mathbf{r}_1) + \phi(\mathbf{r}_2)]\} \rangle = 0, \quad (4.7)$$

that follows from Eq. (4.4), in conjunction with the assumption that the correlation function depends only on relative distance, will be useful as well.

We first consider the case illustrated by Fig. 4.1(a) where a Gaussian beam goes through a large disordered medium. The field-field correlation function at all positions following the disordered medium can be exactly computed and takes the form

$$\begin{aligned} \frac{C_E(\mathbf{r}_1, \mathbf{r}_2; z)}{E_0^2} &= \left[\frac{w}{w(z)}\right]^2 \exp\left(-ik_0 \frac{\mathbf{r}_1^2 - \mathbf{r}_2^2}{2R(z)}\right) \\ &\times \exp\left(-\frac{\mathbf{r}_1^2 + \mathbf{r}_2^2}{w(z)^2}\right) \exp\left(-\frac{|\mathbf{r}_1 - \mathbf{r}_2|^2}{\sigma(z)^2}\right) \end{aligned} \quad (4.8)$$

reminiscent of that of Gaussian beams.

This correlation function is characterized in terms of three z -dependent functions: the beam waist $w(z)$, the radius of curvature $R(z)$, and the correlation length $\sigma(z)$. Each of these is simply related to a reduced Rayleigh range $z_R^* = z_R/M$, with

conventional Rayleigh range $z_R = k_0 w^2 / 2$ and beam quality factor $M^2 = 1 + 2w^2 / \sigma^2$.

The resulting coefficients

$$\left[\frac{w(z)}{w} \right]^2 = \left[\frac{\sigma(z)}{\sigma} \right]^2 = 1 + \left(\frac{z - z_0}{z_R^*} \right)^2 \quad (4.9)$$

and

$$\frac{R(z)}{z - z_0} = 1 + \left(\frac{z_R^*}{z - z_0} \right)^2 \quad (4.10)$$

take the same form as a usual Gaussian beam focused at z_0 . Lastly, as in Fig. 4.1(b), an ideal lens with focal length f at position z_L gives new Gaussian beam parameters defined by

$$\frac{w'}{w} = \frac{\sigma'}{\sigma} = f \left[(z'_0 - z_L - f)^2 + z_R^{*2} \right]^{-1/2} \quad (4.11)$$

and

$$(z'_0 - z_L)^{-1} = f^{-1} - \left[(z_L - z_0) + \frac{z_R^{*2}}{z_L - z_0 - f} \right]^{-1}$$

where the first expression defines the magnification and the second is analogous to the usual lens makers equation [84]. While this leaves M^2 unchanged, the Rayleigh range is altered owing to the change in w . All together these relations fully define field-field correlation function C_E throughout an ideal imaging system.

In most quantum-gas experiments, optical potentials are created using laser light in the far detuned limit, thereby experiencing a potential proportional to the optical intensity

$$I(\mathbf{r}; z) = \frac{c\epsilon_0}{2} |E(\mathbf{r}; z)|^2 \quad (4.12)$$

not the electric field directly. The ensemble-averaged intensity

$$\langle I(\mathbf{r}; z) \rangle = \frac{c\epsilon_0}{2} C_E(\mathbf{r}, \mathbf{r}; z), \quad (4.13)$$

simply related to the field-field correlation function in Eq. (4.8), contains no information about the optical speckle except for the changed M^2 .

As discussed in the next section, the power spectral density (PSD) of the intensity

$$\begin{aligned} \rho(\mathbf{k}; z) &= \langle \tilde{I}(\mathbf{k}; z) \tilde{I}^*(\mathbf{k}; z) \rangle \\ &= \frac{\pi^2 w^2(z)}{4M^2} \exp\left\{-\frac{\mathbf{k}^2 w^2(z)}{4M^2}\right\}, \end{aligned} \quad (4.14)$$

computed using Eq. (4.8), describes the momentum-change imparted by the speckle potential to a moving atomic wavepacket.

4.2 Correlation length

The field-field correlation length

$$c_E(z)^2 = \frac{\iint |C_E(\mathbf{r}_1, \mathbf{r}_2; z)| |\mathbf{r}_1 - \mathbf{r}_2|^2 d^2\mathbf{r}_1 d^2\mathbf{r}_2}{\iint |C_E(\mathbf{r}_1, \mathbf{r}_2; z)| d^2\mathbf{r}_1 d^2\mathbf{r}_2} \quad (4.15)$$

$$= \frac{2w(z)^2 \sigma(z)^2}{2w(z)^2 + \sigma(z)^2} \approx \sigma(z)^2 \quad (4.16)$$

obtained from Eq. (4.8), sets the scale over which the electric field retains its spatial coherence. The field-field correlation length is minimized at $z = z_0$, and is always larger than σ . Generally, speckle beams operate in the regime $w \gg \sigma$, where there are many speckle grains within a large beam, giving the final approximate relation.

As was already noted in our ray-optics discussion, this has important implications for experiment design. For cold atom experiments such as ours, the large

momentum-change imparted by short-length scale speckle is essential, where a correlation length at or below the micron scale is desirable. Since the correlation length available for typical commercial diffusers ranges from $10\ \mu\text{m}$ to $100\ \mu\text{m}$, an additional focusing stage is required.

A focusing lens can easily take the $10\ \mu\text{m}$ to $100\ \mu\text{m}$ correlation length available for typical commercial diffusers and create a beam with sub-micrometer correlation length at its focus. Fig. 4.1(c) compares the correlation length of a beam with (red solid) and without (red dashed) a focusing lens for the specific case of an initial laser beam of wavelength $\lambda = 532\ \text{nm}$ with Gaussian beam parameters: focal point $z_0 = 0$, beam waist $w = 25\ \text{mm}$ and correlation length $\sigma = 100\ \mu\text{m}$. This beam is focused by a lens of focal length $f = 100\ \text{mm}$, the correlation length at the focus is $c_E = 0.96\ \mu\text{m}$. The remaining derived beam parameters are $M^2 \approx 1.25 \times 10^5$, $z_R \approx 3.7\ \text{km}$, and $z_R^* \approx 10.4\ \text{m}$.

In [85], the spacetime evolution of three-dimensional (3D) optical speckle is studied using the ABCD ray-matrix techniques. The optical speckle they studied results from a diffuse object that is illuminated by a Gaussian-shaped laser beam. The field-field correlation length obtained from this approach agrees with our results. In addition, the intensity-intensity correlation length in z direction is calculated in [85]. In the case the optical speckle is focused by a lens with focal length f , the on-axis intensity-intensity correlation length in z direction L_z is of the order of the depth of focus $4f^2/kw^2$. Using the parameters in Fig. 4.1(c), in the focal plane, $L_z \approx 5.4\ \mu\text{m}$. In the free propagation case, L_z grows as $4z^2/kw^2$, and $L_z \gg c_E(z)$ in the far field where $z \gg w$.

4.3 Impact of apertures

In the case of focusing optical speckle as shown in Fig. 4.1(b), a lens of focal length f and diameter $D_L \ll w$ is placed at $z = z_L \leq k_0\sigma^2$. The field in the plane $z = z_L$ before the lens, $E^-(\mathbf{r}; z_L)$ is essentially unchanged from field $E^+(\mathbf{r}; 0)$. The field $E^-(\mathbf{r}; z_L)$ passes through the lens aperture, where it acquires a position dependent phase and is truncated outside the lens. The emerging field $E^+(\mathbf{r}; z_L)$ propagates to the focal plane $z = f + z_L$ where it is

$$E_f(\mathbf{r}) = \frac{-ik_0}{2\pi f} e^{-ik_0 r^2/2f} \int_{|\mathbf{r}'| < \frac{D_L}{2}} d^2\mathbf{r}' E^+(\mathbf{r}'; 0) e^{ik_0 \mathbf{r} \cdot \mathbf{r}'/f}. \quad (4.17)$$

When $\sigma \ll D_L \ll w$, the field-field correlation function at the focal plane is

$$C_{E,f}(\mathbf{r}_1, \mathbf{r}_2) \approx C_0 \exp\left[-\frac{ik_0(\mathbf{r}_1^2 - \mathbf{r}_2^2)}{2f}\right] \times \exp\left[\frac{-k_0^2\sigma^2(\mathbf{r}_1 + \mathbf{r}_2)^2}{16f^2}\right] \frac{J_1(k_c \Delta r/2)}{k_c \Delta r/2}. \quad (4.18)$$

Here $C_0 = k_0^2 E_0^2 D_L^2 \sigma^2 / 8f^2$ is the peak correlation amplitude; $\Delta r = |\mathbf{r}_1 - \mathbf{r}_2|$ is the relative position coordinate; and J_1 is a Bessel function of the first kind. The ratio

$$k_c = k_0 \frac{D_L}{f} \quad (4.19)$$

is a cutoff above which the PSD of the intensity

$$\rho_f(k) = C_0^2 \frac{2}{\pi k_c^2} \left[\cos^{-1}\left(\frac{k}{k_c}\right) - \frac{k}{k_c} \sqrt{1 - \frac{k^2}{k_c^2}} \right] \quad (4.20)$$

is strictly zero. Eq. (4.20) is valid near the optical axis where $|\mathbf{r}_1|, |\mathbf{r}_2| \ll w(z)$.

4.4 Field and intensity probability distribution

In the previous sections, we focused on the average properties of speckle fields. Here we extend this discussion to predict the probability distribution of electric field strength $P(E)$ and intensity $P(I)$. Our approach focuses first on $P(E)$, and consists of two steps: (1) we find the regime when the central limit theorem applies, thereby assuring a Gaussian probability distribution; (2) we identify $\langle E \rangle$ and $\langle E^2 \rangle$ as the lowest moments of the distribution, fully defining the Gaussian distribution.

We now interpret the electric field

$$E(\mathbf{r}; z) = \frac{-ik_0}{2\pi z} \int d^2\mathbf{r}' E^-(\mathbf{r}') e^{-i\phi(\mathbf{r}')} e^{-k_0|\mathbf{r}-\mathbf{r}'|^2/2z},$$

of Eq. (4.3) as a random variable constructed from a sum over incoherent complex phasors. The cross correlation function (CCF) $\langle E(\mathbf{r}_1; z)E(\mathbf{r}_2; 0) \rangle$ specifies the range over which the initial random field contributes to the final field. The closed form expression for this CCF is similar to the field-field correlation function in Eq. (4.8); the length scale for the decay of correlations $\sigma_{\text{CCF}}(z)$ again obeys Eq. (4.9), but with $M_{\text{CCF}}^2 = (1 + w^2/\sigma^2)^2$. When $w \gg \sigma$, i.e., the initial waist is much larger than the speckle size, the resulting Rayleigh range reduces to $z_{\text{R,CCF}} = k_0\sigma^2/2$: as if each random source was an individual Gaussian beam with extent σ . The criterion that a field $E(\mathbf{r}; z)$ have contributions from many incoherence sources is therefore $\sigma_{\text{CCF}}(z)/\sigma \gg 1$, i.e., $z \gg z_{\text{R,CCF}}$.

This identifies the central limit theorem's regime of applicability, and we now consider $E(\mathbf{r}; z)$ as a complex valued Gaussian random variable. The probability

distribution for electric field is therefore a function of two independent degrees of freedom, here we select the quadrature variables E and E^* , giving $P(E, E^*)$. Most moments of this quantity are easy to identify using Eqs. (4.3), (4.4), (4.6) and (4.7): $\langle E \rangle = \langle E^2 \rangle = 0$, and similarly for E^* . Then Eqs. (4.5) and the following discussion assure us that $\langle EE^* \rangle = \langle |E|^2 \rangle$ takes on a non-zero value. Together these fully define the Gaussian probability distribution for electric fields

$$P(E, E^*) = \frac{1}{\pi \langle |E|^2 \rangle} \exp\left(-\frac{|E|^2}{\langle |E|^2 \rangle}\right), \quad (4.21)$$

and using Eq. (4.13), the intensity distribution

$$P(I) = \frac{1}{\langle I \rangle} \exp\left(-\frac{I}{\langle I \rangle}\right) \quad (4.22)$$

follows directly. The intensity of a speckle field obeys an exponential distribution and the mean of speckle intensity $\langle I \rangle$ should be equal to its standard deviation $\sqrt{\langle I^2 \rangle}$.

4.5 Simulated speckle and the comparison to experiment

Having now fully set the stage for understanding and creating speckle laser beams, we turn to laboratory confirmation of key prediction of these models relevant to cold atom experiment: the field-field correlation length C_E and the distribution of intensities $P(I)$.

In our lab, we directed a collimated laser beam (waist $w \approx 25$ mm) through a diffuser (divergence angle $\theta_d = 0.5^\circ$, and aperture $D = 20$ mm) focused immediately by a lens (focal length $f = 30$ mm) as depicted in Fig. (4.1) and quantified the

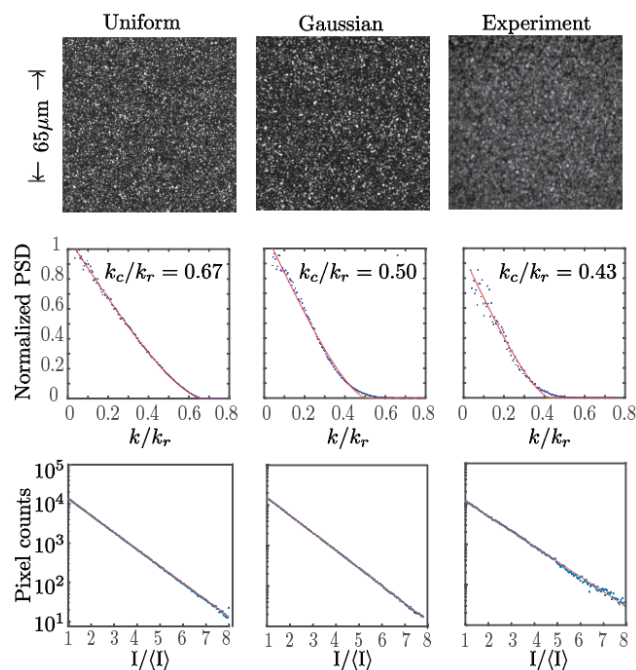


Figure 4.2: Simulated and measured optical speckle. The columns in the figure correspond to: simulated speckle with uniform laser beam, simulated speckle from a Gaussian laser beam and measured speckle. In each column, the first row shows the intensity of the optical speckle field. The second row shows the PSD of the intensity shown in the first row (symbols). The red curve shows a fit of Eq. (4.20) to the data, along with the resulting k_c . The third row histograms the intensity from the first row.

optical speckle formed at the focal plane. We then imaged the optical speckle onto a charge coupled device (CCD) camera with Keplerian telescope with magnification $M = 46$. The CCD's 1024×1280 array of $4.8 \mu\text{m}$ pixels gave a $100 \mu\text{m} \times 130 \mu\text{m}$ magnified field of view with $0.1 \mu\text{m}$ pixels.

Our analytic results for C_E are valid in the Gaussian beam limit ($w \ll D$) or uniform illumination limit ($w \gg D$). Because our experiment has $w \approx D$, we numerically simulated the optical speckle to compare with our measurements and both models.

For the numerical simulation, the desired optical speckle field $E_{i,j}$ is represented by a 1024×1280 array at the focal point of the lens. We use the optical Fourier transform property of lenses to compute this efficiently, whereby the field a focal distance beyond the lens is related to the Fourier transform of the field a focal distance prior to the lens (which we will term the Fourier plane). An important aspect of this method is that the $0.1 \mu\text{m}$ grid spacing in the focal plane transforms to a 1.5 mm grid spacing in the Fourier plane.

Our simulation progresses as follows. (1) We first initialize $E_{i,j}(z = 0)$ to the field of either a uniform field or a Gaussian beam. (2) We then imprint random phases on each point ¹. (3) We set the field outside our physical aperture to zero. (4) Then we back-propagate the field to the Fourier plane and take the Fourier transform to obtain the field at the focal plane.

Fig. (4.2) compares our measured speckle with numerics and our analytic

¹The grid size is much larger than the correlation length of the diffuser, so the imprinted phase at each grid point is uncorrelated with all other points.

model; the three columns depict: the case of a uniformly illuminated aperture, Gaussian illumination, and experiment. The top row shows that intensity at the focal plane is qualitatively similar for all three cases. In the middle row, the PSD (computed from the intensity in the top row, and plotted by blue symbols), highlights the differences. In each case, we fit Eq. (4.20) the PSD and extract k_c from the fits (red curves). Because Eq. (4.20) was derived for a uniformly illuminated aperture it provides a good fit to the uniform illumination case but deviates at large k for Gaussian illumination and experiment. In contrast, the numerics for Gaussian illumination and the experiment are indistinguishable. In the bottom row, we histogram the intensity distribution and verify that in all three cases we recover the expected exponential fall-off.

Chapter 5: Enhanced transport of spin-orbit-coupled Bose gases in disordered potentials

In materials, microscopic electron scattering processes partly govern the macroscopic conductivity and AL predicts a metal-insulator transition. Increasing a system's conductivity therefore requires some change in these scattering processes. The most straightforward mechanism is to reduce the disorder strength. Here we describe an alternative approach in which spin-orbit coupling (SOC) greatly suppresses the backscattering and thereby increases the conductivity. We then propose a realization of this effect using a cold-atom Bose-Einstein condensate (BEC) with laser-induced SOC [35] and disorder from optical speckle.

SOC is a ubiquitous phenomenon in physical systems that describes the interaction between a particle's spin and its momentum. When SOC is combined with a transverse magnetic field (in the sense of Zeeman shifts, not Lorentz forces), gaps in the dispersion relation can open at spin-degeneracy points. The opening of these gaps modifies the electrons' scattering processes and affects transport. AL was first realized for ultracold-cold atomic systems [72, 73] in 2008, and the experimental techniques are now well established. Shortly thereafter, techniques for creating SOC in the cold atom lab were demonstrated [35]. Together, this makes cold-atom

systems an ideal platform to study the interplay between AL and SOC.

An optical speckle is a powerful tool for creating disordered potentials for atomic systems [86]. The strength of the resultant potential is under direct experimental control: the spatial correlation length is tunable and the correlation function is well known. Here we analytically and numerically study backscattering in speckle potentials of quasi-1d spin-orbit coupled BECs (SOBECs) and compare to the case without SOC. We show that SOC can reduce the scattering processes for specific momentum states. In the broader context, our results suggest that in thin nanowires, SOC might significantly decrease resistance and improve energy efficiency in electronic devices.

In Sec. 5.1, we analytically calculate the probability of an initial momentum state being scattered by the speckle potential to any final momentum state and show that SOC can reduce backscattering. In Sec. 5.2, we describe numerical simulations of quasi-1d BECs starting in different momentum states subject to a speckle potential with and without SOC. We show that even with the higher-order scattering processes and interaction between particles present in the numerical simulations, SOC can reduce the localization effects of disorder and enhance transport.

5.1 Scattering of an SOBEC from a speckle potential

We now focus on the motion of spin-orbit coupled bosons in a speckle-induced disorder potential. In this section, we develop a Fermi's golden rule (FGR) approach for scattering from a disorder potential, both with and without SOC, schematically

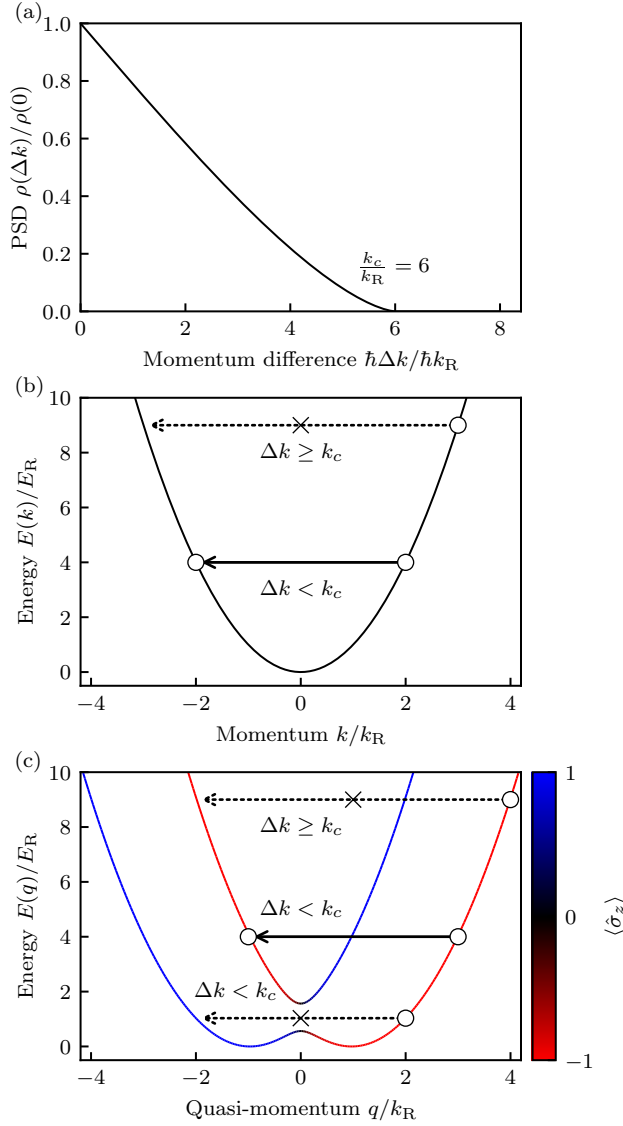


Figure 5.1: Fermi's Golden Rule. Momentum are expressed in units of the single-photon recoil momentum k_R used to create SOC in (c). (a) Representative PSD for optical speckle with $k_c = 6k_R$. (b) Free particle dispersion relation. The dashed arrow marks the boundary above which the FGR rate vanishes, while the solid arrow provide an example with non-zero rate. (c) SOC dispersion relations computed for $\delta = 0$ add $\Omega_R = 1E_R$ colored according to the expectation value $\langle \sigma_z(q) \rangle$, with arrows marked as in (b). Note the transition through the gap in the dispersion relation at $E \approx E_R$ where the FGR rate is nearly zero.

depicted in Fig. 5.1. The first order scattering processes captured by the FGR are possible when a matrix element (here from the disorder potential) can couple energetically degenerate initial and final states (here momentum or quasi-momentum states). We will see that the strength of this coupling is proportional to the PSD of the speckle potential, an example of which is shown in Fig. 5.1(a). As depicted in Fig. 5.1(b), this implies an absence of scattering for momenta differences larger than the speckle-cutoff k_c . Adding SOC, as in Fig. 5.1(c), can suppress scattering for additional wavevectors. Because a spin-independent speckle potential has no spin-changing matrix element, the energetically allowed transition at an energy $E/E_R \approx 1$ between states of opposite spin is strongly suppressed. The following discussion quantifies these observations.

5.1.1 Spinless atoms

For spinless free particles, the unperturbed Hamiltonian $H = \hbar^2 k^2 / 2m$ implies that we study scattering between initial and final momentum states, labeled by $|k_0\rangle$ and $|k_f\rangle$ respectively. Figure 5.1(b) depicts examples by open circles, with arrows connecting initial states to final states.

The time evolution of the initial state $|\psi(0)\rangle = |k_0\rangle$ subject to the speckle potential $V(x)$ may always be expressed as

$$|\psi(t)\rangle = \sum_k C_{k,k_0}(t) e^{-i\omega_k t} |k\rangle, \quad (5.1)$$

with $C_{k,k_0}(0) = \delta_{k,k_0}$ and $\hbar\omega_k = \hbar^2 k^2 / 2m$. The coefficients $C_{k,k_0}(t)$ are governed by

the time-dependent Schrödinger equation giving the exact expression

$$C_{k_f, k_0}(t) = C_{k_f, k_0}(0) + \frac{1}{i\hbar} \sum_k \langle k_f | \hat{V} | k \rangle \int_0^t d\tau e^{i\omega_{k_f, k}\tau} C_{k, k_0}(\tau). \quad (5.2)$$

with

$$\omega_{k, l} = \omega_k - \omega_l, \quad \text{and} \quad \hat{V} = \sum_x V(x) |x\rangle \langle x|. \quad (5.3)$$

An order-by-order perturbation theory is typically obtained by recursively inserting the integral expression for $C_{k_f, k_0}(t)$ back into the integrand; unfortunately, the general problem is intractable and we truncate the perturbation series at first order. This term is effectively obtained by replacing $C_{k_f, k_0}(\tau)$ with $C_{k_f, k_0}(0) = \delta_{k_f, k_0}$, and find

$$C_{k_f, k_0}(t) = \delta_{k_f, k_0} + \frac{1}{i\hbar} \int_0^t d\tau \langle k_f | \hat{V} | k_0 \rangle e^{i\omega_{k_f, k_0}\tau}. \quad (5.4)$$

Unfortunately, we do not know $V(x)$ for any specific realization of the speckle potential.

In Chpt. 4 we characterized optical speckle in terms of second-order statistical metrics such as the PSD, here equal to $\rho(k_f - k_0) = \langle \langle k_f | \hat{V} | k_0 \rangle \langle k_0 | \hat{V} | k_f \rangle \rangle$, where the double-brackets indicate the ensemble average. The resulting ensemble averaged transition probability

$$P_{f,0}(t) = \frac{\rho(k_f - k_0)}{\hbar^2} \left[\frac{2}{\omega_{f,0}} \sin \left(\frac{\omega_{f,0}t}{2} \right) \right]^2 \quad (5.5)$$

is a sharply peaked function centered at $\omega_{f,0} = 0$ with width $2\pi/t$, showing that a narrow range of energy matching states can be populated. For long times, $\omega_{f,0}t \gg 1$ the quantity in square brackets converges to a scaled Dirac delta function $t \times \delta(\omega_{f,0})$.

Figure 5.1(a) displays the normalized PSD for a speckle potential computed with $k_c = 6k_R$, reminding us that $\rho(k) = 0$ for $k \geq k_c$. Our FGR expression allows two types of scattering processes for the free particle dispersion shown in Fig. 5.1(b). In the first process, depicted by the black arrow, the atom's initial momentum is reversed, changed by $\Delta k = 2k_0$; as indicated by the dashed line, this process is second-order forbidden for $k_0 \geq k_c/2$. In the second process (not pictured), the atom's momentum is only infinitesimally changed: spreading the wave-packet, but leaving the average momentum unchanged. This picture shows that backscattering is essential for momentum-relaxation.

5.1.2 Spin-orbit coupled atoms

Our 1D SOC [35] is created by illuminating a two-level atom with a pair of counter-propagating lasers with wavelength λ_R tuned to drive stimulated Raman transitions between states $\{|q + k_R, \uparrow\rangle, |q - k_R, \downarrow\rangle\}$. Here $\hbar k_R = 2\pi\hbar/\lambda_R$ and $E_R = \hbar^2 k_R^2/2m$ are the single-photon Raman recoil momentum and energy respectively. Subject to this Raman coupling, the atoms obey the 1D Hamiltonian

$$\hat{H}(q) = \left[\frac{\hbar^2 q^2}{2m} + \frac{\hbar^2 k_R^2}{2m} \right] \hat{1} + \left(\frac{\hbar^2 k_R q}{m} + \frac{\delta}{2} \right) \hat{\sigma}_z + \frac{\hbar \Omega_R}{2} \hat{\sigma}_x, \quad (5.6)$$

where $\{\hat{1}, \hat{\sigma}_x, \hat{\sigma}_y, \hat{\sigma}_z\}$ are the identity and Pauli operators, respectively. Here q is the quasi-momentum, Ω_R is Raman coupling strength, and δ is the detuning from the two-photon Raman resonance condition. The resulting dispersion relations, plotted in Fig. 5.1(c) for $\delta = 0$ and $\Omega_R = E_R$, have energies $E^\pm(q)$ labeled by q along with \pm to indicate if they are in the upper or lower band.

These new energies and their associated amplitudes

$$|q, \pm\rangle \propto a_{\pm}(q) |q - k_{\text{R}}, \downarrow\rangle + b_{\pm}(q) |q + k_{\text{R}}, \uparrow\rangle$$

change the potential scattering processes, which we again compute using an FGR expression. The coefficients

$$a_{\pm}(q) = \pm \frac{\Omega_{\text{R}}}{2} \quad \text{and} \quad b_{\pm}(q) = \pm \frac{\Delta(q)}{2} + \frac{\sqrt{\Delta^2(q) + \Omega_{\text{R}}^2}}{2}.$$

along with the quasi momentum dependent detuning

$$\Delta(q) = \frac{2\hbar^2 q k_{\text{R}}}{m} + \delta \quad (5.7)$$

fully define these superposition states.

Following the same FGR argument presented above for initial states $|q_0, -\rangle$ in the lower dispersion scattering from a spin-independent speckle potential, we find scattering probabilities

$$P_{f,0}^{\pm}(t) = \frac{\rho(\Delta q)}{\hbar^2} \left| \frac{2 \sin(\omega_{f,0}^{\pm} t)}{\omega_{f,0}^{\pm}} \langle q_f, \pm | e^{i\Delta q x} | q_0, - \rangle \right|^2 \quad (5.8)$$

expressed in terms of the quasimomentum and energy differences $\hbar\Delta q = \hbar q_f - \hbar q_0$ and $\hbar\omega_{f,0}^{\pm} = E^{\pm}(q_f) - E^{-}(q_0)$. For most initial states $|q_0, -\rangle$, such as two higher-energy states marked in Fig. 5.1(c), the scattering is essentially unchanged from our spinless example, with scattering occurring between energy-matched states with the same initial and final spin. In contrast, for initial states residing in the SOC energy gap there is no energy-matched state of the same spin available for backscattering; as indicated by the dashed line scattering is greatly suppressed. We note that that backscattering is not completely blocked, because the energy matching states $|\pm q_0, -\rangle$ are not spin-eigenstates and do have some spin-overlap.

5.1.3 Computed scattering rates

We now use these FGR expressions to compute the scattering rates for both forward scattering and backscattering processes. Because we are interested in transport properties, we define forward scattering processes as those that leave the sign of the group velocity unchanged and backscattering processes as those that do reverse the direction of motion. We therefore consider initial states $|q_0, -\rangle$ in the lower band with positive group velocity. Because the lower energy SOC dispersion plotted in Fig. 5.2 can have a pair of minima located at $\pm q_{\min}$, we always select $q_0 > q_{\min}$ to assure positive group velocity. We numerically evaluated the FGR for ^{87}Rb atoms illuminated with $\lambda_{\text{R}} = 790$ nm Raman lasers, giving $E_{\text{R}} = h \times 3.7$ kHz, and for speckle with $k_c = 6k_{\text{R}}$. The $t = 13.4$ ms interaction time was selected to be experimentally relevant.

The right panels of Fig. 5.2 show the normalized scattering rate computed for four different values of Ω_{R} , with the backscattering rate plotted in black and forward scattering plotted in red. These rates combine the contributions from the \pm bands in Eq. (5.8).

Fig. 5.2(a), computed for $\Omega_{\text{R}} = 0$ (equivalent to the case with no SOC), shows two key effects. First, the diverging forward- and back-scattering rates at low energy follow from the diverging density of states (DoS) in 1D. Second, as expected, the rate of backscattering (black) falls to zero when $\delta q > k_c$, while forward scattering (red) simply falls with the DoS.

Fig. 5.2(b) and Fig. 5.2(c) show cases with a well resolved SOC energy gap.

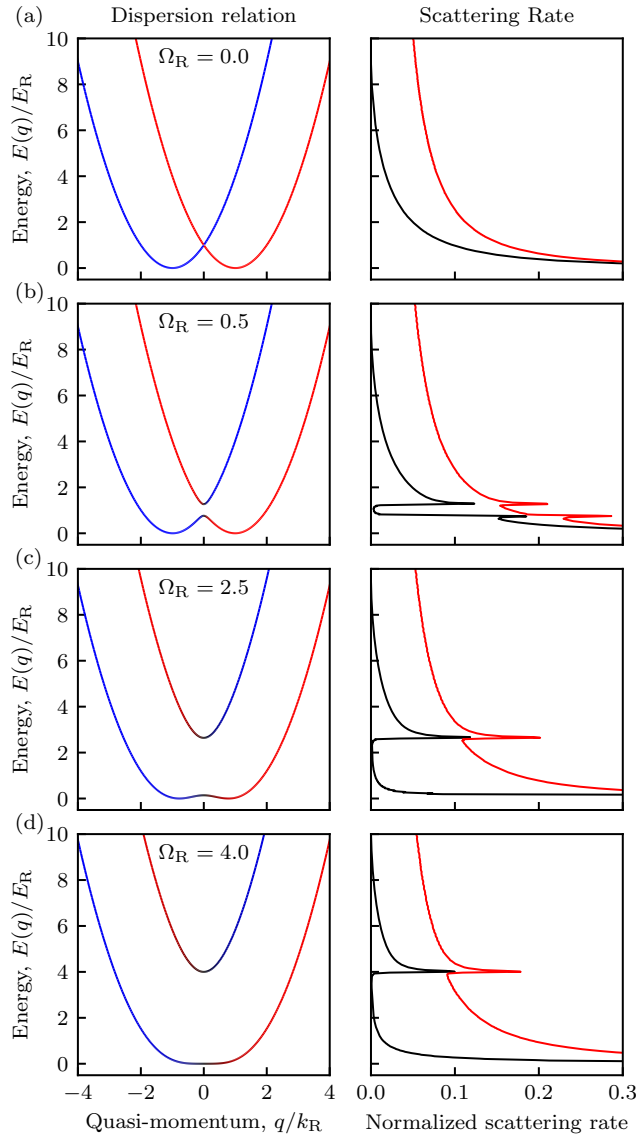


Figure 5.2: Fermi golden rule scattering rate for $\Omega_R/E_R = 0, 0.5, 2.5$ and 4.0 . Left column shows SOC dispersion relations computed for each Ω_R , colored as in Fig. (5.1). Right column shows normalized scattering rate as a function of initial energy for the initial state $|q_0, -\rangle$ with $q_0 \geq q_{\min}$, i.e., in the bottom dispersion and to the right of the higher momentum local energy minimum. The backscattering rate is plotted in black and the forward scattering plotted in red.

As expected, backscattering is nearly completely suppressed for initial energies in the energy gap, while forward scattering is hardly changed. In addition, a pair of singular features border of the energy gap, resulting from the diverging DoS and the local extrema of the dispersions. Fig. 5.2(d) shows the same phenomena, but just as the two minima at $\pm q_{\min}$ have merged into a single minimum at $q_{\min} = 0$.

We, therefore, conclude, for non-interacting particles backscattering and momentum relaxation is nearly completely suppressed for atoms starting in the SOC energy gap.

5.2 Numerical simulation of GPE

Our single particle FGR results only describe short-time scattering from a disorder potential, they cannot describe the full approach to equilibrium. To bridge the gap between the FGR and the physical system, we need to account for both higher order scattering processes and interparticle interactions. In our proposed SOBEC realization all aspects of SOC Hamiltonian and the speckle potential are tunable, making SOBECs an ideal system for exploring enhanced transport in 1D quantum wires.

5.2.1 Gross-Pitaevskii equations

Here we numerically study the deceleration of a SOBEC initially moving in a speckle potential using the time-dependent Gross-Pitaevskii equation (GPE). The

time-dependent GPE

$$i\hbar\partial_t\Psi(\mathbf{r}, t) = \left[-\frac{\hbar^2}{2m}\nabla^2 + V(\mathbf{r}) + g_{3D}|\Psi(\mathbf{r}, t)|^2 \right] \Psi(\mathbf{r}, t) \quad (5.9)$$

is a non-perturbative dynamical description [87] of a large number of interacting identical bosons occupying the same spatial mode $\Psi(\mathbf{r}, t)$, normalized to the total atom number, $N = \int d^3\mathbf{r}|\Psi(\mathbf{r}, t)|^2$. The interaction strength $g_{3D} = 4\pi\hbar^2 a_s/m$ can be expressed in terms of the s -wave scattering length a_s . This GPE provides a good description of low-temperature spin-polarized BECs, with negligible thermal excitations [88].

Since our focus is on 1D transport, we must first obtain a 1D description of our 3D system [89]. Here we, we assume that the potential $V(\mathbf{r}) = V(x) + V_\perp(y, z)$ can be separated into a weak longitudinal potential $V_\parallel(x)$ along with a strongly confining transverse potential $V_\perp(y, z)$. When the single-particle energy spacing from $V_\perp(y, z)$ greatly exceeds all other energy scales, the 3D wavefunction can be factorized into

$$\Psi(\mathbf{r}, t) = \psi(x, t)\phi(y, z), \quad (5.10)$$

containing a longitudinal term of interest giving the 1D density $n(x) = |\psi(x, t)|^2$, and a transverse term $\phi(y, z)$, normalized to unity, assumed to be the ground state of the transverse potential. Inserting this ansatz into the GPE and integrating out the transverse degrees of freedom, gives the 1D GPE

$$i\hbar\partial_t\psi = \left[-\frac{\hbar^2}{2m}\partial_x^2 + V(x) + g|\psi|^2 \right] \psi, \quad (5.11)$$

suitable for studying single-component 1D bosons in a speckle potential with 1D

interaction strength

$$g = g_{3\text{D}} \int dydz |\phi(y, z)|^4. \quad (5.12)$$

For compactness of notation, here and below, we shall omit the functional dependence of ψ on x and t .

The two-component 1D spinor GPE describing SOBECs extends Eq. (5.6) to include interactions, and consists of a pair of coupled non-linear differential equations

$$i\hbar\partial_t\psi_\uparrow = \left[\frac{\hbar^2}{2m} (-i\partial_x + k_{\text{R}})^2 + \frac{\delta}{2} + V(x) + g_{\uparrow\uparrow}|\psi_\uparrow|^2 + g_{\uparrow\downarrow}|\psi_\downarrow|^2 \right] \psi_\uparrow + \frac{\Omega_{\text{R}}}{2}\psi_\downarrow \quad (5.13)$$

$$i\hbar\partial_t\psi_\downarrow = \left[\frac{\hbar^2}{2m} (-i\partial_x - k_{\text{R}})^2 - \frac{\delta}{2} + V(x) + g_{\downarrow\downarrow}|\psi_\downarrow|^2 + g_{\uparrow\downarrow}|\psi_\uparrow|^2 \right] \psi_\downarrow + \frac{\Omega_{\text{R}}}{2}\psi_\uparrow \quad (5.14)$$

including the interaction strengths $g_{\uparrow\uparrow}$, $g_{\uparrow\downarrow}$, and $g_{\downarrow\downarrow}$. Here we focus on the specific case of ^{87}Rb atoms [9] in the $F = 1$ ground state manifold and have selected $|\uparrow\rangle = |m_F = 0\rangle$ and $|\downarrow\rangle = |m_F = -1\rangle$. The interactions can be parameterized in terms of an s -wave pseudo-potential $(g_{0,3\text{D}} + g_{2,3\text{D}}\vec{F}_\alpha \cdot \vec{F}_\beta)\delta(\mathbf{r}_i - \mathbf{r}_j)$ now dependent on spin. In ^{87}Rb 's $F = 1$ manifold $g_{0,3\text{D}} = 100.86 \times 4\pi\hbar^2 a_{\text{B}}/m$ is vastly larger than $g_{2,3\text{D}} \approx -4.7 \times 10^{-3} \times g_{0,3\text{D}}$, where a_{B} is the Bohr radius [90,91]. The interaction coefficients reduce to effective 1D interaction strengths just as in the single component case, and are related to the generic coefficients [92,93] via $g_{\uparrow\uparrow} = g_0$ and $g_{\downarrow\downarrow} = g_{\uparrow\downarrow} = g_0 + g_2$. Table 5.1 summarizes the parameters used in our simulations.

Our simulation results are divided into two sections: Sec. 5.2.2 hones our understanding by considering a single-component BEC evolving in a speckle potential, and then in Sec. 5.2.3 we contrast to the case with SOC. In both sections, we simulate initially trapped BECs accelerated to an initial momentum k_0 or quasi-momentum q_0 and we study their deceleration. All the results are averaged over 20 speckle

realizations, as in Fig. 4.2(b). The average speckle potential $h \times 200 \text{ Hz} \approx 0.05E_R$ was selected to be weak enough to cause no trapping effect yet strong enough to produce significant deceleration within 16ms.

5.2.2 Single component systems

The simulations are performed in three steps to as accurately as possible model a realistic experimental sequence. First, we initialize a ground state BEC in a harmonic trap using imaginary time evolution [94], giving the density distribution plotted as the filled red curve in Fig. 5.3(b)], and follow with real-time evolution. Second, because the BEC's narrow momentum distribution is centered at $k = 0$, we briefly apply a linear potential αx with time-evolution approximately described by the phase factor $\exp(ik_0x)$, a momentum translation operator that transforms $|k = 0\rangle$ to $|k_0\rangle$. Third, having prepared our $|k_0\rangle$ initial state, we replace the harmonic potential with a speckle potential (with $k_c/k_R = 6$) and follow the time evolution for 16 ms. Fig. 5.3(a) shows a representative disorder potential that we use in the simulations. Fig. 5.3(b) captures the main result of this section: when $k_0 > k_c/2$ the time-evolution is almost unchanged by the speckle potential, while slowly moving initial states are both decelerated and exhibit considerable interference.

Figure 5.3(c) plots the ensemble-averaged momentum $\langle k(t) \rangle$ as a function time for a range of initial states with k_0 from near-zero to $k_0/k_R = 3.3$, and Fig. 5.3(d) plots the final momentum k_f as a function of k_0 . At $t = 0$, the average momentum is $\langle k(t) \rangle = k_0$; for $k_0 \gtrsim k_c/2$ the BEC evolves ballistically, leaving $\langle k(t) \rangle$ unchanged,

Description	Symbol	Value
^{87}Rb atomic mass	m	1.42×10^{-25} kg
Raman laser wavelength	λ_{R}	790 nm
Recoil energy	E_{R}	$h \times 3.678$ kHz
Dipole trap frequency	$\omega/2\pi$	10 Hz
Angle of Raman beams	θ_{R}	180°
Speckle potential cut off	k_c	$6k_{\text{R}}$
Average speckle potential	$\overline{V(x)}$	$0.05E_{\text{R}}$
Grid spacing	δx	66 nm
Grids points (single-component)	N_x	$2^{14} + 1$
Grids points (SOC)	N_x	$2^{13} + 1$
Atom number	N	2×10^5
Chemical potential	μ	$h \times 300$ Hz

Table 5.1: Simulation parameters

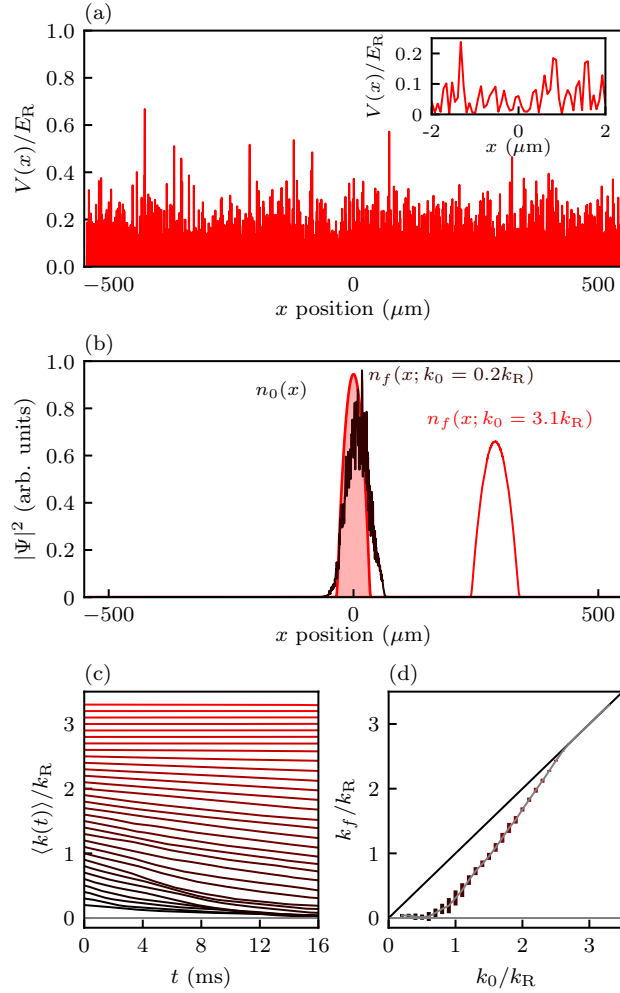


Figure 5.3: Single-component GPE simulation with $k_c/k_R = 6$. (a). Representative disorder potential used in our simulations. The inset shows an expanded view with visible structure. (b) Density distributions. The filled red curve depicts the initial density distribution, while the black and red curves show the final-state density distributions for initial momenta $|k_0 = 0.2k_R\rangle$ and $|k_0 = 3.1k_R\rangle$, above and below $k_c/2$, respectively. (c) Mean momentum. $\langle k(t) \rangle$ averaged over 20 speckle realizations is plotted for a range of initial momentum in the range of 0 to $3.3k_R$, the $t = 0$ point of each curve marks the initial k_0 . (d) Deceleration. The colored symbols plot $k_f = \langle k(t = 16 \text{ ms}) \rangle$ as a function of k_0 along with their standard deviations, and the black line marks $k_f = k_0$ corresponding to ballistic motion.

while $\langle k(t) \rangle = k_0$ falls rapidly for smaller k_0 . Both of these observations are consistent with our FGR analysis which showed a complete absence of momentum-changing backscattering for $k_0 \geq k_c/2$, and with rapidly increasing backscattering as k falls to zero.

5.2.3 SOBECs

As in the single-component case, simulations with SOC begin with three steps aligned with the experiment, however, the process of preparing the initial quasimomentum state $|q_0, -\rangle$ is considerably more elaborate than preparing a momentum state $|k_0\rangle$ in a single component system. (1) As before, we initialize a ground state BEC in a harmonic trap using imaginary time evolution, spin polarized in state $|k_0 = 0, \downarrow\rangle$. (2) We then use a combination of adiabatic and unitary evolution (described below) to transform this state into $|q_0, -\rangle$ for $\delta = 0$ and Ω_R ranging from $0.5E_R$ to $8E_R$. (3) Lastly, we again remove the harmonic potential and again follow the time evolution with a speckle potential ($k_c/k_R = 6$) for 16 ms.

Our procedure (2) begins with the observation that in a frame moving with velocity $\hbar\delta k/m$, the detuning δ present SOC Hamiltonian in Eq. (5.6) is Doppler-shifted [95, 96] to $\delta + 2\hbar^2\delta k k_R/m$. Our first task is to adiabatically transform the initial state $|k_0 = 0 \downarrow\rangle$ into $|q_{\min}, -\rangle$, a ground state SOBEC with quasi-momentum centered at $q = q_{\min}$. $|q_{\min}, -\rangle$ is the global minima of the SOC dispersion, but with $\delta = 2\hbar^2(q_0 - q_{\min})k_R/m$. Fig. 5.4(a) shows the SOC dispersion for $\Omega_R = E_R$, $\delta = 2\hbar^2(q_0 - q_{\min})k_R/m$ and $q_0 = 2.0k_R$. Fig. 5.4(b) shows the SOC dispersion for

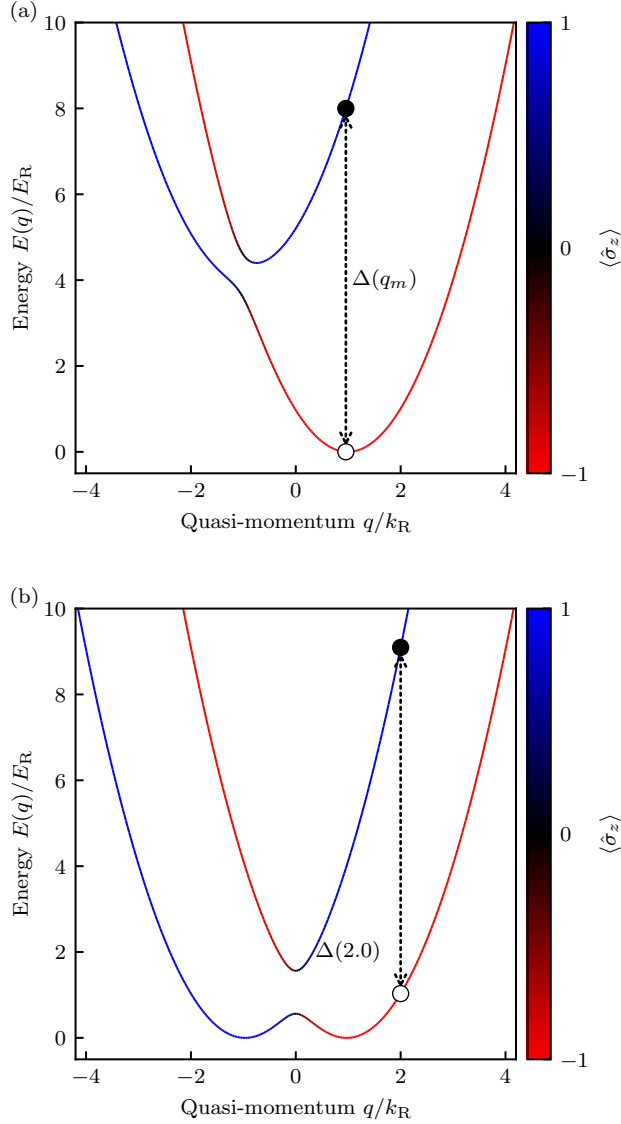


Figure 5.4: Make SOC eigenstates $|q_0, -\rangle$. (a). The SOC dispersion relation with $\delta = 2\hbar^2(q_0 - q_{\min})k_R/m$, $\Omega_R = E_R$. The dashed line indicates the detuning $\Delta(q_{\min})$ between $|q_{\min}, -\rangle$ and $|q_{\min}, +\rangle$. (b). The SOC dispersion relation with $\delta = 0$, $\Omega_R = E_R$. The dashed line indicates the detuning $\Delta(q_0)$ between $|q_0, -\rangle$ and $|q_0, +\rangle$, with $q_0 = 2.0k_R$ as an example. δ in (a) is tuned such that $\Delta(q_{\min})$ is equal to $\Delta(q_0 = 2.0k_R)$ in (b).

$\Omega_R = E_R$, $\delta = 0$. In both Fig. 5.4(a) and Fig. 5.4(b), the dashed lines indicate the detuning $\Delta(q)$. δ in Fig. 5.4(a) is determined such that $\Delta(q_{\min})$ in Fig. 5.4(a) and $\Delta(q_0 = 2.0k_R)$ in Fig. 5.4(b) are equal. We transfer to state $|q_{\min}, -\rangle$ by ramping up the Raman coupling strength from zero to Ω_R on a time scale slow compared to $\hbar/\Delta(q_0)$. In the slow ramp-up process, the harmonic trap provides the restoring force required to keep the state at local minima of the dispersion [35], i.e., with zero group velocity. Lastly, we diabatically set $\delta = 0$ and apply momentum kick $\exp[i(q_0 - q_{\min})x]$, giving the desired state $|q_0, -\rangle$.

Figures 5.5(a) and (b) show representative density distributions $n(x) = |\psi_{\uparrow}(x, t)|^2 + |\psi_{\downarrow}(x, t)|^2$ before and after a 16 ms time evolution with $\Omega_R = 2E_R$, both (a) with no interactions and (b) with interactions. In both cases, the pink shaded curve depicts the initial density distribution, while the final density distributions for initial quasimomenta of $q_0 = 1.2k_R$ and $2.0k_R$ are shown by the black and red curves respectively. In both cases the momentum exchange for backscattering is below k_c , however, as with the FGR results, this direct simulation shows that the initial state prepared with energy within the SOC energy gap experiences a negligible change in velocity, independent of the presence of interactions.

While the free particle group velocity is simply related to wave-vector by $v = \hbar k/m$, atoms evolving according to the SOC dispersions, as in Fig. 5.2, have group velocity given by the more complex relation

$$\frac{v_{\pm}}{v_R} = \frac{q}{k_R} \left\{ 1 \pm \left[\left(\frac{q}{k_R} \right)^2 + \left(\frac{\Omega_R}{4E_R} \right)^2 \right]^{-1/2} \right\}, \quad (5.15)$$

for atoms in state $|q, \pm\rangle$, expressed in units of the recoil velocity $v_R = \hbar k_R/m$.

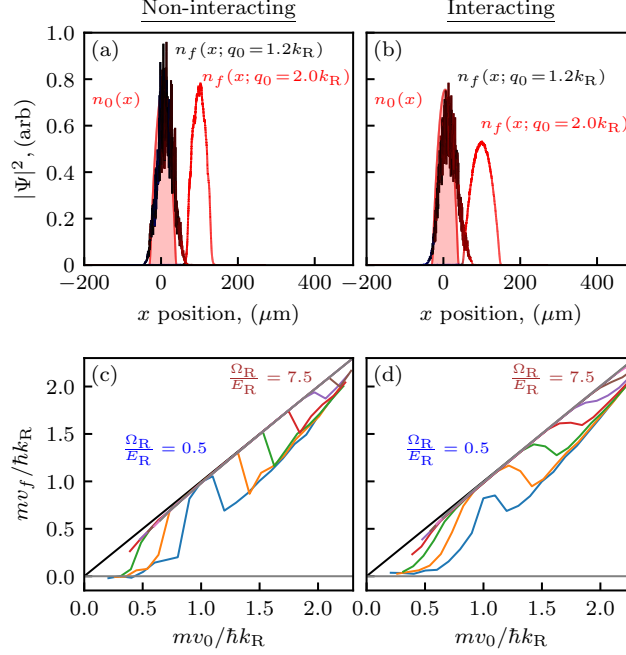


Figure 5.5: Motion in the presence of speckle and SOC. The left column was computed without interactions and the right column added interactions. (a) and (b) Density distributions colored by their magnetization according to the color bar in Fig. 5.1. The shaded curve depicts the initial density distribution, while the remaining red and black curves were computed for $q_0 = 2.0k_R$ (in the SOC gap) and $q_0 = 1.2k_R$ (below the SOC gap), respectively. (c) and (d) Ensemble averaged final group velocity plotted as a function of initial group velocity for coupling strengths from $0.5E_R$ to $7.5E_R$, spaced by $1.0E_R$. The results in (c) and (d) were averaged over 20 random speckle realizations.

Because we are interested in transport phenomena, it is this group velocity, not the quasimomentum, that is the quantity of primary interest.

Fig. 5.5(c) and Fig. 5.5(d) plot the final group velocity v_f as a function of initial group velocity v_0 after a 16 ms period of free evolution, both (c) with no interactions and (d) with interactions, and with Ω_R from $0.5E_R$ to $7.5E_R$. As compared to the simulations without SOC in Fig. 5.3(d), these curves show a near-complete suppression of relaxation for velocities near $v_0 \approx v_R$, in the SOC energy gap, and with an increasing window of suppression with increasing Ω_R .

Lastly, we see that interaction effects do play a role, leading to more rapid deceleration. The origin of this effect can be understood by comparing the red curves in Figs. 5.5(a) and 5.5(b): adding interactions leads to a mean-field driven expansion of the BEC, increasing the range of velocities present. As a result, when the SOC energy gap is small (small Ω_R), a significant fraction of the BEC's velocity distribution falls outside the SOC energy gap, thereby sampling points in the dispersion where first-order backscattering is allowed. At larger Ω_R , motion is near-ballistic near the center of the SOC gap, but the transition from ballistic to decelerated is smoothed as compared to the case with no interactions.

5.3 Conclusion

Our analytical and numerical studies of the transport of SOBECs in disorder potentials clearly show dramatically enhanced transport for initial states in the SOC energy gap. The enhanced transport described here results from the same physics

giving rise to a spin transistor in Ref. [97], which also relied on a combination of kinematic and matrix-element effects to yield non-reciprocal appearing transport behavior. In Sec. 6.1, we describe an explicit experimental proposal using laser speckle derived from 532 nm green laser and an off-the-shelf optical diffuser. In this proposal, SOC is generated from a pair of 790 nm laser beams intersecting at the atoms, and initial states would be prepared as described above. The protection from backscattering is independent of quantum statistics: non-interacting Fermions would experience a conductivity increased by the factor predicted by the FGR when the Fermi energy resides in the SOC gap. As with the interacting SOBEC we analyzed, we expect that Fermionic systems with moderate interactions would show gains in conductivity, however, the details of this latter case would necessitate future study.

Reference [98] showed that in lattices, the type of 1D SOC in Eq. (5.6) has the same dispersion as the edge modes of 2D Z_2 topological insulators [99]. Together with our finding, this indicates that 1D nanowires with SOC either of the Rashba [100] or linear-Dresselhaus [45] type should provide the same protection to backscattering from spin-independent disorder as would be observed at the edge of a topological insulator.

Chapter 6: The evolution of BECs in disordered potentials

In this chapter, we report the experimental study of the evolution of BECs in disordered potentials. In Sec. (6.1), we present the optical design diagrams of both the speckle beam and the Raman beams which are used to generate spin-orbit coupling as discussed in Sec. (5.2.3). And we discuss the reasons behind these designs. In Sec. (6.2), we show the experimental results of the evolution of BECs under the pulses of speckle potentials, both in the short term and in the long term. Based on our analytical study and numerical simulations, we show the results of characterizing the PSD of the speckle potentials by using the short-term speckle pulses data and measuring the average speckle potential by using the long-term speckle pulses data. In Sec. (6.3), we measure the deceleration of spinless BECs in the speckle potentials and compare them with our simulation results shown in Ch. (5).

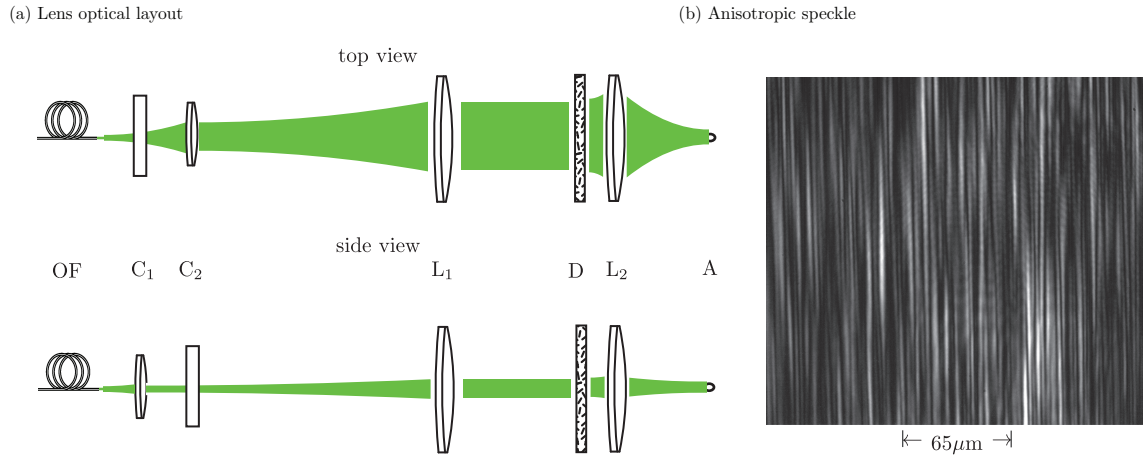


Figure 6.1: Optical design. (a). The design of optics viewed in two directions. OF denotes optical fiber. Lenses C_1 and C_2 are cylindrical lenses: C_1 focuses the beam in the vertical direction; and C_2 focuses the beam in the horizontal direction. L_1 is a spherical lens that collimates the beam. D is the optical diffuser that imprints random phase on the beam. L_2 is an aspherical lens that focuses the beam to the atoms labelled with A. (b) Experimental image of optical speckle with anisotropic correlation length.

6.1 Optical design

6.1.1 Speckle beam design

In practice, the speckle beam must satisfy two requirements. The first is anisotropic field-field correlation length: small along \mathbf{e}_x and large along \mathbf{e}_y and \mathbf{e}_z so that high-momentum scattering occurs predominantly along \mathbf{e}_x . The second is that the beam width along \mathbf{e}_x should uniformly illuminate the elongated atomic ensemble (with an expected diameter of about $50 \mu\text{m}$). To observe the effect of SOC-suppressed transport, the speckle potential must couple energy matched states across the SOC gap, shown by the dashed line in Fig. 5.1(c). This implies PSD of speckle potential along \mathbf{e}_x satisfies $k_c \gtrsim 4k_R$, informing the selection of beam-size and lenses. The requirement that the correlation length along \mathbf{e}_y be large implies that at the diffuser plate, the beam is much smaller along \mathbf{e}_y than along \mathbf{e}_x .

To satisfy these joint requirements, we created the speckle beam shown in Fig. 6.1(a), which begins with a 532nm laser beam emanating from an optical fiber. The beam out of an optical fiber travels through the cylindrical lens C_1 (focusing along \mathbf{e}_y) before encountering a cylindrical lens C_2 (focusing along \mathbf{e}_x) as shown in Fig. 6.1(a), given more rapid divergence along \mathbf{e}_x than \mathbf{e}_y . The beam is then collimated by L_1 , a $f = 250 \text{ mm}$ spherical lens, giving beam width of around 25 mm along \mathbf{e}_x and less than $500 \mu\text{m}$ along \mathbf{e}_y (on the same scale the diffuser plate's correlation length).

The beam then traverses the diffuser plate (Edmund Optics part number #47-

680, with divergence angle $\theta_d = 0.5^\circ$) and is focused by L_2 , a $f = 30$ mm lens. Figure 6.1(b) shows a test image of the speckle beam at the focal plane, its intensity correlation length is less than $0.5 \mu\text{m}$ along \mathbf{e}_x and about $10 \mu\text{m}$ along \mathbf{e}_y . The beam widths along both directions are about $250 \mu\text{m}$.

6.1.2 Raman beams design

We generate Raman coupling with lasers of wavelength $\lambda \approx 790$ nm. The k vector of the laser beams is

$$k_r = \frac{2\pi}{\lambda}. \quad (6.1)$$

When two Raman beams intersect at an angle θ_R as shown in Fig. (6.2), the two-photon recoil vector is defined as

$$k_R = k_r \sin \frac{\theta_R}{2}. \quad (6.2)$$

As shown in Fig. 5.1(c), the detuning between states $|q + k_R, \uparrow\rangle$ and $|q - k_R, \downarrow\rangle$ is

$$\Delta(q) = \frac{2\hbar^2 q k_R}{m} + \delta. \quad (6.3)$$

δ here is the detuning between two spin states and $\Delta(q)$ increases with k_R . As described in Sec. (5.2.3), one of the steps in the process we prepare the SOC quasi-momentum state $|q_0, -\rangle$ is adiabatic evolution. We achieve this by ramping up the Raman coupling strength from zero to Ω_R on a time scale slow compared to $\hbar/\Delta(q_0)$. In our experiments, we are limited by the lifetime of BECs, so we prefer to ramp up Raman coupling fast, but still slow compared to $\hbar/\Delta(q_0)$. For this reason, we want to make k_R as large as possible. In this design, it means a large enough intersection

angle of θ_R . On the other hand, we also want k_R to be small enough so that k_c/k_R is large enough and the speckle potentials can couple more energy matching states shown as the circles in Fig. (5.1). Here k_c is the cut off in the PSD of the speckle potentials. In our experiment, the two Raman beams and the speckle beam are focused on the atoms by the same lens L_1 . At the largest θ_R , $k_c/k_R \approx 3$.

For the above two reasons, it is a trade-off between small and large θ_R and we need to find a good spot by doing tests experimentally. So for the optical design, we need to be flexible in changing the angle. As shown in Fig. (6.2), we use a triangular prism to combine the two Raman beams and align them to be parallel. The triangular prism is put on a transnational stage which can move in the perpendicular direction of the two incident Raman beams. By moving the prism, the distance between the two Raman beams can be changed and the distance is mapped to the distance at the lens L_1 which determines the angle θ_R .

6.2 Evolution of spinless BEC under speckle pulsing

In Ch. (4), we derived a Gaussian beam model of the speckle beam and calculated the field-field correlation function, the PSD, and the intensity distribution. In the experiments, the engineered speckle beam is focused at the atoms and it is hard to directly measure the average intensity of the speckle beam at the atoms. Direct measurements of the PSD and k_c is even harder. In some experiments carried out previously that involved a speckle beam [72, 74], the researchers set up an identical beam at the test bench and measure the average intensity and the PSD of the test

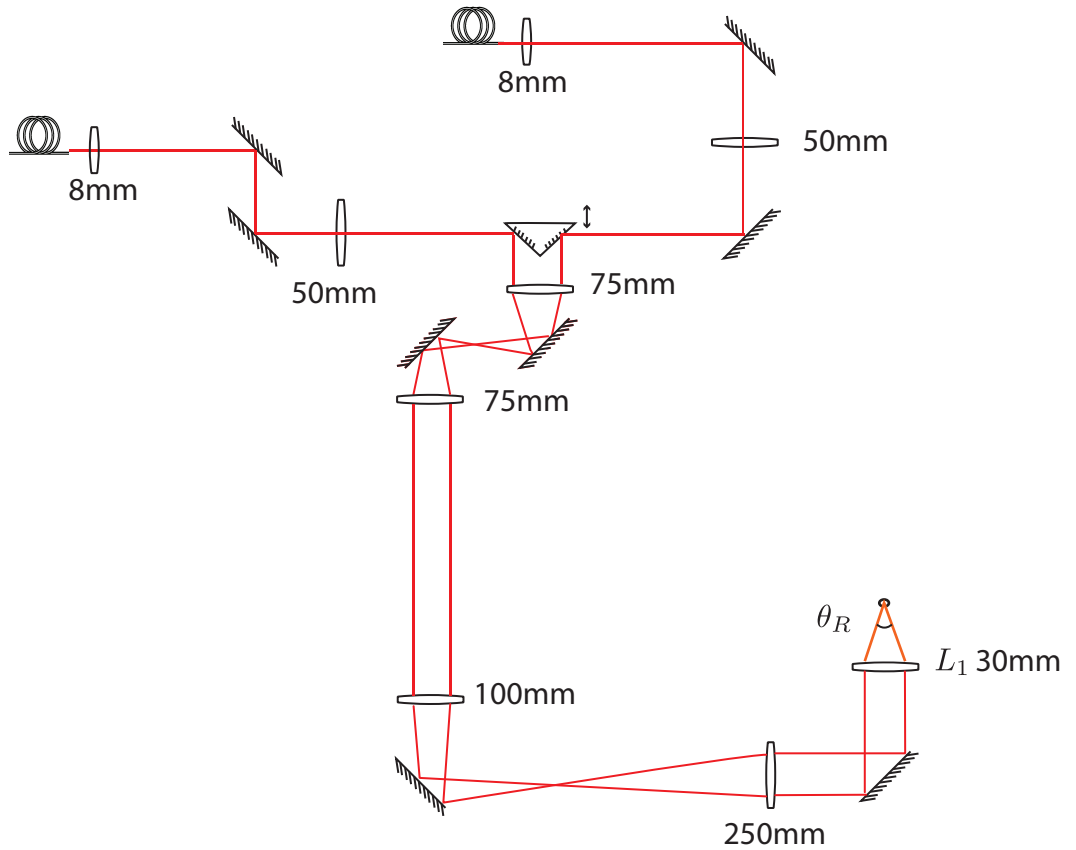


Figure 6.2: Raman beams design. The optical diagram of Raman beams. We use a triangular prism to align two Raman beams, the distance between two Raman beams at the prism is mapped to the distance at the lens L_1 by two relay imaging systems. The prism is put on a translational stage which can move in the perpendicular direction of the two incident Raman beams. By moving the prism, the distance between the two Raman beams can be changed which determines the angle θ_R .

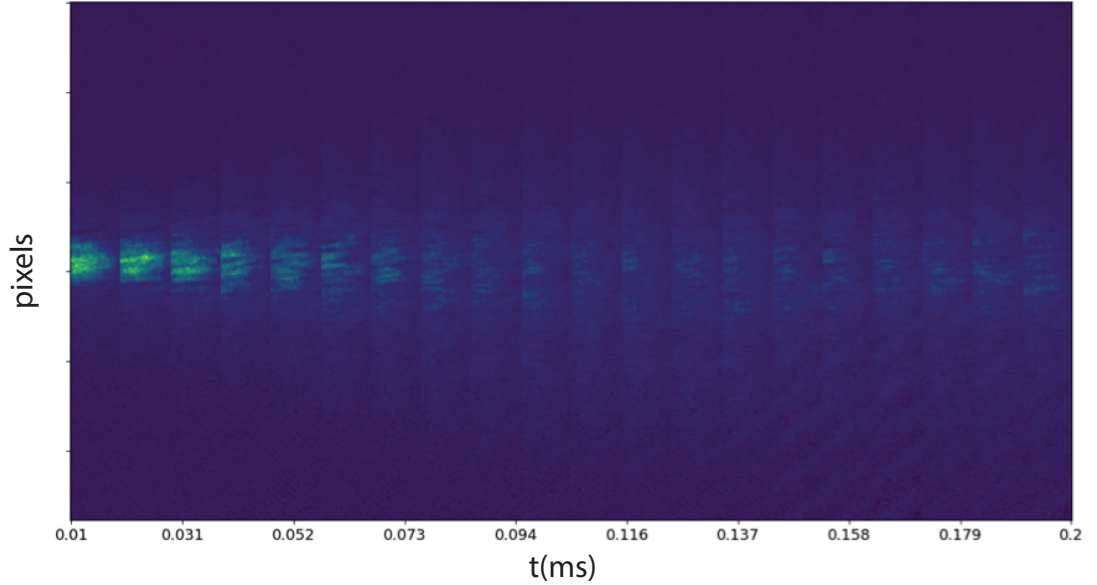


Figure 6.3: Absorption images of atoms after the evolution under speckle potentials and TOF. The BECs are released from the dipole trap, the pulses of the speckle potentials are turned on immediately for a various amount of time, followed by TOF. The absorption images are stacked up horizontally according to the speckle pulse duration.

speckle beam. The power and the PSD of the speckle beam in the experiments are assumed to be the same as those of the test beam, but no direct measurements were done to the best of our knowledge. Inspired by [101], we designed and carried out an experiment that allowed us to measure the average intensity and the PSD of the speckle beam by using the evolution of spinless BECs under the speckle potentials.

In [101], the diffraction of a Bose-Einstein condensate from a one-dimensional optical lattice is studied. In very short time,

$$T_{pulse} \ll t_{RN} = \frac{\hbar}{\sqrt{U_0 E_L}} = \frac{T_{ho}}{\pi}, \quad (6.4)$$

the atoms are mainly scattered to the $|\pm 2k_L\rangle$ momentum states. Since in the

Raman-Nath approximation, the atoms move by a very small distance, the kinetic energy term in the Hamiltonian is neglected. The atomic momentum changes from $|k = 0\rangle$ to $|\pm 2k_L\rangle$, which corresponds to the nonzero components in the PSD of the lattice potential. This inspires us to measure the PSD of the speckle potential and the cutoff k_c by using the short-term speckle beam pulses.

As the pulse duration increases beyond t_{RN} , the apparent edge of the momentum distribution is bounded by a maximum momentum k_{max} . The observed value of k_{max} can be used to determine the lattice depth U_0 ,

$$U_0 = \frac{\hbar^2 k_{max}^2}{2M} \quad (6.5)$$

Once the edge of the distribution reaches k_{max} , the distribution partially collapses to $|k = 0\rangle$ at $T_{ho}/2$. The process approximately repeats itself every $T_{ho}/2$. The collapse and revival phenomena can be qualitatively explained in a classical picture. The atoms released from different positions in a harmonic trap become stationary every half of the period. The collapse and revival are not complete in [101], at $T_{ho}/2$ there are always some higher momentum orders remain. The reason is that the lattice potential is not perfectly harmonic.

In contrast to the lattice pulsing, in the speckle beam pulsing, the speckle potential contains a continuous spectrum of spatial frequency. It is completely anharmonic and no collapse and revival should be expected. For long speckle pulsing time, the momentum states should reach a stationary distribution. In analogy to the law of equipartition, the kinetic energy of the atoms under this stationary distribution should be half of the average speckle potential. This inspired us to measure

the average speckle potential by using the width of the momentum distribution for a long speckle pulsing time.

6.2.1 Short term speckle pulsing

To measure the PSD and the cutoff k_c of the speckle potentials with short term speckle pulsing, we derive the evolution of the momentum states under two approximations. The first is the Raman-Nath approximation, atoms do not move far during the pulse. The second is that the evolution time is short compared to $\hbar/V(x)$, so atoms do not acquire a phase comparable to 2π . Consider Hamiltonian

$$\hat{H} = \frac{\hbar^2 k^2}{2m} + V(x). \quad (6.6)$$

The time evolution operator is

$$\hat{U}(t) = \exp\left\{-i\frac{\Delta t}{\hbar} \left[\frac{\hbar^2 k^2}{2m} + V(x)\right]\right\}, \quad (6.7)$$

Define E_c as the energy associated with k_c , $\tau = \frac{\Delta t}{\hbar} E_c$, $\hat{k} = \frac{k}{k_c}$ and $S(x) = \frac{V(x)}{E_c}$

$$\hat{U}(t) = \exp\left\{-i\tau \left[\hat{k}^2 + S(x)\right]\right\}. \quad (6.8)$$

Expand the operator to second order,

$$\hat{U}(t) = \exp\left\{-i\tau\hat{k}^2/2\right\} \exp\{-i\tau S(x)\} \exp\left\{-i\tau\hat{k}^2/2\right\}. \quad (6.9)$$

We assume the initial state is $|k=0\rangle$, so the third term does not contribute. And we measure the distribution in k space, so we can ignore the first term. The second term governs the short time evolution. To the lowest order,

$$\hat{U}(t) |k=0\rangle = |k=0\rangle - i\tau S(x) |k=0\rangle \quad (6.10)$$

Expand $S(x)$ in k space,

$$S(x) = \sum_{k,k'} \tilde{S}(k - k') |k\rangle\langle k'| \quad (6.11)$$

So

$$\hat{U}(t) |k = 0\rangle = |k = 0\rangle - i\tau \sum_{\delta k} \tilde{S}(\delta k) |\delta k\rangle \quad (6.12)$$

The probability distribution of momentum states at time τ is

$$P(k, \tau) = \tau^2 |\tilde{S}(k)|^2 + \delta_{k,0}. \quad (6.13)$$

It is proportional to the PSD of the speckle potential $|\tilde{S}(k)|^2$ ignoring the central peak at $k = 0$.

In the experiments, we put an iris right before the diffuser D in 6.1. By opening and closing the iris, we can control the size of the beam which determines k_c of the speckle potential PSD in the focal plane. As the model we derived in Ch. (4) shows, the speckle beam size at the focal plane does not change with the beam size at the diffuser. The beam size at the focal plane is determined by the field-field correlation length at the diffuser. So the average speckle potential depth is proportional to the power of the beam which we can control when we change the size of the iris.

We did the experiments for two iris sizes, 6.5 mm and 15 mm, which correspond to $k_c = 0.65k_r$ and $k_c = 1.30k_r$, respectively. Here k_r is defined with the largest recoil k vector of atoms scattered by a 532 nm light beam focused by a one inch $f = 30$ mm lens.

$$k_r = \frac{2\pi}{532\text{nm}} \sin \frac{\theta_R}{2} \quad (6.14)$$

$\theta_R \approx 45^\circ$ is shown in Fig. (6.2). The average speckle potentials are made equal in both cases by controlling the power of the beam after the iris.

We prepare BECs in a cross dipole trap, at $t = 0$, we turn off the dipole trap and release the atoms for time-of-flight (TOF). Immediately after the dipole trap is turned off, we turn on the speckle beam and pulse for a short period of time, ranging from 20 μs to 250 μs . After 18 ms TOF, we take absorption images of the atoms.

To compare with the experimental data, we simulate the process numerically. In the numerical simulation, we prepare the ground state of BECs in a dipole trap. At $t = 0$, turn off the dipole trap and release the atoms. Immediately after, the speckle potential is turned on for a duration of 50 μs or 100 μs , followed by free evolution for up to 20 ms. We keep track of the momentum distribution of the atoms during the evolution.

As Fig. (6.4) shows, the simulation is done under two kinds of speckle potentials with different k_c to compare with the experimental data. The left panel of Fig. (6.4) is for the speckle potential with $k_c = 1.48k_r$ and the right panel for the speckle potential with $k_c = 0.80k_r$. Fig. 6.4(c) and Fig. 6.4(d) show the momentum distribution of atoms immediately after a 50 μs speckle pulsing, the results are averaged over 20 speckle realizations. The red curves are proportional to the PSD of the two kinds of speckle potentials, respectively. From Fig. 6.4(c) and Fig. 6.4(d) we can see the tail of the momentum distribution of atoms after short-term speckle pulsing matches with the PSD of the speckle potentials. The results agree with the analytical calculation of the momentum distribution in Eq. (6.13), which predicts the momentum distribution to be a central δ function plus a tail that is proportional to the PSD of the speckle potentials.

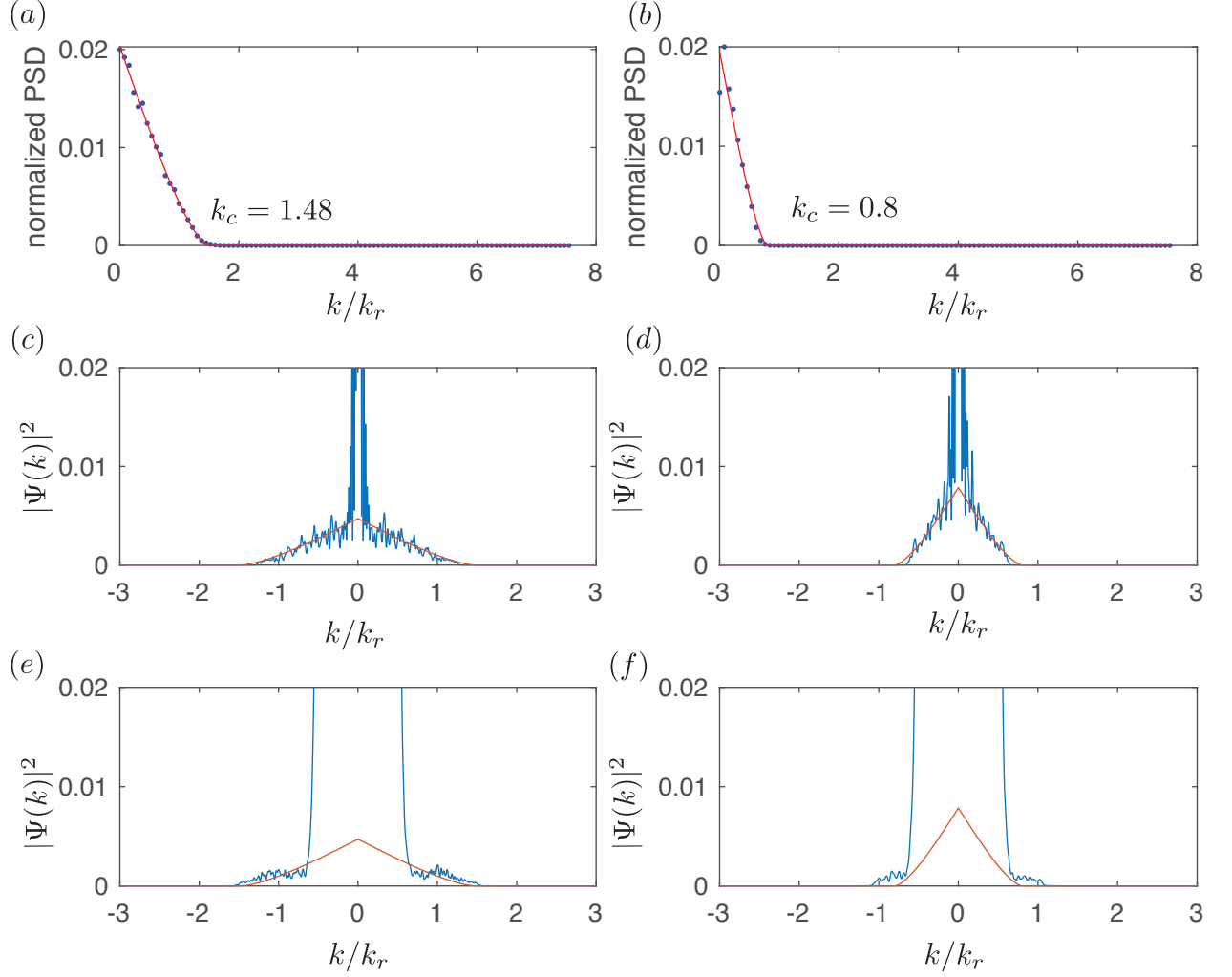


Figure 6.4: Simulation of short-term speckle pulsing. The left panel is for speckle potential with $k_c = 1.48k_r$, and the right panel for $k_c = 0.8k_r$. (a) and (b) verify the k_c of both speckle potentials by plotting their PSD. (c) and (d) are the momentum distribution of atoms after released from the dipole trap and evolve under speckle pulses for $50 \mu s$. The red curves are proportional to the corresponding PSD of the speckle potential. The momentum distribution is an average of 20 speckle realizations. (e) and (f) are the momentum distribution of atoms after released from the dipole trap and evolve under speckle pulses for $50 \mu s$ followed by a 20 ms free expansion. The results are averaged over 20 speckle realizations.

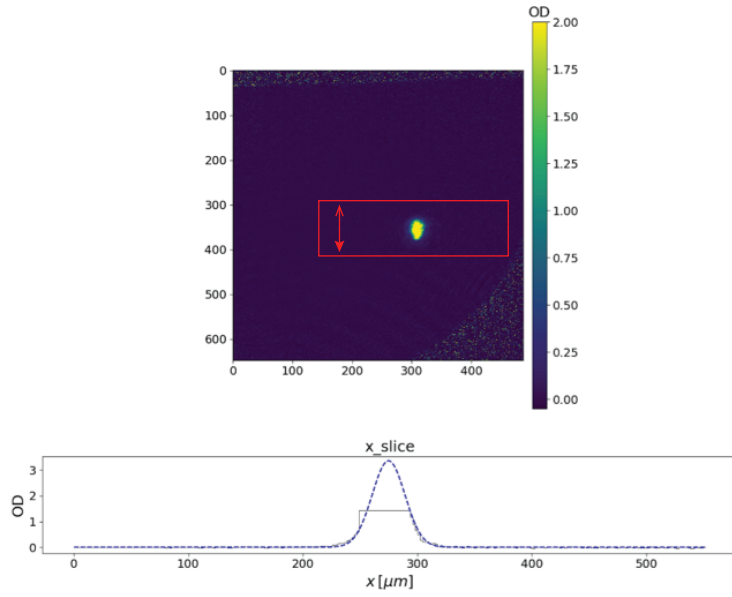


Figure 6.5: A sample of absorption images of atoms and analysis. The red square is a selected region of interest and the red arrow indicates the direction we take average. The masked and averaged spatial distribution of atoms (black curve) and a fitted Gaussian curve (blue dashed) are plotted below.

Fig. 6.4(e) and Fig. 6.4(f) show the momentum distribution of atoms after a $50 \mu\text{s}$ speckle pulse and a 20 ms time-of-flight (TOF). During the TOF, the mean-field expansion of the atoms broadens the momentum distribution. Both the central peak and the tail of the momentum distribution become broader after the TOF. In Fig. 6.4(f), for the speckle potential of smaller k_c , the tail of the momentum distribution is broadened more significantly. The broadened momentum distribution after TOF makes it harder to distinguish the speckle potentials with the tail of the momentum distribution.

Fig. 6.5 and Fig. 6.6 show the analysis results of the absorption images after

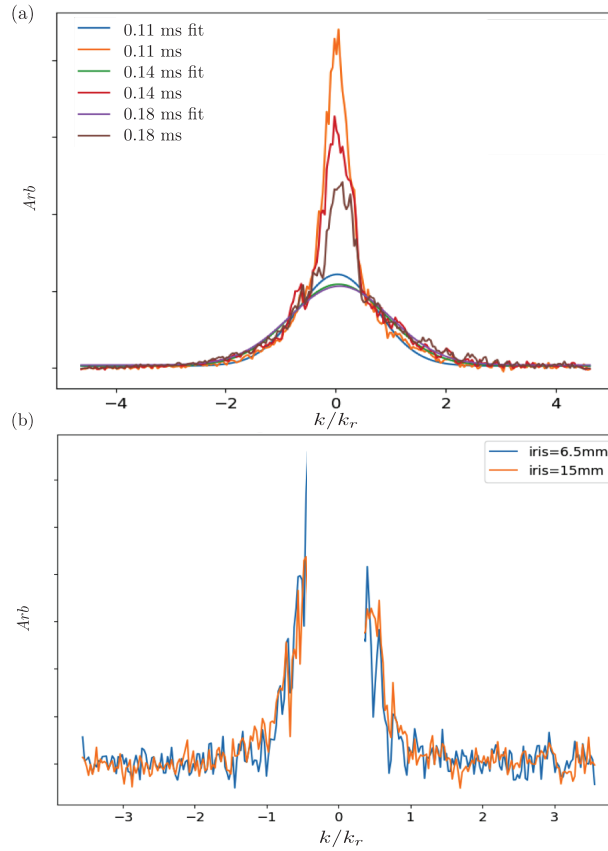


Figure 6.6: Momentum distribution after short-term speckle pulses and 18 mm TOF.

(a). A few samples of momentum distribution of atoms without mask, along with fitted Gaussian curves to the masked momentum distribution. (b). The tails of the momentum distribution after short-term pulses of speckle potential with different PSD. The PSD of the speckle potentials are controlled by the iris sizes and the results are averaged for speckle pulsing time ranging from $80 \mu\text{s}$ to $150 \mu\text{s}$.

TOF for two kinds of speckle potentials generated with different iris sizes. During TOF, the momentum distribution of atoms is mapped to their spatial distribution. From the absorption images, we can compute the momentum distribution from the spatial profile of the atoms. In the analysis, from the absorption images of atoms after TOF shown in Fig. 6.5, we select a region of interest around the center of the atoms indicated by the red square. And compute the average spatial distribution of atoms along the horizontal direction (red arrow). The central peak of this average spatial distribution is masked to show the detail of the tails. Fig. 6.5 shows an example of the masked averaged spatial distribution along x direction (black curve) and a Gaussian fit (blue dashed curve). The resultant tails of the spatial distribution are averaged over short-term speckle pulsing duration ranging from $80 \mu\text{s}$ to $150 \mu\text{s}$. The tails of the spatial distribution are then converted to that of the momentum distribution in a unit of k_r .

Fig. 6.6(a) shows a few samples of the averaged momentum distribution along x direction without a mask for short-term speckle pulsing, along with fitted Gaussian curves to the masked momentum distribution. From Fig. 6.6(a) we can see it is necessary to mask the central peak of the momentum distribution in order to analyze the width of the tails. Fig. 6.6(b) is the momentum distribution of atoms after short-term pulses of speckle potentials with different PSD, averaged over pulsing duration ranging from $80 \mu\text{s}$ to $150 \mu\text{s}$. From Fig. 6.6(b), it is hard to tell the difference between the two curves for two reasons. First, in the absorption images, the signal-noise-ratio at the tails of the density profile is low. Just by taking the average, it is hard to reduce the noise and see the clear tails as in the numerical simulation

in Fig. 6.4. Second, as the simulation results show in Fig. 6.4(e) and Fig. 6.4(f), during TOF, the mean-field expansion broadens the momentum distribution more significantly for speckle pulsing with smaller k_c . So the width of the tails of the momentum distribution for the pulsing of two kinds of speckle potentials is closer to each other after TOF than before. For the two reasons, we conclude we can not quantitatively measure the k_c of the speckle potential by using the absorption images after short-term speckle pulsing and TOF.

6.2.2 Long term speckle pulsing

In the experiments, it is important to know the average speckle potential at the atoms. But unfortunately, it is hard to measure the power of the speckle beam directly at the atoms and infer the average speckle potential. Because in the experiments, we can not put a power meter anywhere we want to measure the power of the beam. And besides, it is the intensity that matters, and we don't have perfect knowledge of the beam size at the atoms. After the closest point to the vacuum glass cell where we can use a power meter to measure the power, the beam goes through lenses, reflected by mirrors, glass cell, or even dichroic mirrors. The power of the beam decreases at each of the optical elements. To the best of our knowledge, for the previous experiments using speckle beams, the average speckle potential was not measured directly. It could be inferred by calculating the power given the power loss at each optical element. Or the power could be measured for an identical speckle beam set up on the test bench and it is assumed the power at

the atoms is the same as the power of the test speckle beam in the focal plane.

Inspired by [101], we obtained the mean potential depth by making the atoms evolve under the speckle beam pulses. Compared with [101], for $t \gg t_{RN}$, we do not expect to see the collapse and revive phenomenon due to the anharmonicity of the speckle potential. Instead, at long speckle pulsing time, the momentum distribution should reach equilibrium and in analogy to the law of equipartition, the average stationary kinetic energy is half of the average total energy which is the initial average speckle potential.

To confirm our understanding, we did numerical simulations of the long-term speckle pulsing. Fig. 6.7 shows the simulation and experimental results of the speckle pulsing for the pulsing duration up to 2 ms. In the simulation, we release the BECs from the dipole trap and immediately turn on the speckle potential. The atoms evolve under the speckle potential and we keep track of the width of the momentum distribution. We did the simulation for different average speckle potential depth ranging from 0 Hz to 1600 Hz, with a 200 Hz spacing. The results are shown as the nine curves, each one is averaged over 20 speckle realizations. When the average speckle potential is zero, the width of the momentum distribution increases driven by the mean-field expansion. From the simulation results shown in Fig. 6.7(a), the width of the momentum distribution increases rapidly after the speckle potential is turned on and becomes stationary after around $0.25 \mu s$. The stationary width increases with the average speckle potential depth.

Fig. 6.7(b) shows the experimental results. In the experiment, we release the atoms from the dipole trap, pulse the speckle potential for up to 2 mm followed

by TOF. The total time for the speckle pulsing and the TOF is 18 ms, a constant for different pulsing duration. We take the absorption images after TOF and fit a Gaussian function to the density profile of the atoms. Fig. 6.7(b) shows the width of the fitted Gaussian function vs the duration of the speckle pulses. The Gaussian width increases with the pulsing duration in short term and becomes stationary after around 0.25 ms, which is consistent with the simulation results.

To infer the average speckle potential from the width of the momentum distribution after long-term speckle pulsing, we compute the average kinetic energy using the fitted Gaussian width of the density profile of atoms after TOF.

$$\langle \hat{K} \rangle = \frac{1}{2} m \left(\frac{\sigma}{\tau} \right)^2 \quad (6.15)$$

Here τ is the time for TOF. The average speckle potential is equal to the average total energy, which is twice the average kinetic energy. In Fig. 6.8(b), the computed total energy is plotted against a photodiode (PD) reading. In our experiments, we use a pick-off mirror to reflect a fixed percentage of the power of the speckle beam to a PD and the reading of the PD in Volt is proportional to the power of the beam at the atoms. We fit a line crossing the origin to the data, by reading the PD we have an estimate of the average speckle potential at the atoms.

To compare with the experimental results, we also did numerical simulations. In the simulations, we release the atoms from the dipole trap at $t = 0$ and pulse the speckle potential for 1 ms followed by a 20 ms free evolution. The simulations are done with two kinds of speckle potentials, $k_c = 0.80k_r$ and $k_c = 1.48k_r$, respectively. For each kind of the speckle potential, the average potential depth ranges from 0 Hz

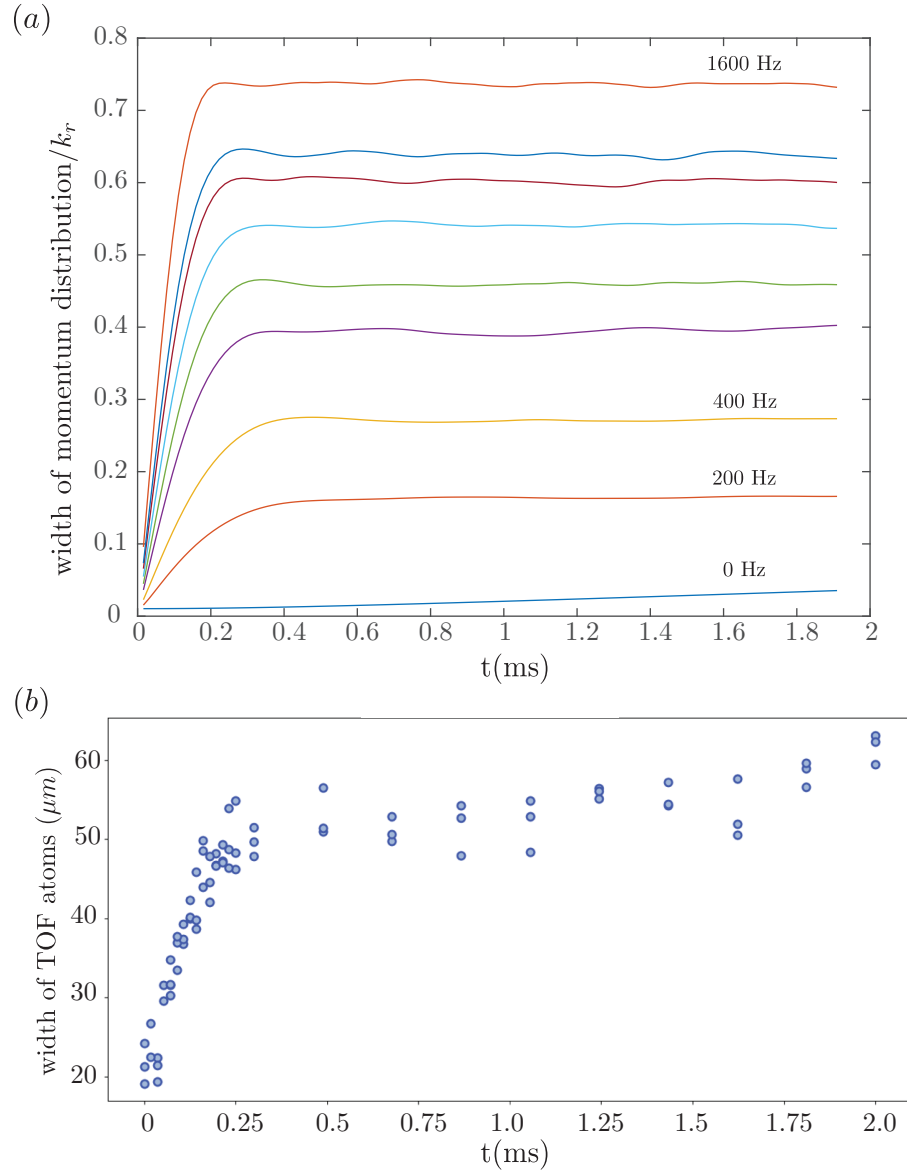


Figure 6.7: The simulation and the experiments of the speckle beam pulsing. (a). The width of the momentum distribution of atoms evolving under the speckle potentials of different potential depth ranging from 0 to 1600 Hz. (b). The Gaussian width of atoms in the absorption images after TOF for different speckle pulsing duration.

to 1600 Hz with a 200 Hz spacing. We compute the momentum distribution and the average kinetic energy at the end of the free evolution. The average total energy is twice the average kinetic energy deducted by the mean-field energy computed from the average kinetic energy in the no-pulsing case. And the resultant average total energy is plotted against the known average potential depth. In agreement with our prediction, the curves are close to the diagonal line (dashed) for both kinds of speckle potentials.

6.3 Transport of spinless BECs in speckle potentials

In Ch. (5), we study the transport of spinless BECs under speckle potentials. As Fig. (5.3) shows, a BEC with a chemical potential ~ 300 Hz travels through speckle potentials with average potential depth ~ 200 Hz, could be scattered by the speckle potential and decelerate. The deceleration of a BEC depends on its initial velocity, the speckle potential depth, and the cutoff k_c in the speckle potential PSD. As Fig. 5.3(d) shows, after evolving under the speckle potentials for 16 mm, the BECs with small initial velocity has more significant deceleration. For BECs with large initial velocity, $k_0 > k_c/2$, the deceleration is minimal during the 16 mm.

In the experiments, we study how BECs with different velocities decelerate. As discussed in Ch. (4), we can make speckle potentials that have the same PSD as the ones we use in our numerical simulations. And as discussed in Sec. (6.2), the average speckle potential depth can be inferred from a PD reading. So an ideal experimental sequence is to have the BEC travel with constant velocity under

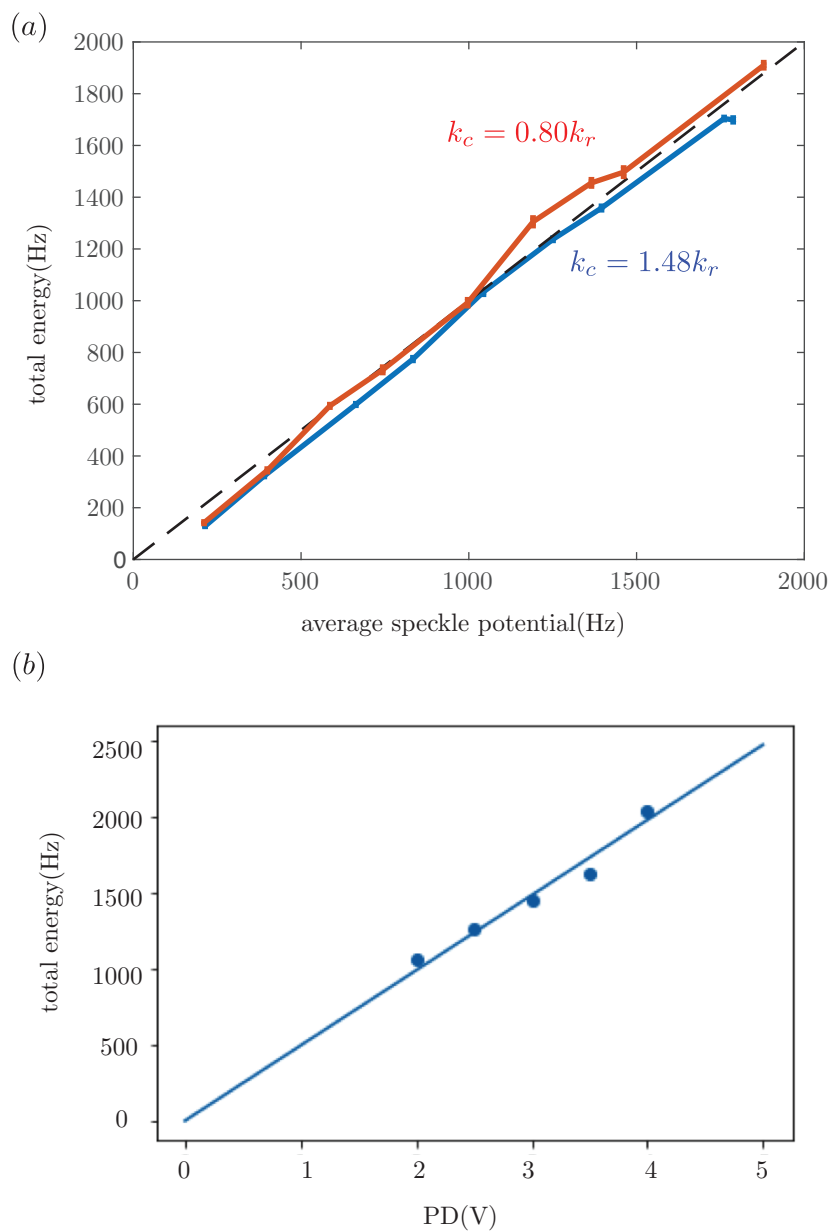


Figure 6.8: Calibration of the average speckle potential depth. (a). In the numerical simulation, the average total energy inferred from the momentum distribution after 20 ms free evolution is plotted against the known average speckle potential depth. The red curve and the blue curve are for the speckle potentials with $k_c = 0.80k_r$ and $k_c = 1.48k_r$, respectively. The dashed line is diagonal. (b). In the experiment, the average total energy computed from long-term speckle pulsing data is plotted against the PD reading.

well-calibrated speckle potential, and the final velocity would be measured by using *insitu* or TOF absorption images. To that end, the first challenge we are faced with is that how to make a BEC travel with a constant velocity for an extensive amount of time (16 mm in the simulation). We make BECs by doing evaporative cooling in a cross dipole trap as discussed in Sec. (2.2.7), so our first choice is to make BECs travel in the cross dipole trap. As Eq. (2.85) suggests, dipole potential is proportional to the intensity of the dipole beam.

In our case, as discussed in 6.1.1, we image atoms in z direction and measure the motion of atoms in x direction. The dipole potential in x direction is a combination of the dipole potential from z dipole beam and x dipole beam. The width of the dipole potential from x dipole beam is the Rayleigh range, which in our case is ~ 1.3 mm. Based on our design, the velocity of atoms corresponds to the recoil k vector k_r is $3.3 \mu\text{m}/\text{ms}$. We expect the atoms to move less than $50 \mu\text{m}$ during the experiment, so the dipole potential from x dipole beam can be ignored.

In x direction, the dipole potential from the z dipole beam is

$$V_{dip}(x) = -V_0 \exp\left\{-\frac{2x^2}{w^2}\right\}. \quad (6.16)$$

where w is the width of the beam at the atoms. Expand the potential at $x = 0$ to second order,

$$V_{dip}(x) \approx -V_0 + \frac{2V_0}{w^2}x^2, \quad (6.17)$$

has a quadratic form. Around the center of the trap, the dipole potential can be approximated by a harmonic potential with frequency $\sqrt{\frac{4V_0}{w^2}}$.

In the ideal case, the atoms would move at a constant velocity in the dipole

trap, meaning the frequency $\sqrt{\frac{4V_0}{w^2}}$ is zero and the z dipole beam is completely turned off. More realistically, if the velocity of the atoms change by less than 5% at the center of the trap in 15 ms, the period of the harmonic oscillation needs to be more than 300 ms. So the trapping frequency is around 3 Hz.

The x dipole beam and the z dipole beam in our experiments are the first order and zeroth-order beams from an AOM, the total power of the two beams are conserved. We optimized the ratio of the power of the two beams to maximize the phase space density of the BECs after the dipole evaporation stage. In the optimized case, the measured trapping frequency in x direction is 21 Hz. In order to decrease the x trapping frequency, we need to allocate more power in the x dipole beam and less in the z dipole beam. But in the process of decreasing the x trapping frequency, a few problems occurred.

Fig. 6.9 shows the BEC with x trapping frequency of 21 Hz compared with the BEC with x trapping frequency of 5.8 Hz. Compared with the BEC in Fig. 6.9(a), the BEC in Fig. 6.9(b) is stretched in the x direction due to small trapping frequency. The signal is much weaker and the large length in x direction makes it hard to accurately detect the center of the atoms and the center-of-mass motion.

Alternatively, we can keep the current dipole trap configuration and decrease the time that BECs travel under speckle potentials. We hope to find the duration of the speckle potential pulses that is as short as possible, but its deceleration effect on the BECs is still significant for speckle potential weak enough not to cause trapping effect.

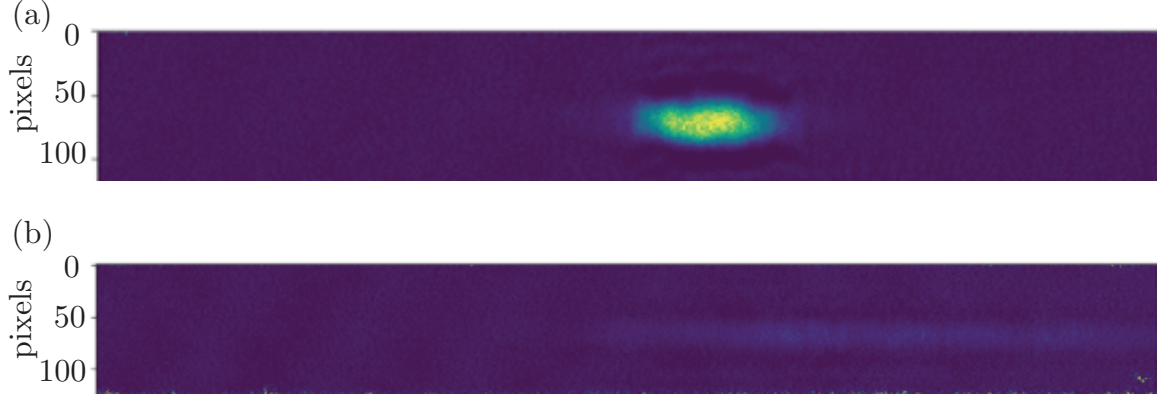


Figure 6.9: *insitu* absorption images of BECs with different dipole parameters. (a) A BEC with x trapping frequency of 21 Hz. (b) A BEC with x trapping frequency of 5.8 Hz

In Fig. 6.10, the blue dots show the oscillation of a BEC in x direction in a dipole trap with x trapping frequency 21 Hz. The center of the atoms is measured from *insitu* images of atoms. At the center of the dipole trap, the atoms are at the maximum velocity v_0 , $mv_0/\hbar = 1.8k_r$. The first time the atoms reach maximum velocity is at 21 ms. We make the atoms do the same dipole oscillation as the blue dots show, at 21 ms, we turn on the speckle potential and hold for 1 ms. After 1 ms, the speckle potential is turned off and we track the center-of-mass motion of the atoms in x direction in the dipole trap. The center-of-mass motion of atoms after the speckle pulse is shown as the orange dots in Fig. 6.10.

The amplitude of the oscillation shown by the orange dots is smaller than the amplitude shown by the blue dots. We fit a sinusoidal function to both and infer the velocities of the atoms at $t = 21$ ms. Without the pulse of speckle potential at $t = 21$ ms, the velocity of the atoms is v_0 , $mv_0/\hbar = 1.8k_r$. With the pulse, the

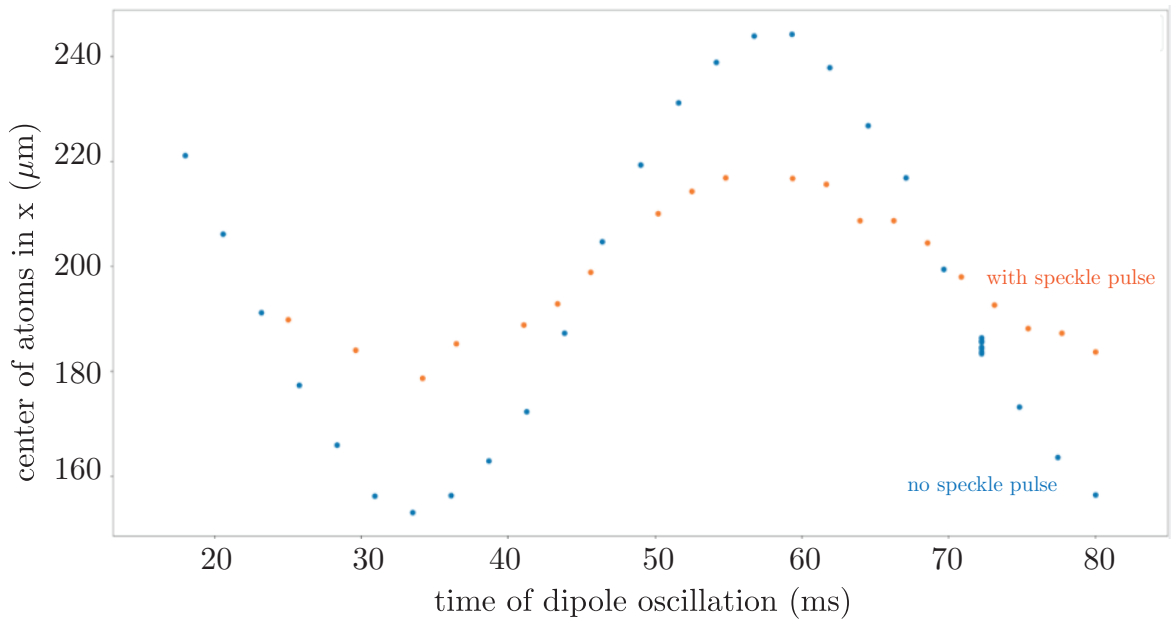


Figure 6.10: Center-of-mass motion in x direction of atoms during dipole oscillation. The blue dots show a full cycle of dipole oscillation without pulses of the speckle potentials. The orange dots show the dipole oscillation of atoms with the same initial velocity as the blue dots show, but with a 1 ms speckle pulse at 21 ms. The average speckle potential depth is ≈ 640 Hz.

velocity of the atoms is v_f , $mv_f/\hbar = 0.7k_r$. This measurement demonstrated that a speckle potential pulse with an average potential depth of ≈ 640 Hz, can have a significant deceleration effect on atoms within 1 ms. This allows us to measure the deceleration of atoms evolving in speckle potentials in our optimized dipole trap, without having to reduce the x trapping frequency.

Using this method, we measured the deceleration of atoms at different velocities v_0 after pulses of speckle potential for 1 ms with an average potential depth of ≈ 500 Hz. Fig. 6.11 shows the experimental measurements compared with the numerical simulation results. The red circles in Fig. 6.11 show the experimental results. In the numerical simulations, we make atoms with different initial velocities evolve under speckle potentials with different potential depth for 1 ms and measure the final velocities. The initial velocities range from $0.2\frac{\hbar k_r}{m}$ to $2.2\frac{\hbar k_r}{m}$. The blue curve and the yellow curve in Fig. 6.11 correspond to speckle potential depth of 500 Hz and 800 Hz, respectively. In the experiments, the average speckle potential depth is inferred from Fig. 6.8. As discussed in Sec. 6.2.2, we use the stationary width of the momentum distribution after long-term speckle pulses to measure the average speckle potential. Here the deceleration measurement is done with a PD reading of 1.0 V, which corresponds to an average speckle potential of ≈ 500 Hz. For initial velocities v_0 , the measured final velocities $v_f = \frac{\hbar k_r}{m}$ are lower than the final velocities in the simulation with average speckle potential of 500 Hz, and are close to those in the simulation with average speckle potential of 800 Hz. There are a few potential causes that can lead to the gap. First, in the measurements of the stationary width of momentum distribution after long-term pulses of speckle potential

shown in Fig. 6.8, the stationary width is noisy which leads to uncertainty in the calculation of average speckle potential depth. Second, as discussed in Sec. 6.2.1, it is hard to measure the k_c of the optical speckle potentials used in the experiments accurately. The difference in k_c of speckle potentials used in the simulations and the experiments can also lead to this gap.

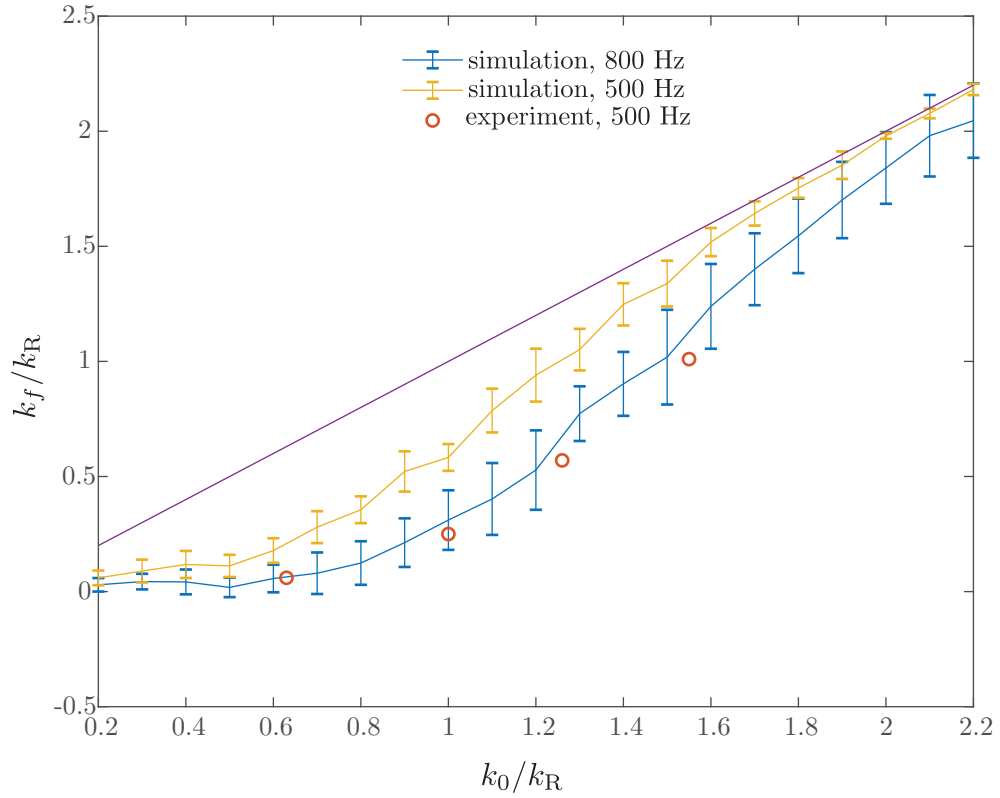


Figure 6.11: Deceleration of atoms after a 1 ms pulse of the speckle potentials. The red circles are the results of measurements in the experiments. The average speckle potential depth inferred from the photo diode reading is ≈ 500 Hz. The blue curve and the yellow curve are the results of numerical simulations. The blue curve is the final velocities vs the initial velocities after evolving under speckle potentials with average potential depth of 800 Hz, and the yellow curve is for speckle potential with average potential depth of 500 Hz. Both the blue curve and the yellow curve are averaged over 20 speckle realizations and the error bars show the standard deviations. The purple line is diagonal.

Appendix A: Calculation results of field-field correlation function

For field-field correlation function, in the free propagation case, the original calculation results are:

$$\begin{aligned} \frac{C_E(\mathbf{r}_1, \mathbf{r}_2; z)}{E_0^2} &= \left[\frac{w}{w(z)} \right]^2 \exp\left(-ik_0 \frac{\mathbf{r}_1^2 - \mathbf{r}_2^2}{2R(z)}\right) \\ &\times \exp\left(-\frac{\mathbf{r}_1^2 + \mathbf{r}_2^2}{w(z)^2}\right) \exp\left(-\frac{|\mathbf{r}_1 - \mathbf{r}_2|^2}{\sigma(z)^2}\right) \end{aligned} \quad (\text{A.1})$$

$$\left\{ \begin{aligned} 1/R(z) &= 1/z - k_0^2 w^2 / 8Az^3 \\ 1/\sigma^2(z) &= k_0^2 w^2 / 8z^2 - k_0^4 w^4 / 64Az^4 - k_0^2 / 16Az^2 \\ 1/w^2(z) &= k_0^2 / 8Az^2 \\ A &= 1/2w^2 + 1/\sigma^2 + k_0^2 w^2 / 8z^2 \end{aligned} \right. \quad (\text{A.2})$$

With a lens,

$$\begin{aligned} \frac{C_E(\mathbf{r}_1, \mathbf{r}_2; z)}{E_0^2} &= \frac{k_0^2 w^2}{4z^2 D} \exp\left[-i \left(\frac{k_0}{2z} + \frac{z_L^2 AB}{2Dz^2} \right) (\mathbf{r}_1^2 - \mathbf{r}_2^2)\right] \\ &\times \exp\left[-\frac{k_0^2 (\mathbf{r}_1^2 + \mathbf{r}_2^2)}{4z^2 D}\right] \exp\left[-\left(\frac{z_L^2 A}{2z^2} - \frac{z_L^4 A^2 B^2}{2k_0^2 z^2 D} - \frac{k_0^2}{8z^2 D} \right) |\mathbf{r}_1 - \mathbf{r}_2|^2\right] \end{aligned} \quad (\text{A.3})$$

where,

$$\left\{ \begin{array}{l} A = 1/2w^2 + 1/\sigma^2 + k_0^2w^2/8z_L^2 \\ B = \frac{k_0^3w^2}{8z_L^3A} - k_0(1/z + 1/z_L - 1/f) \\ C = \frac{k_0^2w^2}{8z_L^2} - \frac{k_0^4w^4}{64z_L^4A} \\ D = \frac{z_L^2AB^2}{k_0^2} + C \end{array} \right. \quad (\text{A.4})$$

Appendix B: Derivation of the moments of random phase factors

In Sec. 4.4, we derive the joint probability density of random electric fields and the probability density of the intensity 4.22 by calculating the moments of the random electric fields. One way to derive the probability density is to separate the phase factor of the electric fields $\exp\{i\phi(\mathbf{r})\}$ into real and imaginary parts $\cos\phi(\mathbf{r})$, $\sin\phi(\mathbf{r})$ and calculate their joint probability density. Here we derive the variance and covariance of $\cos\phi(\mathbf{r})$ and $\sin\phi(\mathbf{r})$ that are used to derive their joint probability density.

Under assumptions:

$$\langle \exp\{-i[\phi(\mathbf{r}_1) - \phi(\mathbf{r}_2)]\} \rangle = \exp\left(-\frac{|\mathbf{r}_1 - \mathbf{r}_2|^2}{\sigma^2}\right), \quad (\text{B.1})$$

and

$$\phi(\mathbf{r}) \sim \text{Uniform}(0, 2\pi). \quad (\text{B.2})$$

$$\begin{aligned}
\langle \exp \{-i [\phi(\mathbf{r}_1) - \phi(\mathbf{r}_2)]\} \rangle &= \langle \cos [\phi(\mathbf{r}_1) - \phi(\mathbf{r}_2)] - i \sin [\phi(\mathbf{r}_1) - \phi(\mathbf{r}_2)] \rangle \quad (\text{B.3}) \\
&= \langle \cos [\phi(\mathbf{r}_1) - \phi(\mathbf{r}_2)] \rangle - i \langle \sin [\phi(\mathbf{r}_1) - \phi(\mathbf{r}_2)] \rangle
\end{aligned}$$

By symmetry,

$$\langle \sin [\phi(\mathbf{r}_1) - \phi(\mathbf{r}_2)] \rangle = \langle \sin [\phi(\mathbf{r}_2) - \phi(\mathbf{r}_1)] \rangle = 0, \quad (\text{B.4})$$

therefore,

$$\langle \cos [\phi(\mathbf{r}_1) - \phi(\mathbf{r}_2)] \rangle = \exp\left(-\frac{|\mathbf{r}_1 - \mathbf{r}_2|^2}{\sigma^2}\right). \quad (\text{B.5})$$

$$\begin{aligned}
\langle \cos [\phi(\mathbf{r}_1) + \phi(\mathbf{r}_2)] \rangle &= \langle \cos [\phi(\mathbf{r}_1) - \phi(\mathbf{r}_2) + 2\phi(\mathbf{r}_2)] \rangle \quad (\text{B.6}) \\
&= \langle \cos [\phi(\mathbf{r}_1) - \phi(\mathbf{r}_2)] \cos [2\phi(\mathbf{r}_2)] \rangle \\
&\quad - \langle \sin [\phi(\mathbf{r}_1) - \phi(\mathbf{r}_2)] \sin [2\phi(\mathbf{r}_2)] \rangle
\end{aligned}$$

$\phi(\mathbf{r}_1) - \phi(\mathbf{r}_2)$ is independent of $\phi(\mathbf{r}_2)$, so

$$\langle \cos [\phi(\mathbf{r}_1) + \phi(\mathbf{r}_2)] \rangle = 0 \quad (\text{B.7})$$

Similarly,

$$\langle \sin [\phi(\mathbf{r}_1) + \phi(\mathbf{r}_2)] \rangle = 0 \quad (\text{B.8})$$

$$\begin{aligned}
\langle \cos [\phi(\mathbf{r}_1)] \cos [\phi(\mathbf{r}_2)] \rangle &= \frac{1}{2} \langle \cos [\phi(\mathbf{r}_1) + \phi(\mathbf{r}_2)] + \cos [\phi(\mathbf{r}_1) - \phi(\mathbf{r}_2)] \rangle & (\text{B.9}) \\
&= \frac{1}{2} \exp\left(-\frac{|\mathbf{r}_1 - \mathbf{r}_2|^2}{\sigma^2}\right)
\end{aligned}$$

$$\begin{aligned}
\langle \sin [\phi(\mathbf{r}_1)] \sin [\phi(\mathbf{r}_2)] \rangle &= \frac{1}{2} \langle \cos [\phi(\mathbf{r}_1) - \phi(\mathbf{r}_2)] - \cos [\phi(\mathbf{r}_1) + \phi(\mathbf{r}_2)] \rangle & (\text{B.10}) \\
&= \frac{1}{2} \exp\left(-\frac{|\mathbf{r}_1 - \mathbf{r}_2|^2}{\sigma^2}\right)
\end{aligned}$$

$$\begin{aligned}
\langle \sin [\phi(\mathbf{r}_1)] \cos [\phi(\mathbf{r}_2)] \rangle &= \frac{1}{2} \langle \sin [\phi(\mathbf{r}_1) + \phi(\mathbf{r}_2)] - \sin [\phi(\mathbf{r}_1) - \phi(\mathbf{r}_2)] \rangle & (\text{B.11}) \\
&= 0
\end{aligned}$$

$$\begin{aligned}
\langle \cos [\phi(\mathbf{r}_1)] \sin [\phi(\mathbf{r}_2)] \rangle &= \frac{1}{2} \langle \sin [\phi(\mathbf{r}_1) + \phi(\mathbf{r}_2)] - \sin [\phi(\mathbf{r}_2) - \phi(\mathbf{r}_1)] \rangle & (\text{B.12}) \\
&= 0
\end{aligned}$$

Appendix C: Squared coupling strength between momentum states

In Sec. 5.1.1, we stated this formula

$$\rho(k_f - k_0) = \langle \langle k_f | \hat{V} | k_0 \rangle \langle k_0 | \hat{V} | k_f \rangle \rangle \quad (\text{C.1})$$

and applied it in the Fermi's golden rule calculation. Here we derive it.

In the basis of momentum states $\{|k\rangle\}$, the matrix element of speckle potential $\hat{V}(x)$ is

$$g(k_1, k_2) = \langle k_1 | \hat{V}(x) | k_2 \rangle. \quad (\text{C.2})$$

The ensemble averaged, squared matrix element is

$$\begin{aligned} \langle |g(k_1, k_2)|^2 \rangle &= \langle \langle k_1 | \hat{V}(x) | k_2 \rangle \langle k_2 | \hat{V}(x) | k_1 \rangle \rangle \quad (\text{C.3}) \\ &= \left\langle \frac{1}{\sqrt{2\pi}} \int V(x_1) \exp\{i(k_0 - k_1)x_1\} dx_1 \frac{1}{\sqrt{2\pi}} \int V(x_2) \exp\{-i(k_0 - k_1)x_2\} dx_2 \right\rangle \\ &= \frac{1}{2\pi} \iint \langle V(x_1)V(x_2) \rangle \exp\{-i\Delta k(x_1 - x_2)\} dx_1 dx_2 \\ &= \rho_V(\Delta k) \end{aligned}$$

Here $\rho_V(\Delta k)$ is the PSD of the speckle potential and $\Delta k = k_2 - k_1$. Since

speckle potential is proportional to the intensity of optical speckle,

$$\rho_V(\Delta k) \propto \rho_I(\Delta k) \tag{C.4}$$

Appendix D: Speckle beam width in the focal plane from a ray optics model

The speckle beam width in the focal plane of a lens can be calculated from a ray optics model, in the limit of large focal length f and small diverging angle $\Delta\theta$.

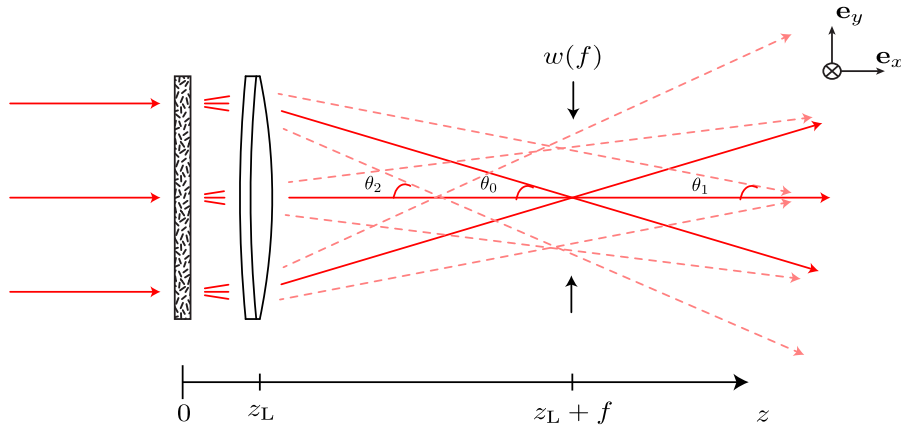


Figure D.1: A ray optics model to calculate the speckle beam width in the focal plane of a lens.

As shown in Fig. D.1, an optical ray hit the edge of a lens is focused to the focal point and form an angle θ_0 with x -axis. After the phase plate, the speckle beam diverges at an angle $\Delta\theta$, and the diverged beams form angles θ_1 and θ_2 with

the x -axis.

$$\theta_1 \approx \theta_0 - \Delta\theta \tag{D.1}$$

$$\theta_2 \approx \theta_0 + \Delta\theta$$

$$f = \frac{D_L}{2 \tan \theta_0}$$

For small $\Delta\theta$,

$$\begin{aligned} w(f) &= D_L \frac{\tan \theta_2 - \tan \theta_1}{\tan \theta_2 + \tan \theta_1} \\ &\approx D_L \frac{\sec \theta_0^2 \Delta\theta}{\tan \theta_0} \\ &= \frac{D_L \Delta\theta}{\sin \theta_0 \cos \theta_0} \end{aligned} \tag{D.2}$$

In the limit of large f , $\sin \theta_0 \approx \frac{D_L}{2f}$, $\cos \theta_0 \approx 1$.

$$w(f) \approx 2f \Delta\theta. \tag{D.3}$$

Appendix E: Second Chern number of a quantum-simulated non-Abelian Yang monopole

QUANTUM SIMULATION

Second Chern number of a quantum-simulated non-Abelian Yang monopole

Seiji Sugawa*[†], Francisco Salces-Carcoba, Abigail R. Perry[‡], Yuchen Yue, I. B. Spielman[†]

Topological order is often quantified in terms of Chern numbers, each of which classifies a topological singularity. Here, inspired by concepts from high-energy physics, we use quantum simulation based on the spin degrees of freedom of atomic Bose-Einstein condensates to characterize a singularity present in five-dimensional non-Abelian gauge theories—a Yang monopole. We quantify the monopole in terms of Chern numbers measured on enclosing manifolds: Whereas the well-known first Chern number vanishes, the second Chern number does not. By displacing the manifold, we induce and observe a topological transition, where the topology of the manifold changes to a trivial state.

The Yang-Mills theory is a non-Abelian gauge field theory that includes a higher gauge symmetry than quantum electrodynamics and now forms a cornerstone of the standard model of particle physics (1, 2). In the Yang-Mills theory, soliton solutions that include monopoles and instantons play a key role, theoretically describing phenomena in high-energy physics (3). The monopole solutions are sources of non-Abelian gauge fields and give rise to a nontrivial topology.

The physical importance of magnetic monopoles was captured in the seminal work by P. A. M. Dirac (4). Dirac considered a phase, now known as the Aharonov-Bohm phase, acquired by an electron with charge q_e moving around a magnetic monopole and showed that the monopole charge must be $q_m = nh/q_e$, where n is an integer and h is Planck's constant. Following from this quantization condition, Gauss's law for the magnetic field \mathbf{B} must take a quantized value $nh/q_e = \int_{S_2} \mathbf{B} \cdot d\mathbf{S}$, which essentially counts the number of magnetic charges inside the manifold S_2 [here S_2 is a closed two-dimensional (2D) surface and $d\mathbf{S} = \mathbf{n} dS$ (\mathbf{n} is a unit vector normal to the surface)]. The integral is topologically robust against deformation of the enclosing manifold as long as the number of monopoles enclosed is unchanged. The field from Dirac monopoles has been observed in a range of physical systems, and the associated topological charge—the first Chern number, often referred to as “the Chern number”—has been measured (5–7). The first Chern number and Abelian monopole field were measured in the parameter space of a spin-1/2 artificial atom (6, 7), and the Dirac monopole

analog was synthesized inside a spinor condensate where the associated spin texture was observed (5). In quantum mechanical systems, gauge fields such as the electromagnetic vector potential \mathcal{A} take central stage (in classical electromagnetism $\mathbf{B} = \nabla \times \mathcal{A}$) and are required to understand nature at the most fundamental level (8). The Yang-Mills theory is a non-Abelian extension of Dirac's magnetic monopole (9) and requires higher-order Chern numbers (higher-order than the first) for its topological characterization.

Here we report on the quantum simulation of a Yang monopole in a 5D parameter space built from an atomic quantum gases' internal states and the measurement of its topological charges by characterizing the associated non-Abelian gauge fields (often called curvatures). To extract the second and higher Chern numbers that result from non-Abelian gauge fields, we developed a method to evaluate the local non-Abelian

Berry curvatures through nonadiabatic responses of the system.

Monopole fields and Chern numbers

An \mathcal{N} dimensional vector gauge field $\mathbf{A}(\mathbf{q}) = (A_1, A_2, \dots, A_{\mathcal{N}})$, where $\mathbf{q} = (q_1, q_2, \dots, q_{\mathcal{N}})$ is the position, is said to be non-Abelian when the vector components $A_\mu(\mathbf{q})$ fail to commute, i.e., $[A_\mu, A_\nu] \neq 0$ ($\mu, \nu \in \{1, \dots, \mathcal{N}\}$), where μ and ν label the different vector components. The resulting curvature is given by

$$F_{\mu\nu}(\mathbf{q}) = \frac{\partial A_\nu}{\partial q_\mu} - \frac{\partial A_\mu}{\partial q_\nu} - i[A_\mu, A_\nu] \quad (1)$$

where i is an imaginary unit; in three spatial dimensions, the components of the magnetic field $B_\mu = \epsilon_{\mu\nu\lambda} F_{\nu\lambda}/2$, where λ is an integer, can be determined from the elements of the $F_{\nu\lambda}$ matrices ($\epsilon_{\mu\nu\lambda}$ is the rank-3 Levi-Civita symbol, and we used Einstein's implied summation convention for repeated indices). In analogy to the Gauss's law with electric charges (monopoles), the first Chern number is equivalently the integral

$$C_1 = \frac{1}{2\pi} \int_{S_2} \mathbf{B} \cdot d\mathbf{S} = \frac{1}{4\pi} \int_{S_2} F_{\mu\nu} dq_\mu \wedge dq_\nu \quad (2)$$

of the magnetic field \mathbf{B} or the Abelian field strength $F_{\nu\lambda}$ over a closed 2D manifold S_2 , where \wedge is the wedge product. The general n th Chern number of a non-Abelian gauge field is the n -wedge product of the non-Abelian curvature

$$\alpha_n C_n = \int_{S_{2n}} \text{tr}[F \wedge F \wedge F \wedge \dots \wedge F] d^{2n}S \quad (3)$$

where α_n ($\alpha_1 = 4\pi$, $\alpha_2 = 32\pi^2$, ...) is a normalization factor and S_{2n} is a closed $2n$ -dimensional manifold (10).

Chern numbers provide a topological classification of monopoles in gauge field theories. The monopoles are generally associated with

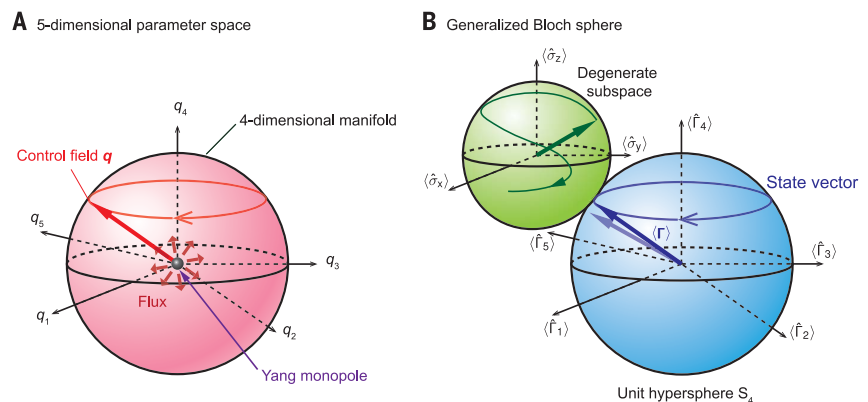


Fig. 1. Non-Abelian monopole and the appearance of nontrivial topology. (A) The 5D parameter space. The system has a topological defect at the origin, a Yang monopole, providing a source of non-Abelian gauge field. The topological invariant associated with the monopole is the second Chern number, defined on an enclosing 4D manifold. (B) Quantum states can be mapped onto generalized Bloch spheres. An additional Bloch sphere, which defines the wave function within each DS, is required to fully define our systems eigenstates. The 5D generalized magnetization vector Γ remains parallel with \mathbf{q} at adiabaticity, and the leading order correction to the adiabatic changes to \mathbf{q} , is a small deflection in Γ .

Joint Quantum Institute, National Institute of Standards and Technology and the University of Maryland, Gaithersburg, MD 20899-8424, USA.

*Present address: PRESTO, Japan Science and Technology Agency (JST), Saitama 332-0012, Japan, and Graduate School of Science, Kyoto University, Kyoto 606-8502, Japan.

[†]Corresponding author. Email: sugawa@yagura.scphys.kyoto-u.ac.jp (S.S.); ian.spielman@nist.gov (I.B.S.) [‡]Present address: Georgia Tech Research Institute, Atlanta, GA 30318, USA.

a divergence in the field strength and can contribute a unit of flux through any enclosing manifold. This generalized flux is quantized and is given by the Chern numbers. In particular, for Yang monopoles, the first Chern number is zero, but the second Chern number is either +1 or -1 (Fig. 1).

Many quantum systems can be described by a Hamiltonian $\hat{H}(\mathbf{q})$ that depends on position \mathbf{q} in parameter space. At each position, the system is characterized by energies $E_\kappa(\mathbf{q})$ and eigenstates $|\kappa(\mathbf{q})\rangle$, where $\kappa \in \{1, \dots, \mathcal{K}\}$ is an index that identifies the eigenstate in our \mathcal{K} -dimensional Hilbert space. A gauge potential called the non-Abelian Berry connection $A_\mu^\beta(\mathbf{q}) = i\langle\beta(\mathbf{q})|\partial/\partial q_\mu|\gamma(\mathbf{q})\rangle$, where $\beta, \gamma \in \{1, \dots, \mathcal{K}\}$, is encoded in the wave functions; thus, for any position \mathbf{q} , each vector component A_μ is represented by a matrix. Chern numbers and curvatures can be then defined by Eqs. 1 to 3 for each well-separated energy level.

Because of these gauge fields, an initial quantum state can acquire a geometric phase as the location in parameter space is adiabatically changed. For nondegenerate quantum systems, the resulting geometric phase is called the Berry phase (11). A quantum state evolving within a degenerate subspace can acquire a Wilczek-Zee geometric phase, a matrix-valued generalization of the Berry phase obtained as the path-ordered line integral of a non-Abelian gauge potential (12-14).

Experimental Hamiltonian

We realized a non-Abelian gauge field by cyclically coupling four levels within the hyperfine ground states of rubidium-87 using radio-frequency and microwave fields (Fig. 2, A and B), essentially forming a square plaquette. The four couplings were parameterized by two Rabi frequencies Ω_A and Ω_B and two phases ϕ_A and ϕ_B arranged so that the sum of the phases around the plaquette was π . This configuration of control fields, along with a detuning $\delta = |g_F|\mu\Delta_B/\hbar$, where g_F is the Landé g factor, μ is the Bohr magneton, Δ_B is the shift in the magnetic field from resonant coupling condition, and $\hbar = h/2\pi$, gave us an experimentally controllable 5D parameter space labeled by the Cartesian coordinates $\mathbf{q} = (-\Omega_B \cos \phi_B, -\Omega_A \cos \phi_A, -\Omega_A \sin \phi_A, \delta, -\Omega_B \sin \phi_B)$. In much the same way that a two-level atom in a magnetic field can be understood in terms of three Pauli matrices, our four-level system is governed by the Hamiltonian

$$\hat{H} = -\frac{\hbar}{2} \mathbf{q} \cdot \hat{\Gamma} = -\frac{\hbar}{2} (q_1 \hat{\Gamma}_1 + q_2 \hat{\Gamma}_2 + q_3 \hat{\Gamma}_3 + q_4 \hat{\Gamma}_4 + q_5 \hat{\Gamma}_5) \tag{4}$$

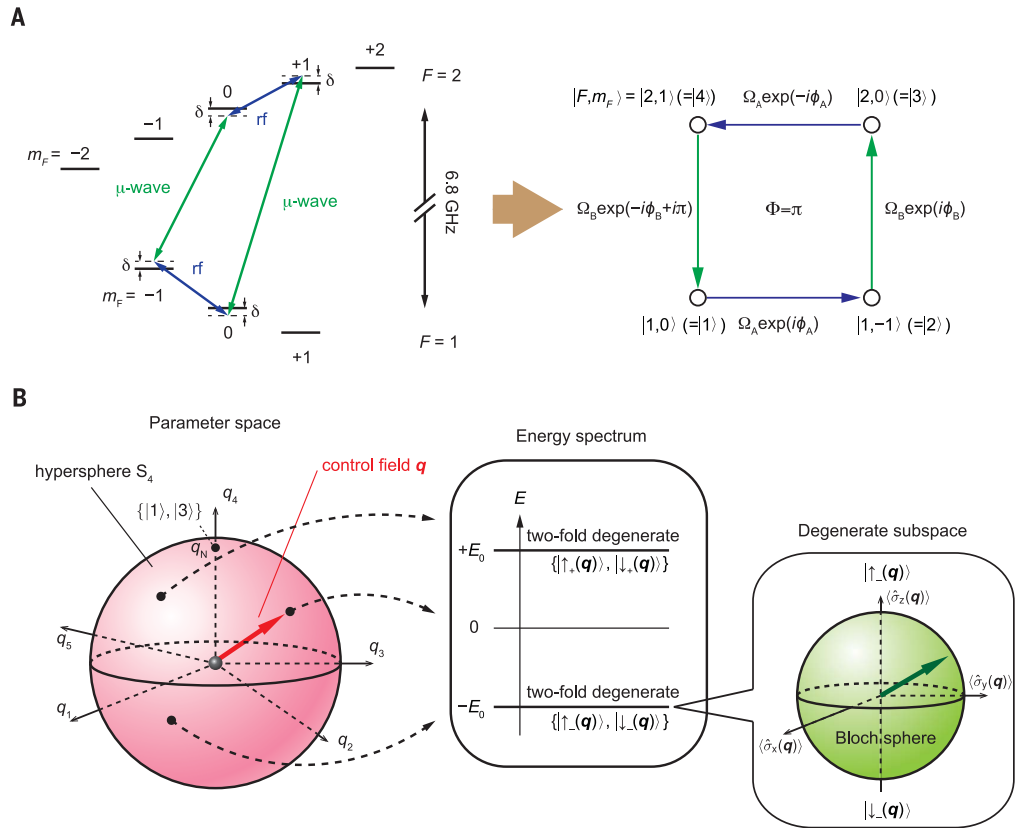
where q_i and $\hat{\Gamma}_i$ ($i = 1, 2, \dots, 5$) are the i th components of \mathbf{q} and $\hat{\Gamma}$ and $\hat{\Gamma}_i$ is represented as the four-by-four Dirac matrices with the hyperfine ground states shown in Fig. 2A taken as the basis. Furthermore, because each of the Dirac matrices

commutes with the time-reversal operator, the system has time-reversal symmetry (15); Kramers theorem then implies that the system has two pairs of degenerate energy states, here with energies $E_\pm = \pm\hbar|\mathbf{q}|/2$. Thus, each energy, labeled by + or -, has two independent eigenstates $|\uparrow^\pm(\mathbf{q})\rangle$ and $|\downarrow^\pm(\mathbf{q})\rangle$; each of these pairs define a degenerate subspace (DS). As shown in Fig. 2B, these DSs are characterized by a generalized magnetization vector $\langle\hat{\Gamma}\rangle = (\langle\hat{\Gamma}_1\rangle, \langle\hat{\Gamma}_2\rangle, \langle\hat{\Gamma}_3\rangle, \langle\hat{\Gamma}_4\rangle, \langle\hat{\Gamma}_5\rangle)$ on a unit 4-sphere in our 5D space. Different configurations within each DS share the same magnetization vector, which can be pictured in terms of an additional 3D Bloch sphere (green sphere in Figs. 1 and 2B). An eigenstate is fully depicted by assigning the two such ‘‘Bloch’’ vectors. The Yang monopole (16, 17) resides at the Hamiltonian’s degeneracy point at $\mathbf{q} = 0$, a singular point where the non-Abelian Berry’s connection diverges. The non-Abelian Berry’s curvatures from our experimental Hamiltonian (Eq. 4) quantum simulates the fields of a Yang monopole.

Quantum control and measurement

We begin by demonstrating the control and measurement capabilities of our system. We first prepared the system in its ground state at the position $\mathbf{q}_0 = q_0(-1, -1, 0, 0, 0)/\sqrt{2}$ in parameter space, where the generalized magnetization is $\langle\hat{\Gamma}\rangle = (-1, -1, 0, 0, 0)/\sqrt{2}$. Then, by ramping ϕ_A , we slowly moved the control vector around the

Fig. 2. Schematics of the experiment. (A) Schematic of our implemented coupling using four hyperfine ground states of rubidium-87. The four states were cyclically coupled with radio-frequency (rf) and microwave fields. The right panel shows the resulting plaquette and the associated coupling parameters. (B) At any point in the 5D parameter space, the energy spectrum forms a pair of twofold degenerate manifolds with the energy gap equal to $\hbar|\mathbf{q}|$, where \mathbf{q} is the control field. Each degenerate subspace can be represented by a Bloch sphere.



Downloaded from <http://science.sciencemag.org/> on September 25, 2020

circle $q(t) = q_0[-1, -\cos(2\pi t/T), -\sin(2\pi t/T), 0, 0]/\sqrt{2}$ shown in Fig. 3A, where T is the full ramp time, and $\mathbf{q}_0 = |q_0| = 2\pi \times 2$ kHz.

After preparing the eigenstate $(|\uparrow^-(\mathbf{q}_0)\rangle + i|\downarrow^-(\mathbf{q}_0)\rangle)/\sqrt{2} = (\sqrt{2}|1\rangle - (1+i)|2\rangle + i\sqrt{2}|3\rangle + (1-i)|4\rangle)/(2\sqrt{2})$ in the ground DS by rotating the control field (15) from the north pole $\mathbf{q}_N = q_0(0, 0, 0, 1, 0)$, we measured the state for different evolution times in this nearly adiabatic ramp (Fig. 3B), and identified the orientation within the DS by performing quantum state tomography, giving the expectation values of the Pauli operators $\hat{\sigma}_i$ ($i = x, y, z$) in the ground DS at \mathbf{q}_N . As seen in

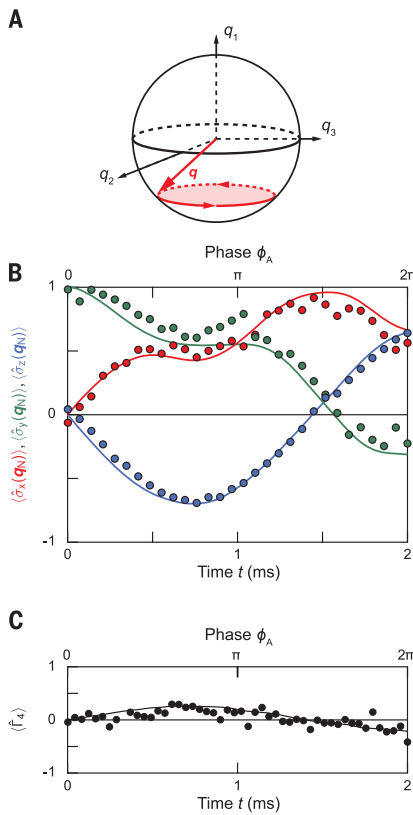


Fig. 3. State evolution under a non-Abelian gauge field. (A) Schematic of the control field trajectory. The two phases (ϕ_A, ϕ_B) were ramped for $T = 2$ ms with the laboratory parameters $\Omega_A/2\pi = \Omega_B/2\pi = 1.41$ kHz and $\delta = 0$. (B) Nearly-adiabatic response of pseudospin magnetization within the ground DS Bloch sphere, showing the nontrivial acquisition of a Wilczek-Zee phase after a 2π -rotation. The solid lines simulate the experiment by numerically solving the TDSE (15). (C) Deflection during the phase ramp. The state was slightly deflected along $\langle \hat{\Gamma}_4 \rangle$, resulting from our finite ramp time (black circles), changing from positive to negative. The black curve shows the theoretically expected linear response based on Eq. 6 (15).

Fig. 3B, after the control field completed one cycle, the orientation of the state vector within the DS differed from its initial value. After one cycle, the Berry's phase from an Abelian gauge field would contribute only an overall phase, leaving the state vector otherwise unchanged. In agreement with our numerical simulation obtained by solving (15) the time-dependent Schrödinger equation (TDSE) for the Hamiltonian in Eq. 4 (curves in Fig. 3B), this shows that the observed evolution resulted instead from the Wilczek-Zee phase derived from a non-Abelian gauge field.

We then measured $\langle \hat{\Gamma}_4 \rangle$ during this ramp and noted a small deflection of the magnetization of the state vector owing to remnant nonadiabatic effects (Fig. 3C). In linear response theory, deviations from adiabaticity can be described in terms of the response of the state vector to a general-

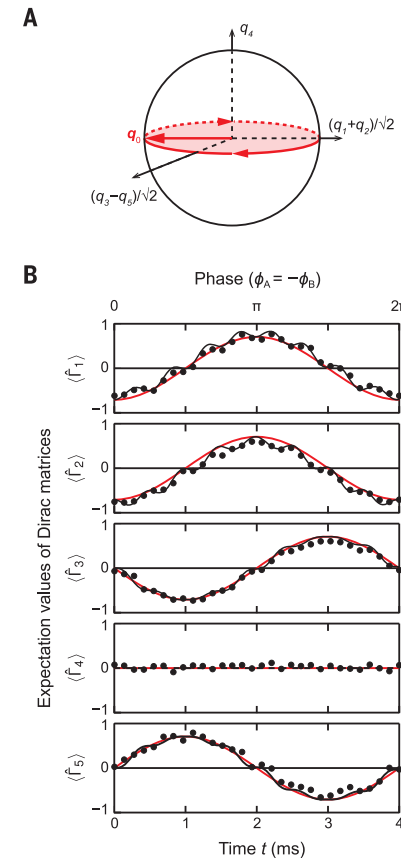


Fig. 4. Generalized magnetization. (A) Schematic of the control field trajectory. The two phases (ϕ_A, ϕ_B) are ramped for $T = 4$ ms with the laboratory parameters $\Omega_A/2\pi = \Omega_B/2\pi = 1.41$ kHz and $\delta = 0$. (B) Quantum states were measured by evaluating the expectation values of the five Dirac matrices. The red curves plot the trajectories expected for adiabatic motion, whereas the black curves are numerical simulations, including our finite ramp time (15).

ized force $\hat{M}_\mu = -(\partial\hat{H}/\partial q_\mu)/\hbar$ acting on the state (Fig. 1B). For a conventional Abelian system, the local force at a fixed time (18, 19)

$$\langle \hat{M}_\mu \rangle = v_\nu \hat{F}_{\mu\nu} + \text{constant} \quad (5)$$

resulting from parameters q_ν changing with velocity v_ν is analogous to the Lorentz force. This relation gives the driving force behind the topological and geometrical charge pumps recently realized in ultracold atoms (20–22). In both crystalline and optical lattices, the same relation underlies the anomalous quantum Hall effect (23–25).

Owing to the phase symmetry of the system for ϕ_A , the generalized geometric force from Eq. 5 is constant for our trajectory, inconsistent with the sign change present in the observed deflection (Fig. 3C). To account for this discrepancy, Eq. 5 can be extended to accommodate non-Abelian gauge fields, giving the generalized geometric force (15, 26)

$$\langle \hat{M}_\mu \rangle = v_\nu \langle \hat{F}_{\mu\nu} \rangle + \text{constant} \quad (6)$$

acting on the state, where the expectation value on the right-hand side is taken for a pure state at adiabaticity and $\hat{F}_{\mu\nu}$ is the Berry curvature of the associated degenerate subspace (26). In contrast to the Abelian case, where the generalized geometric force is simply the product of the local Berry curvature and the velocity, the force in Eq. 6 also depends on the quantum state within the DS. As we saw, even for adiabatic motion, Wilczek-Zee phases can lead to considerable evolution within the DS, making Eq. 6 essential for describing generalized geometric forces.

The sign change in Fig. 3C is now explained by the dependence of the geometric force on the state as it evolved within the DS. If the gauge field is Abelian, independent of the state within the DS, the force components should be constant in the spherical coordinate along the path for constant ramp velocity. The sign change reveals that the quantum state acquired a Wilczek-Zee phase from a non-Abelian gauge potential, contributing to the geometric force. Indeed, the solid curves depict the prediction of our TDSE simulations (15) and confirm that the geometric force in our experiment cannot be derived from an Abelian gauge potential.

In general, we can observe the full magnetization of the state vector by carefully measuring the expectation values (15) of all five operators $\hat{\Gamma}_i$. To demonstrate this capability, we moved along the circle $\mathbf{q}(t) = q_0[-\cos(2\pi t/T), -\cos(2\pi t/T), -\sin(2\pi t/T), 0, \sin(2\pi t/T)]/\sqrt{2}$ shown in Fig. 4A, starting from $|\uparrow^-(\mathbf{q}_0)\rangle = (\sqrt{2}|1\rangle - |2\rangle + |4\rangle)/2$ at $t = 0$, and obtained $\langle \hat{\Gamma}(t) \rangle$. Figure 4B shows that $\langle \hat{\Gamma}(t) \rangle$ nearly followed the adiabatic trajectory (red curves), almost oriented parallel to \mathbf{q} , but slightly deflected owing to the nonadiabaticity [TDSE simulation (15) shown by black curves in Fig. 4B].

Non-Abelian Berry curvatures and Chern numbers

With the ultimate goal of evaluating Chern numbers in mind, we characterized the non-Abelian Berry curvatures on spherical manifolds in parameter space. Accordingly, we adopt spherical coordinates described by a radius q and four angles $\theta_1 \in [0, \pi]$, $\theta_2 \in [0, \pi/2]$, ϕ_1 , and ϕ_2 that are related to our experimental control parameter space via $\Omega_A = q \sin \theta_1 \cos \theta_2$, $\Omega_B = q \sin \theta_1 \sin \theta_2$, $\delta = q \cos \theta_1$, $\phi_1 = (\phi_A + \phi_B)/2$, and $\phi_2 = (\phi_A - \phi_B)/2$.

After preparing the system in its ground state at \mathbf{q}_0 , we measured the deflection along the θ_1 direction, while rotating the control field along $\mathbf{q}_\pm(t) = q_0[-\cos(2\pi t/T), -\cos(2\pi t/T), \mp \sin(2\pi t/T), 0, \mp \sin(2\pi t/T)]/\sqrt{2}$ by ramping ϕ_1 from 0 to $\pm\pi$ (half-circles in Fig. 5A). The geometric force M_{θ_1} is directly obtained from the deflection of $\langle \hat{\Gamma}_4 \rangle$. Figure 5B plots the deflection during this ramp for four different initial states (marked by |A>, |B>, |C>, and |D> in Fig. 5D) within the DS, manifesting the state dependence of the geometric force in the non-Abelian gauge field in contrast to Abelian cases. The net deflection during any given ramp gives the integrated geometric force.

To confirm that our drive was in the linear response regime, we measured the geometric force as a function of ramp time T (Fig. 5C). From both the data and TDSE simulations (dashed curves), the geometric force (solid curves) is almost linear with respect to velocity for $T \geq 12\pi/q$.

The components of the Berry curvatures can be reconstructed from the integrated geometric force. Owing to the symmetry of our experimental Hamiltonian, the geometric force components must be almost constant in spherical coordinates during the ramp in the linear response regime. By measuring the geometric force experienced by four independent initial states all within the DS, we determined the four independent parameters present in the 2-by-2 matrices describing each element (labeled by β and γ) of the representation of the non-Abelian Berry curvature $F_{\nu\lambda}^{\beta\gamma}$. Following this procedure for $T \geq 12\pi/q$, we obtained $2q_0^2 \hat{F}_{\theta_1\phi_1} = 0.01(3)\hat{I}_0 + [-0.06(5), 0.08(5), 0.98(3)] \cdot \hat{\sigma}$, in agreement with the theoretical value, $2q_0^2 \hat{F}_{\theta_1\phi_1} = \hat{\sigma}_z$ (here, \hat{I}_0 is the identity operator).

We thoroughly investigated the state dependence of the geometric force by studying the evolution of 225 initial states covering the Bloch sphere of the initial DS (Fig. 5D). For each initial state, we recorded the deflection after a 250- μ s ramp to obtain the Berry curvature component $\langle \hat{F}_{\theta_1\phi_1} \rangle$. Figure 5D shows the initial-state Bloch sphere colored according to the curvature; the theoretically computed result (top) is in good agreement with experimental result (bottom).

By changing the path and the direction along which we measure the deflection, other components of the curvatures can be measured. For example, by rotating the control field along $\mathbf{q}_\pm(t) = q_0[-\cos(2\pi t/T), -\cos(2\pi t/T), \mp \sin(2\pi t/T), 0, \pm \sin(2\pi t/T)]/\sqrt{2}$ by ramping ϕ_2 and evaluating the deflection along the θ_2 direction at \mathbf{q}_0 , we obtained $2q_0^2 \hat{F}_{\theta_2\phi_2} = -0.08(3)\hat{I}_0 + [-0.12(5),$

$-0.07(5), 1.00(3)] \cdot \hat{\sigma}$, also in good agreement with the theoretical value, $2q_0^2 \hat{F}_{\theta_2\phi_2} = \hat{\sigma}_x$.

Just as in classical electromagnetism, where the fields from electric or magnetic sources fall off as $1/q^2$, the non-Abelian gauge field strength also follows a $1/q^2$ scaling law, as required by the generalized Gauss's law (see Eq. 2) that defines the second Chern number. By repeating the same Berry curvature measurement ($\hat{F}_{\theta_2\phi_2}$) for different q_0 , while keeping $2\pi/qT = 0.25$ constant to remain in the linear response regime, the Berry curvature components ($\hat{F}_{\theta_2\phi_2}$) indeed had the $1/q^2$ scaling of a monopole source (Fig. 5E); this also suggests that $\langle \hat{F}_{\theta_2\phi_2} \rangle$ diverges at $q \rightarrow 0$.

Taken together, these fields provide sufficient information to extract the second Chern number of a 4-sphere with radius q_0 . We evaluate the second Chern number using the relation

$$C_2 = \frac{3q_0^4}{4\pi^2} \int_{S_4} \text{tr}[F_{\theta_1\theta_1} F_{\theta_2\theta_2}] d^4S \quad (7)$$

where S_4 defines the 4-sphere and $d^4S = \sin^3 \theta_1 \sin 2\theta_2 d\theta_1 d\theta_2 d\phi_1 d\phi_2$. Equation 7 relies on the rotational symmetry of $\hat{H}(\mathbf{q})$, which gives the numerically confirmed (15) relations $\text{tr}[F_{\theta_1\theta_1} F_{\theta_2\theta_2}] = \text{tr}[F_{\theta_1\theta_2} F_{\theta_2\theta_1}] = \text{tr}[F_{\theta_1\theta_2} F_{\theta_2\theta_1}]$. From the non-Abelian Berry curvature measurements in the

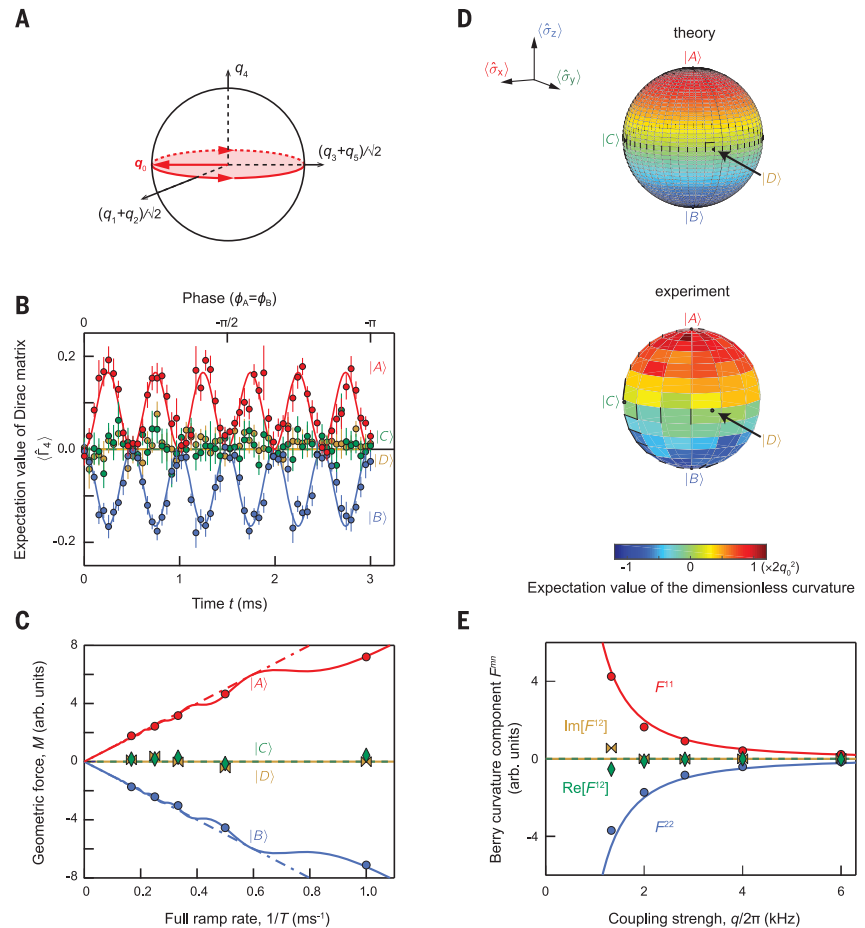


Fig. 5. Deflection of states within the ground-state manifold owing to non-Abelian Berry curvatures. (A) Schematic of the control field trajectory. (B) Deflections along θ_1 were measured during the $T = 6$ ms ramp. $\langle \hat{\Gamma}_4 \rangle$ was measured for four independent initial states (|A>, |B>, |C>, and |D>) within the DS at \mathbf{q}_0 . Here $|A\rangle = (\sqrt{2}|1\rangle - |2\rangle + |4\rangle)/2$ and $|B\rangle = (-|2\rangle + \sqrt{2}|3\rangle - |4\rangle)/2$ are the basis states for the DS. $|C\rangle = (|A\rangle + |B\rangle)/\sqrt{2}$, and $|D\rangle = (|A\rangle + i|B\rangle)/\sqrt{2}$. (C) Geometric force as a function of $1/T$ measured for the four initial states (|A>, |B>, |C>, and |D>) at \mathbf{q}_0 . The dashed lines assume linearity, and the solid curves are the outcomes of our TDSE simulations (15). (D) Expectation values of the non-Abelian Berry curvature ($\hat{F}_{\theta_1\phi_1}$) in the ground state manifold at \mathbf{q}_0 are mapped onto Bloch spheres associated with the state within the DS at \mathbf{q}_0 . The four initial states used in (A) to (C) are also shown in the theoretical (top sphere) and the experimental (bottom sphere) plots. (E) $1/q^2$ scaling in the strength of the curvature. The matrix components of the curvature ($\hat{F}_{\theta_2\phi_2}$) are evaluated for various q_0 . The data show excellent agreement with the theory that exhibits $1/q^2$ dependence (solid lines).

previous section, we directly obtained $C_2 = 2q_0^4 \text{tr}[F_{\theta_1\phi_1}(\mathbf{q}_0)F_{\theta_2\phi_2}(\mathbf{q}_0)] = 0.97(6)$ for the ground state, consistent with the theoretical value $C_2 = 1$. We repeated the measurements for the excited state and found $C_2 = 2q_0^4 \text{tr}[F_{\theta_1\phi_2}(\mathbf{q}_0)F_{\theta_2\phi_1}(\mathbf{q}_0)] = -0.93(6)$, also in agreement with the theoretical value $C_2 = -1$. These nonzero Chern numbers inform us that the manifold is topologically nontrivial.

Because the system is time-reversal symmetric, the first Chern form is zero, and therefore Eq. 3 for the first Chern number should be zero for both degenerate manifolds. Indeed, all the measured non-Abelian Berry curvatures were traceless ($q_0^2 \text{tr}[\hat{F}_{\theta_1\phi_1}] = -0.08(3)$ and $q_0^2 \text{tr}[\hat{F}_{\theta_1\phi_2}] = 0.01(3)$ for the ground state, and $q_0^2 \text{tr}[\hat{F}_{\theta_1\phi_2}] = -0.02(3)$ and $q_0^2 \text{tr}[\hat{F}_{\theta_2\phi_1}] = 0.00(3)$ for the excited state), so that the first Chern number, which is the surface integral of the trace of the

individual curvatures, was also zero. Thus, the nontrivial topology of the monopole field is not expressed by a first Chern number.

Topological transition

We concluded our measurements by inducing a topologically nontrivial-to-trivial transition of the manifold by displacing the 4-sphere in parameter space from the origin by an amount $\mathbf{q}_{\text{offset}} = q_{\text{offset}}(\mathbf{q}_0/q_0)$ (Fig. 6A). The topological transition occurs at the critical displacement $q_{\text{crit}} = q_0$ when the Yang monopole departs the manifold. Figure 6B shows our observed transition of the second Chern number from ± 1 , for the ground and excited states, to zero as the offset coupling q_{offset} was increased. This transition is associated with the topology of the manifold changing from topologically nontrivial to trivial. The smoothness of the observed transition was

caused by the breakdown of the linear response near the transition point. Our theory [continuous curves in Fig. 6B, and see (15)] shows that slower ramps enlarge the region in which linear response is valid and make the transition sharper (Fig. 6B). Topological transitions have been observed in a range of experiments (6, 7, 25); however, in all of these cases, the observed topological phases were only identified by a Dirac monopoles' first Chern number and enclosing 2D manifolds. By contrast, in our system, the first Chern number is zero everywhere and the second Chern number characterizes the topological phase, arising from a Yang monopole at the origin of parameter space. The opposite topological charges observed in the ground or excited manifolds result from a monopole in one manifold acting as an antimonopole in the other. With these Chern number measurements, we confirmed that the engineered topological singularity in our system indeed simulated a Yang monopole.

Discussion and outlook

Our work can be extended to other quantum systems, including ions, thermal atoms, and superconducting qubits. The Chern number characterizes a source of gauge field with high symmetry, a symmetry that naturally arises in particle physics in contexts such as quantum chromodynamics.

The monopole field and the second Chern number have been discussed theoretically in the context of 4D quantum Hall effect (4DQH) (27, 28), spin-Hall effect (29), exotic charge pumping (30), and fermionic pairing (31) in condensed matter systems. The model we explored experimentally is equivalent to the (4 + 1)-D lattice Dirac Hamiltonian relevant to 4DQH. The 4DQH is a generalized quantum Hall effect and is the root state of a family of topological insulators, which are obtained by a dimensional reduction procedure (32). The observed transition in Fig. 6B can be regarded as the type of phase transition present in the band topology of 4DQH systems. A conformal mapping from a 4D spherical manifold in parameter space to a 4D crystal momentum space, 4-torus, directly recasts our Hamiltonian as the Dirac Hamiltonian.

Our observation lays the groundwork for simulating objects in high-energy physics with atomic quantum systems. Lattice extensions of our work, where lattice sites or bands play the role of spin states, may allow quantum simulation of emergent many-body dynamics with non-Abelian gauge fields with highly controllable ultracold quantum gases systems (33–36).

REFERENCES AND NOTES

1. C. N. Yang, R. L. Mills, *Phys. Rev.* **96**, 191–195 (1954).
2. G. Hooft, *Nature* **448**, 271–273 (2007).
3. G. Hooft, *Nucl. Phys. B* **79**, 276–284 (1974).
4. P. A. M. Dirac, *Proc. R. Soc. Lond. Ser. A* **133**, 60–72 (1931).
5. M. W. Ray, E. Ruokokoski, S. Kandel, M. Möttönen, D. S. Hall, *Nature* **505**, 657–660 (2014).
6. M. D. Schroer et al., *Phys. Rev. Lett.* **113**, 050402 (2014).
7. P. Roushan et al., *Nature* **515**, 241–244 (2014).
8. Y. Aharonov, D. Bohm, *Phys. Rev.* **115**, 485–491 (1959).
9. C. N. Yang, *J. Math. Phys.* **19**, 320–328 (1978).
10. N. Manton, P. Sutcliffe, *Topological Solitons* (Cambridge Univ. Press, 2004).

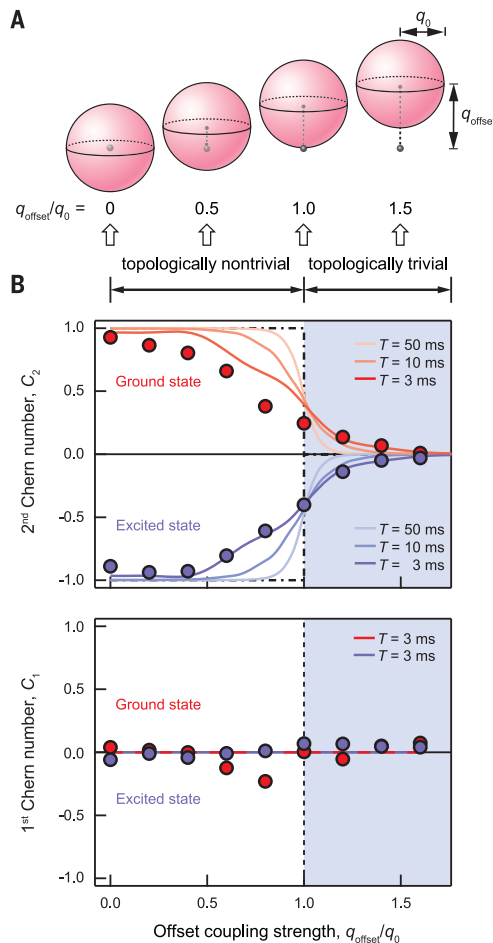


Fig. 6. Topological transition from a Yang monopole. (A) Schematic illustration of the topological transition. Suitable spherical manifolds with radius q_0 were offset from the origin by q_{offset} to evaluate both C_1 and C_2 . At the critical value ($q_{\text{crit}} = q_0$), the monopole exits the manifolds. (B) Chern numbers extracted from experiment. When the manifold crossed $q_{\text{crit}} = q_0$, $|C_2|$ decreased from unity to zero (top panel), whereas C_1 was constantly zero for both the ground (red) and the excited (blue) states (bottom panel). Numerical simulations (solid lines; $T = 3, 10,$ and 50 ms) and analytic theory (dash-dot lines) are also shown. The data were taken for $T = 3$ ms.

11. M. V. Berry, *Proc. R. Soc. Lond. Ser. A* **392**, 45–57 (1984).
12. F. Wilczek, A. Zee, *Phys. Rev. Lett.* **52**, 2111–2114 (1984).
13. K. Toyoda, K. Uchida, A. Noguchi, S. Haze, S. Urabe, *Phys. Rev. A* **87**, 052307 (2013).
14. T. Li *et al.*, *Science* **352**, 1094–1097 (2016).
15. See supplementary materials.
16. Y. Hatsugai, *New J. Phys.* **12**, 065004 (2010).
17. Our non-Abelian gauge field is SU(2) symmetric, where the generator can be, for example, the Pauli matrices.
18. V. Gritsev, A. Polkovnikov, *Proc. Natl. Acad. Sci. U.S.A.* **109**, 6457–6462 (2012).
19. J. E. Avron, M. Fraas, G. M. Graf, O. Kenneth, *New J. Phys.* **13**, 053042 (2011).
20. H.-I. Lu *et al.*, *Phys. Rev. Lett.* **116**, 200402 (2016).
21. M. Lohse, C. Schweizer, O. Zilberberg, M. Aidelsburger, I. Bloch, *Nat. Phys.* **12**, 350–354 (2016).
22. S. Nakajima *et al.*, *Nat. Phys.* **12**, 296–300 (2016).
23. N. Nagaosa, J. Sinova, S. Onoda, A. H. MacDonald, N. P. Ong, *Rev. Mod. Phys.* **82**, 1539–1592 (2010).
24. G. Jotzu *et al.*, *Nature* **515**, 237–240 (2014).
25. M. Aidelsburger *et al.*, *Nat. Phys.* **11**, 162–166 (2015).
26. M. Kolodrubetz, *Phys. Rev. Lett.* **117**, 015301 (2016).
27. S.-C. Zhang, J. Hu, *Science* **294**, 823–828 (2001).
28. H. M. Price, O. Zilberberg, T. Ozawa, I. Carusotto, N. Goldman, *Phys. Rev. B* **93**, 245113 (2016).
29. S. Murakami, N. Nagosa, S.-C. Zhang, *Phys. Rev. B* **69**, 235206 (2004).
30. Y. E. Kraus, Z. Ringel, O. Zilberberg, *Phys. Rev. Lett.* **111**, 226401 (2013).
31. C.-H. Chern, H.-D. Chen, C. Wu, J.-P. Hu, S.-C. Zhang, *Phys. Rev. B* **69**, 214512 (2004).
32. X.-L. Qi, T. L. Hughes, S.-C. Zhang, *Phys. Rev. B* **78**, 195424 (2008).
33. Y.-J. Lin *et al.*, *Phys. Rev. Lett.* **102**, 130401 (2009).
34. J. Ruseckas, G. Juzeliūnas, P. Öhberg, M. Fleischhauer, *Phys. Rev. Lett.* **95**, 010404 (2005).
35. P. Hauke *et al.*, *Phys. Rev. Lett.* **109**, 145301 (2012).
36. E. A. Martinez *et al.*, *Nature* **534**, 516–519 (2016).

ACKNOWLEDGMENTS

The authors would like to thank A. Polkovnikov and M. Kolodrubetz for discussion. **Funding:** This work was partially supported by the U.S. Army Research Office's Atomtronics MURI, and by the U.S. Air Force Office of Scientific Research's Quantum Matter MURI, National Institute of Standards and Technology, and NSF through the Physics Frontier Center at the Joint Quantum

Institute. S.S. acknowledges the Japan Society for the Promotion of Science (fellowship for research abroad). **Author contributions:** S.S. conducted the experiment, performed the theoretical work, and analyzed the data. S.S., A.R.P., F.S.-C., and I.B.S. contributed to the rubidium Bose-Einstein condensate apparatus. All authors substantially participated in the discussion and the writing of the manuscript. S.S. and I.B.S. conceived of the project. **Competing interests:** The authors declare no competing interests. **Data and materials availability:** All data are available in the manuscript or the supplementary materials.

SUPPLEMENTARY MATERIALS

www.sciencemag.org/content/360/6396/1429/suppl/DC1
Materials and Methods
Supplementary Text
Figs. S1 to S3
References (37, 38)
Database S1

15 February 2017; accepted 27 April 2018
10.1126/science.aam9031

Second Chern number of a quantum-simulated non-Abelian Yang monopole

Seiji Sugawa, Francisco Salces-Carcoba, Abigail R. Perry, Yuchen Yue and I. B. Spielman

Science **360** (6396), 1429-1434.
DOI: 10.1126/science.aam9031

Going beyond the first Chern number

Topological properties of physical systems are reflected in so-called Chern numbers: A nonzero Chern number typically means that a system is topologically nontrivial. Sugawa *et al.* engineered a cold atom system with a nonzero second Chern number, in contrast to condensed matter physics, where only the first Chern number is usually invoked. The exotic topology relates to the emergence of a type of magnetic monopole called the Yang monopole (known from theoretical high-energy physics) in a five-dimensional space of internal degrees of freedom in a rubidium Bose-Einstein condensate. The results illustrate the potential of cold atoms physics to simulate high-energy phenomena.

Science, this issue p. 1429

ARTICLE TOOLS

<http://science.sciencemag.org/content/360/6396/1429>

SUPPLEMENTARY MATERIALS

<http://science.sciencemag.org/content/suppl/2018/06/27/360.6396.1429.DC1>

REFERENCES

This article cites 35 articles, 3 of which you can access for free
<http://science.sciencemag.org/content/360/6396/1429#BIBL>

PERMISSIONS

<http://www.sciencemag.org/help/reprints-and-permissions>

Use of this article is subject to the [Terms of Service](#)

Science (print ISSN 0036-8075; online ISSN 1095-9203) is published by the American Association for the Advancement of Science, 1200 New York Avenue NW, Washington, DC 20005. The title *Science* is a registered trademark of AAAS.

Copyright © 2018 The Authors, some rights reserved; exclusive licensee American Association for the Advancement of Science. No claim to original U.S. Government Works

Appendix F: Equations of state from individual one-dimensional Bose
gases

PAPER • OPEN ACCESS

Equations of state from individual one-dimensional Bose gases

To cite this article: F Salces-Carcoba *et al* 2018 *New J. Phys.* **20** 113032

View the [article online](#) for updates and enhancements.



PAPER

Equations of state from individual one-dimensional Bose gases

F Salces-Carcoba¹, C J Billington^{1,2}, A Putra¹, Y Yue¹, S Sugawa^{1,3} and I B Spielman¹¹ Joint Quantum Institute, National Institute of Standards and Technology, and University of Maryland College Park, Gaithersburg, MD 20899, United States of America² School of Physics and Astronomy, Monash University, Victoria 3800, Australia³ Present address: PRESTO, Japan Science and Technology Agency (JST), Saitama 332-0012, Japan, and Graduate School of Science, Kyoto University, Kyoto 606-8502, Japan.E-mail: pacosalces@gmail.com

Keywords: quantum gases, atomic physics, one-dimensional Bose gas, equation of state

OPEN ACCESS

RECEIVED
17 August 2018REVISED
12 October 2018ACCEPTED FOR PUBLICATION
9 November 2018PUBLISHED
23 November 2018Original content from this work may be used under the terms of the [Creative Commons Attribution 3.0 licence](https://creativecommons.org/licenses/by/4.0/).

Any further distribution of this work must maintain attribution to the author(s) and the title of the work, journal citation and DOI.



Abstract

We trap individual 1D Bose gases and obtain the associated equation of state by combining calibrated confining potentials with *in situ* density profiles. Our observations agree well with the exact Yang–Yang 1D thermodynamic solutions under the local density approximation. We find that our final 1D system undergoes inefficient evaporative cooling that decreases the absolute temperature, but monotonically reduces a degeneracy parameter.

1. Introduction

Strongly interacting systems are ubiquitous in modern physics, from astrophysical objects such as neutron stars to the myriad of correlated electron systems in condensed matter. Experimental developments in ultracold atomic physics enable multiple avenues to explore interacting quantum matter, for example with optical lattices [1], Feshbach resonances [2] or mediated long-range interactions [3]. Furthermore, tailored potentials can reduce the effective dimensionality of cold atomic gases; for example, a 2D optical lattice can partition a 3D system into an array of 1D gases [4–6]. Remarkably, the theory of a 1D Bose gas (1DBG) with contact repulsive interactions is exactly solvable at all temperatures [7, 8], making it an ideal system to benchmark experiment against theory.

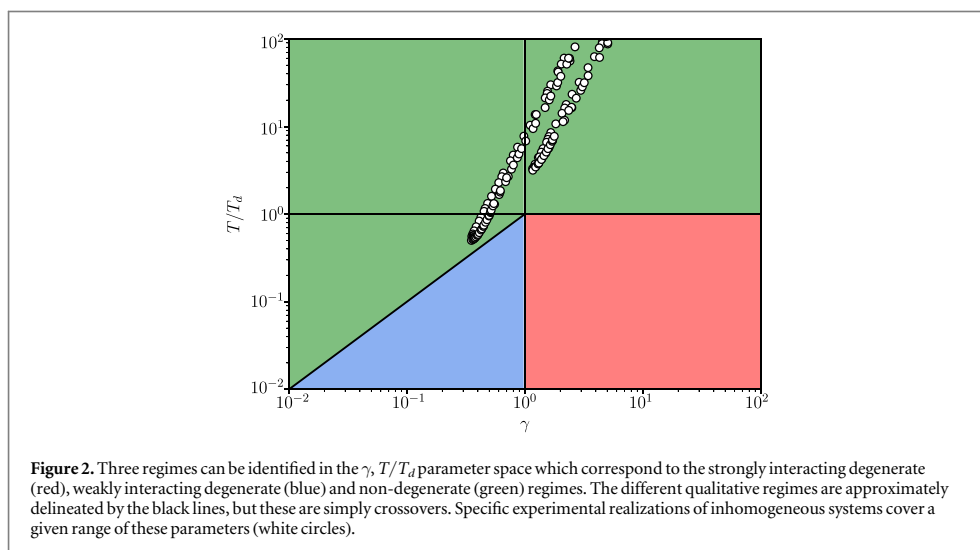
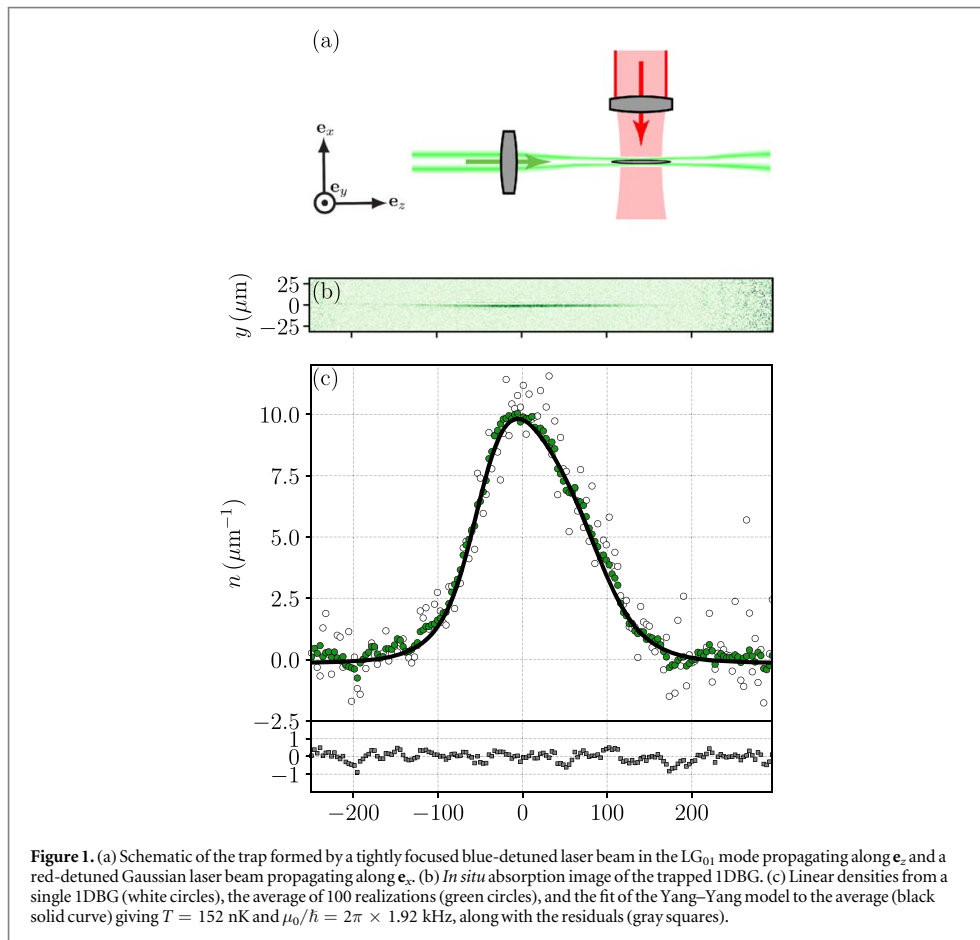
In cold atomic gases, the ≈ 5 nm range [2] of the interatomic potential is vastly smaller than the $\gtrsim 100$ nm interatomic spacing, hence interactions are well described by a local contact potential with strength g . This gives the 1D Hamiltonian

$$H = \sum_i \left[-\frac{\hbar^2}{2m} \frac{\partial^2}{\partial z_i^2} + V(z_i) \right] + g \sum_{i \neq j} \delta(z_i - z_j), \quad (1)$$

for N interacting bosons of mass m which in the absence of a potential, i.e. $V(z) = 0$, becomes the Lieb–Liniger [7] Hamiltonian.

Lieb and Liniger showed that eigenstates of this Hamiltonian are parametrized by the dimensionless interaction parameter $\gamma = mg/\hbar^2 n$, where n is the density. Here the relevance of interactions increases with decreasing density. For $\gamma \ll 1$ mean-field theory accurately describes the system, while for $\gamma \gg 1$ the atoms strongly avoid one another and behave much like weakly interacting fermions. Yang and Yang extended this solution to non-zero temperature [8] and cold atom experiments have validated the accuracy of the ‘Yang–Yang’ thermodynamics [9–11].

Here we study the physics of individual 1DBGs using ^{87}Rb atoms in an optical ‘tube trap’ (figure 1(a)) and benchmark the thermodynamic equation of state (EoS) against Yang–Yang thermodynamics. Our individual-system realization bridges an existing gap in experiments, on the one hand avoiding the issue of ensemble averaging present in realizations using optical lattices [4–6, 10] and on the other hand enabling the future study of 1D multi-component systems not viable using magnetic confinement potentials [12, 13].



The physics of 1DBGs can be divided into three qualitative regimes [14] shown in figure 2. For sufficiently high temperatures (green region) the EoS is dominated by thermal effects and approaches that of a non-interacting classical gas. Below the degeneracy temperature $T_d = \hbar^2 n^2 / 2mk_B$, where k_B is Boltzmann's constant, and for weak interactions ($\gamma \ll 1$), the reduced thermal fluctuations allow Bose statistics to weigh in [15], creating a phase fluctuating degenerate gas. For lower temperatures where $T/T_d < 2\gamma$ (blue region), the thermal energy falls below the chemical potential and the system is well described by the Gross–Pitaevskii equation (GPE). In contrast, for systems with large interactions ($\gamma \gg 1$) the EoS resembles that of an ideal Fermi gas [10], with the formation of a Fermi surface for $T < T_d$ (red region). Yang–Yang thermodynamics provides EoS's encompassing all of these regimes, relating quantities like the particle, entropy and pressure densities to the chemical potential μ and temperature T , e.g. $n(\mu, T)$.

In trapped systems, the confining potential $V(z) \geq 0$ can often be treated as an inhomogeneous chemical potential $\mu(z) = \mu_0 - V(z)$ which allows for multiple regimes to be present in a single 1DBG. We define μ_0 as the local chemical potential at $V(z) = 0$. This can be quantitatively understood [16] within the local density approximation (LDA) allowing the density profile $n(z, T)$ to be interpreted as an EoS $n(\mu(z), T)$. As a consequence, the EoS can be experimentally determined from a well-calibrated trapping potential $V(z)$ and the observed density profiles.

We extract this $n(\mu(z), T)$ EoS from *in situ* absorption images [17–19] of individual systems (figure 1(b)), eliminating ensemble averaging. Because we obtain the 1D density directly, we do not apply the inverse Abel transform [18] thereby avoiding added noise. We benchmark our measurement against the Yang–Yang EoS (figure 1(c)), from which other thermodynamic quantities become readily available (e.g. free energy, entropy and pressure).

This manuscript is organized as follows: in section 2, we describe our experimental setup and data acquisition protocol; in section 3, we address the different calibration aspects of our analysis; in section 4, we discuss the results; and in section 5, we conclude.

2. Experiment

We prepare cold atoms beginning with a magneto-optical trap followed by vertical magnetic transport [20] into a magnetic quadrupole trap, ultimately loading a 1064 nm crossed optical dipole trap [21, 22]. This gives $N \approx 2 \times 10^5$ atom Bose–Einstein condensates (BECs) of ^{87}Rb in the $5 S_{1/2} |F = 1, m_F = 0\rangle$ hyperfine ground state with ≈ 70 Hz mean trapping frequencies. The atoms are then transferred into the composite high aspect-ratio trap shown in figure 1(a). This trap includes a red-detuned ($\lambda_G = 1064$ nm) Gaussian beam along \mathbf{e}_x with waist $w_G = 203(2)$ μm providing reduced longitudinal confinement owing to its larger waist as compared to the ≈ 70 μm crossed dipole beam waist. A transverse ‘tube trap’ along \mathbf{e}_z is provided by a blue-detuned ($\lambda_{LG} = 532$ nm) Laguerre–Gauss (LG_{01}) beam, tightly focused to a waist of $w_{LG} = 5.6(5)$ μm . In our standard configuration these beams have powers $P_G = 0.8(1)$ W and $P_{LG} = 1.0(1)$ W, giving a peak transverse trapping frequency $\omega_{\perp}/2\pi = (\omega_x \omega_y)^{1/2}/2\pi = 17(2)$ kHz.

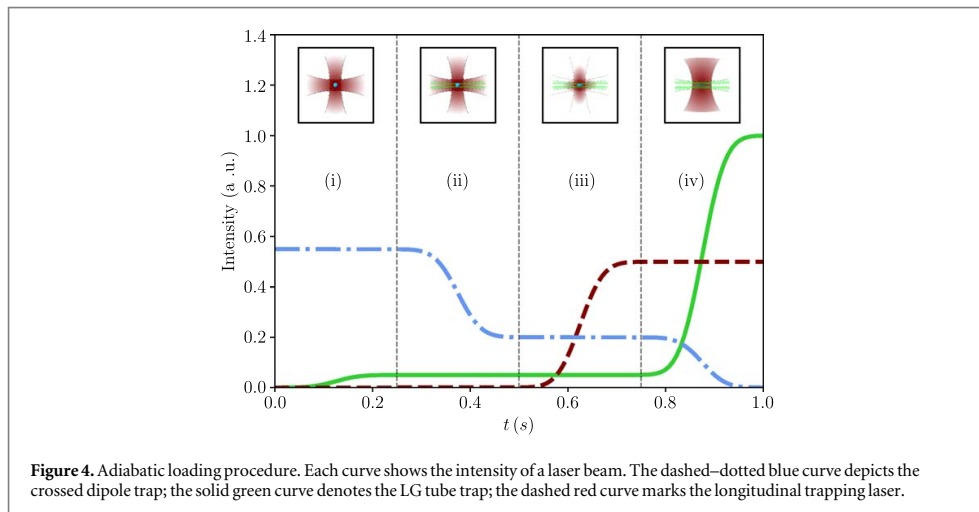
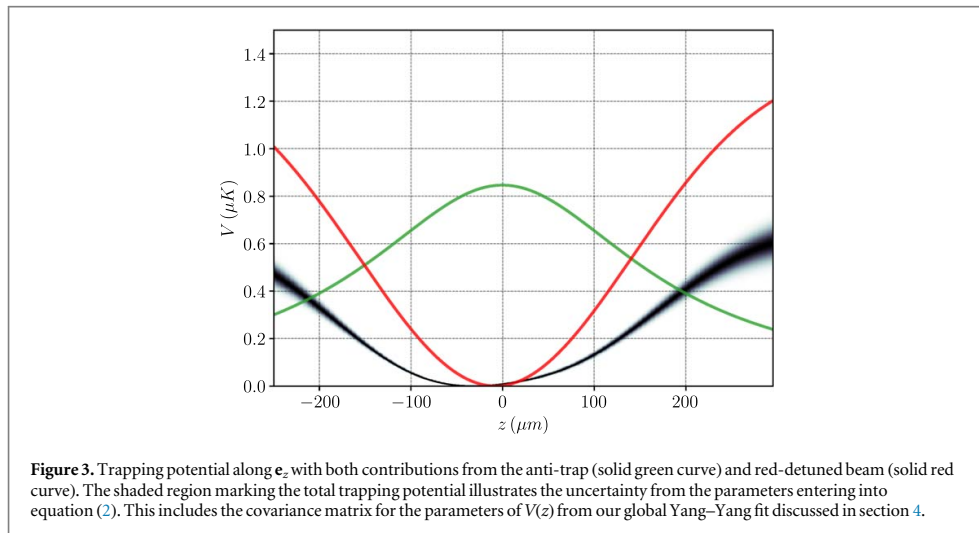
The transverse zero-point energy from ω_{\perp} produces an anti-confining potential along \mathbf{e}_z due to the divergence of the LG beam. The anti-trapping potential shown in green in figure 3 significantly alters the overall longitudinal potential

$$V(z) = \frac{\hbar\omega_{\perp}^{(0)}}{1 + (z - z_a)^2/z_R^2} + V_t \exp\left(-\frac{2z^2}{w_G^2}\right) - V_0, \quad (2)$$

where $\omega_{\perp}^{(0)}/2\pi$ denotes the peak transverse trapping frequency; z_a is the center of the anti-trap; z_R is the Rayleigh range of the LG beam; and V_0 is an energetic offset chosen such that the minimum of the potential is zero. The black shaded curve in figure 3 shows the combined anharmonic potential of the longitudinal trap (red curve) and the anti-confining potential. Small amplitude longitudinal dipole oscillations in the combined potential have frequency $\omega_z/2\pi = 12.1(2)$ Hz.

Figure 4 depicts our four step loading scheme. (i) We first ramp up the intensity of the LG beam from zero in 250 ms until the tube trap can suspend atoms against gravity. Because the 3D system is always larger than 30 μm , the ≈ 5 μm LG beam only captures a small fraction of the initial 3D ensemble. (ii) We then lower the intensity of the crossed dipole trap in 250 ms, allowing the atoms outside the tube trap to fall away. (iii) We then ramp up the final 1064 nm longitudinal trap in 250 ms. (iv) In the final 250 ms we simultaneously increase the intensity of the LG beam to its final value while removing the crossed dipole trap.

These 250 ms ramps were chosen to be adiabatic with respect to all the confining potentials. Monopole and dipole modes of the 1DBG can be induced by both beam misalignment and excessive ramp rates in this scheme. Our ramp times were chosen to mitigate these residual excitations.



We control the temperature of the 1DBG by varying the temperature T_{3D} of the initial 3D Bose gas. We tune T_{3D} by adjusting the depth of the crossed dipole trap, covering the range from $T_{3D} = 34\text{--}320$ nK, with an observed BEC transition at $T_{3D}^c \approx 160$ nK. We determine T_{3D} with time-of-flight measurements. The number of atoms in the 1DBG increases with decreasing T_{3D} due to the increasing 3D density as T_{3D} falls. Gravitational sag is a complicating factor: as the crossed dipole trap decreases, the 3D ensemble lowers due to gravity, but the vertical alignment of the tube trap does not. We mitigate this effect by increasing the crossed dipole power after the final evaporation such that the crossed dipole potential is in a fixed vertical position prior to loading the tube trap.

3. Imaging

We derive the density $n(z)$ from *in situ* absorption images. Our imaging system has a resolution of $1.85(5) \mu\text{m}$ and magnification that maps one $5.6 \mu\text{m}$ sensor pixel to $0.84(1) \mu\text{m}$ in the object plane. In preparation for imaging, we apply a $20 \mu\text{s}$ repump pulse to transfer the $5 S_{1/2} |F = 1, m_F = 0\rangle$ atoms into the $5 S_{1/2} |F = 2\rangle$ hyperfine manifold. We then image [23] with a circularly polarized $\lambda_p = 780$ nm probe beam resonant with the $5 S_{1/2} |F = 2\rangle$ to $5 P_{3/2} |F = 3\rangle$ transition for $20 \mu\text{s}$ at an average intensity of $I = 2.5 I_{\text{sat}}$, where $I_{\text{sat}} = 1.67 \text{ mW cm}^{-2}$ is the saturation intensity of the resonant atomic transition. An image of the probe beam following absorption I_a , the probe without atoms present I_p , and a dark frame with no probe present I_b , are each recorded on a charge-coupled device camera. From these images we obtain the absorbed fraction

Table 1. Table summarizing the different parameters of $V(z)$. The calibrated values and their uncertainties were used as the central values and bounds for the fit.

Parameter	Calibrated value	Value from fit	Calibration method
$\omega_{\perp}/2\pi$	17 (4) kHz	17 (2) kHz	Transverse expansion in TOF
z_a	0(10) μm	$-7.670(8)$ μm	Alignment precision
z_R	185(29) μm	185(5) μm	Intensity profile of LG beam
V_t/k_B	-1.17 (25) μK	-1.37 (6) μK	Intensity profile of Gaussian beam
w_G	203 (2) μm		Intensity profile of Gaussian beam
$\omega_z/2\pi$ $V(z)$	12.13 (20) Hz		Small amplitude dipole oscillations
δz		8.19 (30) μm	

$f = (I_p - I_a)/(I_p - I_d)$. For each set of experimental parameters we repeat the experiment for ≈ 100 realizations.

Our image analysis is a multiple step process. We first preprocess the raw images to correct for background artifacts and improve the signal-to-noise ratio by a factor of ≈ 10 . We then extract the linear densities using an absorption model that includes a modest Lamb–Dicke suppression. As compared to a naïve model, $n(z)$ increases by as much as 30%. This process leaves our qualitative results unchanged.

We reconstruct an optimal I_p^{opt} for each I_a as a linear sum of I_p from all realizations by minimizing the sum squared difference between I_p^{opt} and I_a away from the atoms [24, 25]. This reconstruction reduces fringing due to vibrational motion that occurred between acquiring I_a and I_p , along with shot noise present on each I_p . We use similar techniques to remove a systematic difference in dark counts between I_a and I_p , as well as to account for structured read-out noise. We then compute mean absorbed fractions \bar{f} over each set of experimental parameters, and use uncentered principal component analysis (PCA) to further suppress shot noise. From \bar{f} and a detector calibrated [17, 26, 27] in units of I_{sat} , we compute ‘naïve’ optical depths using the standard solution to the Beer–Lambert (BL) law [27], which we sum along columns to produce ‘naïve’ linear densities.

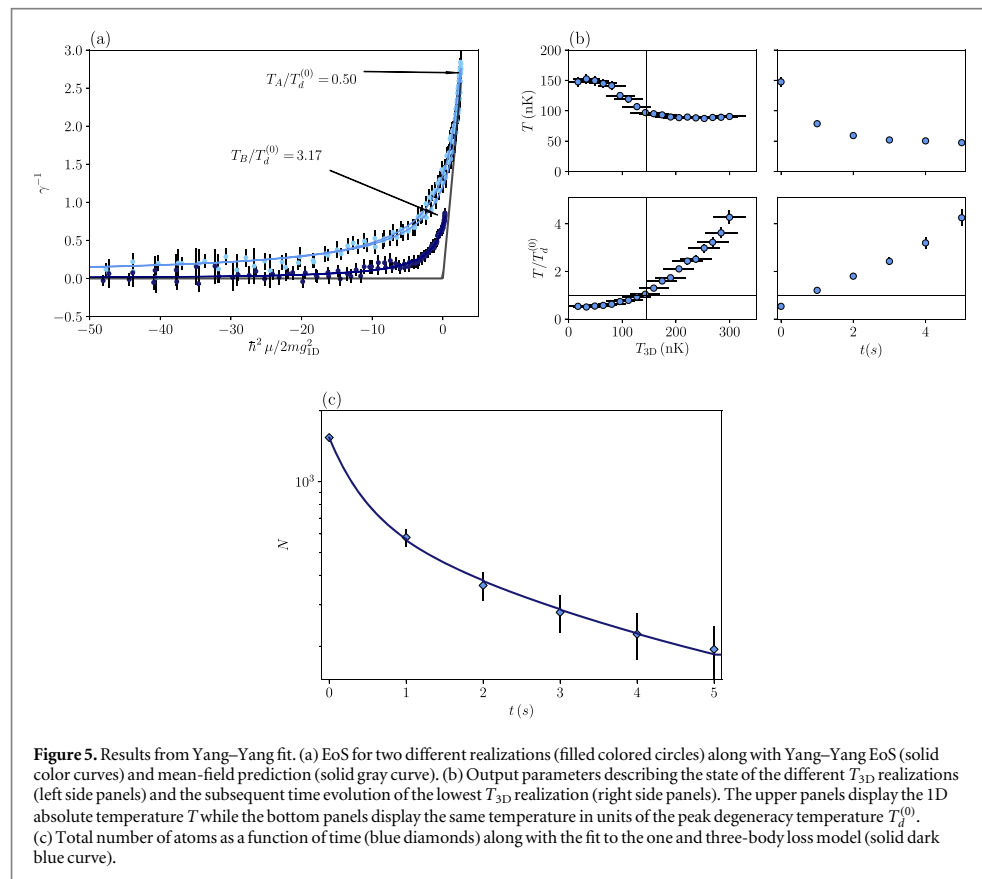
We take into account the fact that the transverse extent of our atom cloud (for a tube trap the radial confinement gives an extent of $\sqrt{\hbar/m\omega_{\perp}} \approx 110$ nm) is below the resolution of both our imaging system and the optical scattering length $\sqrt{3\lambda_p^2/2\pi^2} \approx 300$ nm. We further incorporate the transverse diffusive motion that atoms undergo during the imaging pulse. Each of these effects violates the assumptions underlying the BL law. In comparison with the naïve BL law, our model for the density agrees at low density but deviates up to 30% at higher densities. This process is described in greater detail in the supplementary material.

4. Results

The results of our image processing are 1D density profiles $n^{(j)}(z)$ confined in the same trapping potential but with one of 24 different initial conditions labeled by j . In the LDA we expect that these density profiles can result from Yang–Yang thermodynamics. For each j , both the temperature $T^{(j)}$ and the overall chemical potential $\mu_0^{(j)}$ are in principle unknown because of the lack of suitable reservoirs. As a result we obtain these quantities from fits to the Yang–Yang EoS and assess their validity in terms of the reduced chi-squared.

For each j , the Yang–Yang EoS predicts the complete density profile as shown in figure 1(c) with just two free parameters $T^{(j)}$ and $\mu_0^{(j)}$. We constrain the fit to the trapping region between the local maxima of $V(z)$. The potential is parametrized by the common set of parameters shown in table 1. We include some of these as additional parameters in our fit shared between all j . In table 1 we show the calibrations by other measurements along with their uncertainties; these are provided as initial guesses and bounds to the Yang–Yang fit. An additional uncalibrated parameter δz accounts for a tiny displacement of the IDBG relative to the center of $V(z)$ for times following the loading protocol. The inclusion of δz leaves the main results unchanged and its value lies within the relative alignment uncertainty of the trap centers. Different combinations of fixed parameters have no qualitative effect on the results. The third column in table 1 shows the potential parameters derived from the Yang–Yang fit. We evaluate the goodness-of-fit with the reduced chi-squared $\chi_{\nu}^2 \approx 1.5$. Lastly, the residuals of the fit show systematic variations in I_a , which are reflected by the gray pixels in figure 1(c).

Figure 5(a) shows the reduced density versus reduced chemical potential for two initial conditions, each plotting different cuts in the EoS $n(\mu, T)$. The continuous curves in figure 5(a) represent the Yang–Yang model with the T and μ_0 from our fits. For small chemical potential these density profiles are well described by the EoS of a non-interacting Bose gas while for $\mu > 0$ they approach the predictions of GPE mean-field theory [14]. The Yang–Yang EoS accurately predicts both regimes. A sharp eye observes an apparent hysteresis loop visible in the trace labeled by A , this results from the spatial dependence of g that follows ω_{\perp} . As shown in figure 3, ω_{\perp} is slightly off-centered, ultimately resulting in the observed behavior. The scattered white dots on figure 2



represent these two traces in the $\gamma, T/T_d$ plane. These data are shown to be either in the interacting regime or below degeneracy, but not in both.

Figure 5(b) summarizes the outcome of all our Yang-Yang fits in which we varied T_{3D} , the initial 3D temperature (left panels); or the hold time t in the 1D trap for our lowest T_{3D} (right panels) cloud. In the top left panel, we observe that as a function of decreasing T_{3D} , the 1D temperature T first remains constant and then counterintuitively increases. In contrast, as shown in the bottom left panel, the degeneracy parameter defined as $T/T_d^{(0)}$, is a monotonically increasing function of T_{3D} showing how the more degenerate 3D clouds result in more degenerate 1DBGs.

For the lowest achievable T_{3D} and as a function of hold time, we see that both the total atom number N and the 1D temperature T drop (top right panel in figures 5(b) and (c), respectively), yet the 1DBG does not become more degenerate (bottom right panel in figure 5(b)). The simultaneous drop in T and N is consistent with evaporative cooling along the longitudinal axis of the tube trap, which has depth of ≈ 700 nK. The inability of such evaporative cooling to increase or even maintain degeneracy results from the slower relative decrease in T with respect to T_d as driven by the atom number loss.

We explore the character of this loss by modeling the atom number decay with a model including one-body loss and three-body loss from photon scattering, background gas collisions and inelastic three-body collisions [5].

Figure 5(c) shows the measured atom number N (blue diamonds). We fit the decay model to the observed number (dark blue curve), giving a one-body loss coefficient $K_1^{1D} = 0.108(2)\text{s}^{-1}$ as well as a three-body loss coefficient $K_3^{1D} = 4.36(7) \times 10^{-29} \text{cm}^6 \text{s}^{-1}$. The value of K_1^{1D} is consistent with the combined vacuum-limited lifetime and estimated off-resonant scattering rate from the static dipole potentials. In contrast, the three-body loss coefficient from our fit is in excess of the intrinsic 3D three-body loss coefficient $K_3^{3D} = 5.8(3) \times 10^{-30} \text{cm}^6 \text{s}^{-1}$ [28] by a factor of ≈ 7.5 . We attribute this enhancement to the difference in the three-body correlation function $g^{(3)}$ [5, 14] from a purely coherent sample. The observed cooling is consistent with initial rapid evaporation as atoms with sufficient kinetic energy [29] overcome the longitudinal barrier of $V(z)$.

5. Conclusions

We realized individually trapped 1DBGs in a crossed dipole trap formed by a blue-detuned LG₀₁ beam and a red-detuned Gaussian beam. We benchmarked the EoS computed from Yang–Yang thermodynamics against the measured density profiles. We found that evaporative cooling along the edges of the tube trap took place although this did not maintain or increase the system’s degeneracy. Our approach enables future exploration of spinor 1DBGs associated with multi-component physics [30, 31], including spin–orbit coupling [32]. This therefore presents a promising venue to study the limits of strongly interacting 1D systems in and out of equilibrium.

Acknowledgments

We thank Max Schemmer for insightful discussions. We acknowledge the support for this work provided by the AROs Atomtronics MURI, NIST and the NSF through the PFC at the JQI.

Appendix A. Image preprocessing and extraction of modeled linear densities

We perform preprocessing of our raw images in order to improve signal to noise and correct for known systematic error, before extracting linear densities from each set of experimental parameters using an absorption model. The analysis pipeline from raw absorption, flat field and dark field images to linear densities is as follows. In the below descriptions of our analysis pipeline we alternately use bold symbols such as \mathbf{u} when we are treating an image array as a vector for the purposes of linear algebra, and ordinary symbols with spatial dependence $u(x, y)$ when we are treating images as functions of space.

A.1. Probe image reconstruction

For each shot we reconstruct an optimal probe image I_p^{opt} as a linear sum of probe images from all shots:

$$\mathbf{I}_p^{\text{opt}} = F\mathbf{c}, \quad (\text{A.1})$$

where $\mathbf{I}_p^{\text{opt}}$ is I_p^{opt} unwrapped into a column vector, F is a matrix containing all probe images as columns and \mathbf{c} is a vector of coefficients. The optimal coefficients are determined by weighted linear regression:

$$(F^T W F)\mathbf{c} = F^T W \mathbf{I}_a, \quad (\text{A.2})$$

where W is a diagonal matrix of weights equal to zero in a region of interest (ROI) about the atoms and one otherwise, and \mathbf{I}_a is the image (as a column vector) from the shot in question of the probe with atoms present. The vector of coefficients \mathbf{c} is determined by numerically solving the linear system, leading to an $\mathbf{I}_p^{\text{opt}}$ that minimizes the sum squared error with \mathbf{I}_a in the region outside the ROI. This probe reconstruction both reduces fringing due to vibrational motion that occurs between exposures within a shot, and reduces shot noise present on each reconstructed probe image on account of the dimensionality reduction entailed by linear regression [24, 25].

A.2. Dark field reconstruction

We correct for a small spatially inhomogeneous systematic difference in counts (≈ 1.2 max, ≈ 0.2 typical) between absorption and probe images, which we attribute to variation in ambient brightness over the 60 Hz mains power cycle (this is systematic rather than random, as each shot is synchronized to begin at the same point in the 60 Hz cycle). We fit a candidate two-dimensional function to the measured average difference between absorption and probe images, which we include as a reference image $\mathbf{I}_d^{\text{sys}}$ in the above linear regression in order to extract a coefficient c^{sys} for each absorption image for how much of this offset was present (we obtain $c^{\text{sys}} \approx 1$ in all cases indicating little shot-to-shot variation in the offset).

We then compute the mean dark frame $\bar{\mathbf{I}}_d$ over all shots, and perform PCA on the set of all dark frames, with two PCA eigenvectors revealing a source of correlated dark noise in the form of spatially sinusoidally varying dark counts with a different phase offset for each shot, which we also observed to be present in the PCA eigenvectors of the probe images (as eigenvectors four and five). We project each absorption image onto these eigenvectors $\mathbf{I}_p^{\text{pca4}}$ and $\mathbf{I}_p^{\text{pca5}}$ of the probe images in order to determine coefficients c^{pca4} and c^{pca5} . A reconstructed dark field image $\mathbf{I}_d^{\text{recon}}$ is then computed for each shot as

$$\mathbf{I}_d^{\text{recon}} = \bar{\mathbf{I}}_d + c^{\text{sys}}\mathbf{I}_d^{\text{sys}} + c^{\text{pca4}}\mathbf{I}_p^{\text{pca4}} + c^{\text{pca5}}\mathbf{I}_p^{\text{pca5}}. \quad (\text{A.3})$$

A.2.1. Absorbed fraction and saturation parameter. Absorbed fraction f and saturation parameter S images are then computed for each shot as

$$f = \frac{I_p^{\text{opt}} - I_a}{I_p^{\text{opt}} - I_d^{\text{recon}}}, \quad (\text{A.4})$$

$$S = \frac{1}{I_{\text{sat}}}(I_p^{\text{opt}} - I_d^{\text{recon}}), \quad (\text{A.5})$$

where I_{sat} is the saturation intensity in camera count units. The ‘naïve’ optical depth for a single shot can then be computed as:

$$\text{OD}_{\text{naïve}} = -\alpha \log(1 - f) + Sf, \quad (\text{A.6})$$

where $\alpha \equiv \sigma_0/\sigma_{\text{eff}} = I_{\text{sat eff}}/I_{\text{sat}}$ is the empirically determined ratio between the ideal two-level and effective scattering cross sections due to imperfect polarization and magnetic field orientation. The average naïve optical depth over all repeated shots for each set of experimental parameters is computed as:

$$\overline{\text{OD}}_{\text{naïve}} \approx -\alpha \log(1 - \bar{f}) + \bar{S}\bar{A}, \quad (\text{A.7})$$

where the mean product of absorbed fraction and \bar{f} and saturation parameter \bar{S} are taken over only the repeated shots for one set of experiment parameters, and where we compute the mean absorbed fraction within the log rather than the mean of the entire log term in order to avoid the systematic error that results from taking the mean of a nonlinear function of noisy data. This naïve optical depth is not accurate across our entire dataset due to our 1D system being narrower transversely than both the optical scattering length $\sqrt{3}\lambda_p^2/2\pi^2$ and our imaging resolution, both of which are violations of the assumptions of the BL law. We continue to compute further reconstructions of this naïve optical depth only for comparison with modeled linear densities which include a correction to the BL law to account for this, presented further below.

A.3. Dimensionality reduction of absorbed fraction

We dimensionally reduce the mean absorbed fractions \bar{f} of each set of experiment parameters in order to reduce the effect of shot noise on column sums of the data. Since the point spread function resulting from diffraction in our imaging system is fixed from shot to shot, this has the effect of projecting the measured absorbed fractions onto the empirically observed point spread function and its most common variations, suppressing spurious apparent absorption due to shot noise in regions where the point spread function results in little absorption.

The dimensionality reduction proceeds as follows. First we crop each mean absorption image $\bar{f}(x, y)$ to the 75-pixel high ROI that entirely contains our imaging system’s point spread function to form $\bar{f}_{\text{ROI}}(x, y)$. Then, for each x position x_i in the image, we extract the vertical lines of $\bar{f}_{\text{ROI}}(x, y)$ from all sets of experiment parameters, at that x pixel and the nearest four x pixels. Treating each vertical line as a vector⁴ $\bar{f}_{\text{ROI}}(x_i) = \bar{f}_{\text{ROI}}(x_i, y)$, we obtain the set of vectors $\{\bar{f}_{\text{ROI}}(x_{i+j}), -2 \leq j \leq 2\}$ and perform uncentered PCA [33], keeping only the first four normalized eigenvectors $\{\hat{v}_n(x_i), n \in [1, 4]\}$. We then project the (also cropped to the ROI) vertical lines $\bar{f}_{\text{ROI}}(x_i)$ of the absorbed fractions for each individual shot at the original x position onto the subspace spanned by these vectors:

$$f_{\text{red}}(x_i, y) = \bar{f}_{\text{red}}(x_i) = \sum_{n=1}^4 [\hat{v}_n(x_i) \cdot \bar{f}_{\text{ROI}}(x_i)] \hat{v}_n(x_i). \quad (\text{A.8})$$

Thus we dimensionally reduce each vertical slice (within the ROI) of each shot’s absorbed fraction onto a basis of four basis functions chosen by uncentered PCA of the vertical slices of all mean absorbed fractions at that x pixel and the nearest four other x pixels. We then compute mean, dimensionally reduced absorbed fractions $\bar{f}_{\text{red}}(x, y)$ for each set of experiment parameters within the ROI (Hereafter any images mentioned should be assumed to be cropped to the ROI).

We observe that to within numerical rounding error, it makes no difference whether the mean absorbed fractions are dimensionally reduced into this space, or the individual absorbed fractions are, before being averaged together again. We do the latter in order to provide a statistical uncertainty estimate in the mean absorbed fraction of a given set of experiment parameters as

$$\Delta \bar{f}_{\text{red}}(x, y) = \frac{\sigma[\{f_{\text{red}}(x, y)\}]}{\sqrt{N}}, \quad (\text{A.9})$$

⁴ The mixed vector versus function-of-space notation here is because we are treating the vertical slices of the images as vectors, performing dimensionality reduction on a slice-by-slice basis, whereas the x coordinate is merely a label selecting which vector we are referring to.

where σ is the standard deviation over all repeated shots for one set of experiment parameters, $\{f_{\text{red}}(x, y)\}$ is the set of all dimensionally reduced absorbed fractions for those shots, and N is the number of repeated shots for that set of experiment parameters.

A.3.1. Saturation parameter at the position of the atoms. Due to the point spread function of our imaging system being larger than the vertical extent of our atomic cloud, the saturation parameter at the location of apparent absorption (after diffraction) does not correspond to the saturation parameter at the actual location of the atoms, which is where saturation effects are relevant. We estimate a saturation parameter $S_0(x)$ for each set of experiment parameters at the estimated y position of the atoms by interpolating the mean saturation parameter for that set of experiment parameters to the y position where there is maximum apparent absorption over all shots. The y position of maximum apparent absorption at each x position is taken to be a quadratic fit $y_0(x) = ax^2 + bx + c$ with parameters determined by maximizing the total absorption over all shots:

$$[a, b, c] = \operatorname{argmax}_{a,b,c} \left(\sum_{\text{shots}} \sum_{x_i} \operatorname{interp}[S(x_i, y)](ax_i^2 + bx_i + c) \right), \quad (\text{A.10})$$

where interp is a one-dimensional spline interpolation function interpolating in the y direction only. The estimated saturation parameter at each x position for each set of experiment parameters is then

$$S_0(x) = \operatorname{interp}_y[\bar{S}(x, y)](y_0(x)). \quad (\text{A.11})$$

A.4. Naïve linear density

We can now compute an improved naïve optical depth for each set of experiment parameters using the dimensionally reduced absorbed fractions and interpolated saturation parameter as:

$$\overline{\text{OD}}_{\text{naïve red}}(x, y) \approx -\alpha \log(1 - \bar{f}_{\text{red}}(x, y)) + S_0(x)\bar{f}_{\text{red}}(x, y), \quad (\text{A.12})$$

and then compute a naïve linear density $n_{\text{naïve}}(x)$ at each x position by dividing by the cross section and integrating along y :

$$n_{\text{naïve}}(x) = \frac{\Delta y}{\sigma_0} \sum_y \overline{\text{OD}}_{\text{naïve red}}(x, y), \quad (\text{A.13})$$

where Δy is the pixel size.

A.5. Modeled linear density

We face three related problems in computing the column density $n_{\text{col}}(x, y)$ given a measured absorbed fraction $f(x, y)$ and saturation parameter $S(x, y)$ via the solution to the BL law [27]:

$$\sigma_0 n_{\text{col}}(x, y) = -\alpha \log(1 - f(x, y)) + S(x, y)f(x, y). \quad (\text{A.14})$$

The first problem is that we do not measure $f(x, y)$ directly—we measure it only after it has diffracted in the y direction, a difference which is not negligible given the size of our atom cloud in that direction. The second problem is that atoms do not only absorb light at their exact location in space, rather they absorb it from a surrounding region of space with cross sectional area given by the absorption cross section σ_0 [34]. The final problem is that our cloud is so small in the y direction that diffusion of atoms during imaging may not be negligible. These latter two problems mean that we cannot infer $n_{\text{col}}(x, y)$ from the usual solution to the BL law, we can only determine the convolution of $n_{\text{col}}(x, y)$ with some absorption profile $g(y)$ that takes into account both the finite absorption region and the diffusion of atoms from their initial positions in the y direction, the direction in which $g(y)$ is not small compared to our atom cloud. With this in mind, the solution to the BL law can be modified to read

$$\sigma_0 (n_{\text{col}} * g)(x, y, t) = -\alpha \log(1 - f(x, y, t)) + S(x, y)f(x, y, t), \quad (\text{A.15})$$

where the convolution is only along the y direction. Atomic diffusion and diffraction imply that the only quantity we have experimental access to is

$$f_{\text{meas}}(x) = \frac{1}{\tau} \int_0^\tau dt \int dy f(x, y, t) = \sum_y \bar{f}_{\text{red}}(x, y) \Delta y, \quad (\text{A.16})$$

that is, we only observe a time average of absorption over the imaging pulse time τ , and we only observe the integral of the undiffracted absorbed fraction, since diffraction preserves this integral.

If the second term of the solution to the BL law dominates, then the naïve linear density is accurate, since all three of diffraction, diffusion and convolution preserve integrals of the absorbed fraction. It is only the log term that causes a problem, since its integral is not conserved under diffraction.

Given a model for $(n_{\text{col}} * g)(x, y, t)$ with a single parameter $n(x)$ for the linear density at each x position and a measurement $f_{\text{meas}}(x)$ for each x position, we can invert (A.16) and (A.15) to obtain the linear density, under the assumptions of the model.

Our model is the following: The absorption profile $g(y)$ is approximated by a Gaussian with unit integral and standard deviation $\sigma_y(t)$ equal at $t = 0$ to the optical scattering length $\sqrt{\sigma_0/\pi} = \sqrt{3\lambda_p^2/2\pi^2}$ and increasing due to atomic diffusion as time elapses. Since the atom cloud is narrower than this absorption profile, we approximate the convolution $(n * g)(x, y, t)$ as:

$$(n * g)(x, y, t) \approx \frac{n_{1D}(x)}{\sqrt{2\pi\sigma_y^2(x, t)}} \exp\left[-\frac{y^2}{2\sigma_y^2(x, t)}\right], \quad (\text{A.17})$$

where $\sigma_y^2(x, t)$ is increasing due to momentum diffusion:

$$\sigma_y^2(x, t) = \frac{\sigma_0}{\pi} + \frac{1}{3}\sigma_{v_y}^2(x, t)t^2, \quad (\text{A.18})$$

where the mean squared y velocity $\sigma_{v_y}^2$ is given by the scattering rate R_{scat} and recoil velocity v_{rec} :

$$\sigma_{v_y}^2(x, t) = \frac{1}{3}(2\pi)^{-1}R_{\text{scat}}(x)v_{\text{rec}}^2 t, \quad (\text{A.19})$$

which is approximating isotropic scattering such that the per-scattering-event expected squared change in velocity is $v_{\text{rec}}^2/3$. The scattering rate, ignoring Doppler shifts away from resonance, is, in terms of the saturation parameter S :

$$R_{\text{scat}}(x) = \frac{\Gamma}{2} \frac{S(x)}{1 + S(x)}. \quad (\text{A.20})$$

Putting this all together, the modeled y variance of the absorption profile is:

$$\sigma_y^2(x, t) = \frac{\sigma_0}{\pi} + \frac{\Gamma}{36\pi} \frac{S(x)}{1 + S(x)} v_{\text{rec}}^2 t^3. \quad (\text{A.21})$$

Over the duration of our imaging pulse, the diffusion described by the second term results in an increase in the absorption profile's standard deviation by $\approx 30\%$ compared to the effect of the non-zero optical scattering length alone.

Using our absorption model (A.17) with an absorption profile with y variance given by (A.21), and saturation parameter $S(x, y)$ given by our estimate $S_0(x)$, our modified BL law solution (A.15) becomes:

$$\sigma_0 n(x) \frac{\exp\left[-\frac{y^2}{2\sigma_y^2(x, t)}\right]}{\sqrt{2\pi\sigma_y^2(x, t)}} = -\alpha \log(1 - f(x, y, t)) + S_0(x)f(x, y, t), \quad (\text{A.22})$$

which, if numerically inverted, defines a function that takes only $n(x)$ as input and returns $f(x, y, t)$ at any given time. Numerically integrating the result in t and y as per (A.16) extends this function into one which takes only $n(x)$ and returns the expected $f_{\text{meas}}(x)$ for that linear density. Numerically inverting *this* function then yields our final aim, of a function that takes as input $f_{\text{meas}}(x)$ from our data and outputs a value of $n(x)$ for the linear density implied by the measured data and the model.

We perform the above computationally non-trivial calculation to extract modeled linear densities from our dimensionally-reduced mean absorbed fractions and interpolated saturation parameters for each set of experiment parameters.

The naïve and modeled linear densities agree at low densities but disagree by up to 20 percent at higher densities, with the naïve method underestimating linear densities compared to those obtained using the absorption model.

Appendix B. Yang–Yang thermodynamics

We use the Yang–Yang model [8] to describe our data. The exact diagonalization of the underlying Hamiltonian is carried out with the use of the thermodynamic Bethe ansatz (TBA) ($T > 0$ Bethe ansatz). From the TBA the following set of first-order integral equations can be derived

$$\epsilon(k) = \frac{\hbar^2 k^2}{2m} - \mu - \frac{k_B T}{2\pi} \int_{-\infty}^{\infty} \frac{2c}{c^2 + (k - q)^2} \ln(1 + e^{-\epsilon(q)/k_B T}) dq, \quad (\text{B.1})$$

$$2\pi f(k)(1 + e^{\epsilon(k)/k_B T}) = 1 + \int_{-\infty}^{\infty} \frac{2c}{c^2 + (k - q)^2} f(q) dq, \quad (\text{B.2})$$

$$n = \int_{-\infty}^{\infty} f(q) dq, \quad (\text{B.3})$$

where m is the mass, k_B is the Boltzmann constant, T is the temperature, μ the chemical potential, and $c = mg/\hbar^2$ is the interaction wavenumber. We use $g = 2\hbar\omega_{\perp}a_{3D}/(1 - Ca_{3D}/l_{\perp})$, where a_{3D} is the three-dimensional s -wave scattering length, C is a constant of order unity [35], and $l_{\perp} = \sqrt{\hbar/m\omega_{\perp}}$ is the oscillator length. Both k and q label momenta. The above equations can be solved recursively to compute n , the linear density, given the values for μ and T , the chemical potential and temperature.

We implement a numerical solver for the YY equations within the LDA that takes the parameters μ , T as its primary input and computes c and g by using the appropriate values of l_{\perp} , a_{3D} and m . We recursively solve for $\epsilon(k)$ and $f(k)$ from which we ultimately compute the density n . We transform all the momentum and energy quantities

$$\tilde{k} = k/\sqrt{2mk_B T/\hbar^2}, \quad (\text{B.4})$$

$$\tilde{E} = E/k_B T, \quad (\text{B.5})$$

so that the first two YY equations read

$$\tilde{\epsilon}(\tilde{k}) = \tilde{k}^2 - \tilde{\mu} - \int_{-\infty}^{\infty} \frac{1}{\pi} \frac{\tilde{c}}{\tilde{c}^2 + (\tilde{k} - \tilde{q})^2} \ln(1 + e^{-\tilde{\epsilon}(\tilde{q})}) d\tilde{q}, \quad (\text{B.6})$$

$$2\pi f(\tilde{k})(1 + e^{\tilde{\epsilon}(\tilde{k})}) = 1 + \int_{-\infty}^{\infty} \frac{1}{\pi} \frac{\tilde{c}}{\tilde{c}^2 + (\tilde{k} - \tilde{q})^2} f(\tilde{q}) d\tilde{q}. \quad (\text{B.7})$$

We denote the Lieb–Liniger kernel (a normalized Lorentzian) as $L(c, q)$. Our numerical solver performs a k -space convolution using the `scipy.signal.fftconvolve` method to evaluate the integrals. For this we use a $N_k = 1024$ points grid that covers the range $k = [-10 k_{\text{th}}, 10 k_{\text{th}}]$, where $k_{\text{th}} = \sqrt{2mk_B T/\hbar^2}$ is the thermal wavenumber. We have explicitly verified that for the parameters in our experiment using different grids give no changes to the predicted EoS. We initialize $\epsilon_0(k) = k^2 - \mu$ and iterate over the following recursive relation

$$\epsilon_{j+1}(k) = \epsilon_0(k) - L(c_0, q) \otimes \ln(1 + e^{-\epsilon_j(q)}), \quad (\text{B.8})$$

where \otimes denotes the Fourier convolution operator. Once the convergence condition $\sqrt{\sum_i (\epsilon_{i,j+1} - \epsilon_{i,j})^2}/N_k < \epsilon_{\text{tol}}$ is satisfied, we solve for $f(k)$ with an initial guess $f_0(k) = [2\pi(1 + e^{\epsilon(k)})]^{-1}$ and the recursive relation

$$f_{j+1}(k) = f_0(k) + L(c_0, q) \otimes f_j(q), \quad (\text{B.9})$$

from which we get to evaluate (B.3). After watching all the unit conversions we get the linear density in particles per meter.

References

- [1] Bloch I, Dalibard J and Zwinger W 2008 Many-body physics with ultracold gases *Rev. Mod. Phys.* **80** 885–964
- [2] Chin C, Grimm R, Julienne P and Tiesinga E 2010 Feshbach resonances in ultracold gases *Rev. Mod. Phys.* **82** 1225–86
- [3] Lahaye T, Menotti C, Santos L, Lewenstein M and Pfau T 2009 The physics of dipolar bosonic quantum gases *Rep. Prog. Phys.* **72** 126401
- [4] Paredes B, Widera A, Murg V, Mandel O, Fölling S, Cirac I, Shlyapnikov G V, Hansch T W and Bloch I 2004 Tonks–Girardeau gas of ultracold atoms in an optical lattice *Nature* **429** 277–81
- [5] Laburthe Tolra B, O’Hara K M, Huckans J H, Phillips W D, Rolston S L and Porto J V 2004 Observation of reduced three-body recombination in a correlated 1d degenerate Bose gas *Phys. Rev. Lett.* **92** 190401
- [6] Kinoshita T, Wenger T and Weiss D S 2004 Observation of a one-dimensional Tonks–Girardeau gas *Science* **305** 1125–8
- [7] Lieb E H and Liniger W 1963 Exact analysis of an interacting Bose gas: I. The general solution and the ground state *Phys. Rev.* **130** 1605–16
- [8] Yang C N and Yang C P 1969 Thermodynamics of a one-dimensional system of bosons with repulsive deltafunction interaction *J. Math. Phys.* **10** 1115–22
- [9] van Amerongen A H, van Es J J P, Wicke P, Kheruntsyan K V and van Druten N J 2008 Yang–Yang thermodynamics on an atom chip *Phys. Rev. Lett.* **100** 090402
- [10] Vogler A, Labouvie R, Stubenrauch F, Barontini G, Guarrera V and Ott H 2013 Thermodynamics of strongly correlated one-dimensional Bose gases *Phys. Rev. A* **88** 031603
- [11] Yang B, Chen Y-Y, Zheng Y-G, Sun H, Dai H-N, Guan X-W, Yuan Z-S and Pan J-W 2017 Quantum criticality and the Tomonaga–Luttinger liquid in one-dimensional Bose gases *Phys. Rev. Lett.* **119** 165701
- [12] Rauer B, Grišins P, Mazets I E, Schweigler T, Rohringer W, Geiger R, Langen T and Schmiedmayer J 2016 Cooling of a one-dimensional Bose gas *Phys. Rev. Lett.* **116** 030402
- [13] Bongs K, Burger S, Dettmer S, Hellweg D, Arlt J, Ertmer W and Sengstock K 2001 Waveguide for Bose–Einstein condensates *Phys. Rev. A* **63** 031602
- [14] Kheruntsyan K V, Gangardt D M, Drummond P D and Shlyapnikov G V 2005 Finite-temperature correlations and density profiles of an inhomogeneous interacting one-dimensional Bose gas *Phys. Rev. A* **71** 053615
- [15] Armijo J, Jacqmin T, Kheruntsyan K and Bouchoule I 2011 Mapping out the quasicondensate transition through the dimensional crossover from one to three dimensions *Phys. Rev. A* **83** 021605
- [16] Kohn W and Sham L J 1965 Self-consistent equations including exchange and correlation effects *Phys. Rev.* **140** A1133–8

- [17] Yefsah T, Desbuquois R, Chomaz L, Günter K J and Dalibard J 2011 Exploring the thermodynamics of a two-dimensional Bose gas *Phys. Rev. Lett.* **107** 130401
- [18] Ku M J H, Sommer A T, Cheuk L W and Zwierlein M W 2012 Revealing the superfluid lambda transition in the universal thermodynamics of a unitary Fermi gas *Science* **335** 563–7
- [19] Mukherjee B, Yan Z, Patel P B, Hadzibabic Z, Yefsah T, Struck J and Zwierlein M W 2017 Homogeneous atomic Fermi gases *Phys. Rev. Lett.* **118** 123401
- [20] Greiner M, Bloch I, Hänsch T W and Esslinger T 2001 Magnetic transport of trapped cold atoms over a large distance *Phys. Rev. A* **63** 031401
- [21] Lin Y-J, Perry A R, Compton R L, Spielman I B and Porto J V 2009 Rapid production of ^{87}Rb Bose–Einstein condensates in a combined magnetic and optical potential *Phys. Rev. A* **79** 063631
- [22] Starkey P T, Billington C J, Johnstone S P, Jasperse M, Helmerson K, Turner L D and Anderson R P 2013 A scripted control system for autonomous hardware-timed experiments *Rev. Sci. Instrum.* **84** 085111
- [23] Genkina D, Aycock L M, Stuhl B K, Lu H-I, Williams R A and Spielman I B 2016 Feshbach enhanced s-wave scattering of fermions: direct observation with optimized absorption imaging *New J. Phys.* **18** 013001
- [24] Ockeloen C F, Tauschinsky A F, Spreeuw R J C and Whitlock S 2010 Detection of small atom numbers through image processing *Phys. Rev. A* **82** 061606
- [25] Li X, Ke M, Yan B and Wang Y 2007 Reduction of interference fringes in absorption imaging of cold atom cloud using eigenface method *Chin. Opt. Lett.* **5** 128–30
- [26] Hueck K, Luick N, Sobirey L, Siegl J, Lompe T, Moritz H, Clark L W and Chin C 2017 Calibrating high intensity absorption imaging of ultracold atoms *Opt. Express* **25** 8670–9
- [27] Reinaudi G, Lahaye T, Wang Z and Guéry-Odelin D 2007 Strong saturation absorption imaging of dense clouds of ultracold atoms *Opt. Lett.* **32** 3143–5
- [28] Burt E A, Ghrist R W, Myatt C J, Holland M J, Cornell E A and Wieman C E 1997 Coherence, correlations, and collisions: what one learns about Bose–Einstein condensates from their decay *Phys. Rev. Lett.* **79** 337–40
- [29] Fedichev P O, Reynolds M W and Shlyapnikov G V 1996 Three-body recombination of ultracold atoms to a weakly bound s level *Phys. Rev. Lett.* **77** 2921–4
- [30] Yang L, Guan L and Pu H 2015 Strongly interacting quantum gases in one-dimensional traps *Phys. Rev. A* **91** 043634
- [31] Yang L and Pu H 2016 Bose–Fermi mapping and a multibranch spin-chain model for strongly interacting quantum gases in one dimension: dynamics and collective excitations *Phys. Rev. A* **94** 033614
- [32] Cole W S, Lee J, Mahmud K W, Alavirad Y, Spielman I B and Sau J D 2017 Spin–orbit coupled bosons in one dimension: emergent gauge field and Lifshitz transition arXiv:1711.05794
- [33] Cadima J and Jolliffe I T 2009 On relationships between uncentred and column-centred principal component analysis *Pak. J. Stat.* **25** 473–503
- [34] Striebel M, Wrachtrup J and Gerhardt I 2017 Absorption and extinction cross sections and photon streamlines in the optical near-field *Sci. Rep.* **7** 15420
- [35] Dunjko V, Lorent V and Olshanii M 2001 Bosons in cigar-shaped traps: Thomas–Fermi regime, Tonks–Girardeau regime, and in between *Phys. Rev. Lett.* **86** 5413–6

Appendix G: Spatial Coherence of Spin-Orbit-Coupled Bose Gases

Spatial Coherence of Spin-Orbit-Coupled Bose Gases

Andika Putra,¹ F. Salces-Cárcoba¹, Yuchen Yue¹, Seiji Sugawa^{2,3} and I. B. Spielman¹

¹*Joint Quantum Institute, National Institute of Standards and Technology, and University of Maryland, Gaithersburg, Maryland 20899, USA*

²*PRESTO, Japan Science and Technology, Tokyo 102-0076, Japan*

³*Graduate School of Science, Kyoto University, Kyoto 606-8502, Japan*

 (Received 15 October 2019; accepted 7 January 2020; published 6 February 2020)

Spin-orbit-coupled Bose-Einstein condensates (SOBECs) exhibit two new phases of matter, now known as the stripe and plane-wave phases. When two interacting spin components of a SOBEC spatially overlap, density modulations with periodicity given by the spin-orbit coupling strength appear. In equilibrium, these components fully overlap in the miscible stripe phase and overlap only in a domain wall in the immiscible plane-wave phase. Here we probe the density modulation present in any overlapping region with optical Bragg scattering and observe the sudden drop of Bragg scattering as the overlapping region shrinks. Using an atomic analog of the Talbot effect, we demonstrate the existence of long-range coherence between the different spin components in the stripe phase and surprisingly even in the phase-separated plane-wave phase.

DOI: [10.1103/PhysRevLett.124.053605](https://doi.org/10.1103/PhysRevLett.124.053605)

Systems with coexisting order parameters, such as ferromagnetic superconductors [1], supersolids [2], or topological Kondo insulators [3], exhibit rich phases with novel phenomena. Spin-orbit-coupled Bose-Einstein condensates (SOBECs) have a complex phase diagram including both “stripe” and “plane-wave” phases. The stripe phase is expected to have coexisting order parameters [4–6] with supersolidlike properties [7] marked by long-range phase coherence and periodic density modulations (confirmed by optical Bragg scattering [8]) simultaneously present. In contrast, the plane-wave phase behaves like a ferromagnetic spinor Bose-Einstein condensate (BEC), where its true many-body ground state is predicted to be massively entangled with application to precision magnetometry [9,10]. In both the stripe and plane-wave phases, we readout a matter wave Talbot interferometer with optical Bragg scattering to detect coexisting periodic density modulations (long-range diagonal order) and system-wide phase coherence (long-range off-diagonal order). Unexpectedly, both phases exhibit both types of order.

Figure 1(a) schematically depicts the stripe and plane-wave phases of SOBECs, showing two salient features [5,6,11]: (1) system-wide periodic density modulations are associated with fully coexisting spin components in the stripe phase, and (2) highly localized density modulations

are present at a domain-wall delineating phase-separated spin components in the plane-wave phase. Initial experiments with Raman coupled ⁸⁷Rb Bose-Einstein condensates (BECs) identified these phases in terms of the degree of spatial overlap of the two spin components [5], but not the microscopic density modulations. Direct observation of these modulations in ⁸⁷Rb BECs is challenging both because the ≈ 400 nm modulation period is below the resolution of even the best quantum gas microscope [12] and the modulation contrast is small. Here we probe these modulations in long-lived equilibrium systems in both the stripe and plane-wave phases.

Our Letter is organized as follows: (i) we introduce the physics of SOBECs, (ii) we describe our experimental setup, (iii) we cross-check our Bragg measurements with established techniques, (iv) we demonstrate the coexistence of diagonal and off-diagonal order in the same system, and (v) we discuss the implications of these measurements on the issues of supersolidity in stripe-phase SOBECs.

SOBECs with Raman coupling.—We realized SOBECs described by the single-particle Hamiltonian

$$\hat{H}_0 = \frac{\hbar^2}{2m} [(q_x - k_R \hat{\sigma}_z)^2 + k_{\perp}^2] + \frac{\delta}{2} \hat{\sigma}_z + \frac{\Omega}{2} \hat{\sigma}_x \quad (1)$$

for particles of mass m . Here, δ and Ω describe Zeeman shifts from longitudinal and transverse fields, respectively, and the spin-orbit coupling (SOC) strength k_R defines the relevant energy scale $E_R = \hbar^2 k_R^2 / 2m$. $\hbar q_x$ is the quasi-momentum along \mathbf{e}_x , $\hbar k_{\perp}$ is the linear momentum in the $\mathbf{e}_y - \mathbf{e}_z$ plane, and $\hat{\sigma}_{x,y,z}$ are Pauli operators. The insets in Fig. 1(a) show the characteristic double-well dispersion

Published by the American Physical Society under the terms of the [Creative Commons Attribution 4.0 International license](https://creativecommons.org/licenses/by/4.0/). Further distribution of this work must maintain attribution to the author(s) and the published article's title, journal citation, and DOI.

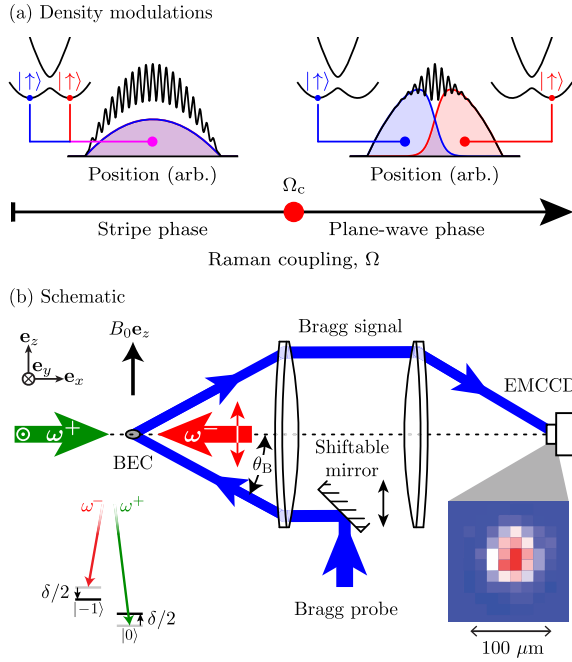


FIG. 1. Experimental concept and setup. (a) Schematic description of small- δ phase diagram with equal spin populations showing the stripe and plane-wave phases. The spatial distribution of the two spin-orbit-coupled spin states is marked in red and blue for $|\uparrow\rangle$ and $|\downarrow\rangle$, respectively, while the total density is in black. The insets depict the dispersion of these states. (b) Laser configuration for realizing SOC system with two-photon Raman transition and detecting scattered Bragg signal from the stripe phase. We choose a bias magnetic field $B_0 \approx 20$ G. The inset shows an example of diffracted Bragg signal as imaged by an EMCCD camera.

associated with SOC, with minima separated by approximately $2k_R$, and energy gap equal to Ω . In our experiments, we use two-photon Raman transitions to introduce the SOC term: the Raman laser wavelength determines the SOC strength $k_R = 2\pi/\lambda_R$; the Raman laser intensities determine Ω ; and the laser frequency differences imbue detuning δ to the SOC system [5,6].

We describe the two spin-components of our system by the spinor wave function $(\psi_\uparrow, \psi_\downarrow)^T$, where the mean-field interaction energy density is

$$\begin{aligned} \varepsilon = & \left[\frac{c_0}{2} + \frac{c_2}{4} \right] [|\psi_\uparrow|^2 + |\psi_\downarrow|^2]^2 - \frac{c_2}{4} [|\psi_\uparrow|^4 \\ & - |\psi_\downarrow|^4] + \frac{c_2}{2} |\psi_\uparrow \psi_\downarrow|^2. \end{aligned}$$

Here c_0 and c_2 describe the inter- and intraspin interaction parameters, respectively, and \bar{n} is the mean density. For dilute Bose gases (with chemical potential $\mu \ll E_R$), the impact of interactions can be parametrized in terms of a

scaled recoil energy $E'_R = E_R + \mu/4$; in this case, the spin mixed, stable ground-state stripe phase, exists in a very narrow range of parameters [5]: with δ between 0 and $c_2\bar{n}/2$; and $|\Omega| < \Omega_c$, with the critical coupling strength $\Omega_c = 4E'_R\sqrt{-2c_2/c_0}$. As depicted in Fig. 1(a) (left), the stripe-phase density

$$\frac{n(x)}{\bar{n}} = 1 + \frac{\Omega}{4E'_R} \cos[k(\Omega)x + \phi]$$

is modulated with wave vector

$$\frac{k(\Omega)}{2k_R} = \left[1 - \left(\frac{\Omega}{4E'_R} \right)^2 \right]^{1/2}. \quad (2)$$

The phase ϕ describing the stripe's location [6,13] results from the preexisting phase difference between the two spin components along with the relative phase between the Raman laser beams. On the contrary, for the plane-wave phase ($|\Omega| > \Omega_c$) shown in Fig. 1(a) (right), density modulations are expected only within the domain wall separating the now polarized spin components.

Experimental setup.—We produced $N = 2.2(3) \times 10^5$ condensed ^{87}Rb atoms in a harmonic trap with frequencies $(f_x, f_y, f_z) = [(105, 67, 40)]$ Hz and chemical potential $\mu = [h \times 1.46(20)]$ kHz. Two Raman lasers, counter-propagating along \mathbf{e}_x , coupled the $|\downarrow\rangle \equiv |f=1, m_F=-1\rangle$ and $|\uparrow\rangle \equiv |f=1, m_F=0\rangle$ hyperfine levels of ^{87}Rb $5S_{1/2}$ electronic ground states. We used the tune-out wavelength [14] $\lambda_R = 790.034(7)$ nm for our Raman lasers which defined the single-photon recoil energy $E_R = h \times 3.678$ kHz and the scaled recoil energy $E'_R/E_R = 1.10(2)$ governing the stripe-phase physics.

We used optical Bragg scattering [15–17] to detect periodic density modulations. The Bragg probe laser, with wavelength $\lambda_B = 780.24$ nm, was ≈ 6.3 GHz red detuned from the $f=1 \rightarrow f'=0, 1, 2$ transition within the D_2 line [18]. This put the Bragg probe beam in the far-detuned limit with respect to the ≈ 6 MHz transition linewidth, the ≈ 10 MHz Zeeman shifts, and the ≈ 300 MHz excited state hyperfine structure. In this limit, the atomic susceptibility is almost entirely real and state independent. Figure 1(a) shows our experimental setup, with atoms located at the focus of a Keplerian imaging system aligned along \mathbf{e}_x . The Raman lasers propagated along \mathbf{e}_x and the Bragg probe had an incident angle θ_B with respect to the optical axes. A shiftable mirror in the back focal plane tuned θ_B from 80 to 280 mrad, allowing the detection of Bragg scattering from structures with period from about 391 to 405 nm; we used $\theta_B \approx 0.15$ rad in these experiments [19]. In ^{87}Rb , the interaction constants [24] are $(c_0, c_2) = (779, -3.61) \times 10^{-14}$ Hz cm³, so the stable ground-state stripe phase was present for $\Omega \lesssim 0.21E_R$ and $-3.3 \text{ Hz} < \delta/h < 0$ Hz.

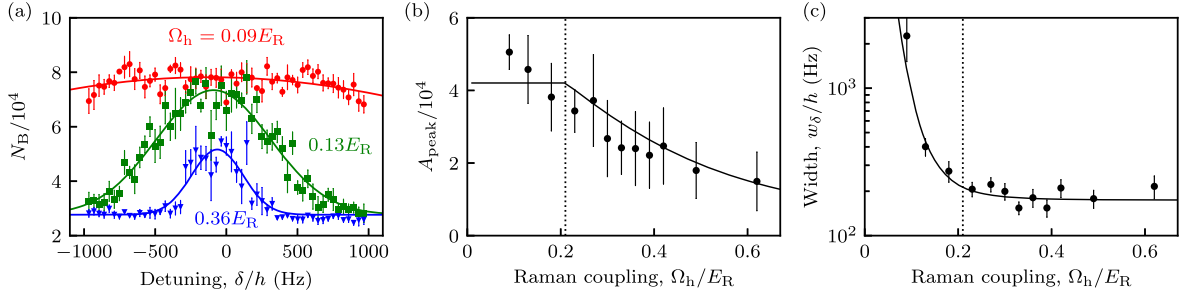


FIG. 2. Bragg-scattering as a function of Ω_h and δ . (a) $N_B(\delta)$ from a $t_B = 100 \mu\text{s}$ pulse for various coupling strengths Ω_h ; each data point is an average of more than four realizations. The solid curves depict Gaussian fits to the data from which the peak amplitude A_{peak} and width w_δ in (b) and (c) are derived. The increased background level as compared to Fig. 1 is from an increased overall atom number. In (b) and (c), the vertical dotted line marks the critical coupling strength at $\Omega_c = 0.21 E_R$, showing that the Bragg amplitude lacks a sharp feature at Ω_c , while the width drops rapidly leading up to Ω_c .

The Bragg diffracted signal, as shown in the inset of Fig. 1(b), was detected with an electron-multiplying charge-coupled device (EMCCD) camera. As described in Ref. [19], we first calibrated our Bragg signal using an optical lattice and found that the signal-to-noise ratio of one occurred for a fractional density modulation of $\eta = 0.06$, providing practical detection threshold.

We prepared our SOBECS from an initial BEC with equal superposition of spin $|\uparrow\rangle$ and $|\downarrow\rangle$ at a desired detuning δ and linearly increased Ω from 0 to Ω_h in 50 ms. We then allowed the system to equilibrate for a hold time t_h . At the transition from stripe to plane-wave phase at $\Omega_c \approx 0.21 E_R$, the expected density modulation contrast is just $\eta = 0.045$, just below our detection threshold. Inspired by Ref. [25], we rapidly ramped Ω to $\approx 7 E_R$ in 200 μs just prior to our Bragg measurement, increasing η to ≈ 0.85 (see Ref. [19]). This rapid ramp was slow compared to the $\approx 4 E_R$ energy spacing between the two branches of the SOC dispersion, but fast compared to the much slower many-body dynamics. In this system, the shortest many-body timescale is the $\gtrsim 2.5$ ms quarter period of our harmonic trap, followed by the ≈ 50 ms timescale for any significant evolution of spin structure [5,19]. As a result, this process simply magnified the amplitude of the SOC driven stripes wherever they were present in the system. We then turned the Raman lasers off and pulsed the Bragg laser with duration t_B ranging from 20 to 100 μs .

Validation of method.—We began by demonstrating our ability to maintain balanced spin mixtures very near $\delta = 0$ in the process of cross-checking our Bragg measurements against earlier time-of-flight experiments [5]. We characterized the transition from the stripe to plane-wave phase as a function of Raman coupling Ω_h and detuning δ . Figure 2(a) shows the number of photoelectrons N_B in our detection region as a function of δ at different values of Ω_h for a fixed hold time $t_h = 1$ s. We observe Bragg scattering in a narrow detuning window that decreases in width and amplitude as Ω_h increases.

Figure 2(b) quantifies the amplitude in terms of the peak height A_{peak} obtained from Gaussian fits to $N_B(\delta)$. We might expect the Bragg scattering amplitude to be constant in the stripe phase $\Omega_h < \Omega_c$ where the spin components mix and then to vanish in the plane-wave phase when the gas becomes locally polarized. However, even when different plane-wave regions phase separate, density modulations are present in the domain wall separating the different phases, allowing some Bragg scattering. The spin healing length $\xi_s/\xi = \sqrt{c_0/[-c_2(\Omega_h^2/\Omega_c^2 - 1)]}$ in terms of the conventional healing length $\xi = \hbar/\sqrt{2m\mu}$. ξ_s sets the domain wall size [5] and diverges at Ω_c . Figure 2(b) shows $A_{\text{peak}}(\Omega_h)$ rapidly falling with increasing coupling strength, consistent with the expected trend. The solid curve is a fit to our scattering model (derived from the above reasoning and developed in Ref. [19]) with the overall Bragg signal as the only free parameter. This model shows only qualitative agreement with data, a point we will return to shortly.

Figure 2(c) plots the Gaussian width w_δ . Even for $\Omega_h < \Omega_c$, a small detuning $\delta \neq 0$ that breaks the degeneracy of the two spin states can cause the initially spatially mixed states to relax into a polarized gas in the lower energy spin state: a plane-wave phase with no Bragg scattering. When $\Omega_h = 0$, there are no spin-changing processes, and the spatially mixed state is stable indefinitely, independent of δ . The width is thus large for small Ω_h (slower spin relaxation) and decreases as Ω_h increases (faster spin relaxation). The width has no marked feature at Ω_c and is well fit by a power law [5], here $a(\Omega_h/E_R)^{-4} + w_\infty$. This indicates that the process by which the spin population polarizes in the presence of detuning is dependent on the Raman coupling strength, but not the initial zero-detuning phase.

In all cases, the detuning window is far wider than the 3.3 Hz range of detuning where the stripe phase is thermodynamically stable. This is as expected: the timescale for the spin populations to reach the expected equilibrium population can be in excess of several seconds

for small detunings (see Refs. [5,19] for a discussion of the equilibration timescale). In what follows, we focus on near-zero detunings that lie within this metastable region and where the physics is governed by Ω_h alone.

Spatial coherence.—Finally, we present our main observation demonstrating the spatial coherence of the SOBECs. Here we altered our measurement procedure to include a free evolution time t_{rev} following the turn-off of the Raman lasers but prior to the Bragg pulse. During this time, the different spin and momentum components that comprised the Raman dressed states underwent free evolution creating a matter-wave Talbot interferometer [17,26,27]. A coherent matter wave with wave vector k_R exhibits a coherence revival after a time period of $T_{\text{rev}} = h/8E_R = 34.0 \mu\text{s}$, during which time momentum components traveling with velocity $\pm 2\hbar k_R/m$ separated by a distance λ_R . Figure 3(a) schematically depicts this behavior: the left panel shows modulations in total density (black) and in each spin component (red and blue) at $t = 0$; the center panel shows that after $T_{\text{rev}}/2$ the modulation pattern in each spin component moved $\pm 1/4$ of the overall modulation period, yielding a flat density profile. The right panel shows the long-time behavior in which the spin components moved a distance comparable to the overall system size.

The periodic revivals in Fig. 3(b) occurred very near the $34 \mu\text{s}$ free-particle Talbot time, only about one-third of our earlier $100 \mu\text{s}$ Bragg pulse time. This indicates that all of our previous measurements inadvertently integrated over about three periods of collapse and revival. To resolve the Talbot signal, we largely mitigated this effect by reducing the pulse time to $t_B = 20 \mu\text{s}$ and averaging over at least four experimental realizations to account for the reduced signal present in each measurement.

Figure 3(c) shows N_B as a function of t_{rev} for a range of Ω_h , each constituting a single horizontal cut through Fig. 3(b). In Fig. 3(c), we observe damped oscillatory behavior that provides a lower bound to the coherence length of the system (other physical effects [17] may also cause the decay of $N_B(t_{\text{rev}})$). Our observations are complicated by the $20 \mu\text{s}$ Bragg pulse which is not short compared to the revival time. We modeled the integrated Bragg signal as a sinusoid with Gaussian decay [28] convolved with our Bragg pulse to obtain

$$N_B(t) = A_{\text{rev}} \int_t^{t+t_B} \frac{dt'}{t_B} \cos^2\left(\frac{\pi t'}{T_{\text{rev}}}\right) e^{-(t'/t_d)^2} + c, \quad (3)$$

as displayed by the solid curves in Fig. 3(c). Here $t_B = 20 \mu\text{s}$ is the Bragg pulse duration and the fitting parameters are revival amplitude A_{rev} , revival period T_{rev} , decay time t_d , and constant c .

Figures 3(d) and 3(e) show the revival amplitude A_{rev} and period T_{rev} as a function of coupling strength Ω_h . The amplitude A_{rev} gradually decreases above $\Omega_h > 0.21E_R$, which we attribute to the onset of phase separation and

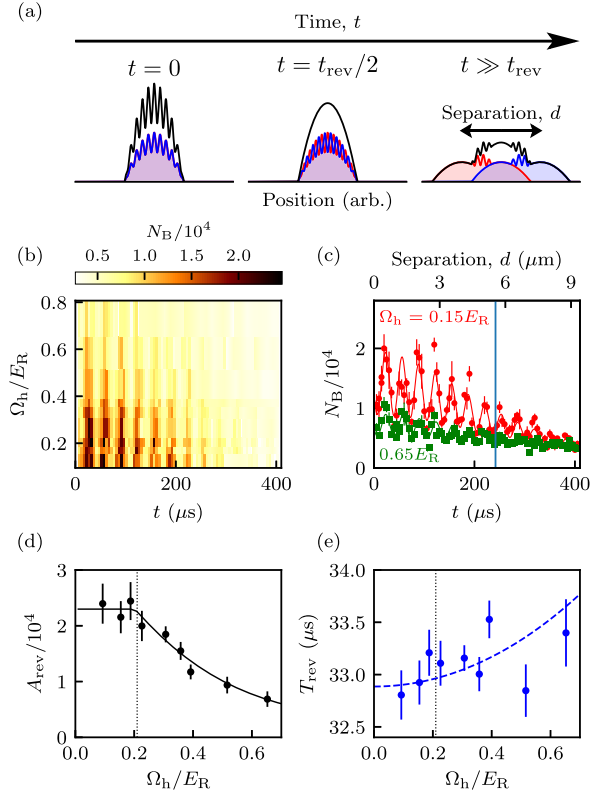


FIG. 3. Periodic revival of Bragg signal at $\delta = 0$ Hz. (a) Schematic representation of evolution of stripes during free evolution. The black, red, and blue curves depict total density, spin-up density, and spin-down density, respectively. (b) Observed Bragg counts N_B from a $t_B = 20 \mu\text{s}$ pulse as functions of (Ω_h, t) . (c) $N_B(t)$ for various coupling strength Ω_h , showing revivals characteristic of an atomic Talbot effect. The solid curves are joint fits of the model described in the text with shared parameters: decay time $t_d = 250 \mu\text{s}$ and background level $c = 3487$ counts. The vertical blue line depicts the separation equal to the calculated Thomas-Fermi radius. (d), (e) depict the amplitude A_{rev} and period T_{rev} obtained from fits to the data in (b). The vertical dotted lines show the predicted transition strength at Ω_c . The dashed blue curve indicates prediction for $T_{\text{rev}}(\Omega)$ shifted down by $1.1 \mu\text{s}$.

subsequent increasing separation between the two plane-wave components. The solid curve depicts the fit to the scattering model described in Ref. [19] with the overall scattering strength as the only free parameter, showing near perfect agreement with experiment. Allowing Ω_c to vary in the scattering model produces a value $\Omega_c = 0.20(1)$, also in agreement with our expectations. Figure 3(e) shows revival periods close to $T_{\text{rev}} = 33 \mu\text{s}$, just below the naive single-particle prediction. Our model in Eq. (2) predicts an increase in T_{rev} for larger Ω_h as the stripe wave vector $k(\Omega)$ falls. This increasing trend is plotted by the blue dashed curve; both this model and the null hypothesis are

consistent with the data. In addition, the energy scale E'_R in Eq. (2) was derived from a variational study of the stripe phase [13]; a similar energy scale—potentially different from E'_R —will be required within the domain wall and a proper variational study would be required to identify its exact value.

Last, the decay time $t_d = 250 \mu\text{s}$ was independent of Ω_n , indicating that the transition from the stripe phase to the plane-wave phase was not associated with any decrease in spatial coherence. During this $250 \mu\text{s}$, the interfering momentum are states separated by $5.8 \mu\text{m}$, comparable to the $R_{\text{TF}} = 5.5 \mu\text{m}$ Thomas-Fermi radius [shown by the vertical line in Fig. 3(c)]. We conclude that the system was fully coherent even in the phase-separated plane-wave phase.

Implications for supersolidity.—As has now been observed with dipolar atoms [29], a traditional supersolid is a phase of matter with two broken symmetries [30]: the broken gauge symmetry of a BEC (giving a superfluid phonon mode) and the broken translation symmetry of a lattice (giving a separate lattice-phonon mode). On one hand, we confirmed that diagonal order is present [8] and demonstrated that this coexists with off-diagonal order: a supersolid? On the other hand, a BEC in a shallow optical lattice has off-diagonal order, with density modulations (diagonal order) simply imprinted by the lattice potential [31]: not a supersolid.

With the Raman lasers off, our system is a two-component spinor BEC with two broken symmetries giving an overall phase (giving a superfluid phonon mode) and a relative phase between the spin components (giving a spin-wave mode); translational symmetry is unbroken: not a supersolid. Adding Raman coupling continuously connects this spinor phase to the stripe phase. For infinitesimal coupling, the modulation period [from Eq. (2)] is externally imposed by the Raman lasers, with a small shift that grows quadratically with Raman coupling. The spatial phase is set both by the relative phase between the Raman lasers and the preexisting relative phase between spin components. Similar to the lattice case, no new symmetries are broken and no new collective modes are created: not a supersolid? Although no new symmetries are broken, the spin-wave mode acquires an inertial contribution from the periodic density modulations inducing a gap at the edge of the associated Brillouin zone, as would be expected of a supersolid's lattice-phonon mode [7]. We conclude that this system shares some properties with conventional supersolids, but is best given its own name: the superstripe phase, as suggested in Ref. [7]. This is similar to the supersmectics proposed in Ref. [32] in which the mode structure of an optical cavity provides the substrate on which smectic correlations develop. The lattice-phonon mode remains undetected, and its observation would be a true smoking gun for observation of superstripes.

This work was partially supported by the Army Research Office's atomtronics Multidisciplinary University Research Initiative (MURI), the Air Force Office of Scientific Research's Quantum Matter MURI, the National Institute of Standards and Technology, and the National Science Foundation through the Physics Frontier Center at the Joint Quantum Institute (Award No. 1430094). We are grateful for the very thoughtful and detailed eleventh hour reading of our manuscript by Qiyu Liang and Alina Pineiro. We appreciate the temperature calibrations performed by Peter Zhou.

-
- [1] B. T. Matthias, H. Suhl, and E. Corenzwit, *Phys. Rev. Lett.* **1**, 449 (1958).
 - [2] Y. Pomeau and S. Rica, *Phys. Rev. Lett.* **72**, 2426 (1994).
 - [3] M. Dzero, K. Sun, V. Galitski, and P. Coleman, *Phys. Rev. Lett.* **104**, 106408 (2010).
 - [4] T. D. Stanescu and V. Galitski, *Phys. Rev. B* **75**, 125307 (2007).
 - [5] Y. J. Lin, K. Jimenez-Garcia, and I. B. Spielman, *Nature (London)* **471**, 83 (2011).
 - [6] T.-L. Ho and S. Zhang, *Phys. Rev. Lett.* **107**, 150403 (2011).
 - [7] Y. Li, G. I. Martone, L. P. Pitaevskii, and S. Stringari, *Phys. Rev. Lett.* **110**, 235302 (2013).
 - [8] J.-R. Li, J. Lee, W. Huang, S. Burchesky, B. Shteynas, F. c. Top, A. O. Jamison, and W. Ketterle, *Nature (London)* **543**, 91 (2017).
 - [9] J. Higbie and D. M. Stamper-Kurn, *Phys. Rev. A* **69**, 053605 (2004).
 - [10] T. D. Stanescu, B. Anderson, and V. Galitski, *Phys. Rev. A* **78**, 023616 (2008).
 - [11] C. Wang, C. Gao, C.-M. Jian, and H. Zhai, *Phys. Rev. Lett.* **105**, 160403 (2010).
 - [12] W. S. Bakr, J. I. Gillen, A. Peng, S. Fölling, and M. Greiner, *Nature (London)* **462**, 74 (2009).
 - [13] Y. Li, L. P. Pitaevskii, and S. Stringari, *Phys. Rev. Lett.* **108**, 225301 (2012).
 - [14] B. Arora, M. S. Safronova, and C. W. Clark, *Phys. Rev. A* **84**, 043401 (2011).
 - [15] M. Weidemüller, A. Hemmerich, A. Görlitz, T. Esslinger, and T. W. Hänsch, *Phys. Rev. Lett.* **75**, 4583 (1995).
 - [16] G. Birkel, M. Gatzke, I. H. Deutsch, S. L. Rolston, and W. D. Phillips, *Phys. Rev. Lett.* **75**, 2823 (1995).
 - [17] H. Miyake, G. A. Siviloglou, G. Puentes, D. E. Pritchard, W. Ketterle, and D. M. Weld, *Phys. Rev. Lett.* **107**, 175302 (2011).
 - [18] C. A. Müller, C. Miniatura, D. Wilkowski, R. Kaiser, and D. Delande, *Phys. Rev. A* **72**, 053405 (2005).
 - [19] See Supplemental Material at <http://link.aps.org/supplemental/10.1103/PhysRevLett.124.053605> for additional details, which includes Refs. [20–23].
 - [20] D. McKay and B. DeMarco, *New J. Phys.* **12**, 055013 (2010).
 - [21] N. Marzari, A. A. Mostofi, J. R. Yates, I. Souza, and D. Vanderbilt, *Rev. Mod. Phys.* **84**, 1419 (2012).

- [22] B. Gadway, D. Pertot, R. Reimann, M. G. Cohen, and D. Schneble, *Opt. Express* **17**, 19173 (2009).
- [23] W. Bao, D. Jaksch, and P. A. Markowich, *J. Comput. Phys.* **187**, 318 (2003).
- [24] A. Widera, F. Gerbier, S. Fölling, T. Gericke, O. Mandel, and I. Bloch, *New J. Phys.* **8**, 152 (2006).
- [25] R. A. Hart, P. M. Duarte, T.-L. Yang, X. Liu, T. Paiva, E. Khatami, R. T. Scalettar, N. Trivedi, D. A. Huse, and R. G. Hulet, *Nature (London)* **519**, 211 (2015).
- [26] H. F. Talbot Esq. F. R. S., *Philos. Mag. J. Sci.* **9**, 401 (1836).
- [27] B. Santra, C. Baals, R. Labouvie, A. B. Bhattacharjee, A. Pelster, and H. Ott, *Nat. Commun.* **8**, 15601 (2017).
- [28] We also considered exponential decay, but the overall χ^2 was increased by a factor of 4.
- [29] G. Natale, R. M. W. van Bijnen, A. Patscheider, D. Petter, M. J. Mark, L. Chomaz, and F. Ferlaino, *Phys. Rev. Lett.* **123**, 050402 (2019).
- [30] M. Boninsegni and N. V. Prokof'ev, *Rev. Mod. Phys.* **84**, 759 (2012).
- [31] M. Greiner, O. Mandel, T. Esslinger, T. W. Hansch, and I. Bloch, *Nature (London)* **415**, 39 (2002).
- [32] S. Gopalakrishnan, B. L. Lev, and P. M. Goldbart, *Phys. Rev. A* **82**, 043612 (2010).

Bibliography

- [1] Herbert Goldstein, Charles Poole, and John Safko. *Classical mechanics*, 2002.
- [2] Jon M Leinaas and Jan Myrheim. On the theory of identical particles. *Il Nuovo Cimento B (1971-1996)*, 37(1):1–23, 1977.
- [3] Markus Fierz. Über die relativistische theorie kräftefreier teilchen mit beliebigem spin. *Helvetica Physica Acta*, 12:3–37, 1939.
- [4] Wolfgang Pauli. The connection between spin and statistics. *Physical Review*, 58(8):716, 1940.
- [5] Richard P Feynman, Robert B Leighton, and Matthew Sands. *The Feynman lectures on physics, Vol. I: The new millennium edition: mainly mechanics, radiation, and heat*, volume 1. Basic books, 2011.
- [6] N. N. Bogolyubov. On the theory of superfluidity. *J. Phys.(USSR)*, 11:23–32, 1947. [Izv. Akad. Nauk Ser. Fiz.11,77(1947)].
- [7] Eugene P Gross. Structure of a quantized vortex in boson systems. *Il Nuovo Cimento (1955-1965)*, 20(3):454–477, 1961.
- [8] Lev P Pitaevskii. Vortex lines in an imperfect bose gas. *Sov. Phys. JETP*, 13(2):451–454, 1961.
- [9] Yuki Kawaguchi and Masahito Ueda. Spinor bose–einstein condensates. *Physics Reports*, 520(5):253–381, 2012.
- [10] Mike H Anderson, Jason R Ensher, Michael R Matthews, Carl E Wieman, and Eric A Cornell. Observation of bose-einstein condensation in a dilute atomic vapor. *science*, pages 198–201, 1995.
- [11] Kendall B Davis, M-O Mewes, Michael R Andrews, Nicolaas J van Druten, Dallin S Durfee, DM Kurn, and Wolfgang Ketterle. Bose-einstein condensation in a gas of sodium atoms. *Physical review letters*, 75(22):3969, 1995.

- [12] William D Phillips. Nobel lecture: Laser cooling and trapping of neutral atoms. *Reviews of Modern Physics*, 70(3):721, 1998.
- [13] Daniel A Steck. Rubidium 87 d line data, 2001.
- [14] S Bize, Y Sortais, MS Santos, C Mandache, A Clairon, and C Salomon. High-accuracy measurement of the 87rb ground-state hyperfine splitting in an atomic fountain. *EPL (Europhysics Letters)*, 45(5):558, 1999.
- [15] Jun Ye, Steve Swartz, Peter Jungner, and John L Hall. Hyperfine structure and absolute frequency of the 87 rb 5p 3/2 state. *Optics letters*, 21(16):1280–1282, 1996.
- [16] GP Barwood, P Gill, and WRC Rowley. Frequency measurements on optically narrowed rb-stabilised laser diodes at 780 nm and 795 nm. *Applied Physics B*, 53(3):142–147, 1991.
- [17] Gregory Breit and II Rabi. Measurement of nuclear spin. *Physical Review*, 38(11):2082, 1931.
- [18] Marlan O Scully and M Suhail Zubairy. Quantum optics, 1999.
- [19] Harold J Metcalf and Peter Van der Straten. Laser cooling and trapping of neutral atoms. *The Optics Encyclopedia: Basic Foundations and Practical Applications*, 2007.
- [20] F Salces-Carcoba, CJ Billington, A Putra, Y Yue, S Sugawa, and IB Spielman. Equations of state from individual one-dimensional bose gases. *New Journal of Physics*, 20(11):113032, 2018.
- [21] Paul D Lett, William D Phillips, SL Rolston, Carol E Tanner, RN Watts, and CI Westbrook. Optical molasses. *JOSA B*, 6(11):2084–2107, 1989.
- [22] P Jeffery Ungar, David S Weiss, Erling Riis, and Steven Chu. Optical molasses and multilevel atoms: theory. *JOSA B*, 6(11):2058–2071, 1989.
- [23] David S Weiss, Erling Riis, Yaakov Shevy, P Jeffrey Ungar, and Steven Chu. Optical molasses and multilevel atoms: experiment. *JOSA B*, 6(11):2072–2083, 1989.
- [24] William Sutherland. Lxxv. a dynamical theory of diffusion for non-electrolytes and the molecular mass of albumin. *The London, Edinburgh, and Dublin Philosophical Magazine and Journal of Science*, 9(54):781–785, 1905.
- [25] Albert Einstein. Über die von der molekularkinetischen theorie der wärme geforderte bewegung von in ruhenden flüssigkeiten suspendierten teilchen. *Annalen der physik*, 322(8):549–560, 1905.
- [26] Marian Von Smoluchowski. Zur kinetischen theorie der brownschen molekularebewegung und der suspensionen. *Annalen der physik*, 326(14):756–780, 1906.

- [27] Paul D Lett, Richard N Watts, Christoph I Westbrook, William D Phillips, Phillip L Gould, and Harold J Metcalf. Observation of atoms laser cooled below the doppler limit. *Physical review letters*, 61(2):169, 1988.
- [28] Jean Dalibard and Claude Cohen-Tannoudji. Laser cooling below the doppler limit by polarization gradients: simple theoretical models. *JOSA B*, 6(11):2023–2045, 1989.
- [29] EL Raab, M Prentiss, Alex Cable, Steven Chu, and David E Pritchard. Trapping of neutral sodium atoms with radiation pressure. *Physical Review Letters*, 59(23):2631, 1987.
- [30] Wolfgang Ketterle, NJ Van Druten, et al. Evaporative cooling of trapped atoms. *Adv. At. Mol. Opt. Phys.*, 37(0):181, 1996.
- [31] A Aspect, Ennio Arimondo, R e al Kaiser, N Vansteenkiste, and C Cohen-Tannoudji. Laser cooling below the one-photon recoil energy by velocity-selective coherent population trapping. *Physical Review Letters*, 61(7):826, 1988.
- [32] Rudolf Grimm, Matthias Weidemüller, and Yurii B Ovchinnikov. Optical dipole traps for neutral atoms. *arXiv preprint physics/9902072*, 1999.
- [33] Charles S Adams, Heun Jin Lee, Nir Davidson, Mark Kasevich, and Steven Chu. Evaporative cooling in a crossed dipole trap. *Physical review letters*, 74(18):3577, 1995.
- [34] HJ Lee, CS Adams, M Kasevich, and S Chu. Raman cooling of atoms in an optical dipole trap. *Physical review letters*, 76(15):2658, 1996.
- [35] Y-J Lin, K Jiménez-García, and Ian B Spielman. Spin–orbit-coupled bose–einstein condensates. *Nature*, 471(7336):83–86, 2011.
- [36] Victor Galitski and Ian B Spielman. Spin–orbit coupling in quantum gases. *Nature*, 494(7435):49–54, 2013.
- [37] Yuichiro K Kato, Roberto C Myers, Arthur C Gossard, and David D Awschalom. Observation of the spin hall effect in semiconductors. *science*, 306(5703):1910–1913, 2004.
- [38] Markus König, Steffen Wiedmann, Christoph Brüne, Andreas Roth, Hartmut Buhmann, Laurens W Molenkamp, Xiao-Liang Qi, and Shou-Cheng Zhang. Quantum spin hall insulator state in hgte quantum wells. *Science*, 318(5851):766–770, 2007.
- [39] Charles L Kane and Eugene J Mele. Z 2 topological order and the quantum spin hall effect. *Physical review letters*, 95(14):146802, 2005.

- [40] B Andrei Bernevig, Taylor L Hughes, and Shou-Cheng Zhang. Quantum spin hall effect and topological phase transition in hgte quantum wells. *science*, 314(5806):1757–1761, 2006.
- [41] David Hsieh, Dong Qian, Lewis Wray, Yiman Xia, Yew San Hor, Robert Joseph Cava, and M Zahid Hasan. A topological dirac insulator in a quantum spin hall phase. *Nature*, 452(7190):970–974, 2008.
- [42] Jay D Sau, Roman M Lutchyn, Sumanta Tewari, and S Das Sarma. Generic new platform for topological quantum computation using semiconductor heterostructures. *Physical review letters*, 104(4):040502, 2010.
- [43] A Yu Kitaev. Unpaired majorana fermions in quantum wires. *Physics-Uspexhi*, 44(10S):131, 2001.
- [44] Yu A Bychkov and Emmanuel I Rashba. Oscillatory effects and the magnetic susceptibility of carriers in inversion layers. *Journal of physics C: Solid state physics*, 17(33):6039, 1984.
- [45] Gene Dresselhaus. Spin-orbit coupling effects in zinc blende structures. *Physical Review*, 100(2):580, 1955.
- [46] K Osterloh, M Baig, L Santos, P Zoller, and M Lewenstein. Cold atoms in non-abelian gauge potentials: from the hofstadter” moth” to lattice gauge theory. *Physical review letters*, 95(1):010403, 2005.
- [47] Julius Ruseckas, G Juzeliūnas, Patrik Öhberg, and Michael Fleischhauer. Non-abelian gauge potentials for ultracold atoms with degenerate dark states. *Physical review letters*, 95(1):010404, 2005.
- [48] Pengjun Wang, Zeng-Qiang Yu, Zhengkun Fu, Jiao Miao, Lianghai Huang, Shijie Chai, Hui Zhai, and Jing Zhang. Spin-orbit coupled degenerate fermi gases. *Physical review letters*, 109(9):095301, 2012.
- [49] Lawrence W Cheuk, Ariel T Sommer, Zoran Hadzibabic, Tarik Yefsah, Waseem S Bakr, and Martin W Zwierlein. Spin-injection spectroscopy of a spin-orbit coupled fermi gas. *Physical Review Letters*, 109(9):095302, 2012.
- [50] Daniel L Campbell, Gediminas Juzeliūnas, and Ian B Spielman. Realistic rashba and dresselhaus spin-orbit coupling for neutral atoms. *Physical Review A*, 84(2):025602, 2011.
- [51] Chunji Wang, Chao Gao, Chao-Ming Jian, and Hui Zhai. Spin-orbit coupled spinor bose-einstein condensates. *Physical review letters*, 105(16):160403, 2010.
- [52] Tin-Lun Ho and Shizhong Zhang. Bose-einstein condensates with spin-orbit interaction. *Physical review letters*, 107(15):150403, 2011.

- [53] Wu Cong-Jun, Ian Mondragon-Shem, and Zhou Xiang-Fa. Unconventional boseeinstein condensations from spin-orbit coupling. *Chinese Physics Letters*, 28(9):097102, 2011.
- [54] Zeng-Qiang Yu and Hui Zhai. Spin-orbit coupled fermi gases across a feshbach resonance. *Physical review letters*, 107(19):195305, 2011.
- [55] Immanuel Bloch, Jean Dalibard, and Sylvain Nascimbene. Quantum simulations with ultracold quantum gases. *Nature Physics*, 8(4):267–276, 2012.
- [56] Nathan Goldman, G Juzeliūnas, Patrik Öhberg, and Ian B Spielman. Light-induced gauge fields for ultracold atoms. *Reports on Progress in Physics*, 77(12):126401, 2014.
- [57] Liang Jiang, Takuya Kitagawa, Jason Alicea, AR Akhmerov, David Pekker, Gil Refael, J Ignacio Cirac, Eugene Demler, Mikhail D Lukin, and Peter Zoller. Majorana fermions in equilibrium and in driven cold-atom quantum wires. *Physical review letters*, 106(22):220402, 2011.
- [58] Jin-Yi Zhang, Si-Cong Ji, Zhu Chen, Long Zhang, Zhi-Dong Du, Bo Yan, Ge-Sheng Pan, Bo Zhao, You-Jin Deng, Hui Zhai, et al. Collective dipole oscillations of a spin-orbit coupled bose-einstein condensate. *Physical review letters*, 109(11):115301, 2012.
- [59] Marco Mancini, Guido Pagano, Giacomo Cappellini, Lorenzo Livi, Marie Rider, Jacopo Catani, Carlo Sias, Peter Zoller, Massimo Inguscio, Marcello Dalmondo, et al. Observation of chiral edge states with neutral fermions in synthetic hall ribbons. *Science*, 349(6255):1510–1513, 2015.
- [60] Yun Li, Lev P Pitaevskii, and Sandro Stringari. Quantum tricriticality and phase transitions in spin-orbit coupled bose-einstein condensates. *Physical review letters*, 108(22):225301, 2012.
- [61] Brandon M Anderson, Gediminas Juzeliūnas, Victor M Galitski, and Ian B Spielman. Synthetic 3d spin-orbit coupling. *Physical review letters*, 108(23):235301, 2012.
- [62] Matthew C Beeler, Ross A Williams, Karina Jimenez-Garcia, Lindsay J LeBlanc, Abigail R Perry, and Ian B Spielman. The spin hall effect in a quantum gas. *Nature*, 498(7453):201–204, 2013.
- [63] BK Stuhl, H-I Lu, LM Aycocock, D Genkina, and IB Spielman. Visualizing edge states with an atomic bose gas in the quantum hall regime. *Science*, 349(6255):1514–1518, 2015.
- [64] Seiji Sugawa, Francisco Salces-Carcoba, Abigail R Perry, Yuchen Yue, and IB Spielman. Second chern number of a quantum-simulated non-abelian yang monopole. *Science*, 360(6396):1429–1434, 2018.

- [65] Andika Putra, F Salces-Cárcoba, Yuchen Yue, Seiji Sugawa, and IB Spielman. Spatial coherence of spin-orbit-coupled bose gases. *Physical Review Letters*, 124(5):053605, 2020.
- [66] Si-Cong Ji, Jin-Yi Zhang, Long Zhang, Zhi-Dong Du, Wei Zheng, You-Jin Deng, Hui Zhai, Shuai Chen, and Jian-Wei Pan. Experimental determination of the finite-temperature phase diagram of a spin-orbit coupled bose gas. *Nature physics*, 10(4):314–320, 2014.
- [67] Philip W Anderson. Absence of diffusion in certain random lattices. *Physical review*, 109(5):1492, 1958.
- [68] Diederik S Wiersma, Paolo Bartolini, Ad Lagendijk, and Roberto Righini. Localization of light in a disordered medium. *Nature*, 390(6661):671–673, 1997.
- [69] Frank Scheffold, Ralf Lenke, Ralf Tweert, and Georg Maret. Localization or classical diffusion of light? *Nature*, 398(6724):206–207, 1999.
- [70] Martin Störzer, Peter Gross, Christof M Aegerter, and Georg Maret. Observation of the critical regime near anderson localization of light. *Physical review letters*, 96(6):063904, 2006.
- [71] Laurent Sanchez-Palencia, David Clément, Pierre Lugan, Philippe Bouyer, Georgy V Shlyapnikov, and Alain Aspect. Anderson localization of expanding bose-einstein condensates in random potentials. *Physical Review Letters*, 98(21):210401, 2007.
- [72] Juliette Billy, Vincent Josse, Zhanchun Zuo, Alain Bernard, Ben Hambrecht, Pierre Lugan, David Clément, Laurent Sanchez-Palencia, Philippe Bouyer, and Alain Aspect. Direct observation of anderson localization of matter waves in a controlled disorder. *Nature*, 453(7197):891, 2008.
- [73] Giacomo Roati, Chiara D’Errico, Leonardo Fallani, Marco Fattori, Chiara Fort, Matteo Zaccanti, Giovanni Modugno, Michele Modugno, and Massimo Inguscio. Anderson localization of a non-interacting bose-einstein condensate. *Nature*, 453(7197):895, 2008.
- [74] SS Kondov, WR McGehee, JJ Zirbel, and B DeMarco. Three-dimensional anderson localization of ultracold matter. *Science*, 334(6052):66–68, 2011.
- [75] Y Yue, CAR Sá de Melo, and IB Spielman. Enhanced transport of spin-orbit-coupled bose gases in disordered potentials. *Physical Review A*, 102(3):033325, 2020.
- [76] Arijeet Pal and David A Huse. Many-body localization phase transition. *Physical review b*, 82(17):174411, 2010.

- [77] Jens H Bardarson, Frank Pollmann, and Joel E Moore. Unbounded growth of entanglement in models of many-body localization. *Physical review letters*, 109(1):017202, 2012.
- [78] Michael Schreiber, Sean S Hodgman, Pranjal Bordia, Henrik P Lüschen, Mark H Fischer, Ronen Vosk, Ehud Altman, Ulrich Schneider, and Immanuel Bloch. Observation of many-body localization of interacting fermions in a quasirandom optical lattice. *Science*, 349(6250):842–845, 2015.
- [79] Rahul Nandkishore and David A Huse. Many-body localization and thermalization in quantum statistical mechanics. *Annu. Rev. Condens. Matter Phys.*, 6(1):15–38, 2015.
- [80] Jae-yoon Choi, Sebastian Hild, Johannes Zeiher, Peter Schauß, Antonio Rubio-Abadal, Tarik Yefsah, Vedika Khemani, David A Huse, Immanuel Bloch, and Christian Gross. Exploring the many-body localization transition in two dimensions. *Science*, 352(6293):1547–1552, 2016.
- [81] Serge Aubry and Gilles André. Analyticity breaking and anderson localization in incommensurate lattices. *Ann. Israel Phys. Soc.*, 3(133):18, 1980.
- [82] Philip George Harper. Single band motion of conduction electrons in a uniform magnetic field. *Proceedings of the Physical Society. Section A*, 68(10):874, 1955.
- [83] Joseph W Goodman. *Speckle phenomena in optics: theory and applications*. Roberts and Company Publishers, 2007.
- [84] Sidney A. Self. Focusing of spherical gaussian beams. *Appl. Opt.*, 22(5):658–661, Mar 1983.
- [85] HT Yura, Steen Grüner Hanson, RS Hansen, and B Rose. Three-dimensional speckle dynamics in paraxial optical systems. *JOSA A*, 16(6):1402–1412, 1999.
- [86] David Clément, Andrès F Varón, Jocelyn A Retter, Laurent Sanchez-Palencia, Alain Aspect, and Philippe Bouyer. Experimental study of the transport of coherent interacting matter-waves in a 1d random potential induced by laser speckle. *New Journal of Physics*, 8(8):165, 2006.
- [87] László Erdős, Benjamin Schlein, and Horng-Tzer Yau. Derivation of the gross-pitaevskii equation for the dynamics of bose-einstein condensate. *Annals of mathematics*, pages 291–370, 2010.
- [88] Franco Dalfovo, Stefano Giorgini, Lev P. Pitaevskii, and Sandro Stringari. Theory of bose-einstein condensation in trapped gases. *Rev. Mod. Phys.*, 71(3):463–512, April 1999.

- [89] Weizhu Bao, Dieter Jaksch, and Peter A Markowich. Numerical solution of the gross–pitaevskii equation for bose–einstein condensation. *Journal of Computational Physics*, 187(1):318–342, 2003.
- [90] E. G. M. van Kempen, S. J. J. M. F. Kokkelmans, D. J. Heinzen, and B. J. Verhaar. Interisotope determination of ultracold rubidium interactions from three high-precision experiments. *Phys. Rev. Lett.*, 88:93201, 2002.
- [91] Artur Widera, Fabrice Gerbier, Simon Fölling, Tatjana Gericke, Olaf Mandel, and Immanuel Bloch. Precision measurement of spin-dependent interaction strengths for spin-1 and spin-2 ^{87}Rb atoms. *New Journal of Physics*, 8(8):152, 2006.
- [92] Tin-Lun Ho. Spinor bose condensates in optical traps. *Phys. Rev. Lett.*, 81(4):742–745, July 1998.
- [93] Tetsuo Ohmi and Kazushige Machida. Bose-Einstein Condensation with Internal Degrees of Freedom in Alkali Atom Gases. *Journal of the Physics Society Japan*, 67(6):1822–1825, June 1998.
- [94] MARIA LUISA Chiofalo, Sauro Succi, and MP Tosi. Ground state of trapped interacting bose-einstein condensates by an explicit imaginary-time algorithm. *Physical Review E*, 62(5):7438, 2000.
- [95] L. W. Cheuk, A. T. Sommer, Z. Hadzibabic, T. Yefsah, W. S. Bakr, and M. W. Zwierlein. Spin-injection spectroscopy of a spin-orbit coupled fermi gas. *arxiv:1205.3483*, 2012.
- [96] A Valdés-Curiel, D Trypogeorgos, E E Marshall, and I B Spielman. Fourier transform spectroscopy of a spin–orbit coupled bose gas. *New Journal of Physics*, 19(3):33025, 2017.
- [97] Maren E. Mossman, Junpeng Hou, Xi-Wang Luo, Chuanwei Zhang, and Peter Engels. Experimental realization of a non-magnetic one-way spin switch. *Nature Communications*, 10(1):3381, 2019.
- [98] Dario Hügél and Belén Paredes. Chiral ladders and the edges of quantum Hall insulators. *Phys. Rev. A*, 89(2):23619, February 2014.
- [99] C. L. Kane and E. J. Mele. z_2 topological order and the quantum spin hall effect. *Phys. Rev. Lett.*, 95(14):146802, September 2005.
- [100] Yu A Bychkov and E I Rashba. Oscillatory effects and the magnetic susceptibility of carriers in inversion layers. *J. Phys. C*, 17(33):6039, 1984.
- [101] JH Huckans, IB Spielman, B Laburthe Tolra, WD Phillips, and JV Porto. Quantum and classical dynamics of a bose-einstein condensate in a large-period optical lattice. *Physical Review A*, 80(4):043609, 2009.